frontiers | Research Topics

Advanced modeling and simulation of nuclear reactors

Edited by
Jingang Liang, Qingming He, Shichang Liu, Yang Liu and Jiankai Yu

Published in
Frontiers in Energy Research

ISSN 1664-8714
ISBN 978-2-83252-031-4
DOI 10.3389/978-2-83252-031-4

About Frontiers

Frontiers is more than just an open access publisher of scholarly articles: it is a pioneering approach to the world of academia, radically improving the way scholarly research is managed. The grand vision of Frontiers is a world where all people have an equal opportunity to seek, share and generate knowledge. Frontiers provides immediate and permanent online open access to all its publications, but this alone is not enough to realize our grand goals.

Frontiers journal series

The Frontiers journal series is a multi-tier and interdisciplinary set of open-access, online journals, promising a paradigm shift from the current review, selection and dissemination processes in academic publishing. All Frontiers journals are driven by researchers for researchers; therefore, they constitute a service to the scholarly community. At the same time, the *Frontiers journal series* operates on a revolutionary invention, the tiered publishing system, initially addressing specific communities of scholars, and gradually climbing up to broader public understanding, thus serving the interests of the lay society, too.

Dedication to quality

Each Frontiers article is a landmark of the highest quality, thanks to genuinely collaborative interactions between authors and review editors, who include some of the world's best academicians. Research must be certified by peers before entering a stream of knowledge that may eventually reach the public - and shape society; therefore, Frontiers only applies the most rigorous and unbiased reviews. Frontiers revolutionizes research publishing by freely delivering the most outstanding research, evaluated with no bias from both the academic and social point of view. By applying the most advanced information technologies, Frontiers is catapulting scholarly publishing into a new generation.

What are Frontiers Research Topics?

Frontiers Research Topics are very popular trademarks of the *Frontiers journals series*: they are collections of at least ten articles, all centered on a particular subject. With their unique mix of varied contributions from Original Research to Review Articles, Frontiers Research Topics unify the most influential researchers, the latest key findings and historical advances in a hot research area.

Find out more on how to host your own Frontiers Research Topic or contribute to one as an author by contacting the Frontiers editorial office: frontiersin.org/about/contact

Advanced modeling and simulation of nuclear reactors

Topic editors
Jingang Liang — Tsinghua University, China
Qingming He — Xi'an Jiaotong University, China
Shichang Liu — North China Electric Power University, China
Yang Liu — Argonne National Laboratory (DOE), United States
Jiankai Yu — Massachusetts Institute of Technology, United States

Citation
Liang, J., He, Q., Liu, S., Liu, Y., Yu, J., eds. (2023). *Advanced modeling and simulation of nuclear reactors*. Lausanne: Frontiers Media SA.
doi: 10.3389/978-2-83252-031-4

Table of contents

Frontiers in Energy Research

TYPE Editorial
PUBLISHED 11 April 2023
DOI 10.3389/fenrg.2023.1189328

EDITED AND REVIEWED BY
Shripad T. Revankar,
Purdue University, United States

*CORRESPONDENCE
Shichang Liu,
✉ liu-sc@ncepu.edu.cn
Jingang Liang,
✉ jingang@tsinghua.edu.cn

RECEIVED 19 March 2023
ACCEPTED 04 April 2023
PUBLISHED 11 April 2023

CITATION
Liu S, Liang J, Yu J, He Q and Liu Y (2023), Editorial: Advanced modeling and simulation of nuclear reactors.
Front. Energy Res. 11:1189328.
doi: 10.3389/fenrg.2023.1189328

Editorial: Advanced modeling and simulation of nuclear reactors

Shichang Liu[1]*, Jingang Liang[2]*, Jiankai Yu[3], Qingming He[4] and Yang Liu[5]

[1]North China Electric Power University, Beijing, China, [2]Tsinghua University, Beijing, China, [3]Massachusetts Institute of Technology Cambridge, Cambridge, MA, United States, [4]Xi'an Jiaotong University, Xi'an, China, [5]Argonne National Laboratory (DOE), Lemont, IL, United States

KEYWORDS

modeling and simulation, reactor analysis methodology, reactor physics, thermal-hydraulics, artificial intelligence, high performance computing

Editorial on the Research Topic
Advanced modeling and simulation of nuclear reactors

Modeling and simulation (M&S) have been playing a significant role in nuclear engineering, since they enable the reproducing of the behavior of nuclear systems through computational models. However, with higher requirements for the safety and economy of nuclear reactors, the traditional M&S methods and tools for reactor analysis are being challenged. In addition, new reactor designs have been proposed, and some new reactors have gradually entered the testing and even engineering stages; the representative new reactor types include the fast-neutron reactor, pebble-bed high-temperature gas-cooled reactor, molten salt reactor, and small modular reactor, *etc.* Research on new pressurized water reactor fuels, and especially research on accident-tolerant fuel, are also in full swing. These new types of reactors and fuels also put forward new requirements for reactor calculation procedures and methods.

Advanced modeling and simulation seek to provide guidance for the design and optimization of current and next-generation reactors with newer and better models, including the ability to incorporate more underlying physics, adopt higher fidelity models, comprise difference scales, and fit various computing hardware (Wang et al., 2017; Chen et al., 2018; Zu et al., 2019a; He et al., 2021; Weng et al., 2021). The new modeling and simulation will benefit the nuclear industry by enabling scientists/engineers to analyze and optimize the performance and reliability of existing and advanced nuclear power plants (Li et al., 2018; Zheng et al., 2018; Zu et al., 2019b; Wang et al., 2021).

We have collected five papers on deterministic, Monte Carlo, and hybrid methods in reactor physics analyses by Than and Xiao, Guo et al., Zhong et al., Zhong et al., and Zhao et al.. Than's work extended the linear prolongation flux update scheme to both regular Coarse Mesh Finite Difference (CMFD) acceleration and partial CMFD acceleration in 2D multi-energy group Monte Carlo k-eigenvalue neutron transport problems. Guo et al.'s work analyzed the convergence characteristic of the neutron source iteration algorithm of the predictor–corrector quasi-static Monte Carlo (PCQS MC) method. It is found that the convergence rate of the iteration algorithm is governed by the effective spectral radius (ESR). The lower the ESR is, the faster the convergence is. In order to reduce the ESR, the asymptotic superhistory method (ASM) was developed for the PCQS MC method in the RMC code. Zhong et al.'s work applied the Monte Carlo code OpenMC to build the Korean system-integrated modular advanced reactor (SMART) full-core model to optimize the SMART power performance effectively and find an efficient neutron reflector choice with good material properties. Zhao et al.'s work analyzed the numerical results of eigenvalues, assembly power distributions, and energy spectrums in the burnup procedure of a small lead-based breeding reactor (SLBR-50) using the Monte-Carlo code RMC.

We have collected three papers on computational fluid dynamics (CFD) and applications by Jiang et al., Wang et al., Li et al.. Jiang et al.'s work carried out an investigation on the vibration response characteristics and influencing factors of the fuel rods of EPR based on ANSYS-APDL. Wang et al.'s work conducted a thermal analysis with helium flow in various channel designs based on CFD methods to determine a dimension-optimized rod bundle channel. An experimental study then followed in order to pick up an appropriate gas flow model through further numerical simulation. Finally, a helium flow in the bundle channels consisting of 217 rods was simulated using this chosen flow model, showing that the method satisfies the requirements of the basic thermal analysis of a newly designed gas-cooled reactor with an open lattice structure. Li et al.'s work analyzed the effect of different ventilation scenes on tritium removal efficiency. The study set up six different ventilation scenes and carried out the numerical simulation of tritium migration and mixing behavior based on Fluent.

We have collected three papers on computer code development, verification, and validation by Zhang et al., Guo et al., and Zhang H. et al.. Zhang B. et al. Developed a lead–bismuth-cooled fast reactor calculation code system named MOSASAUR to meet the simulation requirements of the lead–bismuth-cooled fast reactor (LBFR) engineering design. Guo et al.'s work built a steady-state model of the NuScale reactor and simulated a turbine trip transient using the thermal hydraulic module CESAR of the severe accident code ASTEC. Zhang H. et al.'s work elaborated the main features of SHARK's "resonance-transport-depletion" coupling system and presented and discussed some verification and validation (VandV) results in the current phase.

We have collected one paper on artificial intelligence applications in nuclear energy by Li et al.. Li et al.'s work analyzed the main theory and feasible improvements of the fine-mesh subgroup method (FSM). Several pin cell and lattice problems were applied to test the performance of the FSM, and the particle swarm optimization method was adopted to find the better group structure.

We have collected one paper on other applications related to the advanced modeling and simulation of nuclear reactors by Lei et al.. Lou et al.'s work analyzed the power level and economy of lead-based modular nuclear power and designed and analyzed the economy of fast reactors of different power levels with a 2,000 equivalent full power day (EFPD) lifetime, such as 100 MWt, 300 MWt, 500 MWt, 700 MWt, and 1,000 MWt thermal power.

With the increasing demands of high-fidelity analysis and the development of computer technology, advanced modeling and simulation are becoming more and more attractive. Neutron transport methods (both deterministic and Monte Carlo methods), CFD, artificial intelligence, and so on show very promising potential for the design and analysis of a new-generation nuclear energy system. The calculation time and footprint consumption will hinder the application of these advanced modeling and simulation methods in industry. In the future, these methods should embrace high-performance computing to accelerate their industry application.

Author contributions

SL, JL, JY, QH and YL contributed to conception and design of the study. SL and JL wrote the first draft of the manuscript. All authors contributed to manuscript revision, read, and approved the submitted version.

Funding

This work was partially supported by Project 12175067 of the National Natural Science Foundation of China, the Natural Science Foundation of Hebei Province (no. A2022502008), the Fundamental Research Funds for the Central Universities (2022JG002), and the Young Elite Scientists Sponsorship Program (2020QNRC001) of the China Association for Science and Technology.

Conflict of interest

The authors declare that the research was conducted in the absence of any commercial or financial relationships that could be construed as a potential conflict of interest.

Publisher's note

References

Chen, J., Liu, Z., Zhao, C., He, Q., Zu, T., Cao, L., et al. (2018). A new high-fidelity neutronics code NECP-X. *Ann. Nucl. Energy* 116, 417–428. doi:10.1016/j.anucene.2018.02.049

He, Q., Zheng, Q., Li, J., Wu, H., Shen, W., Cao, L., et al. (2021). NECP-MCX: A hybrid monte-carlo-deterministic particle-transport code for the simulation of deep-penetration problems. *Ann. Nucl. Energy* 151, 107978. doi:10.1016/j.anucene.2020.107978

Wang, J., Liu, S., Li, M., Xiao, P., Wang, Z., Wang, L., et al. (2021). Multiobjective genetic algorithm strategies for burnable poison design of pressurized water reactor. *Int. J. Energy Res.* 45 (8), 11930–11942. doi:10.1002/er.5926

Wang, K., Liu, S., Li, Z., Wang, G., Liang, J., Yang, F., et al. (2017). Analysis of BEAVRS two-cycle benchmark using RMC based on full core detailed model. *Prog. Nucl. Energy* 98, 301–312. doi:10.1016/j.pnucene.2017.04.009

Weng, M., Liu, S., Liu, Z., Qi, F., Zhou, Y., and Chen, Y. (2021). Development and application of Monte Carlo and COMSOL coupling code for neutronics/thermohydraulics coupled analysis. *Ann. Nucl. Energy* 161, 108459. doi:10.1016/j.anucene.2021.108459

Zhao, C., Lou, L., Zhang, B., Zhou, B., Peng, X., and Wang, L. (2022). Research of the neutronics performance improvement based on the small lead-based fast reactor slbr-50. Available at SSRN 4065478.

Zheng, Y., Du, X., Xu, Z., Zhou, S., Liu, Y., Wan, C., et al. (2018). Sarax: A new code for fast reactor analysis part i: Methods. *Nucl. Eng. Des.* 340, 421–430. doi:10.1016/j.nucengdes.2018.10.008

Zu, T., Xu, J., Tang, Y., Bi, H., Zhao, F., Cao, L., et al. (2019). Necp-atlas: A new nuclear data processing code. *Ann. Nucl. Energy* 123, 153–161. doi:10.1016/j.anucene.2018.09.016

Zu, T., Xu, J., Tang, Y., Bi, H., Zhao, F., Cao, L., et al. (2019). NECP-atlas: A new nuclear data processing code. *Ann. Nucl. Energy* 123, 153–161. doi:10.1016/j.anucene.2018.09.016

frontiers | Frontiers in Energy Research

METHODS
published: 15 July 2022
doi: 10.3389/fenrg.2022.963990

Analysis on Emergency Treatment Effect of Tritium Leakage Accident in the Nuclear Reactor Under Different Ventilation Conditions

Changjun Li, Xingfu Cai, Mingqing Xiao, Yonggang Huo, Peng Xu and Sufen Li*

Xi'an Research Institute of High Technology, Xi'an, China

The high-pressure tritium leakage is a typical nuclear leakage accident, which can cause radioactive harm. The study aims at the tritium leakage problem in the high-pressure vessel of a nuclear reactor, installing a typical tritium leakage scenario and establishing the thermodynamic model of tritium leakage behavior which describes the transient process of tritium leakage. To analyze the effect of different ventilation scenes on tritium removal efficiency, the study sets up six different ventilation scenes and carries out the numerical simulation of tritium migration and mixing behavior based on Fluent. The result shows that different ventilation scenes will form different swirl distributions; the more complex the swirl distribution is, the faster the tritium concentration decreases. The shortest time required to decrease tritium concentration in space to the background level at the ventilation rate of 1 $m^3 s^{-1}$ is about 830 s and the longest time is about 1100 s. The overall tritium removal efficiency can be effectively improved when the swirl concentration distribution area is opposite to the exhaust outlet position. The setting method of ventilation is optimized, which provides technical support for the emergency treatment of tritium leakage accidents in the room.

Keywords: tritium leakage, emergency treatment, optimal ventilation, nuclear reactor, tritium removal efficiency

Edited by:
Shichang Liu,
North China Electric Power University, China

Reviewed by:
Wenxi Tian,
Xi'an Jiaotong University, China
Chen Hao,
Harbin Engineering University, China

****Correspondence:***
Xingfu Cai
17791477740@sina.cn

Specialty section:
This article was submitted to Nuclear Energy, a section of the journal Frontiers in Energy Research

Received: *08 June 2022*
Accepted: *10 June 2022*
Published: *15 July 2022*

Citation:
Li C, Cai X, Xiao M, Huo Y, Xu P and Li S (2022) Analysis on Emergency Treatment Effect of Tritium Leakage Accident in the Nuclear Reactor Under Different Ventilation Conditions. Front. Energy Res. 10:963990. doi: 10.3389/fenrg.2022.963990

INTRODUCTION

Tritium is one of the raw materials for nuclear fusion reactions. It will decay and release beta rays in the natural environment, which poses radioactive hazards to people and the environment (Mei et al., 2020). Therefore, tritium gas is usually stored in high-pressure vessel of a nuclear reactor in the process of tritium storage. The pressure inside the storage vessel is hundreds of normal atmospheres, and the tritium gas will quickly leak into the air and form a radioactive environment when the storage vessel is damaged accidentally due to external action. Ventilation is considered to be the best emergency treatment method for tritium leakage that can effectively decrease the tritium concentration in the room. However, different ventilation scenes have different effects on tritium removal efficiency. Therefore, it is of great practical significance to study the emergency treatment effect of tritium leakage accidents in high-pressure vessels of a nuclear reactor under different ventilation conditions.

In terms of tritium release experimental study, a great deal of research studies about intentional tritium release experiments and numerical simulation of three-dimensional fluid have been carried out aiming at nuclear fusion tritium safety. From the 1980s to the early 21st century, Los Alamos National Laboratory (LANL) built a Tritium Systems Test Assembly (TSTA) (Carlson et al., 1985;

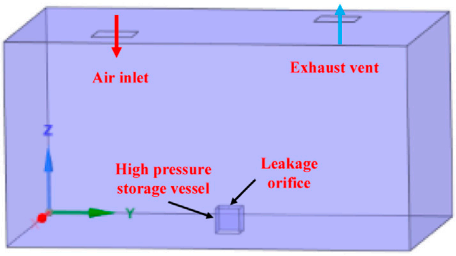

FIGURE 1 | Physical model.

Hayashi et al., 1998; Kobayashi et al., 2008) and the Japan Atomic Energy Research Institute (JAERI) built a Caisson Assembly for Tritium Safety (CATS) (Hayashi et al., 2000; Iwai et al., 2001; Yasunori et al., 2001; Cristescu et al., 2005; Munakata et al., 2010) to carry out a series of experimental studies on intentional tritium release behavior and tritium removal performance. However, the ventilation scene in the experiment is single, and there are few studies on the influencing factors of tritium removal efficiency. In terms of numerical simulation of tritium leakage, many scholars have also carried out a lot of research works on tritium behavior simulation. Li et al. (2020) carried out a numerical simulation of tritium diffusion in low-pressure tritium leakage accidents of tritium storage vessels in closed and open spaces. Liu (2017)and Liu et al. (2017) studied the effect of ventilation on tritium concentration and tritium diffusion in a TBM glove box under tritium leakage accident conditions, but few ventilation scenarios were set. Wei (2021) carried out simulation research on the tritium migration and tritium removal behavior under accident conditions in a tritium plant room and analyzed the effects of room ventilation design, temperature conditions, and wall materials on tritium removal. In emergency ventilation optimization design, Arjmandi et al. (2022) studied the effects of four ventilation scenarios on indoor virus propagation and realized the optimal design of ventilation system to minimize the indoor COVID-19 virus propagation. However, the tritium gas is essentially different from virus, and the optimal design of a ventilation system to reduce virus transmission may not be applicable to tritium gas.

To sum up, a lot of research work has been carried out on tritium behavior simulation under tritium leakage accident conditions at home and abroad, and the influence of ventilation on tritium concentration has been analyzed. However, the setting of the ventilation scene is also single, and there is less research on tritium leakage accidents to maximize the tritium removal efficiency of ventilation system optimization design. In this study, the numerical simulation of high-pressure tritium release behavior in a confined space is carried out according to the characteristics of fixed and rapid tritium release in a tritium leakage accident of high-pressure storage vessel, which is compared with CATS test data. Six different ventilation scenes are set, and the influence of different ventilation scenes on tritium removal efficiency is analyzed. The study will get the shortest ventilation time required to decrease tritium concentration to the background level for the tritium leakage accident in a room and provide the ventilation setting methods with the highest tritium removal efficiency, which provides technical support for the emergency treatment of tritium leakage accident.

TRITIUM LEAKAGE BEHAVIOR MODEL IN A NUCLEAR REACTOR

The pressure inside the storage vessel is hundreds of normal atmospheres; when the tritium gas is stored in a high-pressure environment, the molecular behavior of tritium deviated from ideal gas behavior. The ideal gas molecular compressibility factor is 1, and the tritium molecular compressibility factor is greater than 1 in a high-pressure environment. To accurately describe tritium leakage behavior in a high-pressure vessel of a nuclear reactor, the study adopts the Abel–Noble equation of state (AN-EOS) (Li et al., 2013) thermodynamic model to modify the molecular specific volume of tritium gas. The relation between the pressure in the vessel and the correction term is given as follows:

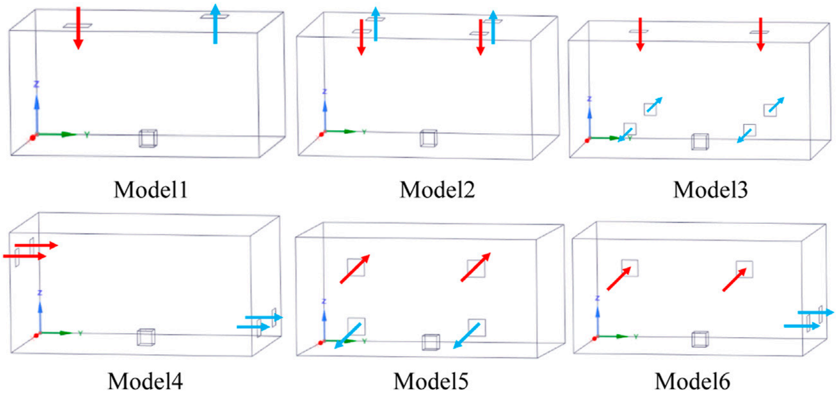

FIGURE 2 | Optimal design of the vent.

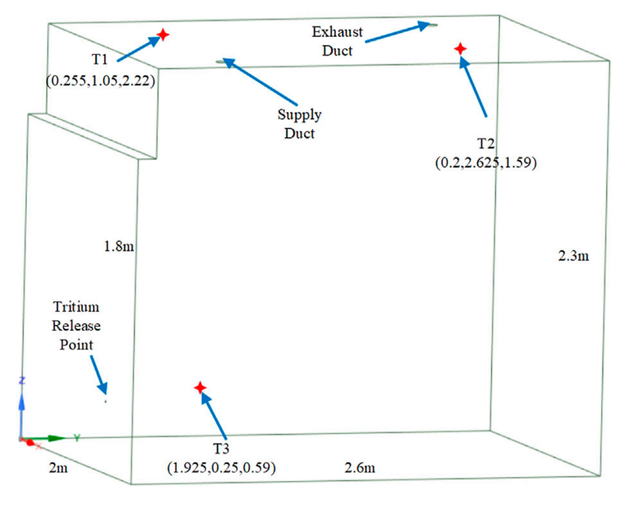

FIGURE 3 | Geometrical model of Caisson.

$$p(v-b)=R_gT, \tag{1}$$

where p is the pressure, v is the specific volume, b is the correction term of gas molecule-specific volume, b = $7.691 \times 10^{-3}\ \mathrm{m}^3\ \mathrm{kg}^{-1}$, R_g is the gas constant, and T is the temperature.

Assuming that the gas leakage process is an isentropic process, according to the AN-EOS model (Johnston, 2005):

$$p(v-b)^k = constant, \tag{2}$$

where k is the ratio of heat capacity.

Because the volume of the high-pressure storage vessel is constant, then,

$$\begin{gathered} \mathrm{d}(\mathrm{V}) = 0, \\ \mathrm{d}(m_i v_i) = 0, \end{gathered} \tag{3}$$

$$\begin{cases} \dfrac{\mathrm{d}p_i}{p_i} = -\mathrm{k}\dfrac{\mathrm{d}v_i}{v_i - b}, \\ \dfrac{\mathrm{d}m_i}{m_i} = \dfrac{\mathrm{d}v_i}{v_i}. \end{cases} \tag{4}$$

Solving equations by an iterative method, we get

$$\begin{cases} v_i^{j+1} = v_i^j\left(1 + \dfrac{Q_m^j}{m_i^j} * \Delta t\right), \\ p_i^{j+1} = p_i^j\left(1 - \mathrm{k} * \dfrac{v_i^{j+1} - v_i^j}{v_i^j - b}\right), \\ m_i^{j+1} = m_i^j - Q_m^j * \Delta t, \\ T_i^{j+1} = \dfrac{1}{R_g} p_i^{j+1}\left(v_i^{j+1} - b\right), \end{cases} \tag{5}$$

where V is the volume of the storage vessel, m_i is the mass inside the storage vessel, v_i is the specific volume inside the vessel, p_i is the pressure inside the vessel, j is the iteration step, Q_m is the mass flow rate at the orifice, Δt is the time step, and T_i is the temperature inside the vessel.

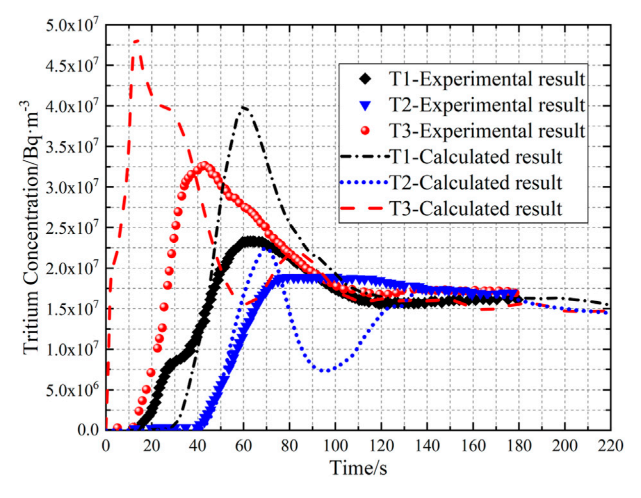

FIGURE 4 | Tritium concentration comparison between experimental results and calculated results at monitoring points.

NUMERICAL SIMULATION OF HIGH-PRESSURE TRITIUM LEAKAGE

Scene Construction

The object of this study is a high-pressure storage vessel of a nuclear reactor, with the pressure of the storage vessel being 34.5 MPa and the temperature being 300 K, ignoring the change of tritium gas mass fraction due to decay in the storage vessel; installing the tritium leakage scene model is as follows:

1) Assuming tritium leakage occurs in a cuboid space, and the cuboid space is 5^{W} m × 3^{D} m × 2.5^{H} m, where installing detritiation vent, as shown in **Figure 1**.
2) The high-pressure storage vessel is simplified as a cube (0.3^{W} m × 0.3^{D} m × 0.3^{H} m), which is placed in the center of the scene ground, as shown in **Figure 1**. A leakage orifice is simplified as a circular hole (10 mm diameter), which remains constant during leakage.

Optimal Design of the Vent

In this study, the tritium leakage numerical simulation is carried out in six ventilation vent designs, and the total area of the air inlet and exhaust outlet in each model is equal. The vents of model 1 and model 2 are set at the roof of the space; the sizes of the inlet and outlet in model 1 are 0.5 × 0.5 m, and the sizes of the inlet and outlet in model 2 are 0.354 × 0.354 m, as shown in **Figure 2** model 1 and model 2. The air inlet of model 3 is set at the roof of the space with a size of 0.354 × 0.354 m, and the outlet is set on the two walls in the x-axis direction with a size of 0.25 × 0.25 m, as shown in **Figure 2** model 3. The air inlet and outlet of model 4 are set on the two walls in the y-axis direction with a size of 0.354 × 0.354 m, as shown in **Figure 2** model 4. The air inlet and outlet of model 5 are set on the front wall with a size of 0.354 × 0.354 m, as shown in **Figure 2** model 5. The air inlet of model 6 is set on the front wall, and the outlet of model 6 is set on the side wall, with both sizes being 0.354 × 0.354 m, as shown in **Figure 2** model 6.

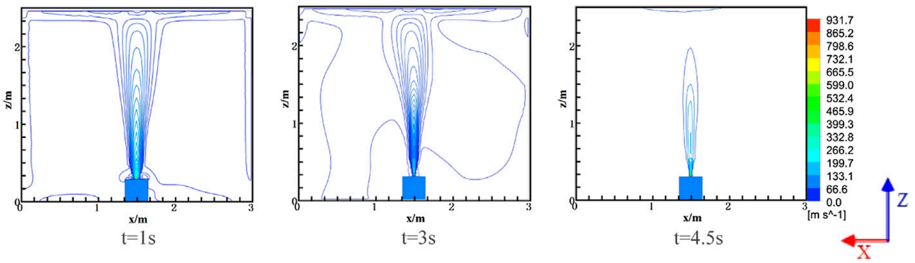

FIGURE 5 | Velocity contour in the XZ plane at y = 2.5 m.

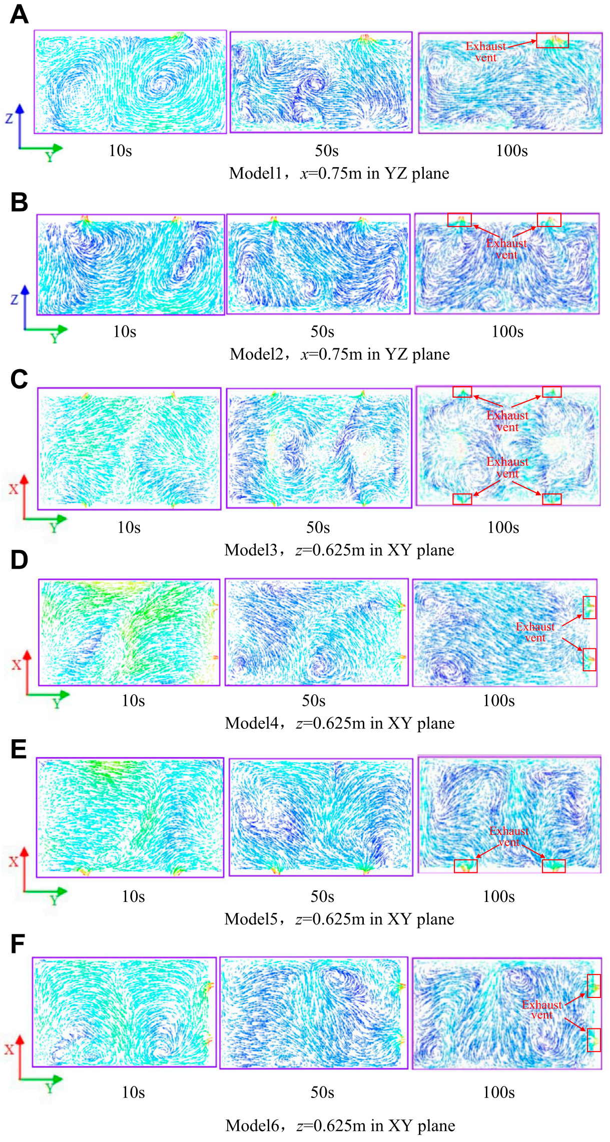

FIGURE 6 | Tritium gas flow velocity vector, m·s^{-1}.

Fluent Numerical Solution

In mesh division, the physical model is divided by an unstructured mesh of poly-hexcore. The leakage orifice adopts local mesh refinement and adds boundary layers to the wall to describe the gas flow in the leakage orifice and the boundary area for refinement.

In the Fluent solver setting, the flow of tritium gas in the air is multiple species transport, and it has complex flow types including jet and diffusion, setting the species transport model and the realizable k–ε turbulence model (Shih et al., 1995).

In the boundary condition setting, the tritium gas leakage outlet is defined as a mass flow inlet and establishes the relationship between mass flow rate, leakage outlet pressure, temperature, and the time by using the user-defined function (UDF) to compile interface codes, and the ventilation duct is defined as the velocity inlet. In the material setting (Huang, 2002), the mole mass of tritium is 6.034 kg kmol^{-1}, and the diffusion coefficient in air is 7.41×10^{-6} m^2 s^{-1}. The wall material of the confined space is calcium-carbonate, and the storage wall material is steel. The semi-implicit method for pressure-linked equations is used to simulate the flow field.

RESULTS AND DISCUSSION

Simulation Verification of "Caisson"

The simulation results were compared with the experimental data of "Caisson" tritium release in JAERI to verify the reliability of the numerical simulation method for tritium leakage (Hayashi et al., 2000). The simulation conditions are the same as the "Caisson" tritium release experiment, and numerical simulation is carried out based on Fluent. **Figure 3** shows the geometrical model of "Caisson," selecting three monitoring points in "Caisson," T1, T2, and T3, to monitor the variation of tritium concentration, as shown in **Figure 4**.

Figure 4 shows the tritium concentration comparison between calculated results and "Caisson" experimental results; the result shows that the tritium concentration at T3 nearest tritium release point increases rapidly in the tritium release initial stage and the tritium concentration at T2 farthest tritium release point

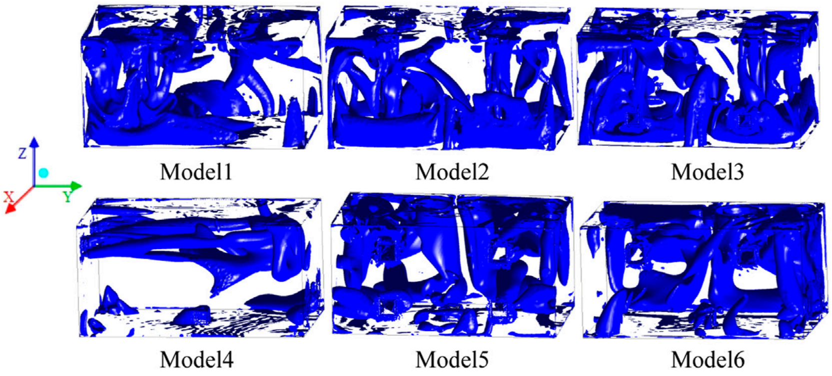

FIGURE 7 | Vortex core region distribution.

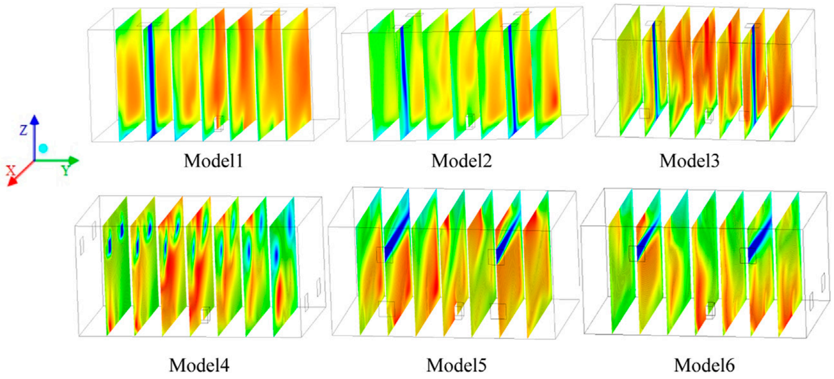

FIGURE 8 | t = 830 s, tritium concentration distribution in the space, kg·m^{-3}.

increases gradually at 40 s. The time of tritium concentration increasing is different between calculated results and experimental results, and the main reason is that the time lag of tritium gas flowing into "Caisson" after release is not considered in simulation. The simulated tritium concentration is larger than that of the experimental, and the tritium concentration variation at monitoring points has obvious fluctuations. The tritium concentration at T2 decreases and increases in the range of 70–120 s before becoming stable, which may be caused by the weak airflow nearing the exhaust outlet. There are some errors in the calculated results that may be caused by less amount of tritium release. The tritium concentration tends to be stable in calculated and experimental results after 120 s of tritium release, and both tritium concentration stable values of calculated results and experimental results are 1.5 × 10^7 Bq m^{-3}. The calculated results are in good agreement with experimental results. The result shows that the model can be used to simulate tritium release behavior.

Transient Behavior of Tritium Leakage

In order to accurately describe the transient behavior of tritium leakage, the tritium leakage process is simulated and gets the XZ plane tritium leakage velocity contour at y = 2.5 m when t = 1s, t = 3s, and t = 4.5 s, as shown in **Figure 5**.

Figure 5 shows the tritium leakage velocity contour in the XZ plane at y = 2.5 m; it can be seen from the simulation results that the leakage rate of tritium gas is large, and the flow in space is jet flow in the early stage of tritium leakage in the high-pressure storage vessel. The jet flow of tritium gas is impeded by the closed space, as shown in **Figure 5** t = 1 s. With the continuous leakage, the leakage velocity of tritium gas decreases, and the jet flow phenomenon weakens gradually, as shown in **Figure 5** t = 4.5 s.

Velocity Vector Distribution

In order to analyze the effect of different ventilation scenes on the tritium gas migration after leakage, the simulation calculation is carried out in six ventilation scenes, with the ventilation flow rate remained at 1 m$^{3 \cdot s^{-1}}$, and the tritium gas flow velocity vectors at different time points in the plane with the exhaust vent in six scene spaces are obtained, as shown in **Figure 6**.

Figure 6 shows the tritium gas flow velocity vector at different time points in the plane with an exhaust vent in six scene spaces. The part labels of **Figures 6A–F** expressed as the 216 location of exhaust vent plane in six scenes space. The figure shows that there are different sizes and quantities of vortexes in the velocity field of

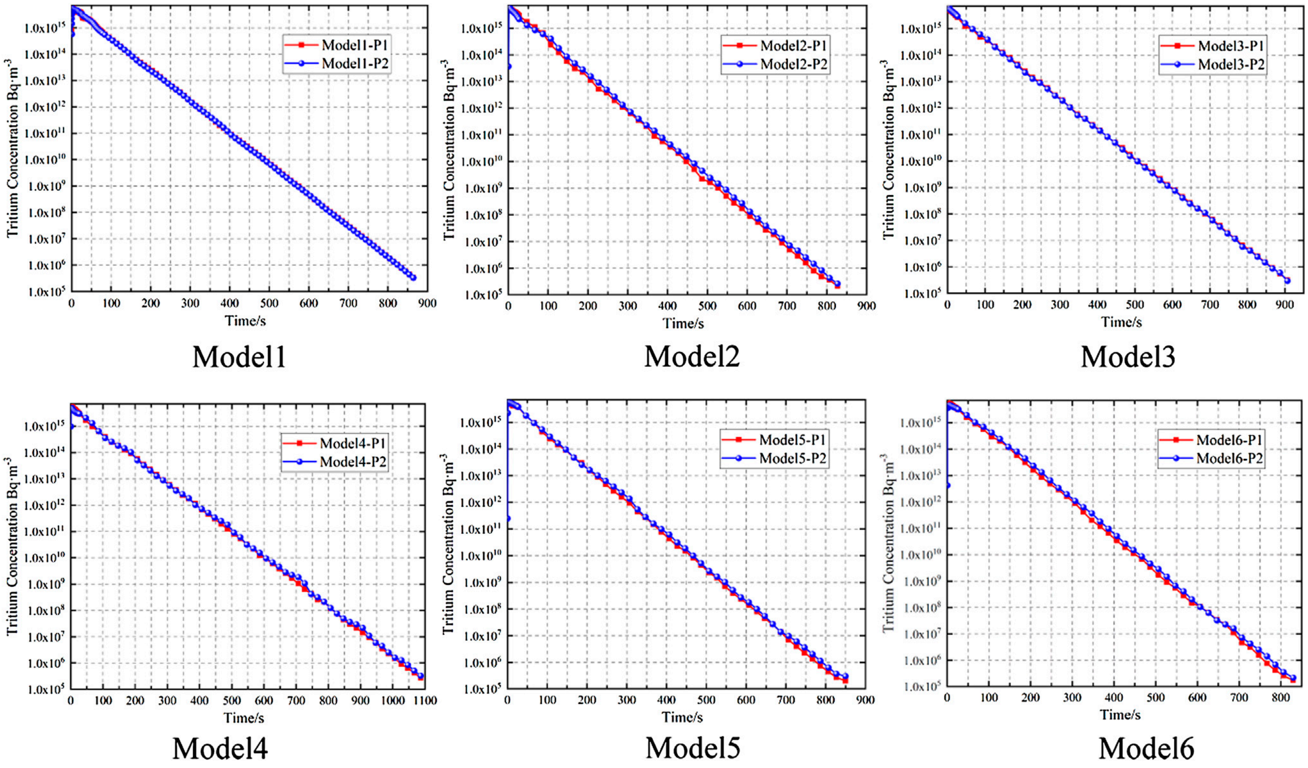

FIGURE 9 | Variation of tritium concentration at monitoring points in the space.

the plane where the exhaust vents of the six models are located. The vortexes in model 1 at 10 s are stronger and approximately symmetric distribution. With the continuous ventilation, the vortex gradually moves away from the vent and mainly distributes in the edge of the plane when the airflow in the space tends to be stable (t = 100 s), and the airflow of the exhaust vent mainly comes from the right bottom of the plane, as shown in **Figure 6A**. Model 2 increases the vent compared with model 1, which leads to a total different formation and distribution of vortex in the plane. There are fewer vortexes in the plane before the airflow in the space is stable, and more vortexes are formed in the plane after the airflow is stable. Moreover, the swirling flow in the plane can flow to the exhaust vent in different directions, as shown in **Figure 6B**. Model 3 increases two exhaust vents and changes the position of the exhaust vent compared with model 2. According to the figure, the gas flow rate is larger, and the vortex phenomenon is not obvious at 10 s. As the velocity of gas flow decreases in the space, the swirling flow of the velocity field intensifies gradually. The vortex distribution is complex at 100 s; however, the airflow of the exhaust vent only comes from the swirl near four corners, and the swirl in the middle area of the plane does not flow to the exhaust vent, as shown in **Figure 6C**. The flow velocity is large, and the vortex phenomenon is not obvious in the plane of model 4 before the airflow is stable, and the vortex is mainly distributed on the side away from the exhaust vent after the airflow is stable (t = 100 s). Most of the airflow in the plane flows to the vortex concentration area, and only a few flows to the exhaust vent, as shown in **Figure 6D**. The swirl intensity is weak in the exhaust vent plane of model 5. When t = 10 s, the airflow velocity is large, and the left airflow flows from left to right and the right airflow flows from right to left; the airflow gradually flows to the two exhaust vents as the airflow rate decreases, as shown in **Figure 6E**. The exhaust vent of model 6 is the same as model 4; the vortex is distributed at the bottom of the plane and approximately symmetric at 10 s, and the left swirling flow is clockwise, while the right swirling flow is counterclockwise. The number of swirling flows in model 6 is more than that in model 4, and the distribution is more complex. The swirling flow in the middle area flows to two exhaust vents, as shown in **Figure 6F**.

Vortex Core Region

The setting of air inlet and exhaust outlet has a great influence on gas flow in the space. In order to analyze the influence of airflow in different ventilation scenes on tritium gas mixing behavior, simulation calculation is carried out on the scene after airflow is stable, obtaining the distribution of vortex core region in the space with a vortex strength of 1 s^{-1}, as shown in **Figure 7**.

Figure 7 shows the distribution of the vortex core region in the space with a vortex strength of 1 s^{-1} after the airflow is stable. The result shows that the vortex core region with a vortex strength of 1 s^{-1} is mainly distributed in the air inlet and a few are distributed in the exhaust vent of the six models. The vortex core region distribution in model 2, model 3, and model 6 is more complex, while the vortex core region distribution in model 4 is less complex. The vortex core region is mainly distributed on the left side of the space in model 1 and the vortex core region is mainly distributed in the lower part of the space in model 2 and model 3, while the vortex core region is mainly distributed in the upper part of the space in model 4, model 5, and model 6. The result shows that the setting of the air inlet has a great influence on the distribution of the vortex core region.

Tritium Concentration Distribution

In order to analyze the tritium concentration distribution in the process of detritiation in the six ventilation scenes, the simulation calculation is carried out at 830 s after tritium leakage, obtaining the tritium concentration distribution in the space, as shown in **Figure 8**. In order to accurately analyze the variation of tritium concentration and quantitatively analyze the ventilation time required to decrease tritium concentration to the background level after a tritium leakage accident, two points P1 and P2 are selected in the space to monitor the variation of tritium concentration, as shown in **Figure 9**. The point P1 (1.5, 2.5, and 1.5) is above the storage vessel, and the point P2 is the point with high tritium concentration in six models, model 1-P2 (0.75, 3.25, and 1.5), model 2-P2 (0.75, 4.375, and 0.625), model 3-P2 (1.5, 2.5, and 2.2), model 4-P2 (2.25, 0.625, and 0.225), model 5-P2 (0.75, 1.875, and 0.625), and model 6-P2 (2.25, 4.375, and 0.625).

Figure 8 shows the tritium concentration distribution of six ventilation scenes at 830 s. The result shows that the tritium concentration of model 1 is lower in the air inlet area and higher in the exhaust outlet area. According to the result of **Figure 7** model 1, the tritium concentration in the swirl concentration distribution region is significantly lower than that in the weak swirl intensity region. Model 2 increases an air inlet and outlet compared with model 1 with the same air inlet and outlet area. Model 2 has a lower tritium concentration in the space except for a higher concentration on the right side of the exhaust vent. There is low tritium concentration in the concentration vortex core region and high tritium concentration in the weak intensity vortex core region, which indicates that the vortex can promote the mixture of air and tritium gas and effectively decrease the tritium concentration. The tritium gas in model 3 is mainly distributed in the central region of the space and is obviously higher than that in model 1 and model 2. Although the vortex core region distribution in model 3 is similar to model 2, the tritium concentration is lower in model 2 with a different exhaust vent setting. The result shows that the tritium concentration is affected not only by the vortex core region but also by the exhaust vent setting. The mass fraction of tritium is less than that of air, and it is distributed in the upper part of the space under the effect of full buoyancy. When the exhaust vent is set on the roof, the diluted tritium gas can be effectively discharged. When the exhaust vent is set at the lower part of the space, it can only decrease local tritium concentration and has a low tritium removal efficiency for the upper part of the space. The tritium concentration in the upper part region is obviously lower than that in the lower part region in model 4, which indicates that the tritium concentration dilutes faster in the upper part affected by swirling flow. According to the results of **Figure 6D** model 4, most of the airflow flows away from the exhaust vent, and only a few airflow flows to the exhaust vent, which leads to a high tritium concentration in an area far away from the exhaust vent and has a low tritium removal efficiency in model 4. There is a little difference in tritium concentration distribution in the space between model 5 and model 6. According to the results of **Figure 6F** model 6, the swirl distribution in the exhaust vent plane is more complex than that in model 5, which makes the tritium concentration decrease faster in model 6 and has higher tritium removal efficiency.

Figure 9 shows the variation of tritium concentration at monitoring points in the space. In order to analyze the tritium concentration variation clearly, the axis of ordinate is distributed logarithmically. The result shows that the tritium concentration at two monitoring points in six ventilation scene spaces has little difference and can be ignored. It needs to ventilate for about 860 s for the tritium concentration in the space to decrease to the background level (Cristescu et al., 2005) (3×10^5 Bq m^{-3}) in model 1, about 830 s in model 2, 910 s in model 3, 1100 s in model 4, 850 s in model 5, and 830 s in model 6. It can be seen that there is less ventilation time in the model with complex vortex core region distribution and more ventilation time in the model with weak intensity vortex core region distribution. When the vortex core region is distributed in the low part area and the exhaust vent is set in the low part of the space, it can only improve local tritium removal efficiency. When the vortex core region is distributed in the lower part area while the exhaust vent is set in the upper part of the space or the vortex core region is distributed in the upper part area with a lower part exhaust vent setting, it can improve overall tritium removal efficiency. The result shows that the tritium removal efficiency is not only affected by swirling flow but also by the exhaust vent position. In summary, model 2 and model 6 require less ventilation time after tritium leakage and has the highest tritium removal efficiency, which can be regarded as optimization emergency ventilation design methods under the tritium leakage accident conditions.

CONCLUSION

Aiming at the problem of tritium leakage accident of high-pressure storage vessel in the room, the study carries out the numerical simulation research of tritium high-pressure release behavior based on Fluent, using UDF to perform the coupling calculation of the AN-EOS tritium leakage model and Fluent, which describes the transient behavior of high-pressure tritium leakage. Then, the simulation calculation of tritium migration and mixing behavior in six ventilation scenes is carried out, and the effect of different ventilation scenes on tritium removal efficiency is analyzed in the study, which realizes the optimal design of emergency ventilation under the tritium leakage accident conditions. The result shows that the tritium gas forms a strong jet flow in the space when the high-pressure storage vessel causing tritium leakage in the room, and the closed space can impede the jet flow of tritium gas. In the tritium removal phase, different ventilation scenes lead to different swirl distributions in the space, and the complex distribution of the vortex core region can effectively promote the mixing behavior of tritium gas. Therefore, the tritium concentration decreases faster in the concentration vortex core region while slower in weak swirl intensity. When the distribution of the vortex core region is opposite to the position of the exhaust vent, the overall tritium removal efficiency in the space can be effectively improved and it can only improve local tritium removal efficiency, while the distribution of the vortex core region is the same with the position of the exhaust vent. Model 2 and model 6 ventilation scenes can form complex vortex core region distributions in the space, which leads to the least ventilation time of tritium concentration to recover to the environmental level and the highest overall tritium removal efficiency. They can be used as the optimal design of tritium leakage emergency ventilation in the room.

DATA AVAILABILITY STATEMENT

The original contributions presented in the study are included in the article/Supplementary Material; further inquiries can be directed to the corresponding author.

AUTHOR CONTRIBUTIONS

CL: writing—original draft. XC: conceptualization and methodology. MX: formal analysis and investigation. YH: validation. PX: writing—review and editing. SL: resources.

REFERENCES

Arjmandi, H., Amini, R., Kashfi, M., Abikenari, M. A., and Davani, A. (2022). Minimizing the COVID-19 Spread in Hospitals through Optimization of Ventilation Systems. *Phys. Fluids* 34 (3), 037103. doi:10.1063/5.0081291

Carlson, R. V., Damiano, F. A., and Binning, K. E. (1985). Operation of the Room Air Tritium Removal System at the Tritium Systems Test Assembly. *Fusion Technol.* 8, 2190–2195. doi:10.13182/fst85-a24607

Cristescu, I.-R., Travis, J., Iwai, Y., Kobayashi, K., and Murdoch, D. (2005). Simulation of Tritium Spreading in Controlled Areas after a Tritium Release. *Fusion Sci. Technol.* 48 (1), 464–467. doi:10.13182/fst05-a966

Hayashi, T., Kobayashi, K., Iwai, Y., Yamada, M., Suzuki, T., O'hira, S., et al. (2000). Tritium Behavior in the Caisson, a Simulated Fusion Reactor Room. *Fusion Eng. Des.* 51-52, 543–548. doi:10.1016/s0920-3796(00)00214-3

Hayashi, T., Kobayashi, K., Iwai, Y., Yamanishi, T., Nishi, M., Okuno, K., et al. (1998). Tritium Behavior Intentionally Released in the Radiological Controlled Room under the US-Japan Collaboration at TSTA/LANL. *Fusion Technol.* 34, 521–525. doi:10.13182/fst98-a11963665

Huang, J. (2002). *Industrial Gas Manual[M]*. Beijing: Chemical Industry Press.

Iwai, Y., Hayashi, T., Kobayashi, K., and Nishi, M. (2001). Simulation Study of Intentional Tritium Release Experiments in the Caisson Assembly for Tritium Safety at the TPL/JAERI. *Fusion Eng. Des.* 54, 523–535. doi:10.1016/s0920-3796(00)00581-0

Johnston, I. A. (2005). *The Noble-Abel Equation of State: Thermodynamic Derivations for Ballistics Modelling[R]*. Melbourne, Australia: Defence Science and Technology Organisation Edinburgh (Australia) Weapons Systems Div.

Kobayashi, K., Hayashi, T., Iwai, Y., Yamanishi, T., Willms, R. S., and Carlson, R. V. (2008). Tritium Behavior Intentionally Released in the Room. *Fusion Sci. Technol.* 54 (1), 311–314. doi:10.13182/fst08-a1820

Li, W., Kou, H., Zeng, X., Cui, Y., Chen, H., and Wang, F. (2020). Numerical Simulations on the Leakage and Diffusion of Tritium. *Fusion Eng. Des.* 159, 111749. doi:10.1016/j.fusengdes.2020.111749

Li, X., Bi, J., and Christopher, D. M. (2013). Thermodynamic Models of Leaks from High-Pressure Hydrogen Storage Systems[J]. *J. Tsinghua Univ. Sci. Technol.* 53 (4), 503–508. doi:10.16511/j.cnki.qhdxxb.2013.04.027

Liu, G., Fu, W., and Song, J. (2017). Study on Relation of Tritium Concentration and Ventilation under Leakage Accident of Glove Box in TES of TBM[J]. *Nucl. Electron. Detect. Technol.* 37 (2), 211–215.

Liu, G. (2017). *Simulation Study of Accidental Tritium Release on Tritium Extraction System of TBM[D]*. Hengyang: University of South China.

Mei, Feng, Wei, Yingjing, Li, Dehong, Wang, Yong, Zhang, Qingli, Wang, Mingliang, et al. (2020). Establishment of Tritium Activity Concentration Standard Device. *J. Radiat. Prot.* 40, 271–277.

Munakata, K., Wajima, T., Hara, K., Wada, K., Takeishi, T., Shinozaki, Y., et al. (2010). Tritium Release Experiments with CATS and Numerical Simulation. *Fusion Eng. Des.* 85, 1250–1254. doi:10.1016/j.fusengdes.2010.03.011

Shih, T. H., Liou, W. W., and Shabbir, A. (1995). A New K-ϵ Eddy Viscosity Model for High Reynolds Number Turbulent Flows[J]. *Comput. fluids* 24 (3), 227–238.

Wei, S. (2021). *Study on Inner Fuel Cycle and Tritium Transport Simulation for CFETR Tritium Plant[D]*. Switzerland: Hefei: University of Science and Technology of China.

Yasunori, I., Hayashi, T., Toshihiko, Y., Kobayashi, K., and Masataka, N. (2001). Simulation of Tritium Behavior after Intended Tritium Release in Ventilated Room[J]. *J. Nucl. Sci. Technol.* 38 (1), 63–75.

Conflict of Interest: The authors declare that the research was conducted in the absence of any commercial or financial relationships that could be construed as a potential conflict of interest.

Frontiers in Energy Research

TYPE Original Research
PUBLISHED 24 August 2022
DOI 10.3389/fenrg.2022.982101

OPEN ACCESS

EDITED BY
Jiankai Yu,
Massachusetts Institute of Technology,
United States

REVIEWED BY
Zhaoyuan Liu,
Qilu University of Technology
(Shandong Academy of Sciences), China
Mohammad Alrwashdeh,
Khalifa University, United Arab Emirates

*CORRESPONDENCE
Lianjie Wang,
wanglianjie@tsinghua.org.cn
Xingjie Peng,
pengxingjiets@126.com

SPECIALTY SECTION
This article was submitted to Nuclear Energy,
a section of the journal *Frontiers in Energy Research.*

RECEIVED 30 June 2022
ACCEPTED 13 July 2022
PUBLISHED 24 August 2022

CITATION
Zhao C, Lou L, Zhang B, Zhou B, Wang L and Peng X (2022), Neutronics performance improvement based on the small lead-based fast reactor SLBR-50.
Front. Energy Res. 10:982101.
doi: 10.3389/fenrg.2022.982101

Neutronics performance improvement based on the small lead-based fast reactor SLBR-50

Chen Zhao, Lei Lou, Bin Zhang, Bingyan Zhou, Lianjie Wang* and Xingjie Peng*

Science and Technology on Reactor System Design Technology Laboratory, Nuclear Power Institute of China, Chengdu, China

The design of high-performance lead-based fast reactors (LFRs) has become a hotspot in the advanced reactor system. This study evaluates the neutronics performance improvement based on the small LFR SLBR-50. Parameter sensitivity analyses are conducted, including height-to-diameter ratio (H/D), reflector assembly arrangement, and pitch-to-diameter ratio in fuel assembly, fuel material, and fuel enrichment partitioning. Numerical results of eigenvalue in burnup procedure, assembly power distribution, and energy spectrum are analyzed using the Monte-Carlo code RMC. Our findings indicate that the fuel material, fuel partitioning, and H/D are the three most important factors in LFR design. The neutronics performance analyses will assist in LFR design.

KEYWORDS

neutronics performance, small lead-based fast reactor, SLBR-50, RMC, energy spectrum

Introduction

Lead-based fast reactor (LFR) (Cinotti, 2009) is one of the six most promising advanced reactor systems among the fourth-generation nuclear reactors (U.S. Doe Nuclear Energy Research Advisory Committee and the Generation IV International Forum, 2002; Cinotti et al., 2010; Zhang et al., 2020a; Zhang et al., 2020b). The lead-based coolant shows good neutronics characteristic in less neutron absorption and moderation, thereby leading to harder neutron spectrum, closed fuel cycle, long-life core without refueling, and better neutron economy. Likewise, the lead-based coolant has better chemical inertness and thermal conductivity. Considering these characteristics, LFR shows good advantages in safety, sustainability, and efficient conversion of uranium.

The idea of LFR was originally proposed for submarine propulsion in 1950s in Russia (Zhang et al., 2020b). The LFR was applied on the nuclear submarine in 1963 (Fazio, 2007), and corrosion behavior was studied for controlling of low oxygen concentrations (Kurata et al., 2008). After the proposition of the fourth-generation nuclear reactor, studies and developments of the lead-based nuclear reactor were conducted. In Russia, SVBR-100 (Zrodnikov et al., 2006; Zrodnikov et al., 2011) and BREST-300 (Smimov, 2012) were designed for power generation. In Europe, a lead-based reactor was rapidly developed under the framework of science project. In addition, a small modular lead-based reactor, SEALER

TABLE 1 Original parameters of the SLBR-50 reactor (Zhao et al., 2021).

Items	Parameter	Items	Parameter
Reactor power	50 MWt	Fuel diameter	8.0 mm
Hot condition average temperature	700 K	Air gap thickness	0.1 mm
fuel enrichment	19.75%	Clad thickness	0.6 mm
Uranium total weight	3,835.3 kg	Clad outer diameter	9.4 mm
CR absorber material	B_4C	Fuel rod distance	10.9 mm
Reflector material	BeO	Assembly box thickness	2 mm
Clad material	Stainless steel	Assembly pitch	93.5 mm
Coolant material	Lead	Assembly inner distance	88.0 mm
Barrel material	Stainless steel	Assembly outer distance	92.0 mm
Fuel assembly amount	144	Active core height	95 cm
Control rod assembly amount	18	Outer reflector diameter	82 cm
Reflector assembly amount	48		

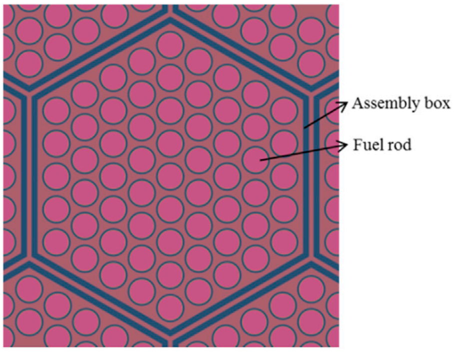

FIGURE 1
Hexagonal assembly geometry of the SLBR-50 reactor (Zhou et al., 2018).

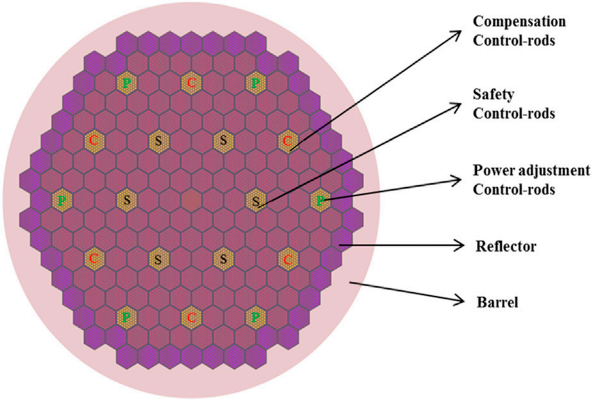

FIGURE 2
Whole-core model of the original design in the SLBR-50 reactor (Zhou et al., 2018).

(Wallenius et al., 2018; LeadCold Reactors Company, 2022), was designed by Swedish LeadCold Company for polar region application. Furthermore, an experimental reactor MYRRHA (Abderrahim and D'hondt, 2007), demonstration reactor ALFRED (Frogheri, 2013; Alemberti, 2020), and prototype reactor ELFR (Frogheri, 2013) have been under research and development. In the United States, a small transportable modular lead-cooled reactor SSTAR (Sienicki, 2005; Smith et al., 2012) was conceptually designed with the cooperation of ANL and LLNL. In Asia, several lead-cooled reactors were designed, such as LSPR (Sekimoto, 2001) and CLEAR-SR (Wang et al., 2015a). In general, the LFR attracted great attention after the proposal of a fourth-generation nuclear reactor system. In addition, large sums of conceptual designs were proposed with different reactor parameters. In conceptual design of the lead-based reactor, the refueling cycle was extended to over 5 years. Several designs, such as the SSTAR reactor, cancelled the refueling procedure in full cycle.

In this study in reactor physics, parameter sensitivity analyses were conducted based on a small LFR SLBR-50 (small lead-based breeding reactor), which was conceptually designed in the Nuclear Power Institute of China for scientific research. Several important designing parameters were analyzed using the control-variates method, such as the core height-to-diameter ratio (H/D), reflector assembly arrangement, pin pitch-to-diameter ratio (P/D) in fuel assembly, fuel material, and fuel enrichment partitioning. In theory, these parameters have a great influence on the neutronics design. In the control-variates method, only one parameter was changed and analyzed. The detailed influences will be analyzed in quantity, and the most important design parameter will be pointed out. In this way, compared with the original reactor design, neutronics performance will be improved with sensitivity analyses and more reasonable design parameters.

In the neutronics design, the Monte-Carlo code RMC (She, 2012; Wang et al., 2015b; Liu et al., 2017) was adopted for critical and burnup calculation with large-scale parallel ability. ENDF/

TABLE 2 Conditions and results of the height-to-diameter analysis.

	Case 1	Case 2	Case 3	Case 4	Case 5
Conditions					
Fuel enrichment	19.75%	19.75%	19.75%	19.75%	19.75%
Uranium weight/kg	3,839.5	3,834.1	3,838.7	3,835.3	3,837.7
Barrel thickness/cm	20	20	20	20	20
Fuel assemblies amount	150	138	120	114	102
Active core equivalent diameter/cm	125.35	120.65	110.65	108.00	102.51
Active core height/cm	91.3	99.1	114.1	120.0	134.2
H/D	0.73	0.82	1.03	1.11	1.31
Results					
Eigenvalue (BOL)	1.01693	1.02089	1.02626	1.02559	1.02084

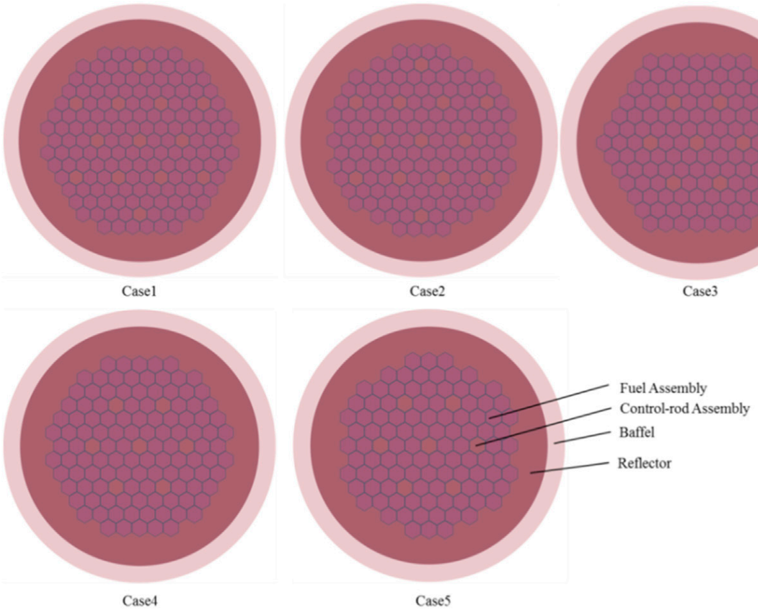

FIGURE 3
Radial core configuration in the height-to-diameter ratio analysis.

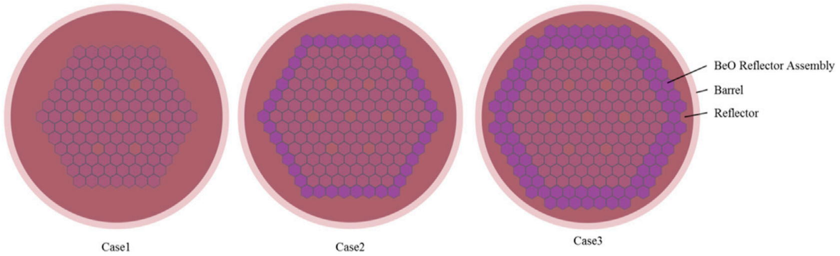

FIGURE 4
Radial core configuration in the reflector analysis.

TABLE 3 Conditions and results of the reflector assembly amount analysis.

	Case 1	Case 2	Case 3
Conditions			
Reflector assembly amount	0	42	84
Fuel enrichment/%	19.75	19.75	19.75
Uranium weight/kg	3,838.7	3,838.7	3,838.7
H/D	1.03	1.03	1.03
Fuel assembly amount	120	120	120
Barrel thickness/cm	10	10	10
Barrel inner radius/cm	80	80	80
BeO Reflector assembly amount	0	42	84
Results			
Eigenvalue (BOL)	1.02989	1.04865	1.04843
Assembly 3D power peak	1.966	1.735	1.721
Assembly 2D power peak	1.499	1.323	1.310

B-VII.0 (Steven, 2006) data library and ACE format cross-section data were applied. In critical transport calculation, the free gas model was built for elastic scatter cross-section, and probability tables were used for unresolved resonance calculation. In burnup calculation, detailed depletion chains containing thousands of isotopes and CRAM (Zhou et al., 2018) depletion method were adopted. Moreover, source convergence acceleration and large-scale parallel methods were applied.

Original design of the SLBR-50 reactor

Table 1 reports the original parameters of the SLBR-50 reactor. The thermal power was 50 MW. The UO_2 fuel enrichment was 19.75%, and the total weight of uranium was 3,835.3 kg. Geometry parameters are presented in the right column of Table 1. Basic hexagonal assembly and whole-core models of SLBR-50 are presented in Figures 1 and 2. The radius for fuel, gap, and clad was 0.4, 0.41, and 0.47 cm, respectively, in each fuel rod. The assembly pitch was 9.35 cm and the box thickness was 0.2 cm for the fuel assembly. In the whole core, 144 fuel, 18 control rod, and 48 reflector assemblies were arranged.

Parameter sensitivity analyses for neutronics performance improvement

In this section, parameter sensitivity analyses were conducted with the fixed-variable method based on the original scheme of the SLBR-50 reactor. Basic parameters were set to be consistent with the original design of SLBR-50, including the reactor power, fuel enrichment, and pin-cell geometry construction. Other important neutronics results were also analyzed in the research, including fuel weight, power peak factor, and energy spectrum. To simplify the fuel weight analyses, it was converted to the comparison of eigenvalue in burnup procedure in certain fuel weight. Key factors for the parameter sensitivity research and performance improvement included the H/D, the reflector assembly arrangement, the P/D in fuel assembly, fuel material, and fuel enrichment partitioning.

As for the calculation condition, it remained same in analyses. A total of 800,000,000 active particles were used (800 generations comprising 100,000 neutrons per generation, of which 200 generations were skipped). The standard deviation of eigenvalue result was 7 pcm, which is reasonable in design calculation.

Height/diameter

Core H/D is one of the important parameters for research, and it has great influence on neutron leakage. In particular, the neutron leakage is more significant in fast reactors with longer

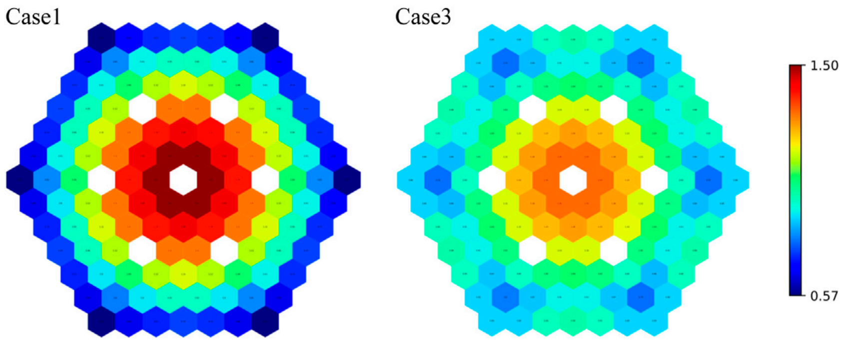

FIGURE 5
Assembly power distribution results on the beginning of life of the reflector amount analysis.

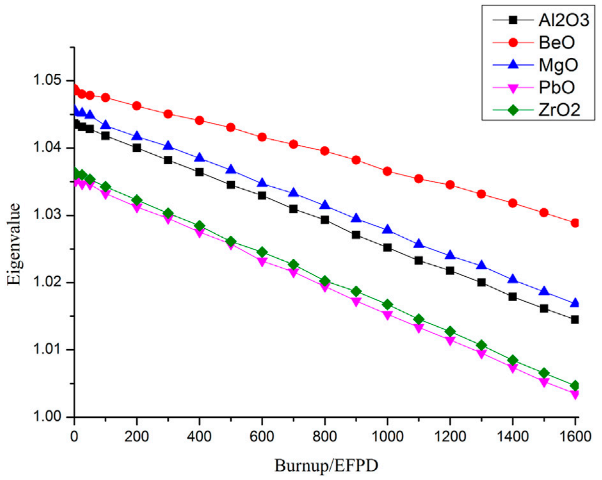

FIGURE 6
Burnup calculation results of the reflector material analysis.

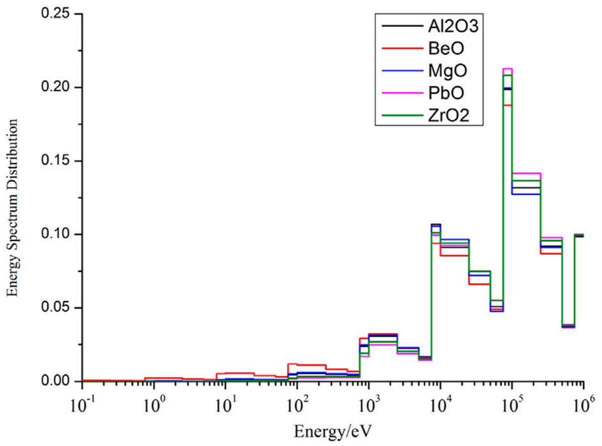

FIGURE 7
Energy spectrum results on the beginning of life of the reflector material analysis.

TABLE 5 Geometry parameters of the pitch-to-diameter ratio analysis.

	Case 1	Case 2	Case 3
Pitch/cm	1.09	1.05	1.00
Diameter/cm	0.94	0.94	0.94
P/D	1.16	1.12	1.06
Assembly size/cm	8.8/9.2/9.35	8.52/8.92/9.07	8.18/8.58/8.73
Coolant gap/cm	0.62	0.62	0.62

neutron free path. To apply the control-variates method in the research of H/D, uranium weight, fuel enrichment, fuel assembly structure, and barrel thickness were set to be consistent. The active core equivalent diameter was calculated from the number of fuel assemblies, and the active core height was adjusted considering the total uranium weight. Furthermore, radial reflectors were neglected in the H/D analysis. Calculation conditions and part of results are listed in Table 2. As shown, the fuel enrichment and barrel thickness were set to 19.75% and 20 cm in all cases, respectively. Radial fuel assembly amount and axial fuel assembly height were adjusted to make the total fuel weight almost consistent in 3,834–3,840 kg. In this way, H/D was verified to range from 0.73 to 1.31 in five cases. Radial cut of the active core of these five cases is presented in Figure 3.

Eigenvalue results of the burnup procedure are presented in Table 2. The eigenvalue result was the largest in case 3 with a H/D close to 1.0, where the neutron leakage could be fully decreased. It can be concluded that the H/D parameter should be close to 1.0 in the reactor physics design, and it shows a great effect on neutron leakage reduction.

Reflector

The reflector outside of the active core is the second research parameter. It is also an effective way to improve the neutron

TABLE 4 Conditions and results of the reflector material analysis.

	Al_2O_3	BeO	MgO	PbO	ZrO_2
Conditions					
Reflector material density*/gcm^{-3}	3.987	2.8	3.6	9.53	5.67
H/D	1.03	1.03	1.03	1.03	1.03
Fuel assembly amount	120	120	120	120	120
Reflector assembly amount	42	42	42	42	42
Results					
Eigenvalue (BOL)	1.04368	1.04885	1.04568	1.03519	1.03643

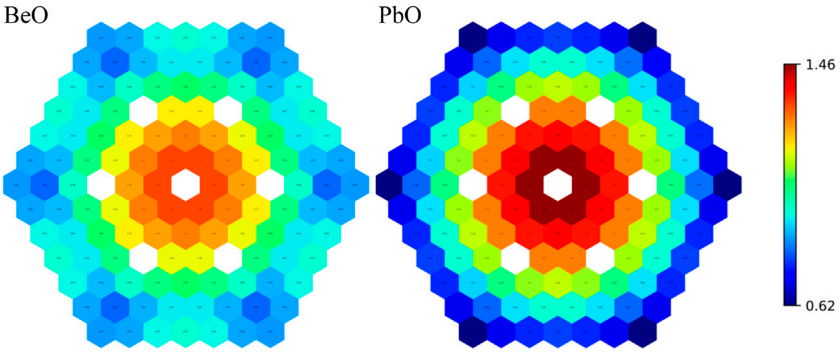

FIGURE 8
Assembly power distribution results on the beginning of life of the reflector material analysis.

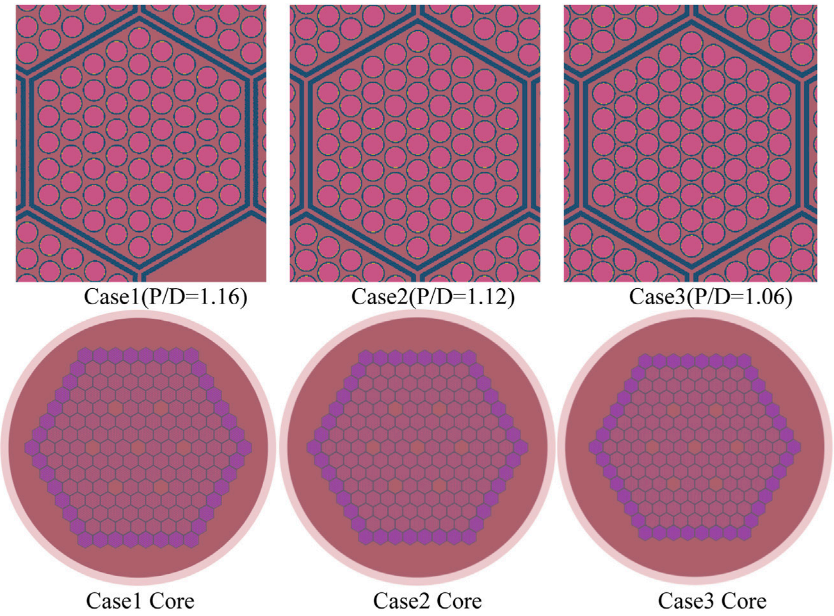

FIGURE 9
Fuel assembly and core structure in the pitch-to-diameter ratio analysis.

reaction rate and reduce the neutron leakage rate. The reflector assembly amount and material need to be analyzed based on case 3 (H/D = 1.03) in the H/D research.

Similar to the H/D research, the fixed-variable method was conducted in the reflector analysis. First, the reflector assembly amount was studied on three cases, as shown in Figure 4. In these three cases, the only difference lied in the amount of reflector assemblies. BeO was conducted as the reflector material in the reflector amount analysis. The reflector barrel was modeled explicitly outside the reactor active core.

Eigenvalue and assembly power peak results are presented in Table 3. Reflector assemblies showed good performance in terms of decreasing neutron leakage. The eigenvalue results increased from 1.02989 to 1.04865 with 42 reflector assemblies. The radial assembly power peak also improved, from 1.499 to 1.323 and 1.310. The detailed radial power distribution of beginning of life (BOL) is presented in Figure 5. These results show that the radial reflector has good performance in eigenvalue improvement, and 42 reflector assemblies were enough. The power flattening and assembly power peak decrease were due to

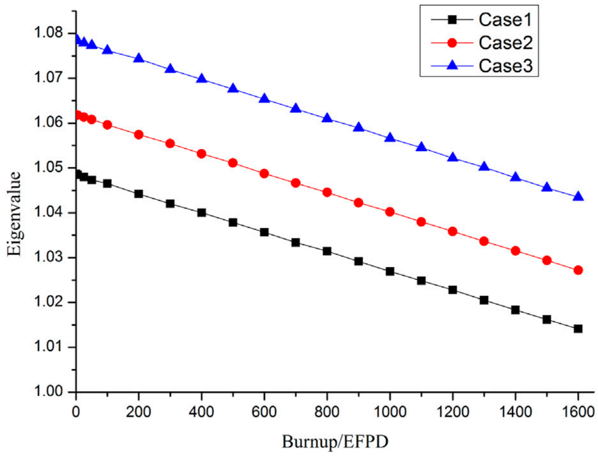

FIGURE 10
Burnup calculation results of the pitch-to-diameter ratio analysis.

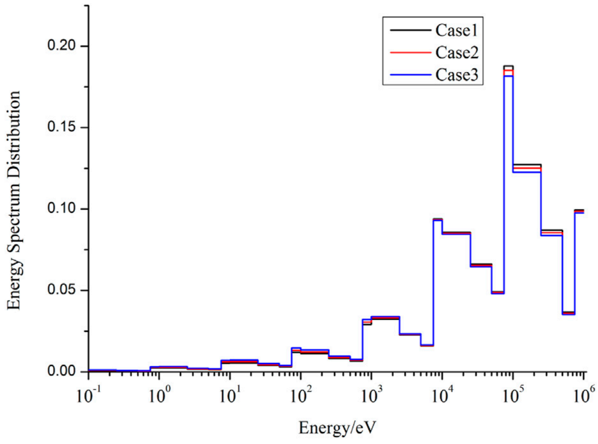

FIGURE 11
Energy spectrum results on the beginning of life of the pitch-to-diameter ratio analysis.

the higher reaction rate of ^{235}U near the reflector assembly, which was caused by the obvious thermalization phenomenon of BeO. The thermalization phenomenon of the BeO reactor can be found in the subsequent reflector material analysis.

Moreover, reflector material was studied with 42 reflector assemblies. According to reference previous study (Liu et al., 2017), Al_2O_3, BeO, MgO, PbO, and ZrO_2 can be applied as the reflector material in LFR. Eigenvalue burnup calculation results are presented in Figure 6, where the EFPD was effective full power days. BOL eigenvalues are listed in Table 4. BeO showed the best performance of eigenvalue results. The eigenvalue result was 1.04885 on the BOL with the BeO reflector, which was 1,366 pcm larger than the PbO reflector.

Further, the energy spectrum and assembly power distribution results on the BOL were analyzed. The energy spectrum was tallied and integrated from 0.1 eV to 1.0 MeV with 28 sectors. The core-averaged energy spectrum results for different reflector materials are shown in Figure 7. The energy spectrum showed the highest distribution in the fast energy range of 10^4 eV–10^6 eV for the PbO material. In the thermal energy range of 1–1000 eV, flux was the highest for the BeO material. These results showed that the BeO reflector material had the best moderation ability. Thermalization of energy spectrum occurred, and the reaction rate was improved with the BeO reflector. In the assembly power distribution results of the BeO reflector, in Figure 8 thermalization phenomenon was also observed. The minimum assembly power peak was in the inner assembly and the outmost fuel assembly showed larger power because of the strong moderation ability of the BeO reflector. Thus, it can be concluded that the reflector material has great influence on the reactor energy spectrum and has further effect on the reaction rate. Energy spectrum is thus an important factor for the research.

Pitch/diameter

The third parameter is in the P/D in the fuel assembly. The P/D parameter influences the scattering and absorbing of coolant, which affects the neutron absorption and leakage. In the P/D parameter research, 42 BeO reflector assemblies were adopted considering the better neutronics performance in reflector analyses. Based on the original SLBR-50 design, three cases were analyzed with different P/D parameters, including 1.16 (case 1), 1.12 (case 2), and 1.06 (case 3). The detailed geometry parameters are shown in Table 5. As for fuel rods, fuel rod diameters remained the same and the pitch was adjusted from 1.09 to 1.00 cm. As for fuel assemblies, the assembly size was changed to maintain equal distance between the outmost fuel rod and assembly box in the three cases. In this way, fuel weight can be consistent in the P/D analysis. The fuel assemblies of these cases are shown in Figure 9. In assembly figures, the decrease in assembly size was too small to be captured. In whole-core figures, the size of the reactor core was reduced as the P/D was decreasing.

Eigenvalue results in the burnup procedure are presented in Figure 10. Case 3 with the smallest P/D showed the best eigenvalue performance. Eigenvalue results of the three cases were 1.04865, 1.06191, and 1.07866, respectively, in BOL. In addition, energy spectrum distributions are presented in Figure 11. The energy spectrum of case 3 was the softest, and the energy spectrum distributions of the three cases showed minor differences compared to reflector material analyses. The

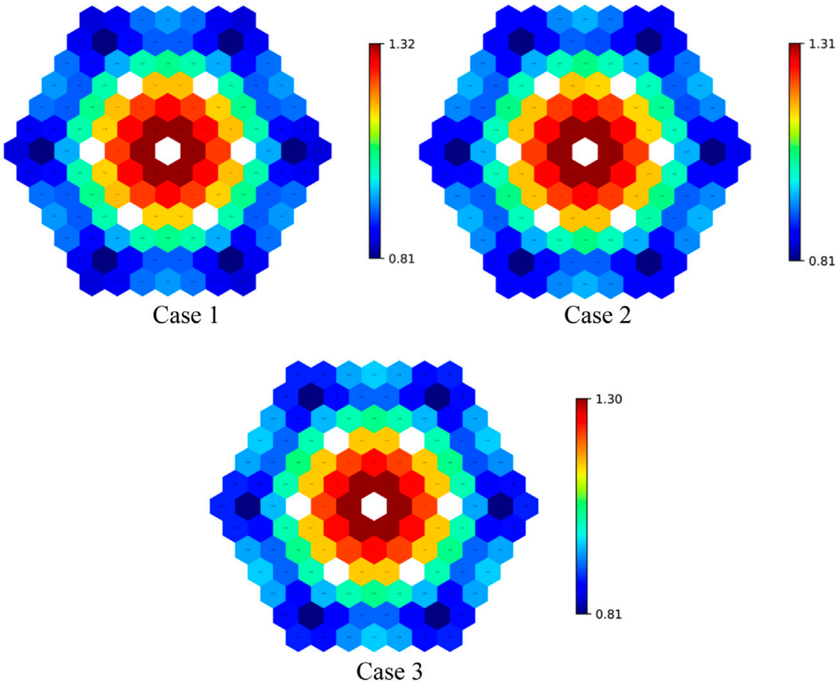

FIGURE 12
Assembly power distribution results on the beginning of life of the pitch-to-diameter ratio analysis.

TABLE 6 Conditions of the fuel material analysis.

	UO$_2$	UN	U-Zr
Conditions			
Fuel material density/gcm^{-3}	10.38	14.32	15.92
Fuel enrichment/%	19.5%	16%	14%
Uranium weight/kg	3,840.2	5,677.2	6,015.2
U-235 weight/kg	741.2	898.7	842.1
H/D	1.03	1.03	1.03
Fuel assembly amount	120	120	120
Barrel thickness/cm	10	10	10
Barrel inner radius/cm	80	80	80
Reflector assembly amount	42	42	42
Fuel assembly P/D	1.16	1.16	1.16

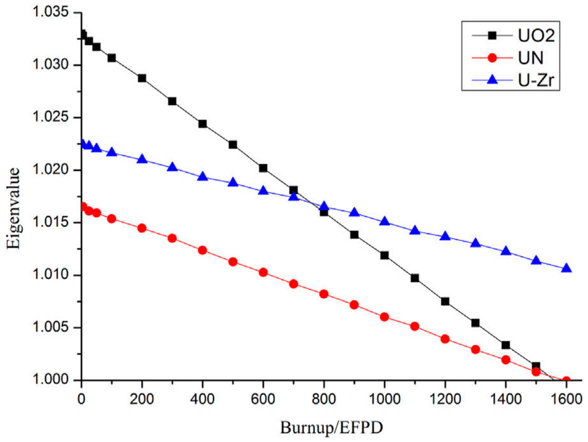

FIGURE 13
Eigenvalue results of the fuel material analysis in the burnup procedure.

assembly power distribution results on BOL are presented in Figure 12. The radial assembly power peak factors were 1.32, 1.31, and 1.30 for the three cases, respectively, which also had unobvious differences.

Based on sensitivity analyses, the P/D parameter had great influence on eigenvalue results. The eigenvalue differences in the BOL can extend to 3,000 pcm in sensitivity analyses. The differences were mainly caused by the neutron absorption for the lead coolant and neutron fission for fuel rods. Decreasing P/D was an effective way to improve eigenvalue and decrease fuel weight. However, the P/D parameter cannot be so small considering the heat exchange capability in thermal-hydraulics analyses.

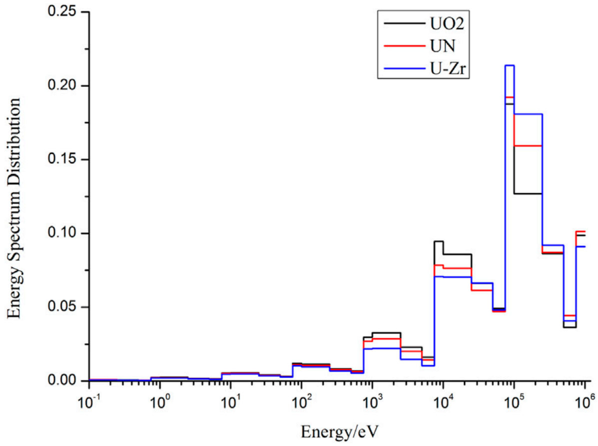

FIGURE 14
Energy spectrum results on the beginning of life of the fuel material analysis.

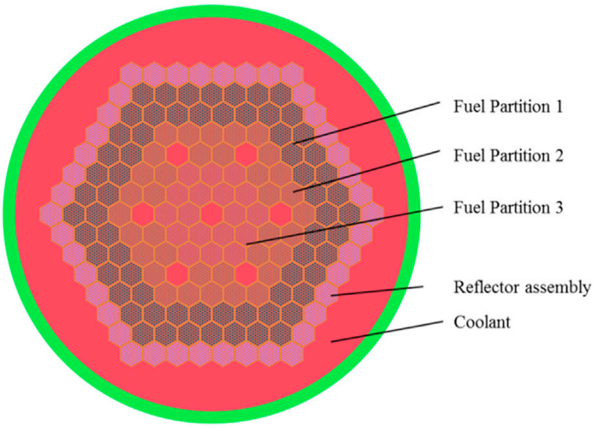

FIGURE 16
Core configuration of the fuel partitioning.

Fuel material

Fuel material is an important factor in the research. The neutron fission absorbing and scattering are affected by fuel materials. In this study, traditional UO_2, new-type UN, and U-Zr alloy fuel materials were analyzed. In the fuel material research, the same fuel assembly and core structure were applied, as shown in Figures 9A,D. Fuel enrichments were adjusted to realize the similar burnup depth with the same reactor geometry design and reactor power. Detailed calculation conditions of the fuel material analysis are listed in Table 6. In particular, fuel densities and uranium weights were significantly different in the analysis. In fuel material analyses, all parameters remained the same, except for fuel material and fuel enrichment.

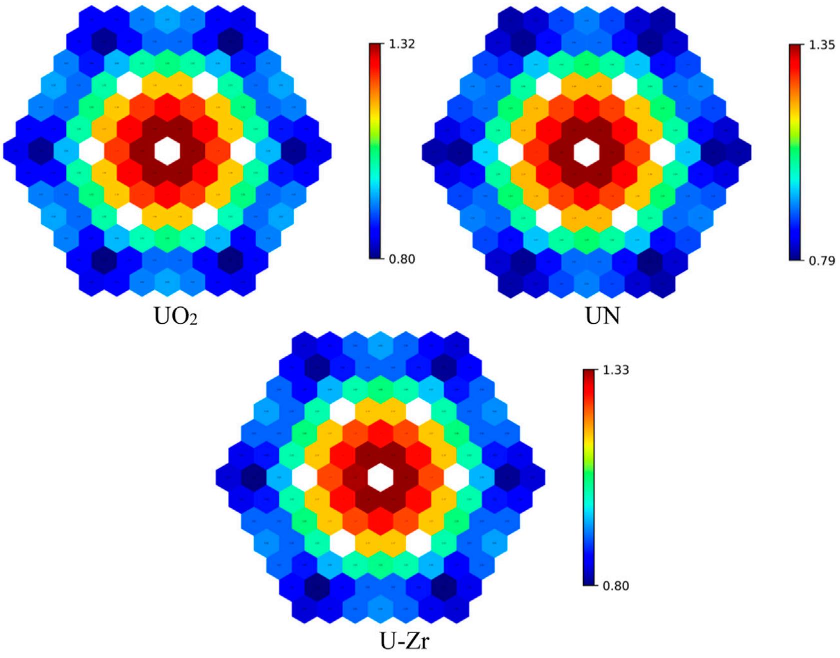

FIGURE 15
Assembly power distribution results on the beginning of life of the fuel material analysis.

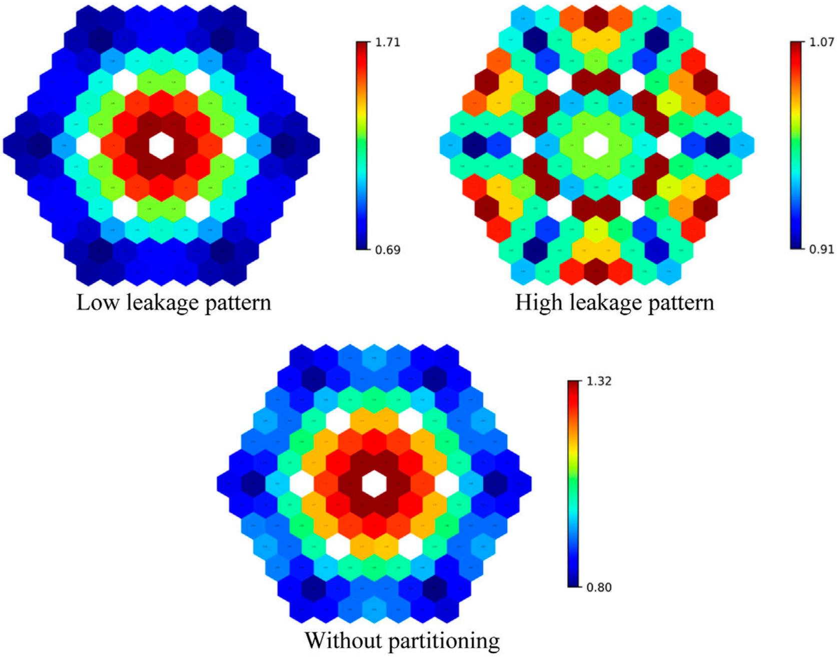

FIGURE 17
Assembly power distribution results on the beginning of life of the radial power flattening analysis.

Eigenvalue results of the fuel material analysis in the burnup procedure are presented in Figure 13. The decrease of eigenvalue results along the burnup procedure is the most obvious for the traditional UO_2 material. The U-Zr material showed the best burnup performance according to the eigenvalue results. The phenomenon was conducted by the different energy spectrum performance of these fuel materials, which is presented in Figure 14. New-type U-Zr and UN materials showed greater energy distribution on fast energy > 10^4 eV. The energy spectrum was harder for the new-type fuel material than traditional UO_2 material. Therefore, more conversion and breeding reaction occurred, and the burnup depth can be extended for new-type materials. Likewise, the assembly power distributions are compared and shown in Figure 15. According to assembly power results, the assembly power peak for these three fuel materials were 1.32, 1.35, and 1.33, respectively. Fuel materials had little influence on the power distribution.

Fuel partitioning

The power flattening is an important parameter in neutronics performance analyses. The most straightforward way to improve power flattening performance is in the fuel partitioning with different enrichment. In this study, the fuel partitioning analyses were based on the U-Zr fuel material. Three kinds of fuel with different levels of enrichment were employed, such as 16%, 14%, and 12%. In this way, the fuel partitioning was analyzed using two patterns, including a low-leakage pattern (high enrichment–fuel inner layout) and high-leakage pattern (high enrichment–fuel outer layout). Furthermore, core loading without partitioning was analyzed as the control group. The core configuration of fuel partitioning is shown in Figure 16.

Assembly power distributions on the BOL are presented in Figure 17. The power peak factor increased from 1.32 to 1.71 in the low-leakage pattern. In contrast, the high-leakage pattern showed a great effect on power flattening, and the power peak factor can be decreased to 1.07. In the high-leakage pattern, higher enrichment–fuel assemblies were located at the edge of the active core to improve the fission reaction rate and realize power flattening.

Conclusion

LFRs show several merits in the advanced reactor systems and have already become a research hotspot in the design of LFR. In this study, parameter sensitivity analyses of neutronics performance improvement were conducted based on a 50-MWt small lead-based reactor (SLBR-50), which was conceptually designed for research.

The research of neutronics performance improvement was conducted with the fixed-variable method in performance improvement. Five key parameters were analyzed, including H/D, reflector assembly arrangement, P/D in fuel assembly, fuel material, and fuel partitioning. As for neutronics results, eigenvalue, assembly power distribution, and energy spectrum were analyzed.

According to parameter sensitivity analyses, it can be concluded that parameters optimization show good effect on decreasing neutron leakage, energy spectrum thermalization, and power flattening, which improves the neutronics performance. As for these parameters, fuel material, fuel partitioning, and H/D are the three most important factors.

In the future, a high-performance lead-based reactor will be designed based on the parameter research.

Data availability statement

The original contributions presented in the study are included in the article/Supplementary Material; further inquiries can be directed to the corresponding author.

Author contributions

CZ: Main researcher and manuscript writer, LL: Researcher, BZ: Researcher, BZ: Researcher, LW: Advisor and director, XP: Advisor and director.

Funding

This work is supported by the National Natural Science Foundation of China (Grant No. 12005215) and China Association for Science and Technology (Young Elite Scientists Sponsorship Program 2019QNRC001).

Conflict of interest

The authors declare that the research was conducted in the absence of any commercial or financial relationships that could be construed as a potential conflict of interest.

Publisher's note

References

Abderrahim, H., and D'hondt, P. (2007). Myrrha: a European experimental ads for R&D applications status at mid-2005 and prospective towards implementation. *J. Nucl. Sci. Technol.* 44, 491–498. doi:10.1080/18811248.2007.9711313

Alemberti, A. (20202012). *The ALFRED project on lead-cooled fast reactor*. ESNII Conf. Adv. fission Res. Horizon 25.

Cinotti, L. (2009). *Lead-cooled fast reactor (LFR) overview and perspectives* Livermore, CA: Lawrence Livermore National Lab (LLNL). LLNL-CONF-414708.

Cinotti, L., Smith, C., and Artioli, C. (2010). *Handbook of nuclear engineering*. chapter 2.

Fazio, C. (2007). "Handbook on lead-bismuth eutectic alloy and lead properties[R]." in *Materials compatibility, thermal-hydraulics and technologies*. Edition. Nuclear science.

Frogheri, M. (2013). The lead fast reactor: Demonstrator (ALFRED) and ELFR design." in *International conference on fast reactors and related fuel cycles*. Paris, France.

Kurata, Y., Futakawa, M., and Saito, S. (2008). Corrosion behavior of steels in liquid lead-bismuth with low oxygen concentrations. *J. Nucl. Mater.* 373, 164–178. doi:10.1016/j.jnucmat.2007.05.051

LeadCold Reactors Company (2022). Available at: http://www.leadcold.com/sealer.html.

Liu, S., Liang, J., Wu, Q., Guo, J., Huang, S., Tang, X., et al. (2017). BEAVRS full core burnup calculation in hot full power condition by RMC code. *Ann. Nucl. Energy* 101, 434–446. doi:10.1016/j.anucene.2016.11.033

Sekimoto, H. (2001). "A long-life small reactor for developing countriesInternational seminar on status and prospects for small and medium sized reactors," in International Seminar on Status and Prospects for Small and Medium Sized Reactors, Cairo, Egypt.

She, D. (2012). *Using generalized laguerre polynomials to compute the matrix exponential in burnup equations*. Knoxville, Tennessee, USA: PHYSOR.

Sienicki, J. (2005). *SSTAR lead-cooled, small modular fast reactor with nitride fuel. Workshop on advanced reactors with innovative fuels ARWIF-2005, NEA*, 16-18. Oak Ridge.

Smimov, V. (2012). "Lead-cooled fast reactor BREST-Project status and prospects [R]," in *Nternational workshop on innovative nuclear reactors cooled by heavy liquid metals: status and perspectives* Pisa

Smith, F., Halsey, W. G., Brown, N. W., Sienicki, J. J., Moisseytsev, A., and Wade, D. C. (2012). Sstar: The US lead-cooled fast reactor(LFR). *J. Nucl. Mater.* 376 (3), 255–259. doi:10.1016/j.jnucmat.2008.02.049

Steven, C. (2006). Benchmarking ENDF/B-VII.0. *Nucl. Data Sheets* 107, 3061–3118. doi:10.1016/j.nds.2006.11.002

U.S. Doe Nuclear Energy Research Advisory Committee and the Generation IV International Forum (2002). *A Technology roadmap for generation IV nuclear energy systems*. Technical report GIF-002-00.

Wallenius, J., Qvist, S., Mickus, I., Bortot, S., Szakalos, P., and Ejenstam, J. (2018). Design of SEALER, a very small lead-cooled reactor for commercial power production in off-grid applications. *Nucl. Eng. Des.* 338, 23–33. doi:10.1016/j.nucengdes.2018.07.031

Wang, K., Li, Z., She, D., Liang, J., Xu, Q., Qiu, Y., et al. (2015). Rmc – a Monte Carlo code for reactor core analysis. *Ann. Nucl. Energy* 82, 121–129. doi:10.1016/j.anucene.2014.08.048

Wang, M., Lian, C., Li, Y., Wang, D., Jiang, J., and Wu, Y. (2015). Preliminary conceptual design of a lead-bismuth cooled small reactor (CLEAR-SR). *Int. J. Hydrogen Energy* 40, 15132–15136. doi:10.1016/j.ijhydene.2015.03.097

Zhang, T., Liu, X., Xiong, J., and Cheng, X. (2020). Comparisons of reduced moderation small modular reactors with heavy water coolant. *Front. Energy Res.* 8, 1–5. doi:10.3389/fenrg.2020.00027

Zhang, T., Xiong, J., Liu, X., Chai, X., Li, W., and Cheng, X. (2020). Conceptual design of an innovative reduced moderation thorium-fueled small modular reactor with heavy-water coolant. *Int. J. Energy Res.* 43, er.4827. doi:10.1002/er.4827

Zhao, C., Lou, L., Peng, X., Zhang, B., and Wang, L. (2021). Application of the spectral-shift effect in the small lead-based reactor SLBR-50. *Front. Energy Res.* 9, 756106. doi:10.3389/fenrg.2021.756106

Zhou, S., Chen, R., Shao, Y., Cao, L., Bai, B., and Wu, H. (2018). Conceptual core design study of an innovative small transportable lead-bismuth cooled fast reactor (SPARK) for remote power supply. *Int. J. Energy Res.* 42, 3672–3687. doi:10.1002/er.4119

Zrodnikov, A., Toshinsky, G., Komlev, O., Dragunov, Y., Stepanov, V., Klimov, N., et al. (2006). Nuclear power development in market conditions with use of multi-purpose modular fast reactors SVBR-75/100. *Nucl. Eng. Des.* 236, 1490–1502. doi:10.1016/j.nucengdes.2006.04.005

Zrodnikov, A., Toshinsky, G., Komlev, O., Stepanov, V., and Klimov, N. (2011). SVBR-100 module-type fast reactor of the IV generation for regional power industry. *J. Nucl. Mater.* 415, 237–244. doi:10.1016/j.jnucmat.2011.04.038

frontiers | Frontiers in Energy Research

TYPE Original Research
PUBLISHED 30 August 2022
DOI 10.3389/fenrg.2022.976602

Check for updates

OPEN ACCESS

EDITED BY
Jiankai Yu,
Massachusetts Institute of Technology,
United States

REVIEWED BY
Yugao Ma,
Nuclear Power Institute of China (NPIC),
China
Xingjie Peng,
Nuclear Power Institute of China (NPIC),
China

*CORRESPONDENCE
Wenbin Wu,
wuwb28@mail.sysu.edu.cn

SPECIALTY SECTION
This article was submitted to Nuclear Energy,
a section of the journal
Frontiers in Energy Research

RECEIVED 23 June 2022
ACCEPTED 01 August 2022
PUBLISHED 30 August 2022

CITATION
Zhong Y, Norman P and Wu W (2022), A feasibility study of SMART reactor power performance optimizations-part 1: Steady-state and burn-up analysis.
Front. Energy Res. 10:976602.
doi: 10.3389/fenrg.2022.976602

A feasibility study of SMART reactor power performance optimizations-part 1: Steady-state and burn-up analysis

Yiming Zhong[1], Paul Norman[1] and Wenbin Wu[2]*

[1]Nuclear Physics Group, School of Physics and Astronomy, College of Engineering and Physical Sciences, University of Birmingham, Birmingham, United Kingdom, [2]Sino-French Institute of Nuclear Engineering and Technology, Sun Yat-sen University, Zhuhai, China

SMART is an integral small pressurized water nuclear reactor design with a rated power output of 100 MWe from 330 MWth, but it needs a higher power output for the United Kingdom energy market. This study applies Monte Carlo code OpenMC to build a full-core model and innovatively adjust the simulation coefficients to approach the reactor operating conditions. The analysis results point out the reasonable optimization's technical direction. The model's sensitivity to ENDF and JEFF nuclear data libraries and spatial division is tested and verified. Then it performs a series of simulations to obtain the core's neutronic parameters, such as neutron energy and spatial distributions, effective neutron multiplication factor k_{eff} and its variation versus depletion. The analysis found that the initially designed core's k_{eff} is 1.22906, and the temperature reactivity defect is 11612 pcm. In 1129 full-power operating days, the k_{eff} will decrease to 0.99126, and the reactor depletes 8.524×10^{26} ^{235}U atoms. However, the outermost fuel assemblies' ^{235}U depletion rate is lower than 45% in this extended refuelling cycle, and their ending enrichment is higher than 2.4%. That means the fuel economy of the original design's two-batch refuelling scheme core layout is insufficient. Improving the thermal neutron fluence in these assemblies may optimize the SMART power performance effectively.

KEYWORDS

small modular reactor, Monte Carlo, sensitivity study, power distribution, burn-up

1 Introduction

Clean and affordable energy is a basic necessity for comprehensive social development. The non-fossil energy sources fraction is continuously rising in many countries' power supply systems (IAEA, 2018). However, the development of nuclear power remains uncertain due to multi reasons (Stoutenborough et al., 2013; Bisconti, 2018). According to the international atomic energy agency (IAEA) definitions, the small modular reactor has less than 300 MW electrical power output and adopts the modular

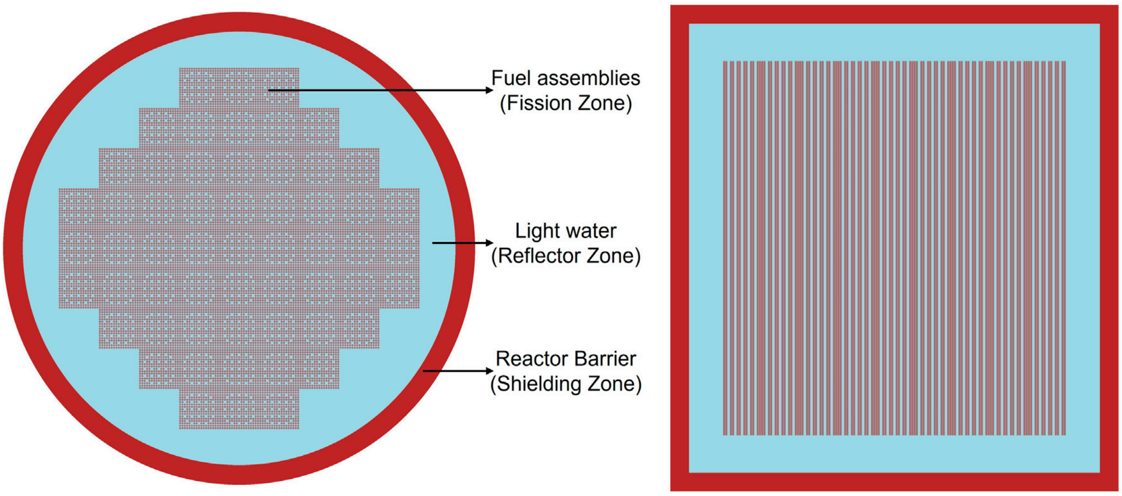

FIGURE 1
Radial and axial view of the OpenMC SMART core.

design concept. The primary components can be mounted within the reactor pressure vessel. The fabricated reactor unit would be shipped for on-site installation. This approach has several advantages, such as the standardization of components and shortening construction schedules.

The Korean system-integrated modular advanced reactor (SMART) (IAEA, 2011; Choi, 2015) is a small integral pressurized water reactor. This technology was licensed for standard design approval (SDA) in July 2012. The SMART reactor core contains 57 fuel assemblies (FA). Each FA has 2 m active height and united into a standard 17 × 17 square assembly of UO_2 ceramic fuel rods with the enrichment of less than 5%. An assembly also has several lumped burnable poison rods made of the mixture of gadolinium oxide Gd_2O_3 and UO_2, and poison rods enrichment is 1.8%. From study works and light water reactor operating experience (Driscoll and Lanning, 1978; Kim et al., 1993; Sadighi et al., 2002), a two-batch refuelling scheme was established to return a cycle of 990 low power density, effective full-power days (EFPD).

Green Frog (GF) Nuclear is a United Kingdom independent power company that is participating in the development of SMART. They noted a higher power output SMART might better satisfy the demand for the United Kingdom market. This study has built a SMART core model by Monte Carlo method code OpenMC and has performed the simulations with the validated settings and conditions. The desired neutronic parameters would be tallied and then reasonably visualized. The results can determine which aspect has the most potential for improving power output. Due to the similarity of core design, the optimizations on SMART have the possibility of being extended to other integral PWR technologies.

2 Methodology

2.1 OpenMC model

OpenMC is a community-developed MC neutron and photon transport simulation code. A hybrid shared-memory parallelism (MP) (Dagum and Menon, 1998) and distributed-memory parallelism (MPI) (Graham et al., 2005) programming model is applied to support code parallelism. The OpenMC depletion function with multiple time integration methods is launched in the update at the late of 2019 (Romano et al., 2015; Paul K; Romano et al., 2021). The functions of OpenMC have been well verified by the developers with other MC method codes, such as MCNP and Serpent (Leppänen et al., 2015; Paul K.; Romano et al., 2021).

TABLE 1 OpenMC calculation speeds with different parallelism models (Unit: Particles/second).

	No parallelism	Shared-memory (30 cores)	Distributed-memory (20 process)
Inactive calculation rate	1708.69	15516.9	15620.1
Active calculation rate	1243.97	9805.36	8632.23

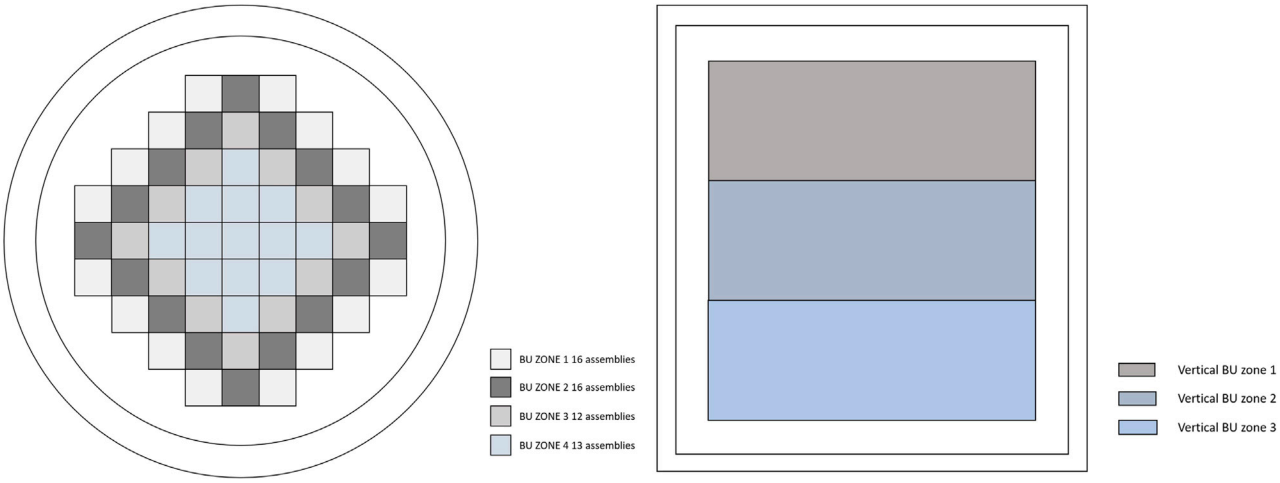

FIGURE 2
4 × 3 Burn-up zone spatial location diagram.

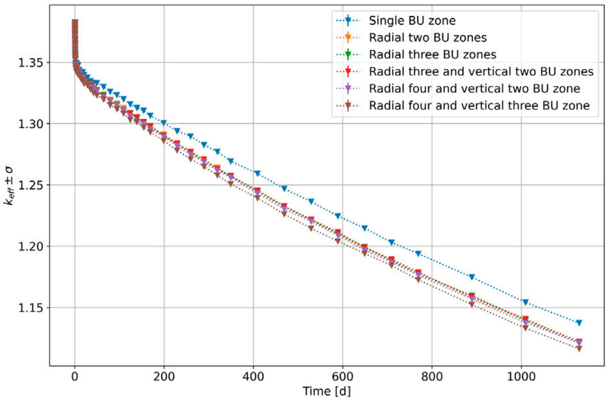

FIGURE 3
The k_{eff} variations in several burn-up calculations with the different number of spatial zones.

A 3D SMART reactor core model has been established. The dimensions of an assembly lattice box are 20.4 cm × 20.4 cm × 200.0 cm. Each assembly has 25 guide tubes for control rods and instrument tubes. The slice plots of the model are given in Figure 1.

The material definition in OpenMC can set the specified material' densities and compositions. Furthermore, OpenMC can use internally stored isotopes' atomic mass and abundance data to determine a kind of material. The enrichment argument could add the isotopes at a specified enrichment in the material. In this case, the enrichment of ^{235}U is set as 4.8% to simulate the enriched uranium oxide fuel.

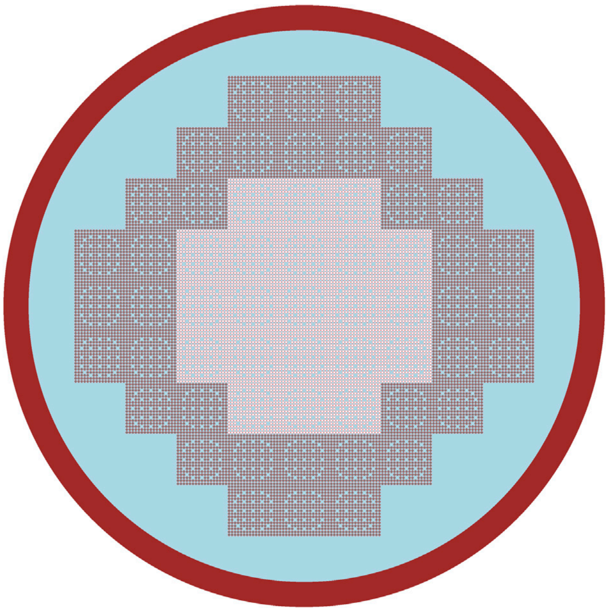

FIGURE 4
Updated OpenMC model of the SMART reactor core to have two enrichment levels (2.4 and 4.8%) for fuel shifting.

2.2 Parallelism efficiency

This study has employed hybrid OpenMP and MPI parallelism methods on the BlueBEAR supercomputer. Both parallelism models could significantly improve the OpenMC simulation speed. The calculation rates within different parallelism models are given in Table 1.

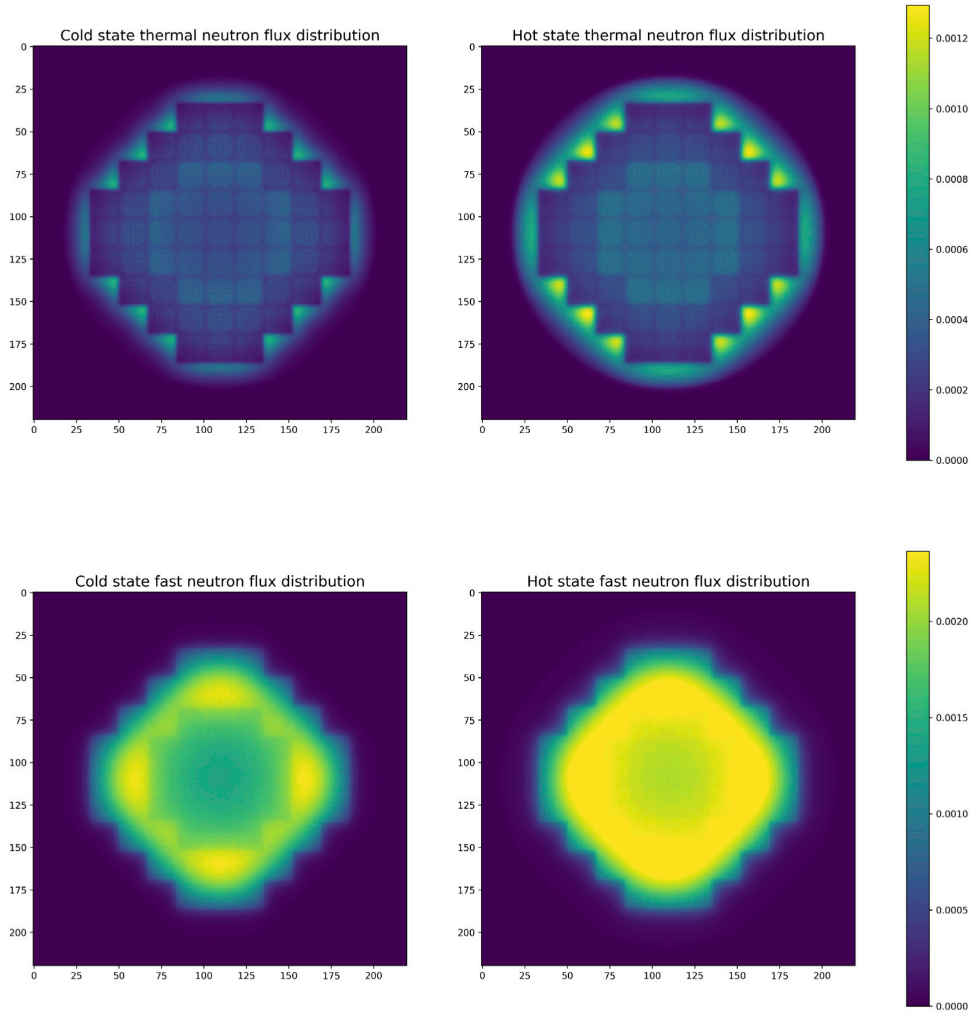

FIGURE 5
The thermal and fast neutron flux distributions in the two-batch refuelling scheme core.

2.3 Sensitivity study

The intrinsic errors of nuclear cross-section libraries will fundamentally affect the accuracy of MC simulation results. The uncertainty analysis of the nuclear database to the continuous-energy MC code is called a sensitivity study. ENDF/B-VII.1, ENDF/B-VIII.0 (Brown et al., 2018), and JEFF 3.3 (Plompen et al., 2020) have been individually employed in the simulations. In the preparing stage, the cited cross-section files are converted from their original format to the OpenMC readable HDF5. The k_{eff} eigenvalue calculation results are $1.29306 \pm 7 \times 10^{-5}$, $1.28870 \pm 8 \times 10^{-5}$, and $1.26958 \pm 7 \times 10^{-5}$. Each simulation would run 250 generations with 100 active ones and a million neutrons.

The result from ENDF/B-VII.1 is the highest. The reactivity is 436 pcm and 2348 pcm higher than its newer version ENDF/B-VIII.0 and JEFF 3.3. ENDF/B-VII.1 was selected to perform the rest of the studies because it was already widely used in multiple mature reactor physics codes. Moreover, OpenMC officially provides a depletion chain based on the ENDF/B-VII.1 libraries. Databases used in neutron transport calculations should keep consistent with the depletion analysis.

2.4 Temperature reactivity coefficients

The selected ENDF/B-VII.1 library provides the incident neutron data at multi temperatures. A series of OpenMC simulations with various temperature settings have been done

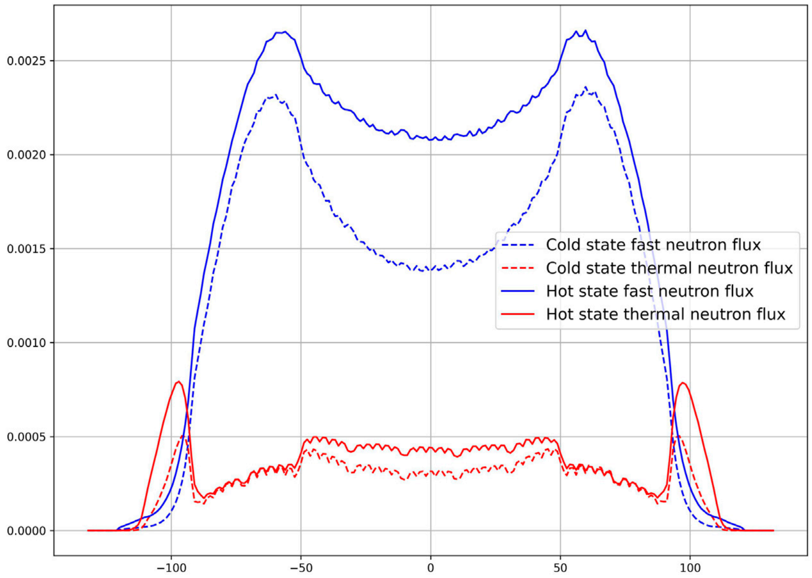

FIGURE 6
Cold and hot state neutron flux distribution viewed along a diameter in the X-axis direction.

to observe the fuel temperature coefficient (FTC) and moderator temperature coefficient (MTC). OpenMC default material temperature is 293.6 K.

The k_{eff} decreases with the temperatures of fuel and moderator going up. For the testing model, all 57 FAs in the core have 4.8% enrichment. When the fuel heats up from 293.6 to 1200 K, the value of k_{eff} decreases from 1.41601 to 1.38364. Furthermore, when the temperature of the moderator is 600 K and water density is 0.7 g/cm^3, the k_{eff} is 1.29312, 12289 pcm lower than the result with the default material temperature.

2.5 Burn-up zone study

To run a spatially based depletion estimation, it is necessary to manually divide the initial reactor core model into many burn-up zones. Then a series of copied fuel materials would be created specifically to fill their corresponding burn-up zones. Hence, the depletion solver will calculate each burn-up zone's characteristic flux and reaction rate, estimating the latest material compositions for the following period.

A series of burn-up calculations have been done to find the reasonable burn-up zone dividing method in both the radial and axial directions. Figure 2 presents an example of burn-up zone spatial positions.

Spatial zones were labelled as burn-up zone 1-4 from the edge to the center in the radial direction. Burn-up zone 1 and 2 respectively occupy 16 FAs, zone3 has 12 FAs, and 13 FAs are loaded in the center area zone 4. In the axial direction, 200 cm height FAs are evenly separated into three zones, labelled as burn-up zone 1–3 from top to bottom. Each burn-up zone was filled with a specially defined fuel material.

Assuming full power operating time for each calculation is 1129 days, longer than 36 months. The entire depletion period was divided into 58 steps with nonuniform step lengths. In the beginning, the step sizes are very short, like an hour, for building the equilibrium of fission product nuclides with large absorption cross-sections. The length of the burn-up step gradually increases with the depletion level as it goes deeper, from an hour to half a year. Figure 3 gives the calculation results.

In this figure, the initial k_{eff} values are very close, about 1.38267. The difference becomes significant as the depletion going deeper. When the model is spatially separated, even though it only has two zones in the radial direction, the difference is 1525 pcm at the ending step. When there are three zones in the axial direction, the k_{eff} value is decreased to around 1.116 at the ending step. The model will adopt 0.7 g/cm^3 water density and 4 × 3 burn-up zone partitions to approach the reactor's full-power operation state.

3 Results and discussion

The above sections have presented the validations and tests for the OpenMC SMART full-core model. This model now should demonstrate credible simulation results and reflect the neutron physics variations due to reactor operations or material

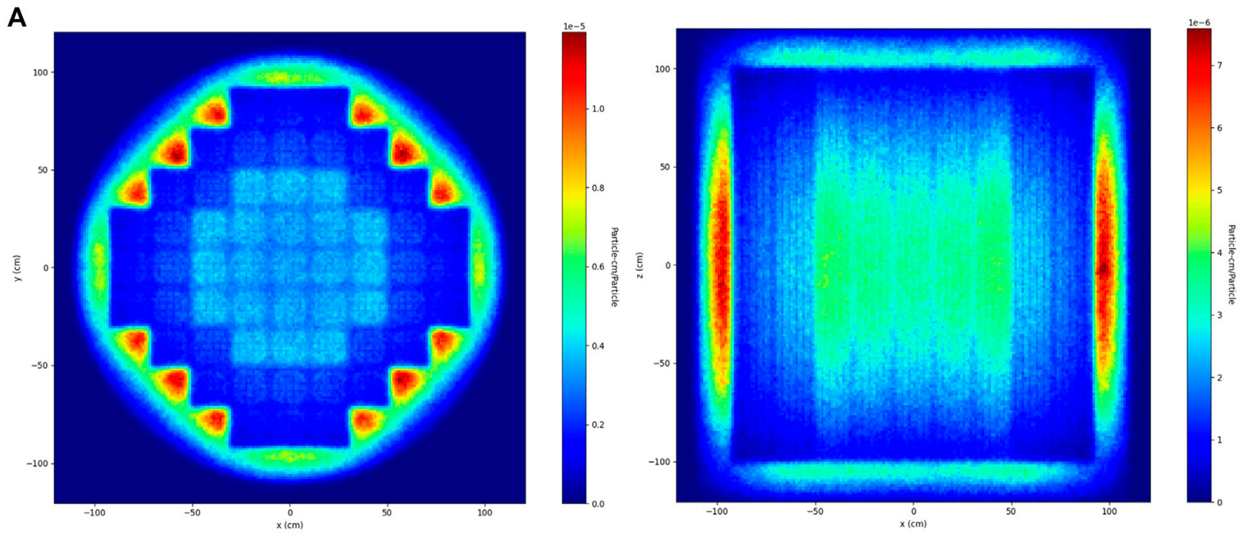

Thermal neutron flux on XY and YZ planes

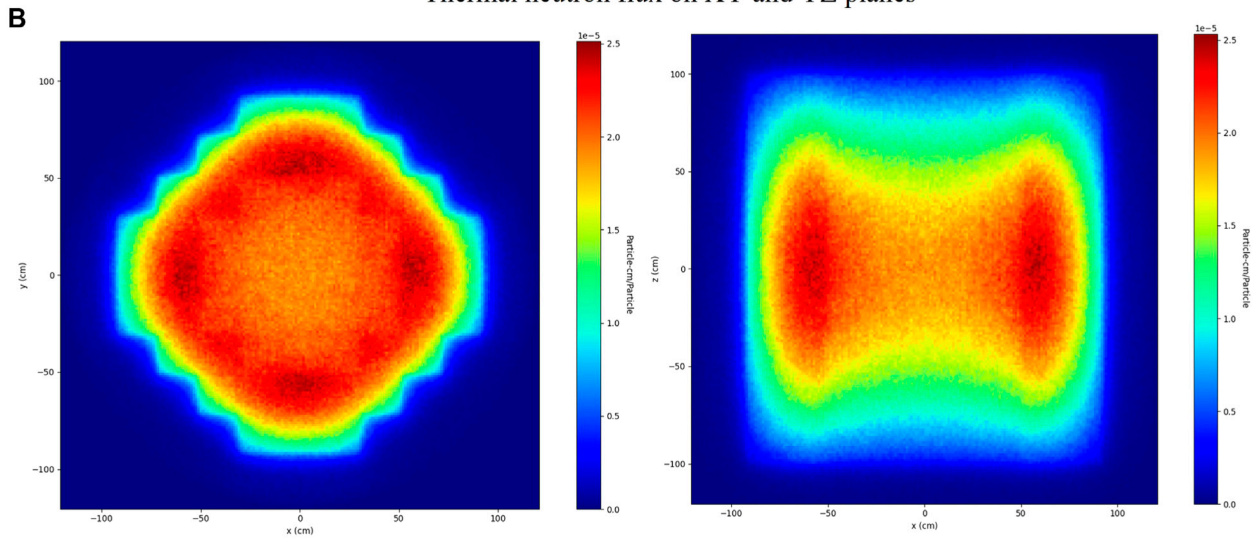

Fast neutron flux on XY and YZ planes

FIGURE 7
The slices of 3D mesh **(A)** thermal and **(B)** fast neutron flux tallying results.

usage. The model has been modified to the initially designed fuel layout, as shown in Figure 4.

The enrichment of 21 FAs in the center area has been redefined as 2.4% to reflect the two-batch refuelling scheme. White pins represent the 2.4% enrichment rods, and the 36 FAs' grey rods contain 4.8% enriched UO_2. Meanwhile, fifteen repeating defined fuel materials are in the burn-up calculation model. The neutron transport simulation results, such as the neutron's energy spectrum, neutron flux and power distributions, will be presented first. Then, burn-up calculation results in one refuelling cycle are used to analyze the reactor uranium economics.

3.1 Neutron transport simulation

3.1.1 Neutron flux spatial distribution

However, the temperature reactivity coefficients or fuel composition changes eventually affect the reactor performance through neutron flux. Therefore, once the core model has been tested and verified, the first goal of this study is to determine the neutron flux distribution in the whole core range.

In OpenMC code, a filter can identify the region in the phase space or set multiple series of energy bins. Two *MeshFilters* were created to define the regular Cartesian mesh grids to cover the model geometry and score the events. Meanwhile, an

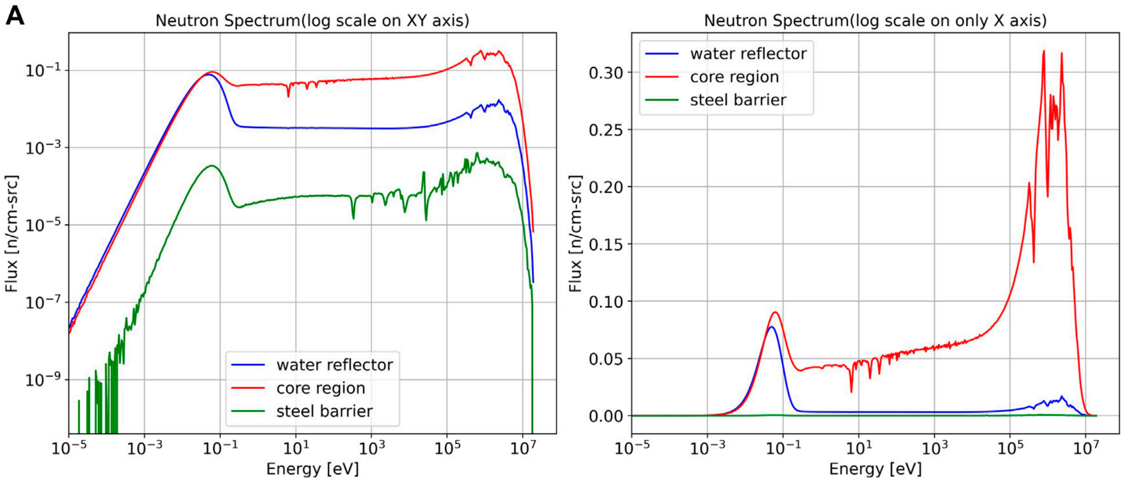

Cold state neutron energy spectrum

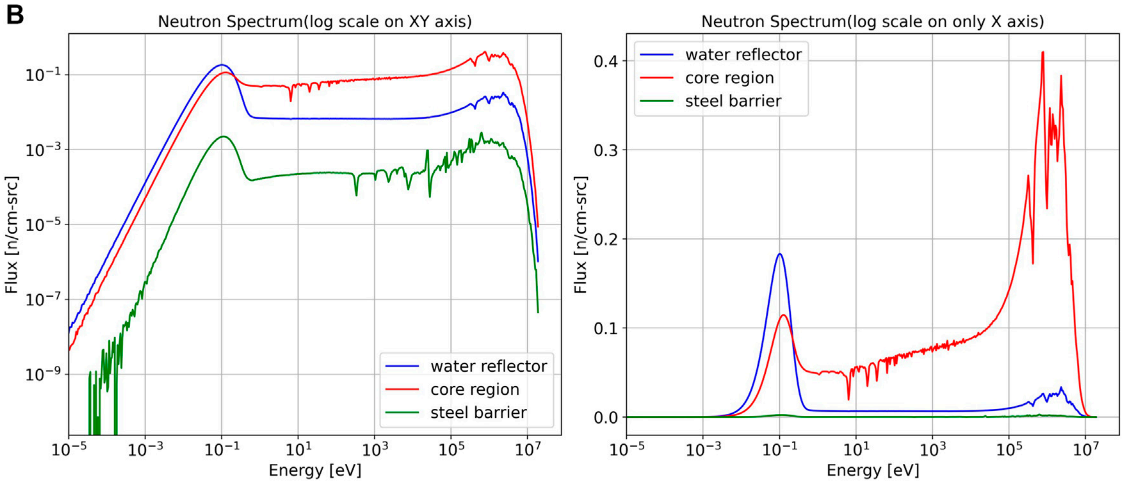

Hot state neutron energy spectrum

FIGURE 8
The steel barrier, reflector, and core's neutron energy spectrums in the **(A)** cold and **(B)** hot states.

EnergyFilter is defined to score events based on incident particle energy, classified into 0–0.625 eV and 0.625–20.0 × 10^6 eV. They represent the thermal and fast energy neutrons.

Figure 5 presents the normalized thermal and fast neutron flux distribution in cold and hot conditions. The cold state means that the moderator and fuel pins are at default temperatures, 293.6 K. The hot state represents the materials at operating temperatures, and water density decrease to 0.7 g/cm^3. The k_{eff} for cold state simulation is 1.34518, for the hot state is 1.22906, and the temperature reactivity defect is 11612 pcm.

The material temperature significantly affects the neutron multiplication, and the spatial distributions of the neutron flux also vary greatly. Thermal neutron flux peaks are outside of the fission zone. A large number of hydrogen atoms can effectively moderate the high-energy neutrons in this area. Conversely, the intensive fast neutron density area is inside the fission zone, surrounding the reloading FAs. When the fission chain reaction is successfully established, the thermal peaks become higher in the reflector area. The data was taken from Figure 5 along the X-axis direction diameter and plotted in Figure 6 to observe the variation. The higher material temperature hardens the neutron spectrum due to the broadened absorption cross-section and lack of moderation. A fraction of leaking thermalized neutrons scatter back to the fission zone.

When the reactor operates, the primary cycle coolant is pumped through the core from the bottom to the top, taking the fission heat and transferring it to the steam generator.

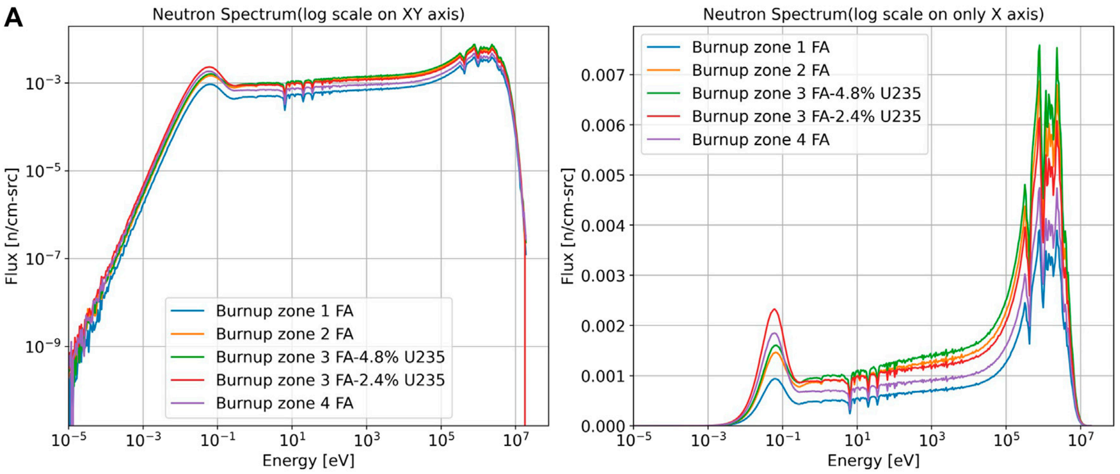

Cold state neutron energy spectrum

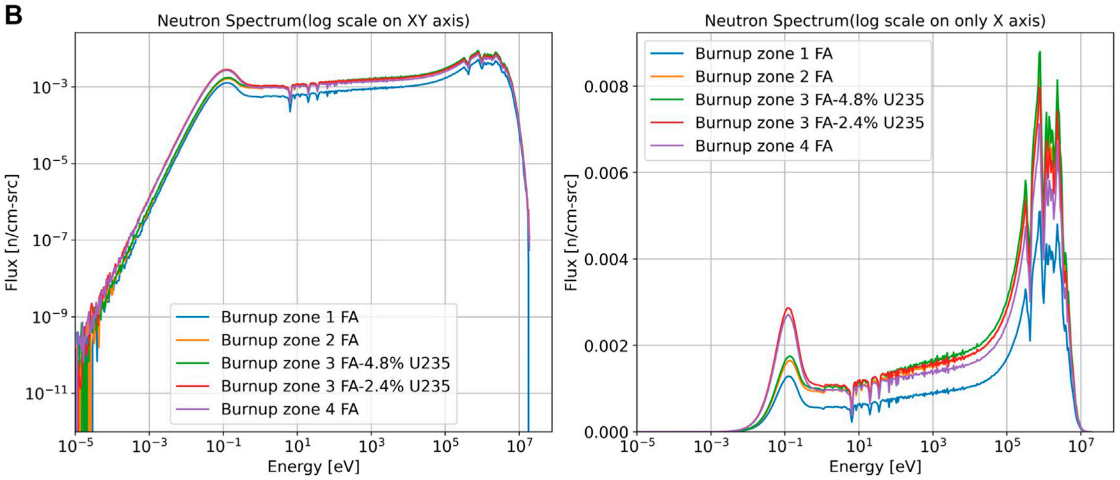

Hot state neutron energy spectrum

FIGURE 9
The neutron energy spectrums of different position fuel assemblies in the **(A)** cold and **(B)** hot states.

Therefore, it is necessary to investigate the spatial neutron distribution inside the core. Figure 7 gives the results.

The entire 3D array tallying results are sliced by XY and YZ planes and then plotted out. Figure 7 also shows the colour bars and scales since each sub-plotting process is independent. Another colour map presents the 3D mesh filter results to distinguish from 2D mesh plots.

The thermal neutron flux density is significant at the water zone's half-height point and decreases in the axial direction. The fast neutron flux density is high at the same axial position. The enriched fuel assemblies produce a more significant amount of fast neutrons than the 2.4% enrichment ones. However, the neutron flux densities at the top and bottom of fuel assemblies are relatively low.

3.1.2 Neutron energy spectrum

In addition to neutron spatial distributions, another important issue that should be determined in the simulation is the neutron energy distribution. The incident neutron's energy would directly affect the occurrence rate of a series of nuclear reactions, not only for fission itself. Figure 8 gives the neutron energy simulation results, where the energy range from 1×10^{-5}—20×10^{6} eV is logarithmically divided into 500 spaces.

In Figure 8, the left-side spectrum has log scales on both *X* and *Y*-axis to observe the results with relatively small values, especially in

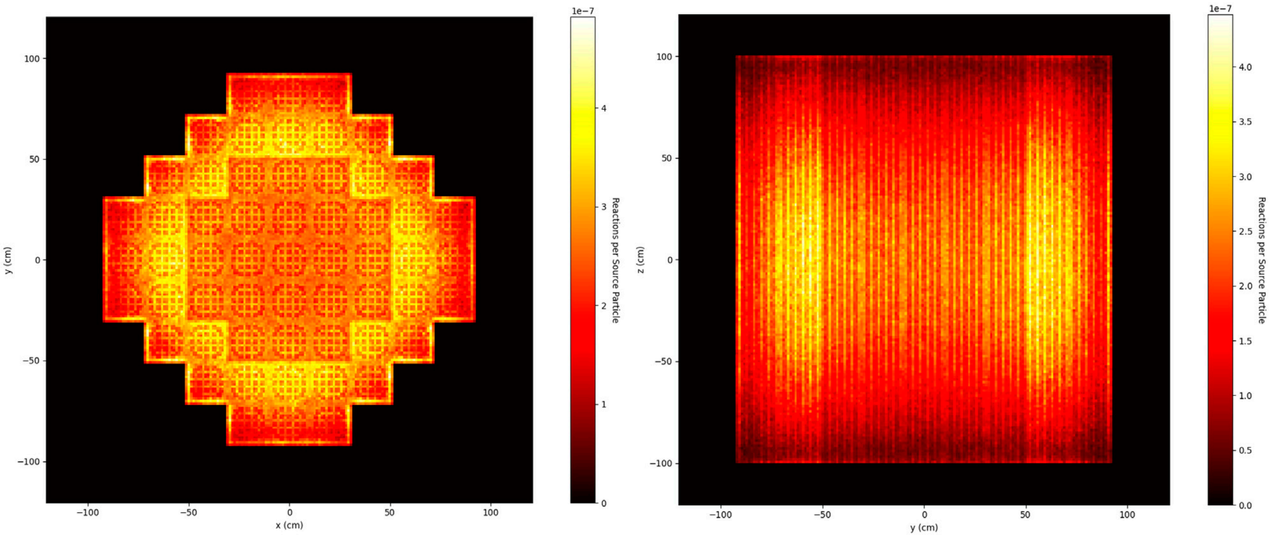

FIGURE 10
The fission rate distributions on the XY and YZ planes.

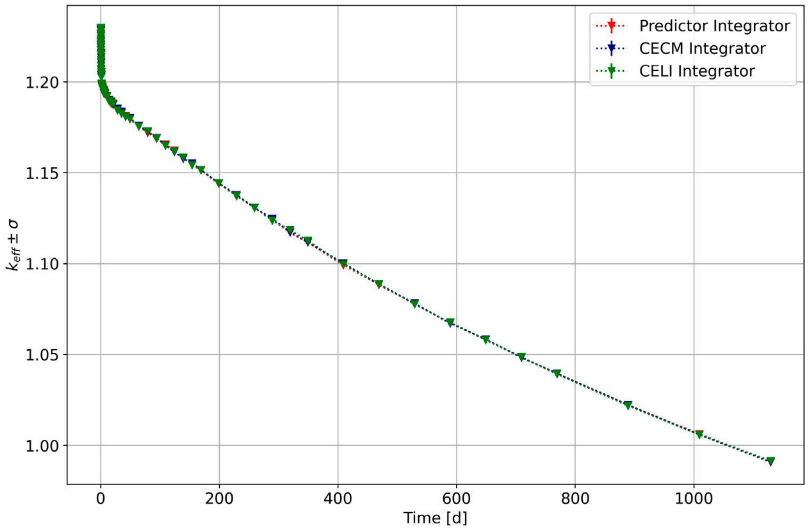

FIGURE 11
Predictor and higher-order integrators depletion results of two batch-scheme core: k_{eff} variations.

the low energy range. The right-side spectrum is different on the Y-axis that is linearly scaled to conveniently observe the peak height difference and oscillations in all energy ranges.

The diagrams represent the neutron energy spectrum in different parts of the model, including the core, the reflector area and the steel barrier. The tallied spectrum has a peak at the thermal energy range, around 10^{-1} eV, and it also has a series of spikes in the fast energy range, from 10^5–10^7 eV. A continuous rising fluctuation links the peaks of the thermal and fast energy range. When the reactor starts up, the entire spectrum rises to a higher level. Moreover, its thermal peak is trending to higher energy due to loss of moderation. The migration of the thermal peak is more evident in the spectrum of the water reflector. In the hot state, a few leakage neutrons will travel through the water reflector and arrive at the steel barrier.

Figure 9 gives a series of spectra in the assemblies located at different burn-up zones. Their variations synchronize with the

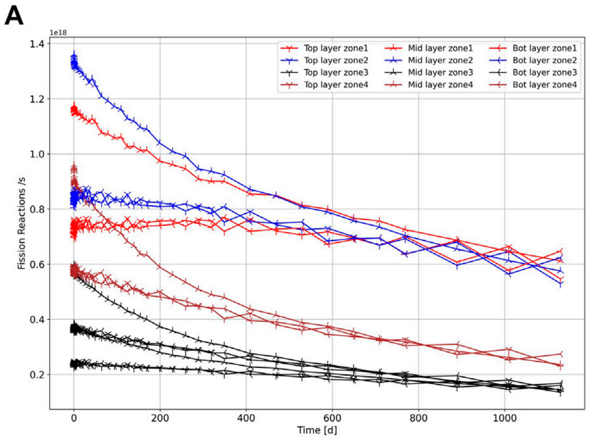

Variations of fission rate

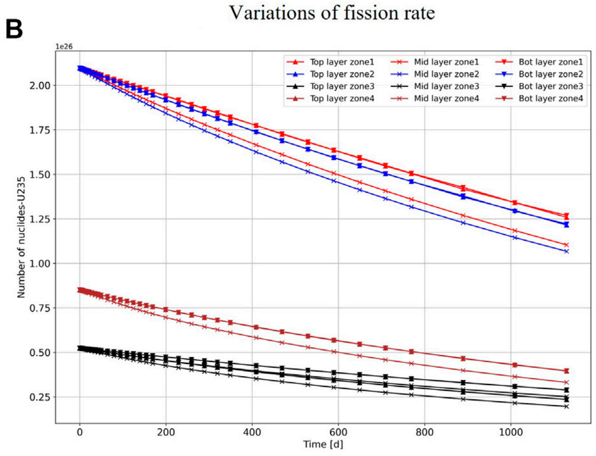

Number of ^{235}U variations

FIGURE 12
Burn-up results of 4 × 3 zones two batch refuelling scheme core, **(A)** fission rate, **(B)** the number of ^{235}U.

range of the entire core cell. The higher material temperature would amplify the radial neutron flux density heterogeneity.

3.1.3 Power distribution

The fission rate is coupled with a 3D mesh filter in the hot state simulation, and the unit is reactions per source particle. Figure 10 presents the fission rate distribution. The highlighted area of the fission reaction rate is highly coincident with the high fast neutron flux density area around the reloading FA zone. The fuel rods do not uniformly produce heat when the reactor is operating. A bright belt surrounds the core edge. The large number of thermal neutrons produced in the water is scattered back and induces an intensive fission reaction in this area.

3.2 Burn-up analysis

3.2.1 Eigenvalue variation

An OpenMC burn-up calculation is a coupling process of a neutron transport operator and a time integration scheme. OpenMC also provides several implementations of different higher-order time-integration algorithms. To further validate the accuracy, another two higher-order algorithms, CE/CM and CE/LI (Isotalo and Sahlberg, 2015), were used to run the same depletion calculation. The calculation results have been presented in Figure 11.

The calculation results show that with the predictor integrator, the value of k_{eff} is 1.22913 at the beginning of the cycle (BOC). Here the result has a 7 pcm improvement from the previous hot state calculation due to the lower neutron histories in the depletions.

After 1129 days of full-power operation, k_{eff} values decrease to 0.99126. The higher order integrators give BOC k_{eff} values are 1.22957. After the same length depletion period, the k_{eff} decreased to 0.99089 and 0.99155 with CE/CB and CE/LI integrators, respectively. This finding explains that the predictor integrator can give reasonable results with a shorter calculating time.

Once the depletion process begins, the fission product ^{135}Xe equilibrium will be built relatively soon, in about 12 h. According to the calculation results, this simulated core can provide more than 990 full power (330 MWth) operating days, just as the original designer stated. However, the k_{eff} of this fuel layout will be lower than one, which means the system is sub-critical after 1129 depletion days. Therefore, the current core design cannot support the cycle length to be 20–30% extended. To further analyze the change in fuel composition and uranium utilization condition, the variations in fission rate and the number of ^{235}U have been plotted.

3.2.2 Fission rate and uranium utilization

Before describing the results, a feature must be pointed out first. In the simulations of two batch refuelling schemes core, the depletion results of two types of FAs in zone3 have been plotted

TABLE 2 The change of ^{235}U number in one refuelling cycle.

Radial zone	Beginning of cycle	End of cycle	Burned ^{235}U	Depletion rate (%)
Zone1	6.2922×10^{26}	3.6316×10^{26}	2.6661×10^{26}	42.28
Zone2	6.2922×10^{26}	3.5057×10^{26}	2.7865×10^{26}	44.28
Zone3	3.1461×10^{26}	1.4994×10^{26}	1.6467×10^{26}	52.34
Zone4	2.5563×10^{26}	1.1258×10^{26}	1.4305×10^{26}	55.95

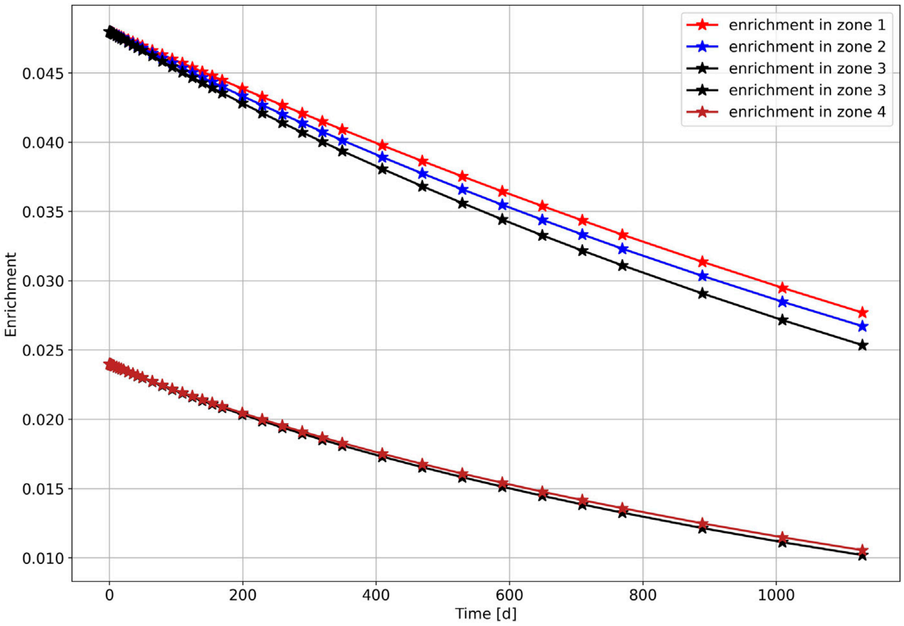

FIGURE 13
The enrichment variations in the radial burn-up zones.

separately. But they are still labelled as radial zone 3 for further comparison.

In Figure 12, the same radial zone diagrams have the same colour to present the data and use a specific marker to represent zones' results at the same height. The fission rate and induced ^{235}U depleting speeds differ in the axial direction. The middle height zone has a more significant fission rate in any radial position. Due to the neutron sampling always being isotropic, the fission rate values are close at all steps in the top and bottom zones. Even though existing oscillations are at a few steps, their mean value still can be fitted in the smoothly decreasing curve.

Table 2 gives the burn-up results for the radial direction. In this table, the amount of burned ^{235}U in a radial zone is the summation of its three corresponding axial zones results.

A total of 8.524×10^{26} ^{235}U atoms have been depleted in one refuelling cycle. The depletion rate is the fraction of burned ^{235}U amount in each radial zone. Central zone 4 has the highest depletion rate, 55.95%, even though the FAs here only have 2.4% enrichment. The utilization of edge area fresh FAs is limited. The depletion rates of zone 1 and 2 are 42.3 and 44.3%. Since the number of FAs in each burn-up zone is not uniform, only studying the number of ^{235}U could lead to misunderstanding results.

In Figure 13, the enrichment of reloading FAs drops to a low level, slightly higher than 1.0%. For the high initial enrichment FAs in the radial zone3, its enrichment significantly drops about 2.53% at the EOC. On the other hand, the high initial enrichment FAs in the rest radial burn-up zones have not been sufficiently depleted. The ending enrichment levels are 2.77 and 2.67% for radial zone 1 and 2. That is still higher than the initial enrichment for the reloading fuels. Figure 13

4 Conclusion

This study has adjusted a full SMART core OpenMC model with operating material temperatures and twelve spatial burn-up zones to approach the operating state reactor core. This model then performed a series of simulations and obtained the reasonable neutronic parameters of the original SMART design. The maximum k_{eff} during reactor operation is 1.22906, and the temperature reactivity defect is 11612 pcm. The k_{eff} decreases to 0.99126 in 1129 full-power operation days. Moreover, the uranium utilization rates are low because the high enrichment fuel assemblies are in the low neutron flux region. The burn-up calculation results show the core outer burn-up zone 3 and 4 have 42.28 and 44.28% ^{235}U depletion rates. These two zones' EOC fuel enrichments are 2.77 and 2.67%. The fuel assemblies surrounding the reloading fuel zone have the most significant fission rate. However, a high fission rate belt surrounding the core edge means that the water can scatter part of thermalized neutrons back to the core. A more reflective material perhaps scatters more thermal neutrons. This update may get extra power output. Future studies will test a set of selected reflector materials in the simulations and try to determine a suitable one for SMART.

Data availability statement

The raw data supporting the conclusion of this article will be made available by the authors, without undue reservation.

Author contributions

All authors contributed to the writing and reviewing of the manuscript. YZ contributed to the modelling and data analysis. All studies are under the guidance and supervised by PN. Wu organized the paper publication process.

Conflict of interest

The authors declare that the research was conducted in the absence of any commercial or financial relationships that could be construed as a potential conflict of interest.

Publisher's note

References

Bisconti, A. S. (2018). Changing public attitudes toward nuclear energy. *Prog. Nucl. Energy* 102, 103–113. doi:10.1016/j.pnucene.2017.07.002

Brown, D. A., Chadwick, M., Capote, R., Kahler, A., Trkov, A., Herman, M., et al. (2018). ENDF/B-VIII.0: The 8th major release of the nuclear reaction data library with CIELO-project cross sections, new standards and thermal scattering data. *Nucl. Data Sheets* 148, 1–142. doi:10.1016/j.nds.2018.02.001

Choi, S. (2015). "Small modular reactors (SMRs): The case of the Republic of Korea," in *Handbook of small modular nuclear reactors* (Sawston, United Kingdom: Woodhead Publishing Limited), 425–465. doi:10.1533/9780857098535.4.379

Dagum, L., and Menon, R. (1998). OpenMP: An industry standard API for shared-memory programming. *IEEE Comput. Sci. Eng.* 5 (1), 46–55. doi:10.1109/99.660313

Fujita, E. K., Driscoll, M. J., and Lanning, D. D. (1978). Design and fuel management of PWR cores to optimize the once-through fuel cycle. United States, Chap. 3. doi:10.2172/6670045

Graham, R. L., Woodall, T. S., and Squyres, J. M. (2005). "Open MPI: A flexible high performance MPI," in International conference on parallel processing and applied mathematics, 228–239.

IAEA (2018). *IAEA annual report 2018 contents*. Vienna, Austria: IAEA.

IAEA (2011) System-integrated modular advanced reactor (SMART). Available at: https://aris.iaea.org/PDF/SMART.pdf. (Accessed April 04 2011).

Isotalo, A., and Sahlberg, V. (2015). Comparison of neutronics-depletion coupling schemes for burnup calculations. *Nucl. Sci. Eng.* 179 (4), 434–459. doi:10.13182/nse14-35

Kim, H. G., Chang, S. H., and Lee, B. H. (1993). Pressurized water reactor core parameter prediction using an artificial neural network. *Nucl. Sci. Eng.* 113 (1), 70–76. doi:10.13182/nse93-a23994

Leppänen, J., Pusa, M., Viitanen, T., Valtavirta, V., and Kaltiaisenaho, T. (2015). The Serpent Monte Carlo code: Status, development and applications in 2013. *Ann. Nucl. Energy* 82, 142–150. doi:10.1016/j.anucene.2014.08.024

Plompen, A. J. M., Cabellos, O., De Saint Jean, C., Fleming, M., Algora, A., Angelone, M., et al. (2020). The joint evaluated fission and fusion nuclear data library, JEFF-3.3. *Eur. Phys. J. A* 56 (7), 1–108.

Romano, Paul K., Josey, C. J., Johnson, A. E., and Liang, J. (2021). Depletion capabilities in the OpenMC Monte Carlo particle transport code. *Ann. Nucl. Energy* 152, 107989. doi:10.1016/j.anucene.2020.107989

Romano, P. K., Horelik, N. E., Herman, B. R., Nelson, A. G., Forget, B., and Smith, K. (2015). OpenMC: A state-of-the-art Monte Carlo code for research and development. *Ann. Nucl. Energy* 82, 90–97. doi:10.1016/j.anucene.2014.07.048

Sadighi, M., Setayeshi, S., and Salehi, A. A. (2002). PWR fuel management optimization using neural networks. *Ann. Nucl. Energy* 29 (1), 41–51. doi:10.1016/S0306-4549(01)00024-X

Stoutenborough, J. W., Sturgess, S. G., and Vedlitz, A. (2013). Knowledge, risk, and policy support: public perceptions of nuclear power. *Energy Policy* 62, 176–184. doi:10.1016/j.enpol.2013.06.098

frontiers | Frontiers in Energy Research

TYPE Original Research
PUBLISHED 31 August 2022
DOI 10.3389/fenrg.2022.987513

OPEN ACCESS

EDITED BY
Jingang Liang,
Tsinghua University, China

REVIEWED BY
Chen Hao,
Harbin Engineering University, China
Donny Hartanto,
Oak Ridge National Laboratory (DOE),
United States
Jinsen Xie,
University of South China, China

*CORRESPONDENCE
Wenbin Wu,
wuwb28@mail.sysu.edu.cn

SPECIALTY SECTION
This article was submitted to Nuclear Energy,
a section of the journal
Frontiers in Energy Research

RECEIVED 06 July 2022
ACCEPTED 08 August 2022
PUBLISHED 31 August 2022

CITATION
Zhong Y, Norman P and Wu W (2022), A feasibility study of SMART reactor power performance optimizations-part 2: Reflector material selection.
Front. Energy Res. 10:987513.
doi: 10.3389/fenrg.2022.987513

A feasibility study of SMART reactor power performance optimizations-part 2: Reflector material selection

Yiming Zhong[1], Paul Norman[1] and Wenbin Wu[2]*

[1]Nuclear Physics Group, School of Physics and Astronomy, College of Engineering and Physical Sciences, University of Birmingham, Birmingham, United Kingdom, [2]Sino-French Institute of Nuclear Engineering and Technology, Sun Yat-sen University, Zhuhai, China

The neutron reflector is a general component in the nuclear reactor design. The original SMART reactor design used light water as a reflector surrounding the fission zone. However, this design has low uranium utilization rates in the outermost fuel assemblies, so poor fuel economy. In this study, six potential reflector materials, i.e., heavy water, graphite, beryllium metal and its oxide, steel, and tungsten carbide has been investigated as the neutron reflector for SMART. Firstly, the materials' cross-sections of neutron scattering and (n, 2n) reactions have been cited from ENDF data libraries and analyzed. This analysis found for the neutrons with energy lower than 1 eV, the ^{9}Be atom has six barn elastic scattering cross-sections, and the ^{9}Be(n, 2n)^{8}Be reaction can compensate for neutron leakage. Then, OpenMC is employed to simulate the effect of these reflector materials on power distribution and depletion. Compared with the original design, the beryllium oxide can improve the initial k_{eff} from 1.22906 to 1.27446, flat the radial direction power distribution. The analysis on both scales agrees that the beryllium oxide is an efficient neutron reflector choice with good material properties.

KEYWORDS

reflector, cross-section, Monte Carlo, power distribution, burn-up

1 Introduction

By analyzing the OpenMC full-core simulation results, the previous study finds low ^{235}U utilization rates in the outside fuel assemblies (FA). The original SMART design uses water surrounding the FAs as the neutron reflector. An efficient reflector can scatter the leaking neutrons back to the core and flat the core radial power distribution (Lamarsh and Baratta, 2001; Stacey, 2018). Due to the smaller size of SMRs' core, the fission-produced neutrons have a higher possibility of entering the reflector than in traditional large PWRs. A crucial factor in determining an integral PWR design's physical viability and fuel economy may be the reflector efficiency. Moreover, the reflector will work in the extensive radiation, high temperature and aggressive chemical environment (Kurosaki and Yamanaka, 2020).

TABLE 1 Material properties of potentially available reflector materials.

Material	Effective isotope	Atomic mass(u)	Melting point (˚C)	Density (g/cm^3)
Light water	^{1}H, ^{16}O	1.00784,15.9949	0	0.997
Heavy water	^{2}H, ^{16}O	2.014102,159949	3.81	1.11
Graphite	^{12}C	12	≈3600	2.26
Beryllium	^{9}Be	9.012182	1287	1.85
Beryllium oxide	^{9}Be, ^{16}O	9.012182, 15.9949	2530	3.02
Stainless steel	^{56}Fe	55.93494	1510	7.92
Tungsten Carbide	^{183}W	183.84	2870	15.63

The selection of reflector material would thus somewhat affect the neutronic performance of SMART. In 2015, S. Dawahra's work (Dawahra et al., 2015a) used Monte Carlo N-Particle (MCNP) to study the reflector effect on the IAEA referencing water-moderated material test reactor (IAEA, 1980). The optional fuel enrichments are 20%, 45%, and 93%. Reflectors chosen have light water, heavy water, beryllium and graphite. Similar research was published in 2016. Farrokh Khoshahval (Khoshahval and Salari, 2016) studied the same types of reflector and their effect on the 5MW$_{\mathrm{th}}$ pool-type light water Tehran research reactor by WIMS-D4 (Deen et al., 1995) and the CITATION (Fowler and Vondy, 1969) codes. Both works agree that beryllium is a particularly effective reflector material for water-cooled reactors. A later published study investigated the feasibility of replacing Be reflector with its oxide BeO in the miniature neutron source reactor (Dawahra et al., 2015b).

^{9}Be atom will produce neutron from (n, 2n) reaction. If the neutron is in the fast energy range, ^{9}Be will produce helium and tritium in the (n, α) reaction. Some USA studies have investigated the beryllium reflector and its composition effect on the research reactors (Ilas, 2013; Puig and Dennis, 2016). The depletion of pre-existing impurities will significantly affect reactivity. Besides the water reactors, researchers also propose using the beryllium-based material in the high-temperature gas-cooled reactor (HTGR). S. Atkinson performed studies (Atkinson et al., 2019) that compared beryllium oxide and nuclear graphite as TRISO fuel containers and reflectors for HTGR U-Battery.

In the PWR design, the vertical and horizontal plates form a supportive component called the assembly baffle, which is the interface between the core and the reactor barrier (Bosch et al., 2021; Ge´rard and Somville, 2009). Generally, there is water between the baffle and core barrier. On the other hand, some

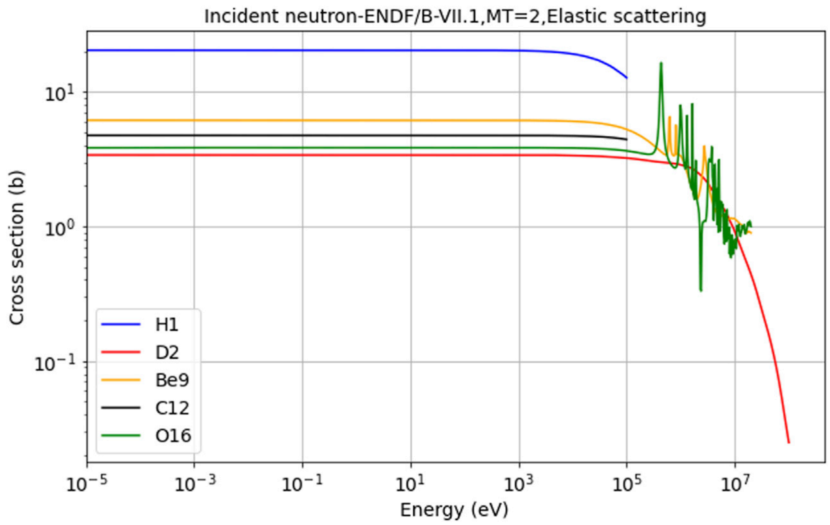

FIGURE 1
Elastic scattering cross-sections (0k) of ^{1}H, ^{2}H, ^{9}Be,^{12}C,^{16}O versus incident neutron energy.

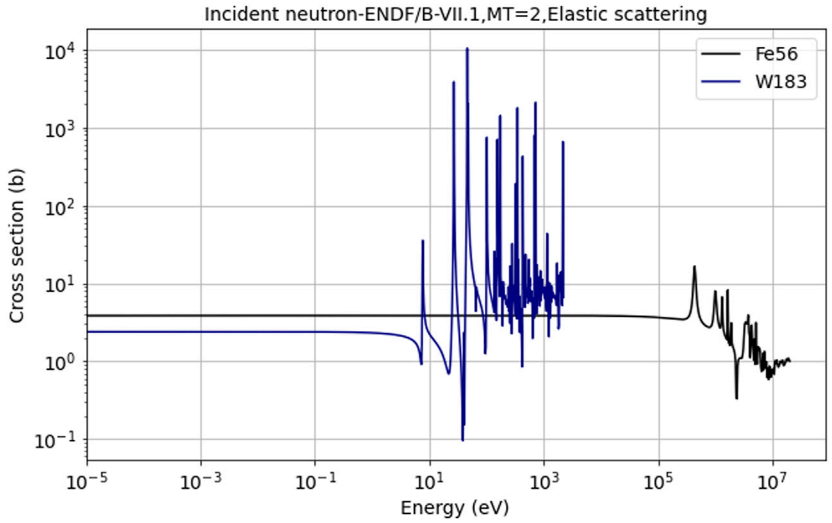

FIGURE 2
The elastic scattering cross-section (0k) of heavy atomic mass isotopes ^{56}Fe, ^{183}W.

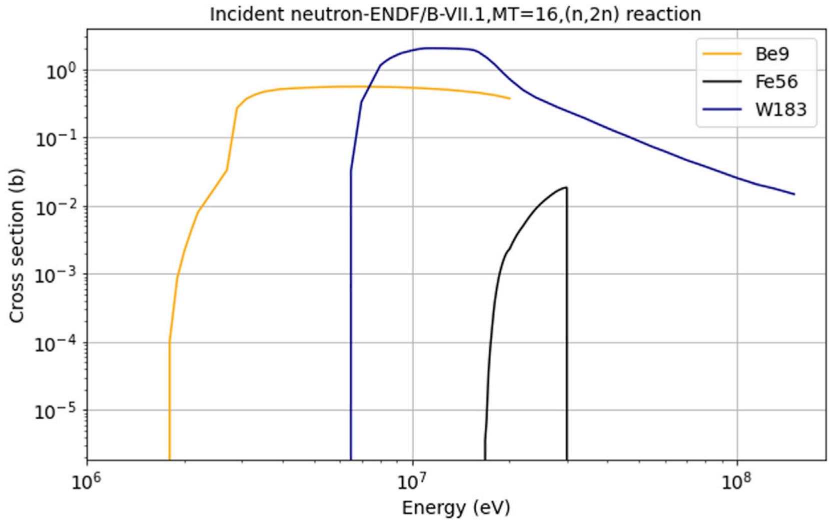

FIGURE 3
(n, 2n) reaction, MT = 16 cross-section distributions of ^{9}Be, ^{56}Fe, ^{183}W.

institutes study the feasibility of heavy material reflectors, like stainless steel walls surrounding the core (Czakoj et al., 2022). Košt'ál' experiment confirms the strong neutron-absorbing effect from the VVER-1000 (Vojackova et al., 2017) heavy reflector' cooling channel water. The related research has already been done by both deterministic and Monte Carlo codes (Sargeni et al., 2016; Taforeau et al., 2019). Sargeni's work focus on core power tilt. This asymmetry problem was first studied by the diffusion code CRONOS2 (Lautard et al., 1992) and then benchmarked by MCNP. In addition, some small integral PWRs inherit technology from large reactors designs with steel reflectors, such as I^{2}S-LWR (Flaspoehler and Petrovic, 2020) and IRIS(Carelli et al., 2004). Besides, some studies are trying to replace the water in the baffle with other light materials such as graphite and beryllium in the long life-cycle small water coolant designs (Bae and Hong, 2015; Wankui et al., 2017).

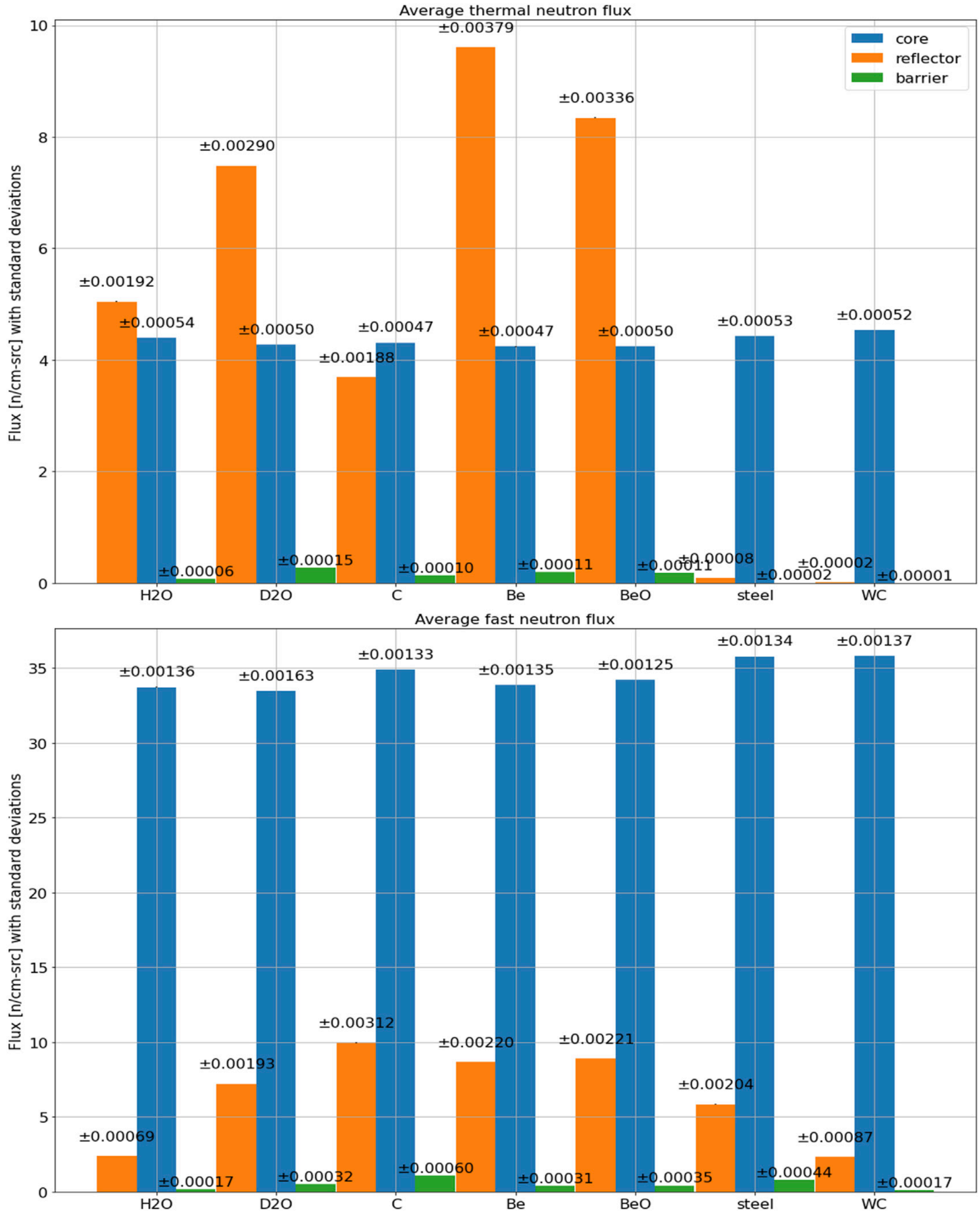

FIGURE 4
Bar charts of thermal and fast neutron flux with standard deviations for core, reflector and barrier.

The author's previous study builds and validates an OpenMC (Romano et al., 2015) SMART full reactor core model with a two-batch refuelling fuel layout (Choi, 2015). The supplementary material section will remind the schematic of this model. This work will first analyze the reflector materials' neutron reaction cross-sections. Then, filling the selected materials into the model's reflector cell in sequence to simulate the reflected-core power performances. Meanwhile, the simulation process acquires the corresponding reaction rates and k_{eff} eigenvalues. The simulation and analysis results will determine the suitable reflector material for SMART.

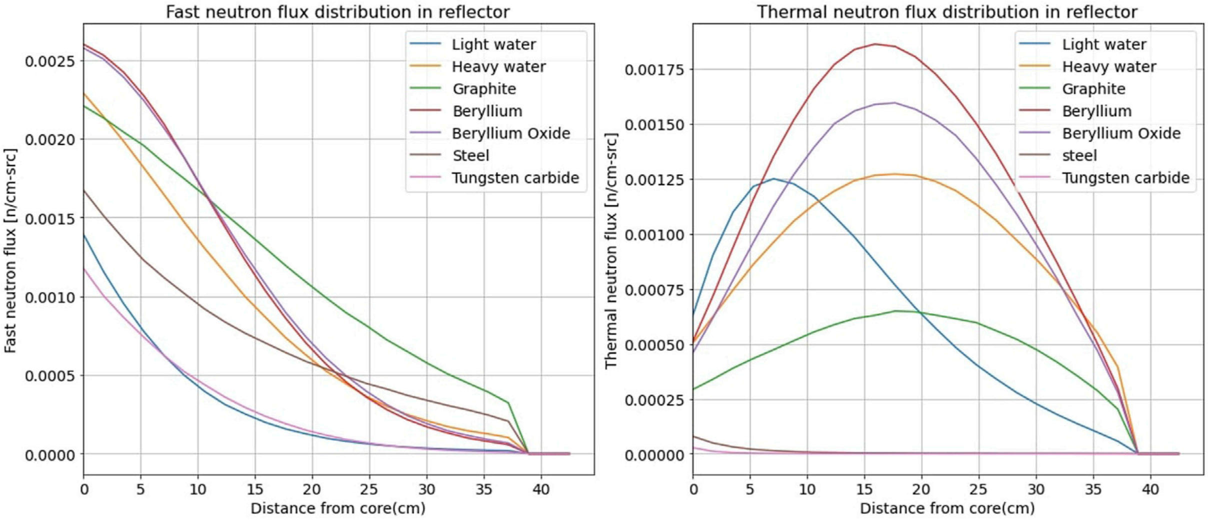

FIGURE 5
Values of neutron flux versus the distance away from FA boundaries.

2 Reflector material

A suitable moderator material is also an acceptable reflector material because of its low absorption cross-section σ_a and high scattering cross-section σ_s. According to the published literature and technical reports, the author selected potential light atomic mass reflector materials such as heavy water, graphite, beryllium, beryllium oxide, and a couple of heavy metal materials: stainless steel and tungsten carbide. Besides these, the water itself is a commonly applied reflector material. Heavy water D_2O and graphite are widely used materials in nuclear reactor designs. Several PWRs utilize heavy water as primary circle coolant and moderator, such as CANDU reactor (Torgerson et al., 2006) from Canada, and IPHWR-700 (Bhadauria et al., 2021) from India.

Many high operating temperature reactor designs use graphite as the moderator, just like the United Kingdom's advanced gas-cooled reactors (AGR). The recently developed pebble-bed HTGR (Zhang et al., 2016) also use graphite to contain TRISO fuel particles. The beryllium-based materials were studied for space reactors due to their low density and outstanding thermal performance (Snead and Zinkle, 2005). The melting points are 1287°C and 2530°C, and thermal conductivities are 200 W m^{-1} K^{-1} (300 K) and 281 W m^{-1} K^{-1} (293 K) for beryllium metal and beryllium oxide, respectively. The neutron irradiation will give negative feedback to the thermal conductivities (Kurosaki and Yamanaka, 2020). Beryllium does not react with water or steam. However, BeO is expensive and toxic. Fabricating metal beryllium with BeO or $Be(OH)_2$ makes it more costly. Therefore, applying beryllium reflectors in SMART should consider the material economy and cost.

Usually, Heavy metal materials are difficult to slow down neutrons, but they can shield the radiation from the core. The application of stainless steel as a neutron reflector has been well studied (Frybort et al., 2020). Tungsten carbide (WC) has a very high melting point at 2870°C, which was a neutron reflector for a nuclear weapon in the early stage of nuclear power development. Meanwhile, tungsten carbide is considered a novel shielding material for SMRs due to its high densities and fast neutron capture cross-section (Giménez and Lopasso, 2018). Similar to beryllium, WC also does not react with water. The material properties of these materials are summarized in Table 1.

The particular reactions' cross-sections have been collected from IAEA evaluated data libraries ENDF for each material (Brown et al., 2018). The OpenMC code reserves a data process Python package. The essential function is analyzing and converting nuclear data from the ACE files and generating libraries in the HDF5 format for the transport solver. In an ENDF dataset, the data would be parameterized by the model calculations and reduced to a tabular form.

3 Results and discussion

3.1 Nuclear data analysis

3.1.1 Elastic scattering

Figure 1 gives the elastic cross-sections for the light atomic isotopes in Table 1. The five isotopes all have possibilities for elastic neutron scattering. For neutrons with energy lower than 1 eV, the cross-section of ^1H is 20 b. For ^2H, ^9Be, and ^{12}C, there are 3.39, 6.15 and 4.75 b. The cross-section values would decrease

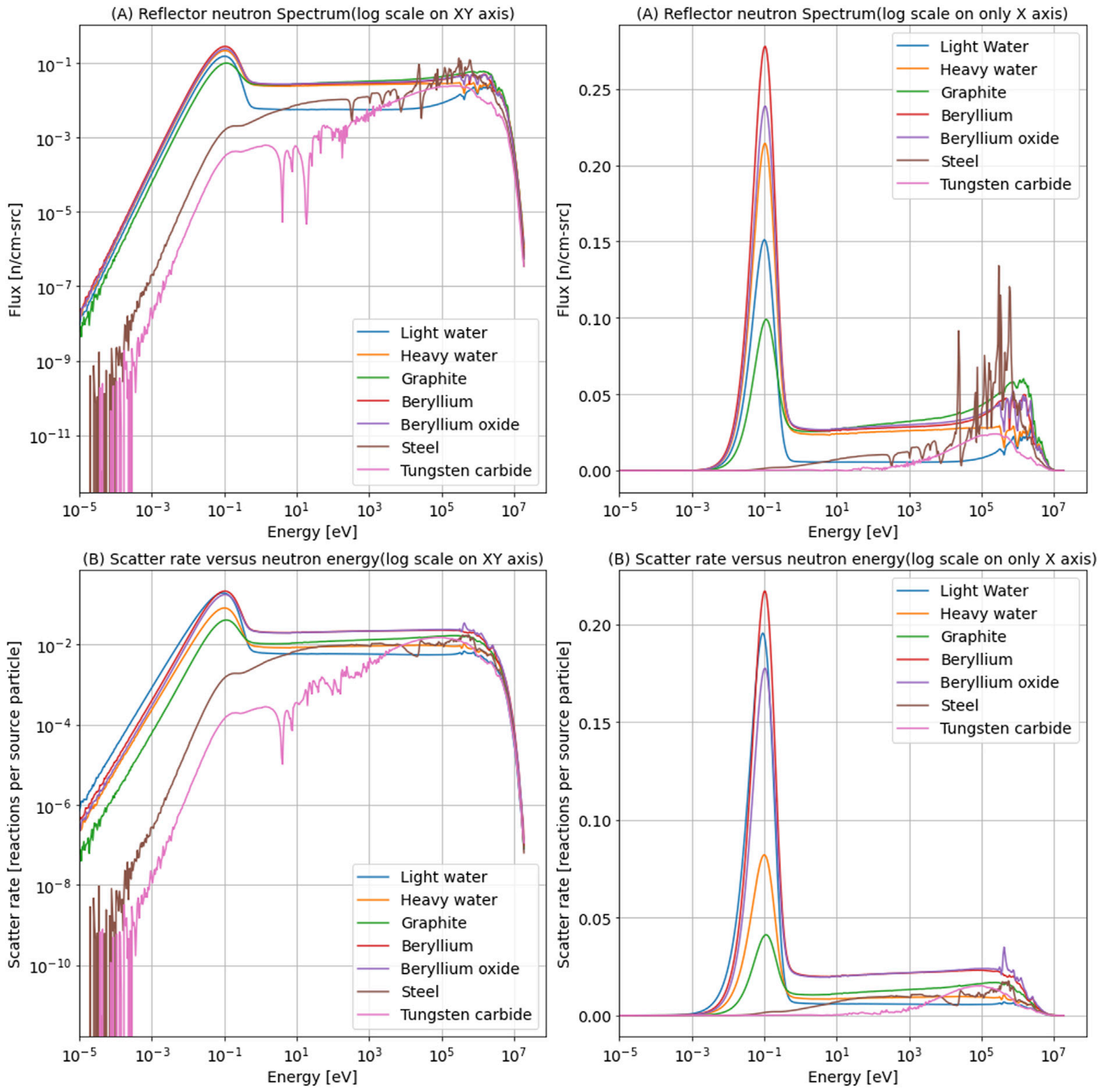

FIGURE 6
The incident neutron energy spectra and scattering reaction energy distributions within reflector materials.

when the incident neutrons speed up. However, they still have the probability of slowing down the fast neutrons. ^{16}O isotope also has a significant elastic scattering cross-section to incident neutrons, and its distribution exists a significant oscillation between the energy range from 10^5–10^7 eV.

Figure 2 gives the resolved resonance energy range elastic scattering cross-section distributions of heavy atomic mass isotopes ^{56}Fe and ^{183}W. In this region, the experimental resolution is enough to observe the resonance and determine its parameters. The sensitivity area of ^{56}Fe is between 10^5 and 10^7 eV. For the lower energy incident neutrons, its σ_s are small than Be^9, about 3.842 b.

3.1.2 (n, 2n) reaction

This study also investigates the potential (n, 2n) reactions. Beryllium can be a neutron multiplier due to the ^{9}Be(n,2n)^{8}Be reaction. Checking the ENDF files of the potential reflector materials, the rich neutron isotopes ^{56}Fe and ^{183}W also have probabilities for (n, 2n) reactions. Their cross-section distributions have been

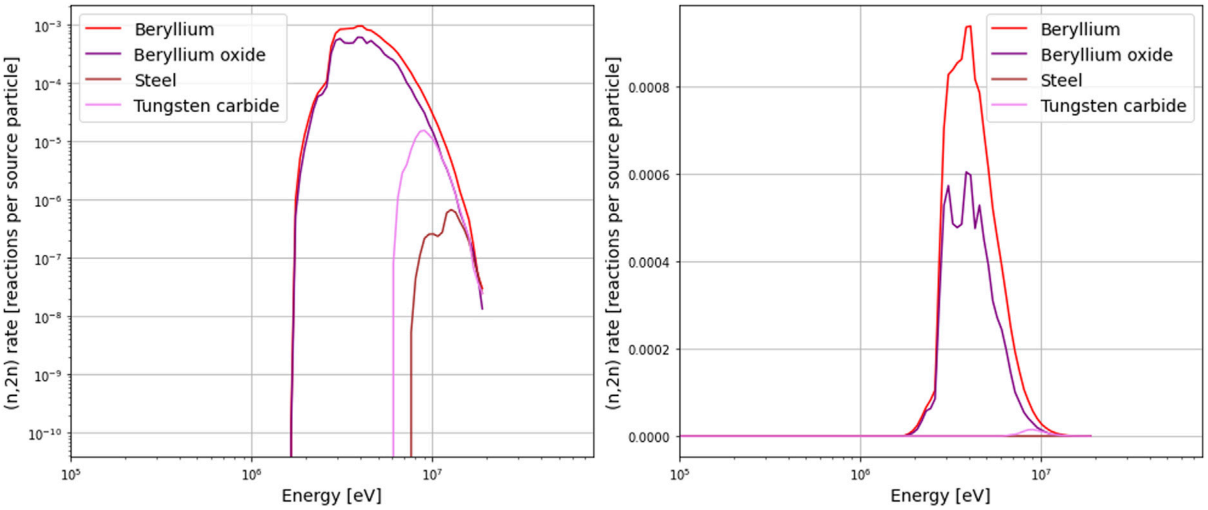

FIGURE 7
The (n, 2n) reaction rate distributions versus incident neutron energy.

TABLE 2 The total scattering rate and absorption rate of reflector materials (units: reactions per source particle).

Reflector materials	Scatter (mean)	Std. dev	Absorption (mean)	Std. dev
Light water	8.829	0.003	0.04862	2×10^{-5}
Heavy water	5.456	0.002	4.81×10^{-4}	3.1×10^{-7}
Graphite	5.116	0.002	8.46×10^{-4}	5.1×10^{-7}
Beryllium	13.34	0.004	0.01194	4×10^{-6}
Beryllium oxide	12.14	0.0036	0.0075	2×10^{-6}
Steel	2.484	0.001	0.0212	1.1×10^{-5}
Tungsten carbide	1.505	0.0006	0.04542	2×10^{-5}

TABLE 3 k_{eff} eigenvalue results of two-batch refuelling scheme core with different material reflectors.

Material	k_{eff}
Light water	$1.22906 \pm 7 \times 10^{-5}$
Heavy water	$1.25921 \pm 7 \times 10^{-5}$
Graphite	$1.25157 \pm 7 \times 10^{-5}$
Beryllium	$1.27613 \pm 7 \times 10^{-5}$
Beryllium oxide	$1.27446 \pm 6 \times 10^{-5}$
Steel	$1.22754 \pm 6 \times 10^{-5}$
Tungsten carbide	$1.21344 \pm 7 \times 10^{-5}$

plotted in Figure 3. The incident neutron must be higher than a particular energy threshold to induce an (n, 2n) reaction.

The ^{9}Be atom has an (n, 2n) reaction threshold of 1.8 MeV. That cross-section would be higher than 0.27 b and stay stable when neutron energy is over 2.9 MeV. Heavy isotope ^{183}W's cross-section is significant for fast energy neutrons, $\sigma_{n,2n}$ is bigger than 2 b for the neutron in the energy range 11–14 MeV. However, $\sigma_{n,2n}$ will decrease lower than 1 b if the incident neutron energy exceeds 19 MeV.

The nuclear data studies in this work are helpful in qualitatively selecting the proper reflector material. However, due to the difference in material densities, the number of isotope atoms in particular geometry spaces would significantly differ. Only comparing the cross-section data could not give reasonable results.

3.2 Reflected core simulation

The simulations record the average flux values of core, reflector and barrier three cells to evaluate the effect of reflectors. Supplementary Figure S1 presents the cells' spatial

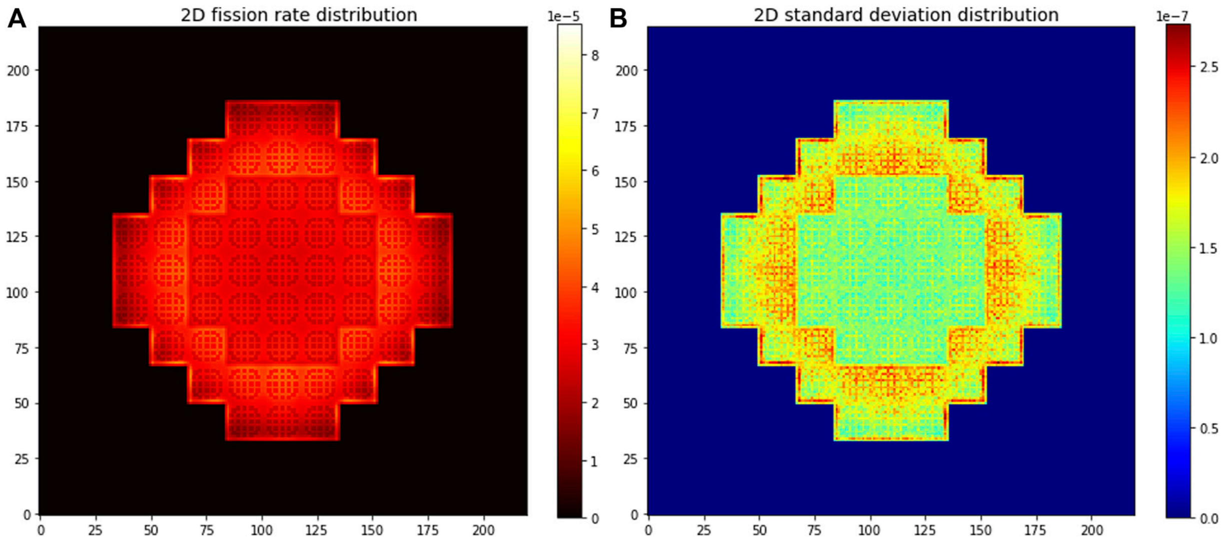

FIGURE 8
Fission rate and standard deviation distributions of two-batch refuelling scheme core with light water reflector.

positions, and this figure also shows how the model is divided into the twelve spatial burn-up zones. The simulations in the following section adopt the operating temperature condition and 0.7 g/cm^3 expanded water density. Figure 4 uses bar height to present the flux values.

For the core, the average fast and thermal neutron flux values are generally close, whatever the reflector material type is. The difference between the maximum and minimum fast neutron flux is 2.1 n/cm-src, and for thermal neutron flux, it is 0.2 n/cm-src. On the contrary, reflector cells' flux values have apparent differences in both energy groups.

The Be metal reflector has the highest average thermal neutron flux, 9.6105 n/cm-src, and the second one is in BeO, 8.3436 n/cm-src. Heavy materials have two orders of magnitude less thermal neutron flux than light materials. For the fast neutrons, its maximum flux is in the graphite reflector. The green bars represent the neutron flux in the steel barrier that should not be neglected. Steel and WC block the most thermal neutrons from getting into the barrier. However, the steel cannot effectively function to shield the fast neutrons. 0.7658 n/cm-src is the most significant remaining fast neutron flux value after the reflection and shield in all simulations.

The neutron flux spatial distribution in particular material reflectors also have been investigated. The reflector geometry in this study is constant. The spatial distribution results can provide a meaningful reference to determine the size of the reflector made by a particular material.

The curves in Figure 5 represent the neutron flux fluctuations in the reflector along the model's diagonal. Four light mass materials and steel reflectors improve the fast neutron flux values near the boundary. The beryllium-based materials give the most significant improvements. Fast neutron moderation in different media produces a series of thermal neutron flux peaks. The thermal neutron flux peak in light water is closer to the boundary than in other light mass reflectors.

The isotopes' cross-section for a particular reaction depends on the incident neutron energy at a specific temperature. Figure 6 shows several tallied reflectors' neutron energy spectra. The plots in Figure 6 could be seen as a supplement to explain the results in Figure 4. The neutron flux integrations are now represented in the energy spaces. The simulations also record the scattering reaction rate and corresponding incident neutron energy.

Observing the spikes located at 10^{-1} eV in Figures 6A,B, the neutron flux in light water is lower than that in heavy water. However, the neutron scattering rate is higher. The beryllium metal reflector has the most significant scattering reaction rate for all energy ranges. When neutron energy is around 10^{-1}eV, the scattering ability of BeO is weaker than light water and beryllium metal. The neutron energy increase will enhance the BeO's reflection ability. The scattering reaction diagrams of Be-based materials overlap, only having a few variances when neutron energy is between 10^5 and 10^6. Meanwhile, the absorption rates have also been recorded in these simulations. Table 2 presents the tally results.

The results in Table 2 show hydrogen atom has a high elastic scattering cross-section but do not have the best reflection ability. The neutron absorption rate of light water is the highest of all potential materials. The (n, 2n) reactions in the materials related to Figure 3 have also been recorded through the simulations. In Figure 7, the beryllium-based materials have much higher possibilities than metal materials to compensate for neutrons by (n, 2n) reaction. The integrated (n, 2n) reaction rates for Be and BeO are $0.013964 \pm 9 \times 10^{-6}$ and $0.009414 \pm 7 \times 10^{-6}$. For steel and tungsten carbide are $0.001803 \pm 1 \times 10^{-6}$ and $0.001924 \pm 2 \times 10^{-6}$.

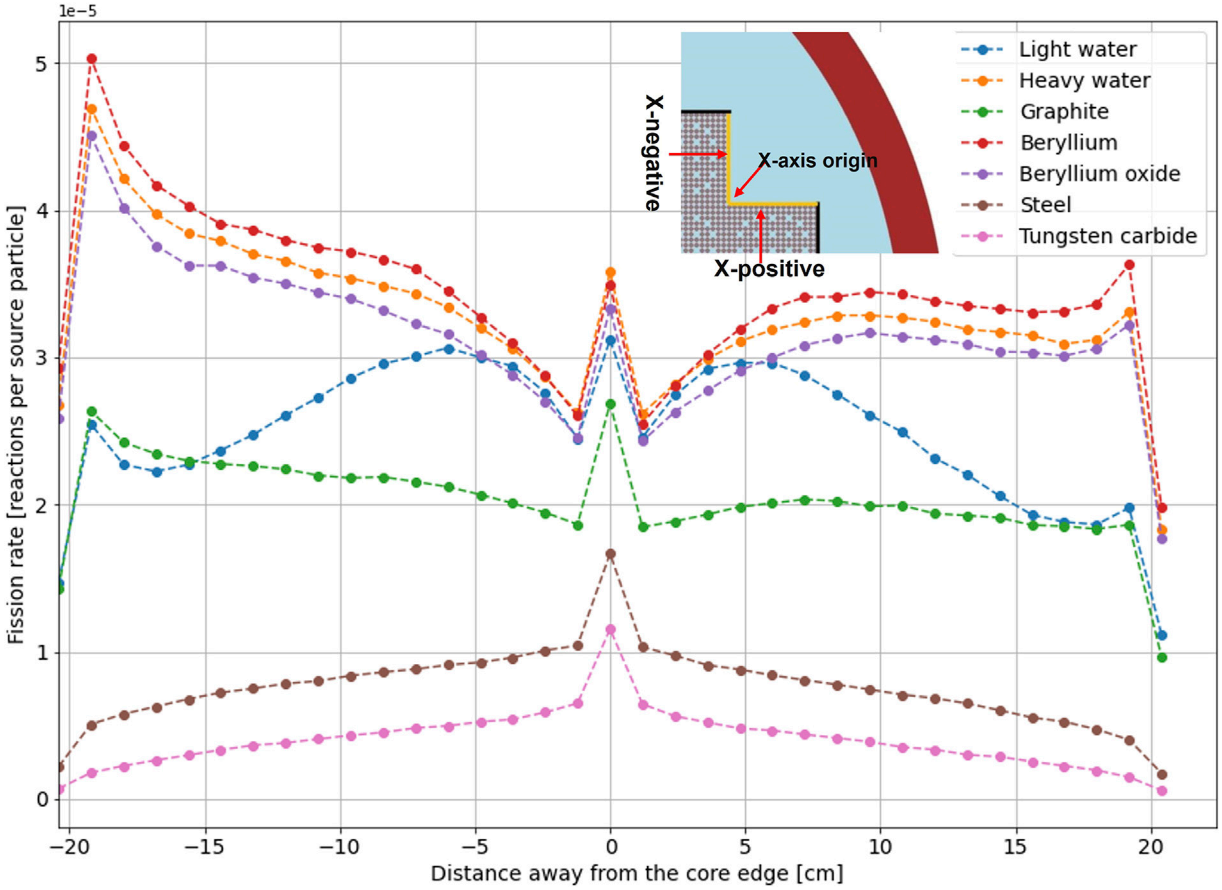

FIGURE 9
Fission rates among the boundary between the fuel assembly and reflector.

Considering that the above-mentioned neutron incident reactions are dispersed, the full-core criticality results are presented in Table 3, which are obtained from material-specific reflective core model simulations.

The variation of k_{eff} represents the upgrade to reactivity from the different reflectors. The beryllium- based materials' reflector gives an extra 4540 pcm improvement. The heavy water and graphite promote the k_{eff} from 1.22907 to a level higher than 1.25, and the enhancement from heavy water is slightly more substantial than graphite. The initial k_{eff} values of heavy metal reflective models are even lower than the original design. The power distributions of different material reflected core have been tallied.

Figure 8 states the fission reaction rate and the associated standard deviation 2D distributions over the entire two-batch refuelling scheme core with the light water reflector. The average fission rate is high in the higher enrichment fuel assembly area and surrounding the reloading fuels. Besides, it can find the power peak along the boundary between the fuel assemblies and reflector. The boundary fission rates also have higher standard deviations. Similar to Figure 8A, the fission rate distributions of other materials reflected models are plotted and combined in one figure. The results will give in Supplementary Figure S2. The scales in these distribution graphs are normalized to show the differences.

To further observe the power peaking on the boundary induced by the proposed reflectors, the tilled fission reaction rates along a characteristic edge are picked up from each distribution graph and plotted in Figure 9. Its legend demonstrates the vertex position and sets it as the origin on the X-axis. The distance along borders express as X-axis' positive and negative values. The selected edge is also highlighted in Supplementary Figure S1. Heavy water brings the most significant effect to the edge vertex in all potential reflectors. However, its improvement for the assembly border is not as substantial as the beryllium reflector. The graphite, steel and tungsten carbide reflectors decrease the original design's boundary power peak and flat the fission rate drops.

The burn-up calculations of reflected-core models also have been done. The k_{eff} value variations of each analysis have been plotted in Figure 10. Compared with the originally designed water reflected core, the aforementioned four types of light materials reflector all improved their depletion diagrams to a

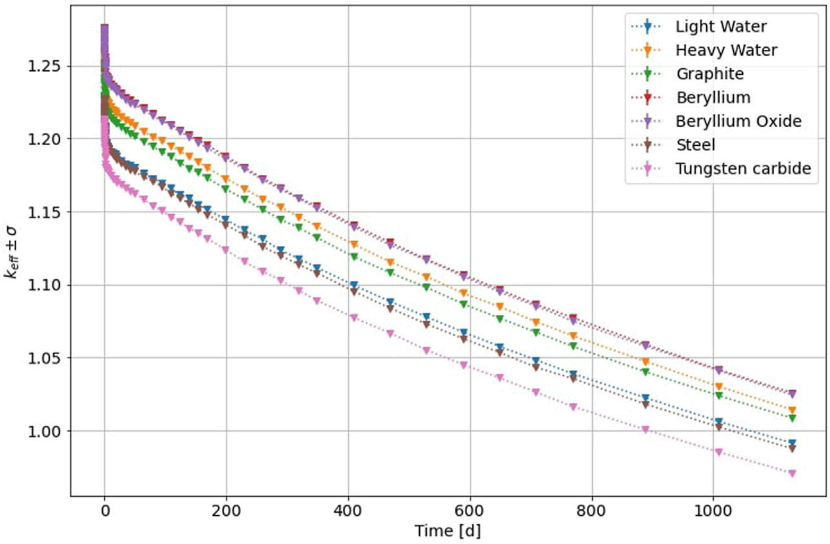

FIGURE 10
The comparison between k_{eff} variations of normal SMART with different reflector materials.

TABLE 4 The k_{eff} values at the beginning and end of the cycle in each of the depletion calculations.

Reflector materials	k_{eff} (BOC)	k_{eff} (EOC)	Depleted reactivity (pcm)
Light water	$1.22957 \pm 32 \times 10^{-5}$	$0.99136 \pm 34 \times 10^{-5}$	23821
Heavy water	$1.25926 \pm 34 \times 10^{-5}$	$1.01431 \pm 34 \times 10^{-5}$	24495
Graphite	$1.25190 \pm 33 \times 10^{-5}$	$1.00848 \pm 30 \times 10^{-5}$	24342
Beryllium	$1.27581 \pm 33 \times 10^{-5}$	$1.02580 \pm 34 \times 10^{-5}$	25001
Beryllium oxide	$1.27526 \pm 34 \times 10^{-5}$	$1.02438 \pm 32 \times 10^{-5}$	25088
Steel	$1.22751 \pm 37 \times 10^{-5}$	$0.98760 \pm 29 \times 10^{-5}$	23991
Tungsten carbide	$1.21310 \pm 36 \times 10^{-5}$	$0.97092 \pm 29 \times 10^{-5}$	24218

higher level, which have EOC k_{eff} higher than 1. The depletion diagrams of beryllium-based material reflector cores always stay at the top of the figure during the whole burn-up process. The depleted reactivity are given in Table 4.

According to the above analysis, the appearance of beryllium-based material reflectors can bring maximum extra reactivity. Therefore, from the neutronic point of view, the beryllium-based materials could be ideal for SMART neutron reflectors to optimize the power output and distribution.

4 Conclusion

The neutron reflectors improve the fission rate and uranium utilization of the outer SMART core FAs. It then optimizes the general power distribution and performance of the SMART design. The simulation results with the selected reflectors show that the light material group could improve the k_{eff}. The improvements from beryllium-based materials are the most significant in this study. In the same depletion period, these two material reflectors let SMART core depletes extra 1180 and 1267 pcm reactivity. The heavy metal reflectors do not bring the extra reactivity in the simulations, and the steel reflector does not shield as much neutron radiation as tungsten carbide. According to the analysis results, the beryllium-based materials are ideal materials for SMART to optimize power performance. Moreover, beryllium oxide has better material properties than its pure metal, such as a higher melting point, reasonable thermal conductivity, and no demand for the individual production process. The future studies will adopt the BeO-reflected core model to investigate the optimized fuel layouts with less fresh fuel demand in the beginning of cycle, and a sustainable refuelling strategy.

Data availability statement

The raw data supporting the conclusion of this article will be made available by the authors, without undue reservation.

Author contributions

All authors contributed to the writing and reviewing of the manuscript. YZ contributed to the modelling and data analysis. All studies are under the guidance and supervised by PN. WW organized the paper publication process.

Conflict of interest

The authors declare that the research was conducted in the absence of any commercial or financial relationships that could be construed as a potential conflict of interest.

Publisher's note

Supplementary material

The Supplementary Material for this article can be found online at: https://www.frontiersin.org/articles/10.3389/fenrg.2022.987513/full#supplementary-material

SUPPLEMENTARY FIGURE S1
OpenMC full core model with two-batch refuelling scheme and twelve burn-up zones spatial division.

SUPPLEMENTARY FIGURE S2
Power distributions of two-batch refuelling scheme core with particular material reflectors.

References

Atkinson, S., Abram, T. J., Litskevich, D., and Merk, B. (2019). Small modular high temperature reactor optimisation – Part 1: A comparison between beryllium oxide and nuclear graphite in a small scale high temperature reactor. *Prog. Nucl. Energy* 111, 223–232. doi:10.1016/j.pnucene.2018.10.017

Bae, G., and Hong, S. G. (2015). A small long-cycle PWR core design concept using fully ceramic micro-encapsulated (FCM) and UO2–ThO2 fuels for burning of TRU. *J. Nucl. Sci. Technol.* 52, 1540–1551. doi:10.1080/00223131.2015.1018364

Bhadauria, M., Kumar, R., and Das, A. K. (2021). Design and investigation of weight bundle simulator for Indian phwr using apdl-a thermal aspect, *EPJ web of conferences. EDP Sciences* 247, 06042.

Bosch, R. W., Van Renterghem, W., Van Dyck, S., Chaouadi, R., Gérard, R., and Somville, F. (2021). Microstructure, mechanical properties and IASCC susceptibility of stainless steel baffle bolts after 30 years of operation in a PWR. *J. Nucl. Mater.* 543, 152615. doi:10.1016/j.jnucmat.2020.152615

Brown, D. A., Chadwick, M. B., Capote, R., Kahler, A. C., Trkov, A., Herman, M. W., et al. (2018). ENDF/B-VIII.0: The 8th major release of the nuclear reaction data library with CIELO-project cross sections, new standards and thermal scattering data. *Nucl. Data Sheets* 148, 1–142. doi:10.1016/j.nds.2018.02.001

Carelli, M. D., Conway, L. E., Oriani, L., Petrović, B., Lombardi, C. V., Ricotti, M. E., et al. (2004). The design and safety features of the IRIS reactor. *Nucl. Eng. Des.* 230, 151–167. doi:10.1016/j.nucengdes.2003.11.022

Choi, S. (2015). "Small modular reactors (SMRs): The case of the Republic of Korea," in *Handbook of small modular nuclear reactors* (Woodhead Publishing Limited). doi:10.1533/9780857098535.4.379

Czakoj, T., Schulc, M., Šimon, J., Jur, V., Košt, M., Ulmanová, J., et al. (2022). The effect of heavy reflector on neutronic parameters of core. *Ann. Nucl. Energy* 168, 108898. doi:10.1016/j.anucene.2021.108898

Dawahra, S., Khattab, K., and Saba, G. (2015b). Investigation of BeO as a reflector for the low power research reactor. *Prog. Nucl. Energy* 81, 1–5. doi:10.1016/j.pnucene.2014.12.001

Dawahra, S., Khattab, K., and Saba, G. (2015a). Study the effects of different reflector types on the neutronic parameters of the 10 MW MTR reactor using the MCNP4C code. *Ann. Nucl. Energy* 85, 1115–1118. doi:10.1016/j.anucene.2015.07.029

Deen, J. R., Woodruff, W. L., and Costescu, C. I. (1995). *WIMS-D4M user manual.* doi:10.2172/197846

Flaspoehler, T., and Petrovic, B. (2020). Radiation environment in the I2S-lwr concept: Part I – radial distribution and its impact on vessel fluence, neutron detectors placement, and radial reflector gamma heating. *Ann. Nucl. Energy* 145, 106272. doi:10.1016/j.anucene.2018.07.021

Fowler, T. B., and Vondy, D. R. (1969). *Nuclear reactor core analysis code: Citation.*

Frybort, J., Sklenka, L., Fejt, F., Suk, P., and Frybortova, L. (2020). Sensitivity analysis of stainless steel reflector for VR-1 training reactor. *EPJ Web Conf.* 247, 08003. Int. Conf. Phys. React. Transit. to a Scalable Nucl. Futur. PHYSOR 2020 2020-March, 1578–1585. doi:10.1051/epjconf/202124708003

Ge´rard, R., and Somville, F. (2009). "Situation of the baffle-former bolts in Belgian units," in *International conference on nuclear engineering* 43512, 521–528.

Giménez, M. A. N., and Lopasso, E. M. (2018). Tungsten carbide compact primary shielding for small medium reactor. *Ann. Nucl. Energy* 116, 210–223. doi:10.1016/j.anucene.2018.02.032

IAEA (1980). *Research reactor core conversion from the use of highly enriched uranium fuels: Guidebook, TECDOC series.* Vienna: International Atomic Energy Agency.

Ilas, D. (2013). Impact of HFIR LEU conversion on beryllium reflector degradation factors. *Oak Ridge National Laboratory*.

Khoshahval, F., and Salari, F. (2016). Sensitivity analyses of the use of different reflector materials on the neutronics parameters of Tehran research reactor. *Prog. Nucl. Energy* 93, 351–361. doi:10.1016/J.PNUCENE.2016.09.009

Kurosaki, K., and Yamanaka, S. (2020). "7.12 - neutron reflector materials (Be, hydrides)," in *Comprehensive nuclear materials*. Editors R. J. M. Konings and R. E. Stoller. Second Edition (Oxford: Elsevier), 382–399. doi:10.1016/B978-0-12-803581-8.11747-3

Lamarsh, J. R., and Baratta, A. J. (2001). *Introduction to nuclear engineering*. Saddle River, NJ: Prentice hall Upper.

Lautard, J. J., Loubière, S., and Fedon-Magnaud, C. (1992). CRONOS: A modular computational system for neutronic core calculations. *IAEA-TECDOC.*

Puig, F., and Dennis, H. (2016). Neutron fluence effects on SLOWPOKE-2 beryllium reflector composition and reactivity. *Nucl. Eng. Des.* 305, 451–460. doi:10.1016/j.nucengdes.2016.05.033

Romano, P. K., Horelik, N. E., Herman, B. R., Nelson, A. G., Forget, B., and Smith, K. (2015). OpenMC: A state-of-the-art Monte Carlo code for research and development. *Ann. Nucl. Energy* 82, 90–97. doi:10.1016/j.anucene.2014.07.048

Sargeni, A., Burn, K. W., and Bruna, G. B. (2016). The impact of heavy reflectors on power distribution perturbations in large PWR reactor cores. *Ann. Nucl. Energy* 94, 566–575. doi:10.1016/j.anucene.2016.03.015

Snead, L. L., and Zinkle, S. J. (2005). Use of beryllium and beryllium oxide in space reactors. *AIP Conf. Proc.* 746, 768–775. doi:10.1063/1.1867196

Stacey, W. M. (2018). *Neutron energy distribution. Nuclear reactor physics*. 3rd Edn.Wiley VCH Verlag GmbH & Co. KGaA (Wiley Online Books).

Taforeau, J., Muller, M., and Salino, V. (2019). Modeling of heavy reflectors using DONJON-5. *Ann. Nucl. Energy* 127, 319–325. doi:10.1016/J.ANUCENE.2018.12.017

Torgerson, D. F., Shalaby, B. A., and Pang, S. (2006). CANDU technology for Generation III+ and IV reactors. *Nucl. Eng. Des.* 236, 1565–1572. doi:10.1016/j.nucengdes.2006.04.020

Vojackova, J., Novotny, F., and Katovsky, K. (2017). Safety analyses of reactor VVER 1000. *Energy Procedia* 127, 352–359. doi:10.1016/j.egypro.2017.08.079

Wankui, Y., Songbao, Z., Yaoguang, L., Weili, N., and Li, D. (2017). Neutron fluence analysis of graphite reflector in SPRR-300 during the whole reactor lifetime. *Ann. Nucl. Energy* 106, 91–96. doi:10.1016/j.anucene.2017.03.046

Zhang, Z., Dong, Y., Li, F., Zhang, Z., Wang, H., Huang, X., et al. (2016). The shandong shidao bay 200 MWe high-temperature gas-cooled reactor pebble-bed module (HTR-PM) demonstration power plant: An engineering and technological innovation. *Engineering* 2, 112–118. doi:10.1016/J.ENG.2016.01.020

frontiers | Frontiers in Energy Research

TYPE Original Research
PUBLISHED 15 September 2022
DOI 10.3389/fenrg.2022.990525

OPEN ACCESS

EDITED BY
Qingming He,
Xi'an Jiaotong University, China

REVIEWED BY
Jingang Liang,
Tsinghua University, China
Wang Yuancen,
China Academy of Engineering Physics,
China

*CORRESPONDENCE
Huanhuan Qi,
qihuan73@126.com
Zhengyan Fang,
f_lapin99@qq.com

SPECIALTY SECTION
This article was submitted to Nuclear Energy,
a section of the journal
Frontiers in Energy Research

RECEIVED 10 July 2022
ACCEPTED 19 August 2022
PUBLISHED 15 September 2022

CITATION
Jiang N, Min G, Fang Z and Qi H (2022), Investigation on vibration response characteristics and influencing factors of the fuel rods of EPR.
Front. Energy Res. 10:990525.
doi: 10.3389/fenrg.2022.990525

Investigation on vibration response characteristics and influencing factors of the fuel rods of EPR

Naibin Jiang[1], Guangyun Min[1], Zhengyan Fang[1]* and Huanhuan Qi[2]*

[1]Sino-French Institute of Nuclear Engineering and Technology, Sun Yat-sen University, Zhuhai, China, [2]Science and Technology on Reactor System Design Technology Laboratory, Nuclear Power Institute of China, Chengdu, China

First, the theory of wet modal analysis and vibration response analysis are introduced, and the semi-empirical vibration equation is derived in this article. Then, the structural models of the fuel rod of M310 and EPR are introduced, and the fuel rod is simplified to a multi-span continuous simply supported beam model subject to multi-point constraints. The fuel rod is simplified as a simply supported beam, and the springs and dimples are equivalent to elastic constraints. In addition, based on ANSYS-APDL, the wet modal analysis and response analysis of fuel rods are carried out. The modal information and transverse vibration response of the fuel rod of M310 and EPR are compared. In addition, combined with the actual operating conditions of EPR, the effects of different transverse and axial flow velocities on the transverse vibration response are discussed. Finally, different failure conditions are designed to explore the impact of clamping failure on the vibration characteristics of the fuel rod of EPR. The results have shown that compared with the fuel rod of M310, the fuel rod of EPR has a lower natural frequency and larger amplitude; the transverse flow velocity has a greater impact on the transverse vibration response; grid failure would reduce the natural frequency of fuel rods, and different positions of failure have different effects on the different-order natural frequencies of fuel rods.

KEYWORDS
fuel rod of EPR, vibration response, modal analysis, clamping failure, flow velocity

Introduction

Structures subjected to an axial or transverse flow are common in many processes related to energy generation and conversion. One important phenomenon limiting the development and reliability of these applications is related to flow-induced vibration (FIV), which arises from the fluid–structure coupling (Kaneko et al., 2014; de Santis and Shams, 2017). FIV is one of the factors that would also endanger the operation safety of nuclear power plants (Liu et al., 2017; Ferrari et al., 2020). For example, many structures of nuclear power plants, such as fuel assembly (Planchard, 1985; Ho et al., 2004), reactor internals (Ansari et al., 2008; Choi et al., 2016), and U-tube steam generators (Hassan et al., 2002; Jiang et al., 2017), would vibrate due to the influences of turbulent flow. This vibration is so-called FIV, which belongs to fluid–structure interaction (FSI) vibration. In a pressurized water reactor (PWR), as the heat source of a nuclear reactor, the operating state of the fuel assembly is directly related to the safety of the reactor (Gu et al., 2006). However, under the action of FIV, the transverse vibration of fuel assembly would cause the width of the flow channels between assembly and assembly to vary. Then, the varying width may cause neutron flux fluctuation (Pázsit and Analytis, 1980; Viebach et al., 2018), which would also cause power oscillation and endanger the stable supply of energy. Incidents due to FIV leading to fuel assembly failure have occurred in the past; hence, it is critically important to consider the FIV during the design process (Blevins, 1979; Païdoussis, 1981; Wang and Ni, 2009). The FIV for fuel assembly subjected to turbulent flow attracts many researchers' interests not only because of its theoretical significance in fluid mechanics but also its applications in nuclear engineering.

Fuel assembly is composed of fuel rods, control rods, spacer grids, and mixing vane grids. Each fuel rod in the fuel assembly is subjected to axial cooling flow and will vibrate vigorously due to the loading imposed by the high axial cooling fluid. To understand the mechanism of the FIV of the fuel rods subjected to fluid loads, many researchers proposed different theories such as self-excited models, parametric excitation models, and forced vibration models (Reavis, 1969; Gorman, 1971; Chen and Wambsganss, 1972). However, the first two of them have fatal defection, limiting their application range. It seems that the forced vibration models are more appropriate, feasible, and could be improved easily (Kaneko et al., 2014). However, the most current dynamics based on forced vibration models for this kind of FIV just consider the effects of the fluid field on fuel rods and fewer effects of fuel rods on the fluid field.

In general cases, the amplitude of FIV of fuel rods is small; nevertheless, it could wear the cladding of fuel rods and make the cladding become thinner (Kim, 2010). This wear phenomenon between fuel rods and cladding is so-called grid-to-rod fretting (GTRF) wear. This progressive GTRF wear of fuel rods is also a key factor that affects the structural integrity of fuel assembly. The GTRF wear is a very complex physical phenomenon, which could be affected by many factors, such as the shape of the springs and the dimples, the clamping force, the flow field in the reactor, and the nonlinear vibration caused by the coolant flow. In addition, manufacturing defects, unreasonable design of fuel rods, and spacer grids may also lead to GTRF wear. In this regard, many researchers have carried out theoretical and experimental research related to GTRF wear, such as research on the FIV mechanism of fuel rods and research on calculation methods of vibration and wear of fuel rods. For example, Rubiolo P. R. has presented a probabilistic method to predict the fretting wear performance of fuel rods. In this approach presented by him, the dynamic response of the nuclear fuel rods can also be calculated by a nonlinear vibration model (Rubiolo, 2006). Kim K. T. has proposed a guideline for fuel assembly and spacer grids to minimize the GTRF wear, which can be used to develop advanced fretting wear resistance technologies (Kim, 2010). Westinghouse has developed a method based on computational fluid dynamics (CFD) to predict the GTRF wear in the fuel inlet region (Yan et al., 2011). These studies have important guiding significance for FIV response and the anti-fretting wear design of fuel rods and can improve the safety and economy of the reactor.

In this work, the FIV responses of M310 and EPR have been studied, and the influencing factors of the response of EPR have also been systematically researched. Compared with M310, EPR has higher power and longer fuel rods. In other words, a more optimized design has been adopted in EPR to meet the higher requirements for safety performance. In order to compare the mode and vibration responses of the fuel rods of M310 and EPR, the models of these two fuel rods are constructed. Then, the mode and vibration responses of the fuel rods of M310 and EPR are compared. The works in this article could provide analytical ideas and a theoretical basis for the optimization of vibration suppression design and the safety evaluation of fuel rods of EPR.

Theoretical analysis

Wet modal analysis

The fuel rod placed in the coolant of the pressure vessel is a typical FSI structure. For an FSI model, the modal analysis is more complicated due to the coupling effect between fluid and structure. However, the wet modal analysis has taken account of the coupling effect. The coupling equation of an FSI model can be written as follows:

$$\begin{aligned}\boldsymbol{M}_{\mathrm{s}}\ddot{\boldsymbol{X}} + \boldsymbol{C}_{\mathrm{s}}\dot{\boldsymbol{X}} + \boldsymbol{K}_{\mathrm{s}}\boldsymbol{X} &= \boldsymbol{F}_{\mathrm{m}}(t) + \boldsymbol{F}_{\mathrm{e}}(t)\\ &= \left(-\boldsymbol{M}_{\mathrm{a}}\ddot{\boldsymbol{X}} - \boldsymbol{C}_{\mathrm{a}}\dot{\boldsymbol{X}} - \boldsymbol{K}_{\mathrm{a}}\boldsymbol{X}\right) + \boldsymbol{F}_{\mathrm{e}}(t),\end{aligned} \tag{1}$$

where $\boldsymbol{M}_{\mathrm{s}}$, $\boldsymbol{C}_{\mathrm{s}}$, and $\boldsymbol{K}_{\mathrm{s}}$ are mass, damping, and stiffness of the structure, respectively, $\boldsymbol{M}_{\mathrm{a}}$, $\boldsymbol{C}_{\mathrm{a}}$, and $\boldsymbol{K}_{\mathrm{a}}$ are fluid additional mass, damping, and stiffness, respectively, $\boldsymbol{F}_{\mathrm{m}}(t)$ and $\boldsymbol{F}_{\mathrm{e}}(t)$ are the fluid loads related and unrelated to vibration, respectively, $\boldsymbol{X}$ represents generalized displacement, and a dot $(\cdot)$ denotes the derivation of time t.

The fluid loads $\boldsymbol{F}_{\mathrm{m}}(t)$ can be moved to the left end of Eq. 1. Then, Eq. 1 can be rewritten as follows:

$$\boldsymbol{M}_{\mathrm{c}}\ddot{\boldsymbol{X}} + \boldsymbol{C}_{\mathrm{c}}\dot{\boldsymbol{X}} + \boldsymbol{K}_{\mathrm{c}}\boldsymbol{X} = \boldsymbol{F}_{\mathrm{e}}(t), \tag{2}$$

where $\boldsymbol{M}_{\mathrm{c}} = \boldsymbol{M}_{\mathrm{s}} + \boldsymbol{M}_{\mathrm{a}}$, $\boldsymbol{C}_{\mathrm{c}} = \boldsymbol{C}_{\mathrm{s}} + \boldsymbol{C}_{\mathrm{a}}$, and $\boldsymbol{K}_{\mathrm{c}} = \boldsymbol{K}_{\mathrm{s}} + \boldsymbol{K}_{\mathrm{a}}$.

For the free vibration without considering damping, Eq. 2 can be simplified into

$$\boldsymbol{M}_{\mathrm{c}}\ddot{\boldsymbol{X}} + \boldsymbol{K}_{\mathrm{c}}\boldsymbol{X} = 0. \tag{3}$$

If let

$$\boldsymbol{X} = \boldsymbol{\phi}\mathrm{e}^{j\omega t}, \tag{4}$$

where ω and $\boldsymbol{\phi}$ are frequency and mode, respectively.

Then, Eq. 4 can be substituted into Eq. 3, and it can be obtained by the eigenvalue equation:

$$(\boldsymbol{K} - \omega^2\boldsymbol{M})\boldsymbol{\phi} = \boldsymbol{0}. \tag{5}$$

By solving Eq. 5, the n-order natural frequency ω_n and n-order mode $\boldsymbol{\phi}_n$ can be obtained.

In this article, the calculation of wet modal analysis is based on ANSYS-APDL.

Response analysis

On the basis of wet modal analysis, further response analysis can be carried out. Then, the vibration behavior of fuel rods can be obtained by response analysis.

According to the modal superposition method, the displacement can be written as follows:

$$\boldsymbol{X} = \sum_{n=1}^{N}\phi_n(x)q_n(t), \tag{6}$$

where $q_n(t)$ and n are generalized displacement and order of mode.

The Rayleigh damping hypothesis is introduced here, and Eq. 6 is substituted into Eq. 2. Then, it can be obtained that

$$\ddot{q}_n(t) + 2\omega_n\xi_n\dot{q}_n(t) + \omega_n^2 q_n(t) = F_n(t), \tag{7}$$

where ξ_n denotes the damping ratio.

Combing with Eq. 6 and assuming that the responses between different modes are independent, it can be obtained that

$$\bar{X}^2(x) = \sum_{i=1}^{N}\sum_{j=1}^{N}\phi_i(x)q_i(t)\phi_j(x)q_j(t) \approx \sum_{i=1}^{N}\phi_i^2(x)q_i^2(t). \tag{8}$$

Furthermore, it can be obtained that

$$\bar{X}_i^2(x) = \phi_i^2(x)q_i^2(t). \tag{9}$$

The vibration of fuel rods is a random vibration. According to the mechanism of random vibration (Jiang et al., 2018), it can be obtained that

$$q_i^2(t) = \int_{-\infty}^{+\infty}|H_i(\omega)|^2 S_{F_n(t)F_n(t)}(\omega)\mathrm{d}\omega, \tag{10}$$

where $|H_i(\omega)|$ and $S_{F_n(t)F_n(t)}(\omega)$ are the module of the transfer function and autocorrelation-based spectrum of generalized function $F_n(t)$, respectively.

By definition, the equation of the autocorrelation-based spectrum can be written as follows:

$$S_{F_n(t)F_n(t)}(\omega) = \frac{\int_0^L\int_0^L\phi_i(x_1)\phi_i(x_2)S_{\mathrm{p}}(x_1,x_1,\omega)\mathrm{d}x_1\mathrm{d}x_2}{\left[\int_0^L m_x\phi_i^2(x)\mathrm{d}x\right]^2}, \tag{11}$$

where $S_{\mathrm{p}}(x_1,x_1,\omega)$ is the cross-correlation spectrum between the linear loads at points x_1 and x_2, and m_x is the linear density at coordinate x.

Assuming that the turbulence flow is statistically uniform, it can be assumed that the lag phase of S_{p} is zero. Then, a coherent function $r_p(\Delta x,\omega)$ that relies only on $\Delta x = |x_1 - x_2|$ can be introduced:

$$r_p(\Delta x,\omega) = \frac{|S_{\mathrm{p}}(\Delta x,\omega)|}{S_{\mathrm{p}}(\omega)}, \tag{12}$$

where $S_{\mathrm{p}}(\omega)$ is the power spectral density of turbulent flow.

Eq. 12 and Eq. 11 are substituted into Eq. 9, the general expression of vibration response can be obtained:

$$\bar{X}_i^2(x) = L^2\phi_i^2(x)\frac{\int_0^L S_{\mathrm{p}}(\omega)\cdot J_i^2(\omega)\cdot|H_i(\omega)|^2\mathrm{d}\omega}{\left[\int_0^L m_x\phi_i^2(x)\mathrm{d}x\right]^2}, \tag{13}$$

$$J_i^2(\omega) = \frac{1}{L^2}\int_0^L\int_0^L\phi_i(x_1)\phi_i(x_2)r_p(\Delta z,\omega)\mathrm{d}x_1\mathrm{d}x_2. \tag{14}$$

It is considered that the vibration displacement of fuel rods can be generated by the pulsating part of turbulent flow. Then, it can be obtained that

$$P = \frac{1}{2}\rho DU^2C_D, \tag{15}$$

where C_D is the drag coefficient related to the geometric properties of fuel rods and Reynolds number, D is the diameter of cladding, and ρ and U are the density and velocity coolant, respectively.

Both uniform fluid excitation and velocity are composed of average and fluctuation terms, which is

$$P = \bar{P} + p, \tag{16}$$

$$U = \bar{U} + u. \tag{17}$$

The relationship between spectral density below can be obtained from the pulsation analysis, which is

$$S_{\mathrm{p}}(\omega) = 4\frac{\bar{P}^2}{\bar{U}^2}S_{\mathrm{u}}(\omega). \tag{18}$$

Furthermore, the spectrum is defined by a positive frequency function, which is

$$S_{\mathrm{p}}(F) = 4\frac{\bar{P}^2}{\bar{U}^2}\bar{u}^2\frac{D}{S_r\bar{U}}\cdot G\left(\frac{fD}{S_r\bar{U}}\right), \tag{19}$$

where $\bar{U}^2$ is the square of velocity fluctuation term, G is the dimensionless shape factor, S_r is the Strouhal number, and f is the circular frequency.

The transfer function can be expressed as follows:

$$|H_i(\omega)|^2 = \frac{1}{16\pi^4 f_i^4}\cdot H_i(f)^2, \tag{20}$$

where $|H_i(f)| = [(1 - f^2/f_i^2)^2 + (2\alpha_i f/f_i)^2]^{1/2}$, and α_i is the constant related to the damping ratio.

Eqs 15–20 are substituted into Eq. 13, which leads to

$$\frac{\bar{X}_i^2}{D^2} = \frac{\bar{u}^2}{\bar{U}^2}\cdot\left(\frac{1}{S_r}\right)\cdot(\rho CD^2)^2\cdot\left(\frac{U}{D}\right)^3\cdot L^2\cdot\frac{1}{16\pi^4 f_i^4}\phi_i^2(x)$$

$$\cdot\frac{\int_0^L J_i^2(f)\cdot H_i(f)^2\cdot G\left(\frac{fD}{S_r\bar{U}}\right)\mathrm{d}f}{\left[\int_0^L m_x\phi_i^2(x)\mathrm{d}x\right]^2}. \tag{21}$$

In order to simplify Eq. 21, we make the following three assumptions here:

a) The coherence function has nothing to do with frequency but only changes the spatial relationship of fluid excitation. Then, it can be obtained that

$$r_p(x) \approx \exp\left(\frac{-|x_1 - x_2|}{L_{\mathrm{c}}}\right), \tag{22}$$

where L_{c} is the correlation length.

b) The spatial correlation is only effective when $L_{\mathrm{c}} \ll L$, which leads to

$$J_i^2(x) \approx 2\frac{L_{\mathrm{c}}}{L}\cdot\frac{1}{L}\int_0^L \phi_i^2(x)\mathrm{d}x. \tag{23}$$

c) The vibration modes are independent, which lead to

$$\int_0^{+\infty} H_i(f)^2\cdot G\left(\frac{fD}{S_r\bar{U}}\right)\mathrm{d}f \approx \frac{\pi f_i}{4\alpha_i}G\left(\frac{f_iD}{S_r\bar{U}}\right). \tag{24}$$

Eqs 22–24 are substituted into Eq. 21, which leads to

$$\frac{\bar{X}_i^2}{D^2} = \mathrm{C}^2\cdot\left(\frac{\rho D^2}{\rho_{\mathrm{eq}}}\right)^2\cdot\left(\frac{D}{L}\right)\cdot\left(\frac{1}{\delta_i}\right)\cdot\left(\frac{U}{f_iD}\right)^{3+\mathrm{Q}}$$

$$\cdot\frac{L\int_0^L\phi_i^2(x)\mathrm{d}x}{\left[\int_0^L\phi_i^2(x)\mathrm{d}x\right]^2}\cdot\phi_i^2(x), \tag{25}$$

where C, f_i, δ_i, and ρ_{eq} are the empirical coefficients measured by experiment, frequency, i-order damping coefficient of mode, and equivalent linear density of fuel rods, respectively.

The root-mean-square (RMS) values of the i-order mode of fuel rods caused by turbulent flow are shown in Eq. 25. This equation is obtained based on some assumptions and experimental data, so it has the property of a semi-empirical equation.

For PWR, the axial flow along the fuel rods is not completely uniform, and the equivalent axial velocity can be expressed as follows:

$$U_{\mathrm{a}}^{\mathrm{e}} = \left[\frac{1}{L}\int_0^L(U_{\mathrm{a}}(x))^{3+\mathrm{Q}}\mathrm{d}x\right]^{1/(3+\mathrm{Q})}, \tag{26}$$

where Q is also the empirical coefficient measured by experiment, and $U_{\mathrm{a}}^{\mathrm{e}}$ is the equivalent axial velocity.

Eq. 26 is substituted into Eq. 25, and it can be obtained that

$$\sigma[X_i(x)]^{\mathrm{a}} = \mathrm{C}(D)\phi_i(x)\left(\frac{\rho D^2}{\rho_{\mathrm{eq}}}\right)\left(\frac{1}{\delta_i}\right)^{0.5}\left(\frac{D}{L}\right)^{0.5}\left(\frac{U_{\mathrm{a}}^{\mathrm{e}}}{fD_i}\right)^{\frac{3+\mathrm{Q}}{2}}$$

$$\left(\frac{L}{\int_0^L\phi_i^2(x)\mathrm{d}x}\right)^{0.5}, \tag{27}$$

where $\sigma[X_i(x)]^{\mathrm{a}}$ is the RMS value due to axial flow.

For PWR, the transverse flow along the fuel rods is variable, which can be expressed as follows:

$$\left(\frac{\bar{U}}{f_iD}\right)^{3+\mathrm{Q}} = \int_0^L\left(\frac{U_{\mathrm{t}}(x)}{f_iD}\right)^{3+\mathrm{Q}}\phi_i^2(x)\mathrm{d}x\bigg/\int_0^L\phi_i^2(x)\mathrm{d}x, \tag{28}$$

where U_{t} is the transverse flow velocity.

Eq 28 is substituted into Eq. 25, and it can be obtained that

$$\sigma[X_i(x)]^{\mathrm{t}} = \mathrm{C}(D)\phi_i(x)\left(\frac{\rho D^2}{\rho_{\mathrm{eq}}}\right)\left(\frac{1}{\delta_i}\right)^{0.5}\left(\frac{D}{L}\right)^{0.5}$$

$$\left(\frac{\int_0^L\left(\frac{U_{\mathrm{t}}(x)}{f_iD}\right)^{3+\mathrm{Q}}\phi_i^2(x)\mathrm{d}x}{\int_0^L\phi_i^2(x)\mathrm{d}x}\right)^{0.5}\left(\frac{L}{\int_0^L\phi_i^2(x)\mathrm{d}x}\right)^{0.5}, \tag{29}$$

where $\sigma[X_i(x)]^{\mathrm{t}}$ is the RMS value due to transverse flow.

For the sake of conservatism, the RMS values under the action of axial and transverse flow are linearly added to estimate the maximum vibration response, which leads to

$$\sigma_i(x) = \sigma[X_i(x)]^{\mathrm{t}} + \sigma[X_i(x)]^{\mathrm{a}}. \tag{30}$$

For modes with similar frequencies, the probability of obtaining a synchronous maximum vibration response is very critical. In this case, the maximum vibration response $\sigma(x)$ estimated from the total vibration response combination of $\sigma_i(x)$, which is

$$\sigma(x) = \left[\sum_{i=1}^{N}\sigma_i^2(x) + 2\sum_{\substack{j=1,N\\ i=1,j-1}}\beta_{ij}\sigma_i(x)\sigma_j(x)\right]^{1/2}, \tag{31}$$

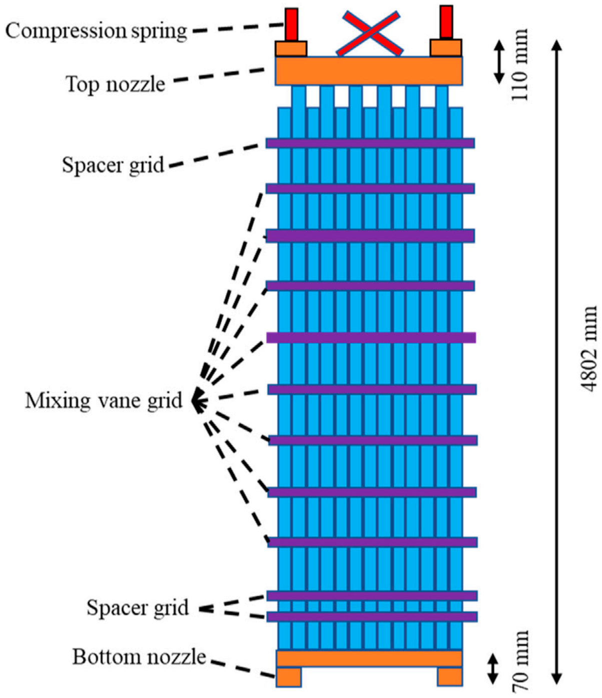

FIGURE 1
Schematic diagram of the AFA-3G LE fuel assembly.

where when the difference between frequency and frequency is less than 10%, $\beta_{ij} = 0.5$. Otherwise, $\beta_{ij} = 0$.

Analysis model

Model simplification

In China, third-generation pressurized water reactors have been adopted in the Taishan nuclear power plant (Peng and Li, 2008), which are EPR designed for Chinese nuclear power plants (CEPR) (Xiao et al., 2015). Compared with the M310 reactor, a more optimized design has been adopted in EPR to meet the higher requirements for safety performance (Gu et al., 2006). Two kinds of fuel assemblies can be used in EPR: one is HTP-type fuel assembly designed by Siemens, and the other one is AFA-3G LE-type fuel assembly designed by AREVA. For the strategic cooperation with France, the type of fuel assemblies for the Taishan nuclear power plant is AFA-3G LE (Gu et al., 2006; Xiao et al., 2015).

The design of the AFA-3G LE-type fuel assembly is based on the AFA-3G L-type fuel assembly. Also, the AFA-3G LE-type fuel assembly has 265 fuel rods and 24 guide tubes arranged in a 17 × 17 pattern. Compared with the AFA-3G L-type fuel assembly widely used in Chinese pressurized water reactors, the AFA-3G LE-type fuel assembly also has different structural characteristics on the grid and fuel rods.

The length of the AFA-3G LE-type fuel assembly is 4,802 mm. The number of grids is eleven, of which eight are mixing vane grids, and the others are three spacer grids. In order to be compatible with EPR, along the flow direction of coolant, the span length of these grids is slightly larger at the bottom of the fuel assembly and slightly smaller at the top of the fuel assembly.

As shown in Figure 1, there are two spacer grids at the bottom of the fuel assembly, and the distance between these two spacer grids is relatively small. There are eight mixing vane grids and one spacer grid on the top of the fuel assembly, which are in the active area of a nuclear reactor.

It can be seen from Figure 2 that the fuel rods of AFA-3G LE fuel assembly are composed of bottom and top end plugs, fuel pellets, springs, and supporting tubes. Considering that pressure inside fuel rods and the strain of cladding may change during operation, such as irradiation creep, swelling, or gas generated during nuclear fission, gas chambers are reserved at the top and bottom of cladding, and the fuel pellets are compressed by springs.

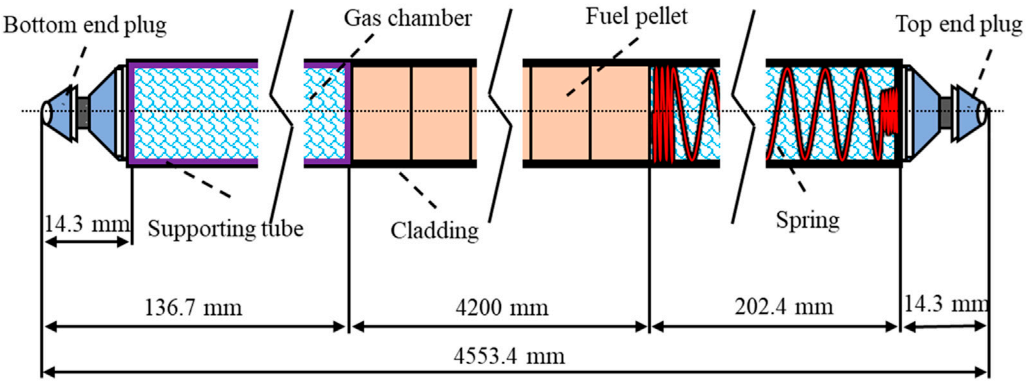

FIGURE 2
Schematic diagram of the fuel rod of EPR.

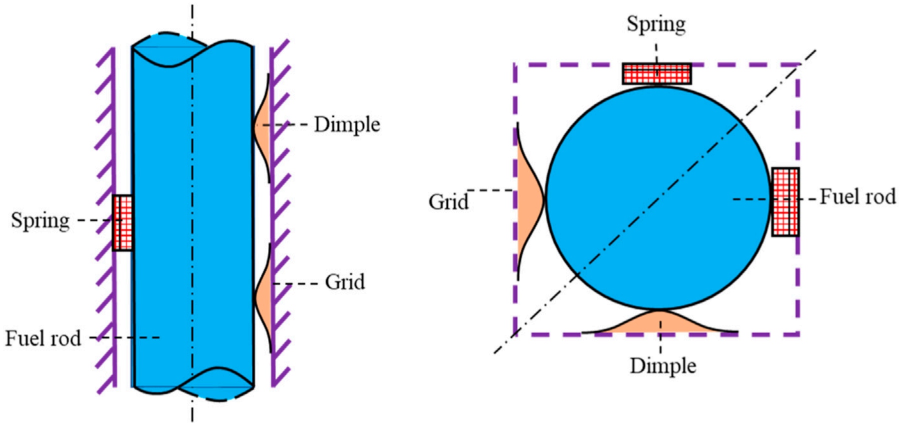

FIGURE 3
Schematic diagram of a fuel rod constrained by the grid.

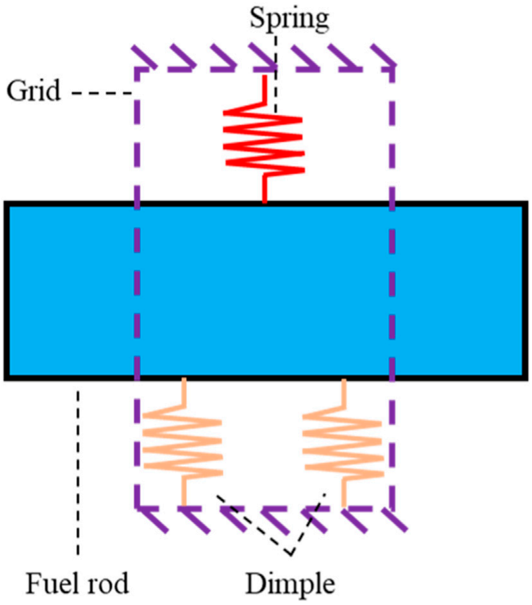

FIGURE 4
Schematic diagram of elastic constraints.

For the AFA-3G LE fuel assembly, the length of each fuel rod is 4,553.4 mm, and the outer diameter and thickness of cladding are 9.5 and 0.57 mm, respectively. The fuel assembly is constrained by a grid at several points in its axial direction. As an in-grid cell component is used to maintain the stability and enhance the stiffness of fuel rods, the grid is composed of several Zr-4 alloy straps welded with each other. As shown in Figure 3, each fuel rod is constrained by two springs and four dimples, keeping the fuel rod's stability. The constraint of the grid to each fuel rod can prevent the fuel rod from transverse jumping and allows axial thermal expansion.

From Figure 3, it can also be obtained that fuel rods are constrained by two springs and four dimples located in each grid. These constraint points are vertical to the axis of fuel rods, and these constraints are symmetrical along the diagonal of the grid. Therefore, a single fuel rod can be simplified as a plane Euler beam, and the dimples and springs are equivalent to elastic constraints, which are shown in Figure 4.

Therefore, it can be obtained from the previous analysis that a fuel rod can be regarded as a model subject to multi-point constraints. Also, in the mechanical analysis, the model subject to multi-point constraints can be regarded as a multi-span continuous simply supported beam.

In summary, a simplified model of fuel rods is shown in Figure 5, with elastic constraints within each grid on the fuel rods.

Model parameters

The factors that affect the vibration characteristics of fuel rods are stiffness and mass. Due to the presence of a gas gap between fuel pellets, the fuel pellets do not provide bending stiffness. Therefore, when analyzing the FIV characteristics of fuel rods, it can be considered that the stiffness of fuel rods is determined by the stiffness of cladding. The contribution of other parts of fuel rods to the stiffness of fuel rods is small, and only the contribution of other parts to the mass of fuel rods is considered.

Considering a unit length fuel rod with a diameter D and a thickness t_d, if the mass of other parts of the fuel rod except the cladding is m_i, then the density of other parts converted into the cladding is

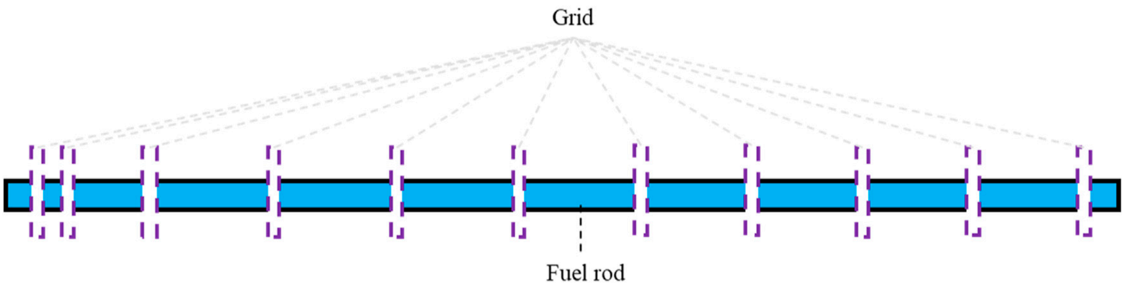

FIGURE 5
Schematic diagram of a multi-span continuous simply supported beam of EPR fuel rods.

TABLE 1 Physical parameters of EPR fuel rods.

Parameter	Value
Length	4,553.4 mm
Diameter	9.5 mm
Cladding thickness	0.57 mm
Young's modulus	76.9 Gpa
Poisson's ratio	0.37

TABLE 2 Real constants used by the Beam4 element.

Parameter	Value
AREA	1.5991×10^{-5}
IYY	1.6005×10^{-10}
IZZ	1.6005×10^{-10}
TKY	9.5×10^{-3}
TKZ	9.5×10^{-3}

$$\rho_{\mathrm{eq,i}} = \frac{4m_i}{\pi\left(D^2 - (D - 2t_{\mathrm{d}})^2\right)}. \tag{32}$$

At the same time, the influence of coolant on fuel rods should be considered in the wet modal analysis of fuel rods. The static fluid loads of coolant to fuel rods can be equivalent to additional mass to fuel rods, and the additional mass is converted into cladding, which is

$$\rho_{\mathrm{eq,w}} = \frac{D^2\rho_{\mathrm{w}}}{D^2 - (D - 2t_{\mathrm{d}})^2}, \tag{33}$$

where $\rho_{\mathrm{w}}$is the density of coolant.

Therefore, the equivalent linear density of fuel rods is

$$\rho_{\mathrm{eq}} = \rho_{\mathrm{eq,w}} + \rho_{\mathrm{c}} + \rho_{\mathrm{eq,i}}, \tag{34}$$

where ρ_{c} is the linear density of cladding.

In addition, the material of cladding of EPR is M5 alloy. Mitchel et al. have exhibited a specific empirical relationship between Young's modulus of M5 alloy and temperature (Dutkiewicz et al., 2017), which is

$$E = \begin{cases} 1.088 \times 10^5 - 54.75T & T \leq 1090K \\ 1.017 \times 10^5 - 48.27T & 1090K < T \leq 1240K \\ 9.210 \times 10^4 - 40.50T & 1240K < T \leq 2027K \\ 1.000 \times 10^4 & 2027K < T \end{cases}, \tag{35}$$

where E is Young's modulus.

Under operating conditions, the average temperature of the nuclear reactor is about 583 K, so Young's modulus of M5 alloy is 76.9 GPa. According to the COGEMA technical report of AREVA, Poisson's ratio of M5 alloy and the density of cladding can be considered as 0.37 and 6,500 kg/m^3, respectively.

Finally, the physical parameters that would be used in the wet modal analysis are shown in Table 1.

The accuracy of the finite element model could directly affect the rationality of calculation results. The multi-span continuous simply supported beam model should be modeled from the key points to the lines, from bottom to top. Then, three-dimensional Beam4 elements are used to simulate fuel rods here, and the Combine14 element is used to simulate the elastic support between the springs, dimples, and fuel rods.

The ANSYS-APDL is used for wet modal analysis, and the block Lanczos method is used to extract modal information here. The real constants that would be used in each element in the ANSYS-APDL are shown in Table 2.

When establishing a finite element model because the density of fuel rods in its axial direction has a different distribution, it is necessary to establish elements on fuel rods by sections. Also, in order to arrange spring elements on fuel rods, it is necessary to establish corresponding nodes according to the actual situation. In order to avoid axial jumps or rotation of fuel rods, the axial translation and rotation displacement of nodes are both constrained.

The technology of the M310 nuclear reactor is very mature, so it is widely used in China. The length of fuel rods of EPR is

TABLE 3 Frequency of EPR/hz.

Direction	1-order	2-order	3-order	4-order	5-order	6-order	7-order	8-order
X-Y	32.124	35.580	38.030	41.576	45.348	49.574	53.942	57.162
X-Z	32.124	35.580	38.030	41.576	45.348	49.574	53.942	57.162

TABLE 4 Frequency of M310/hz.

Direction	1-order	2-order	3-order	4-order	5-order	6-order
X-Y	31.130	38.109	40.364	43.702	47.624	51.451
X-Z	31.130	38.109	40.364	43.702	47.624	51.451

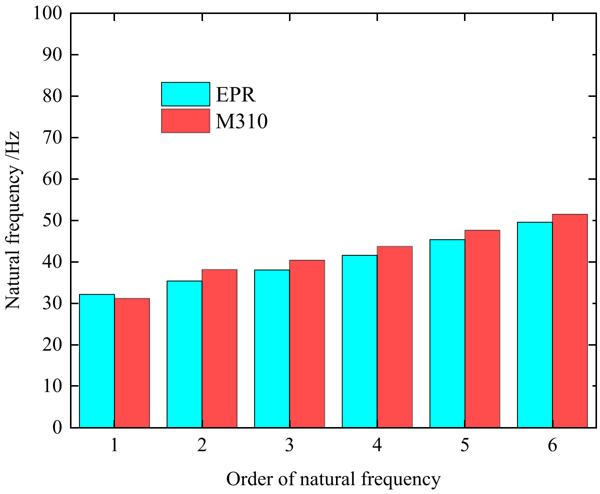

FIGURE 6
Natural frequency of fuel rods of EPR and M310.

longer than M310, and the number of grids of them is also different. So, their vibration characteristics would also be different. Based on this concept, the wet modal analysis of M310 is also carried out here, and the differences in wet modal analysis between M310 and EPR are also compared.

Numerical example: wet modal analysis

Through the simplified model and model parameters in Table 1 and Table 2, the corresponding finite element model can be established. The natural frequency of fuel rods of EPR and M310 can be extracted by the block Lanczos method, which is shown in Figure 8, Table 3 and Table 4.

It can be seen from Table 3 and Table 4 that the natural frequencies on the X-Y and X-Z planes for M310 and EPR are equal. The reason is that the geometric structure and constraints of the finite element model are highly symmetrical. Then, based on this concept, the results of one of the planes can be used for analysis for simplicity. From Figure 6, the 1-order natural frequency of EPR is larger than that of M310, but when the mode order is greater than 1-order, the natural frequency of EPR is smaller than that of M310, mainly because the length of EPR fuel rods is longer than that of M310.

The effective mass coefficient can be used to judge whether the order of modal truncation is reasonable. When the modal order is equal to 16 (X-Y and X-Z planes), the effective mass coefficient of the model of EPR is approximately 1. When the modal order is equal to 12 (X-Y and X-Z planes), the effective mass coefficient of the model of M310 is approximately 1. Based on this concept, the first 16-order vibration modes of EPR and the first 12-order vibration modes of M310 are listed in Figure 7.

For the slender structure of fuel rods, the low-order vibration modes are the most important for the analysis of vibration characteristics. From Figure 7, it can be found that the vibration modes of the fuel rods of M310 and EPR are quite different due to the differences in the number and distribution of their grids. Along the axis direction of fuel rods (from bottom to top), the maximum displacement of the 1-order vibration mode of the fuel rods of M310 occurs between the 1-st grid and the 2-nd grid because the span spacing between these two grids is longer than that between other grids. For the fuel rods of EPR, the distribution between grids is relatively uniform, so the vibration mode is different from that of M310.

Compared with the measured value of natural frequency of the fuel rods of EPR, the error of natural frequency and modes obtained by Beam4 and experimental results is within 3%, so the simulation results presented in this article can be thought to be consistent with the measured results. Therefore, the current numerical model can also be used for the subsequent response analysis of fuel rods.

Numerical example: response analysis

In order to further consider the differences in the response of the fuel rods of M310 and EPR under operating conditions, the

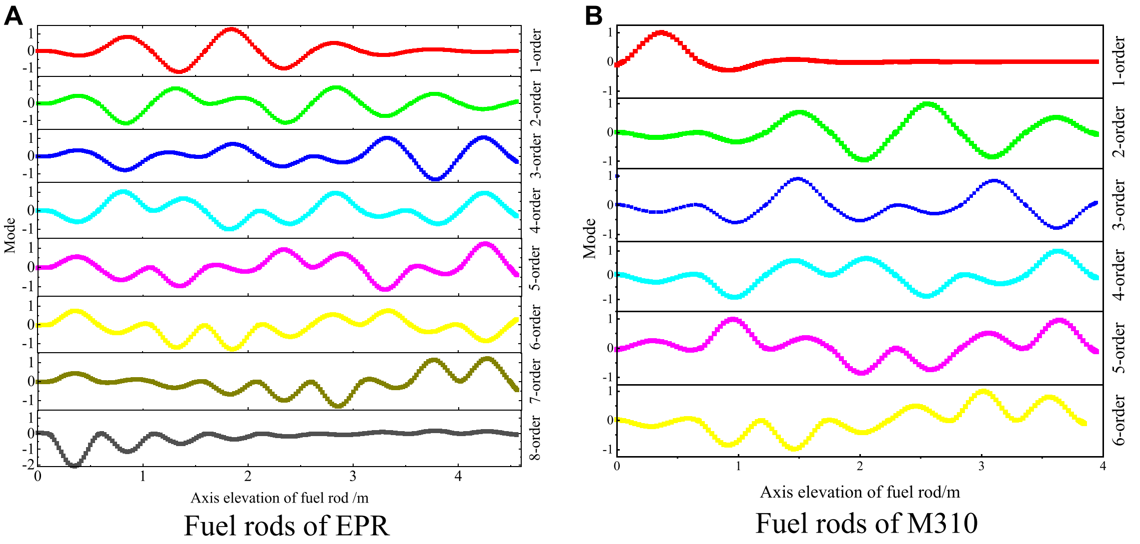

FIGURE 7
Vibration modes on X-Y plane. **(A)**: EPR fuel rod vibration modes on X-Y plane. **(B)**: M310 fuel rod vibration modes on X-Y plane.

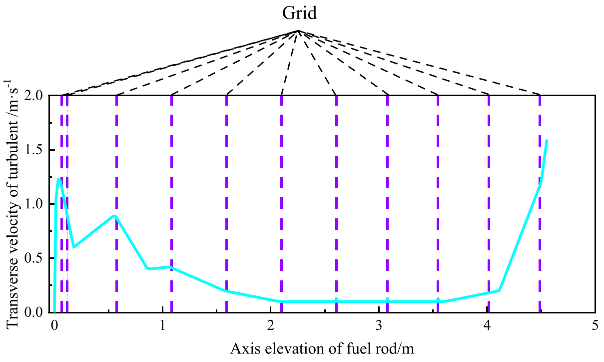

FIGURE 8
Transverse flow velocity of EPR.

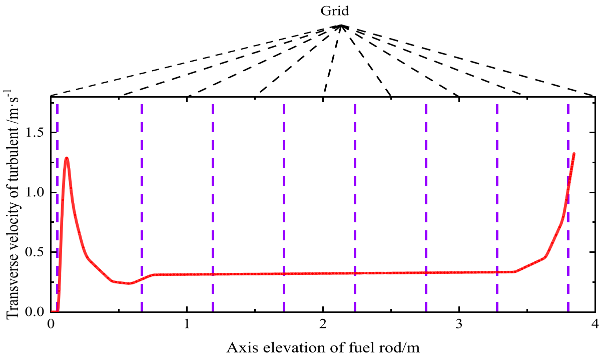

FIGURE 9
Transverse flow velocity of M310.

vibration response under the action of transverse and axial flow can be obtained by the theoretical equation introduced in Eqs 28 and 30. Then, it is necessary to introduce the calculation parameters for vibration response.

In order to obtain the vibration response caused by the transverse flow, the vibration modes obtained in Figure 7 are used to calculate the weighted velocity of the transverse flow. Under operating conditions, the transverse flow along the axial direction of fuel rods is not uniform. The simplified transverse flow velocity of M310 and EPR with the axial direction of fuel rods is shown in Figures 8 and 9.

In order to calculate the vibration response caused by axial flow, it is necessary to obtain the distribution of axial flow velocity. Because the distribution of the axial rate of flow in PWR is approximate, the average flow velocity at the inlet of the reactor core is selected for calculation here. Under operating conditions, the inlet flow velocity of M310 and EPR is different. The average rate of flow at the inlet of the reactor core is shown in Table 5**.**

Since the structural parameters such as the diameter of fuel rods are almost the same as in M310 and EPR fuel assemblies, it can be considered that the C and Q values in Eqs 28 and 30 of axial and transverse flow are the same in the normalized PSD excitation spectrum of fuel rods, which are obtained from experiments.

Under turbulent excitation, the damping of fuel rods consists of two parts, namely, the hydrodynamic damping under the

TABLE 5 Inlet rate of flow and velocity.

PWR type	Inlet rate of flow	Cross-sectional area (m)	Average inlet flow velocity
EPR	122,320 m^3/h	5.93^2	5.73 m/s
M310	74,220 m^3/h	4.35^2	4.74 m/s

TABLE 6 Linear density of fuel rods.

Section	Value
Top end plug	1.384 kg/m
Gas chamber	0.215 kg/m
Fuel pellet	0.795 kg/m
Bottom end plug	1.052 kg/m

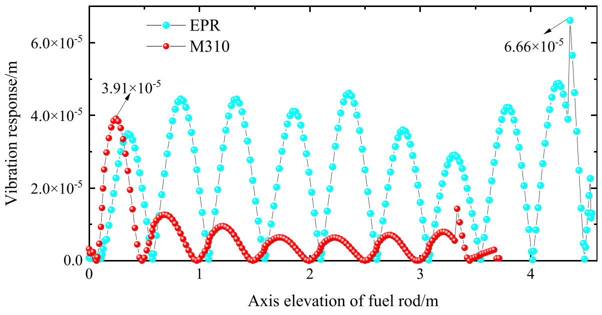

FIGURE 10
Vibration response of fuel rods.

interaction between fluid and fuel rods and the inherent mechanical damping between fuel rods and the support structure. In this article, the damping ratio used is 4.4%.

When calculating the vibration response because the volume density of each section of fuel rods is different, the linear density of each section is also different, as shown in Table 6.

The results of natural frequency and modes obtained above would directly affect the vibration response of fuel rods. Combing Eq. 28–30 to compile a program for the calculation of vibration response. Then, the total response of fuel rods of M310 and EPR can be obtained. Since the fuel rod is a symmetrical structure, the vibration response of the X-Y plane is similar to that of the X-Z plane. Therefore, the vibration response of any plane can be taken for analysis. Considering the vibration response on the X-Y plane as an example for analysis, as shown in Figure 10.

It can be found that in Figure 10, along the axial direction of fuel rods, the vibration response of EPR is more uniform than that of M310. The maximum vibration response of M310 is located between the spans of the first two grids, and this value is much greater than the peak value of the other spans. However, the maximum vibration response of EPR is located between the last 10-th and 11-th grids.

It can also be noted that affected by the structure of fuel rods, the linear density of fuel rods would change suddenly along the axial direction, and the vibration response of fuel rods would change correspondingly at the nodes where the linear density changes suddenly. According to the comparison shown in Figure 10, the maximum vibration response of M310 is slightly smaller than that of EPR. It can also be judged that the vibration of EPR is more unstable than that of M310 under similar operating conditions.

Influencing factor

Velocity

Due to the influences of reactor internals of pressure vessels, the axial velocity of fuel rods at different positions is different (Barbier, et al., 2009). Although the flow direction of coolant is mainly axial, due to its structural characteristics, there is a large amount of irregular transverse turbulence in the fuel assembly (Mulcahy et al., 1980). The transverse flow velocity is also not uniformly distributed along the axial direction of the fuel rods. The numerical research of the vibration response characteristics of fuel rods of EPR under different axial and transverse flow velocities is carried out.

In order to study the distribution of flow field in the lower head of a pressure vessel for EPR, EDF conducted a scale model test, which is Juliette (Barbier et al., 2009). In this scale model experiment, it can be found that under normal operating conditions, the inlet flow velocity in the center of the core is large, while the flow velocity around it is small. The distribution of the flow field is shown in Figure 11 (Puragliesi et al., 2016).

In Figure 11, the red line is the axis of the inlet nozzle of the coolant, and each small circle represents the fuel assembly. The number of small circles is the distribution coefficient of flow velocity. Taking 6.88 as an example, it represents that the inlet flow velocity of the fuel assembly is 6.88% greater than the average flow velocity.

In order to research the effect of different axial flow velocities on the vibration response of fuel rods under actual operating

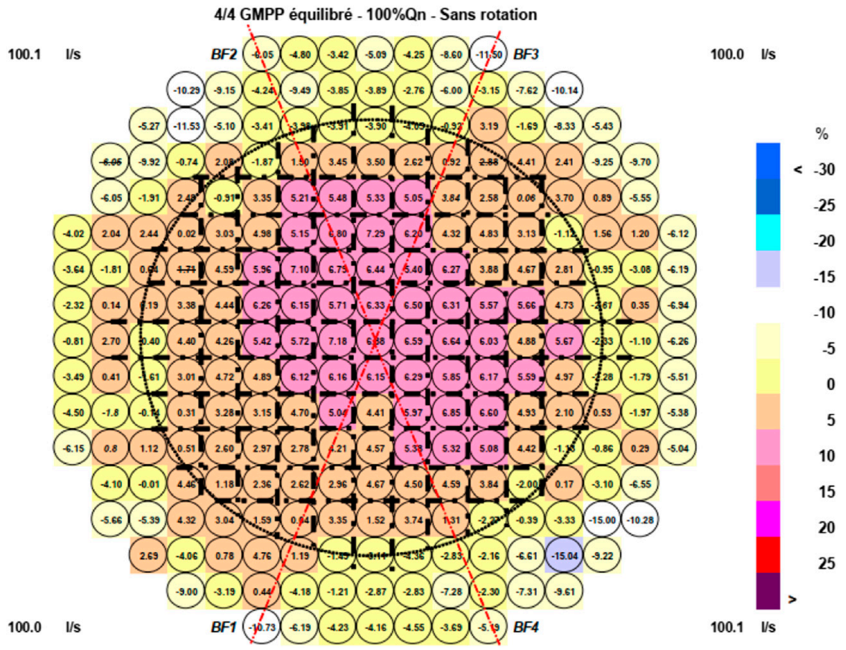

FIGURE 11
Distribution of inlet rate of flow of EPR core.

TABLE 7 Axial flow velocity.

Distribution coefficient	Axial velocity
-15.00	4.87 m/s
-10.73	5.12 m/s
-6.19	5.38 m/s
-2.30	5.60 m/s
1.31	5.81 m/s
5.39	6.04 m/s
7.29	6.15 m/s

conditions, different inlet distribution coefficients of flow velocity were selected. The axial flow velocity of fuel rods is calculated, which is

$$U_a = q \cdot \frac{Q_q}{A}, \tag{36}$$

where Q_q, q, and A are the average flow velocity, distribution coefficient of flow velocity, and cross-sectional area of the core, respectively.

According to Eq. 36, it can be obtained that the axial flow velocity is as shown in Table 7.

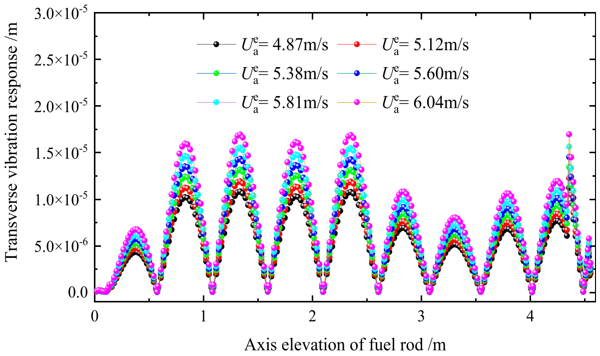

FIGURE 12
Transverse vibration response under different axial flow velocities.

The axial distribution of the transverse response of the fuel rod under different axial flow velocities is obtained. Similarly, taking the results on the X-Y plane as an example, as shown in Figure 12.

By analyzing the results in Figure 12, it can be found that the axial vibration response of fuel rods would increase with the increase of axial velocity. This indicates that the axial flow velocity has a great influence on the axial vibration response, and the differences in the inlet flow velocity of the core need to be strictly controlled.

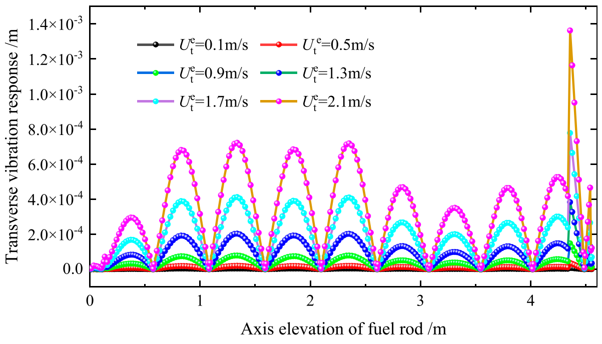

FIGURE 13
Transverse vibration under different transverse flow velocities.

TABLE 8 Failure working conditions.

Number	Introduction
C.1	Springs and dimples failure of grid 1
C.2	Springs and dimples failure of grid 2
C.3	Springs and dimples failure of grid 3
C.4	Springs and dimples failure of grid 4
C.5	Springs and dimples failure of grid 5
C.6	Springs and dimples failure of grid 6
C.7	Springs and dimples failure of grid 7
C.8	Springs and dimples failure of grid 8
C.9	Springs and dimples failure of grid 9
C.10	Springs and dimples failure of grid 10
C.11	Springs and dimples failure of grid 11
C.12	Springs and dimples failure of grids 1 and 2

For the convenience of description, the definition of equivalent transverse velocity is introduced here, which is

$$U_t^e = \int_0^L \left(\frac{U_t(x)}{f_i D}\right)^{3+Q} \phi_i^2(x)\mathrm{d}x, \tag{37}$$

where U_t^e is the equivalent transverse velocity.

Under actual operating working conditions, the transverse flow velocity would vary greatly with the axial direction of fuel rods. Transverse velocity is mainly reflected by the large flow velocity at both ends of fuel rods and the small flow velocity in the middle of fuel rods. In this article, the axial velocity of fuel rods is selected as 5.7 m/s, and the equivalent transverse velocity is selected as 0.1 m/s, 0.5 m/s, 0.9 m/s, 1.3 m/s, 1.7 m/s, and 2.1 m/s. Then, the vibration response of fuel rods under corresponding conditions is calculated.

By analyzing the results in Figures 12 and 13, it can be found that the transverse vibration response of fuel rods would increase with the increase of transverse velocity. By comparing Figure 12 and Figure 13, it can also be found that the transverse vibration response under the transverse flow velocity is larger than that of the axial flow velocity, so the influences of transverse flow velocity on transverse vibration response are greater.

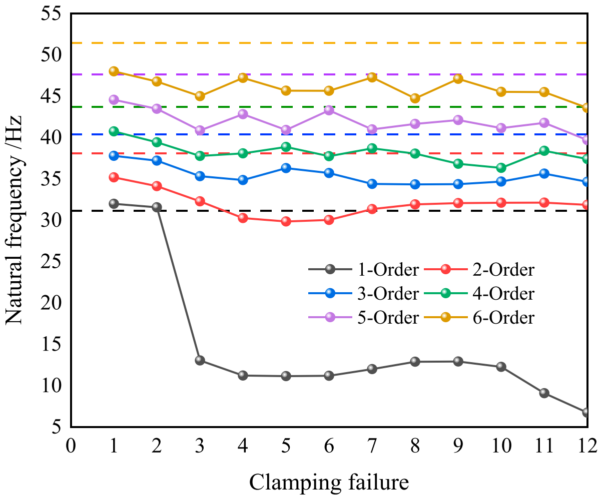

FIGURE 14
Natural frequency under clamping failure and no clamping failure.

Clamping failure

During the design of fuel assembly, in addition to considering the material and structure of fuel rods, it is also necessary to properly confirm the clamping force of springs and dimples on the grid to the fuel rods. When the clamping force is too small, the fretting wear between fuel rods and the grid will be increased. When the clamping force is too large, the fuel rods will be deformed due to excessive constraints.

In this article, the clamping failure is considered as the failure of the support in the grid as shown in Figure 3, that is, all springs and dimples in one grid lose their elastic constraints on the fuel rods. Then, 12 failure working conditions are set for wet modal analysis and response analysis of EPR fuel rods. The corresponding 12 failure working conditions are shown in Table 8.

Under the abovementioned 12 failure working conditions, through the wet modal analysis of fuel rods, the influences of clamping failure on the mode are obtained. Taking the results of the X-Y plane as an example, as shown in Figure 14, where the dotted line represents the natural frequency of the fuel rods without clamping failure.

It can be found from Figure 14 that the natural frequency of the fuel rods would decrease under the clamping failure. The order of natural frequency and the position of clamping failure

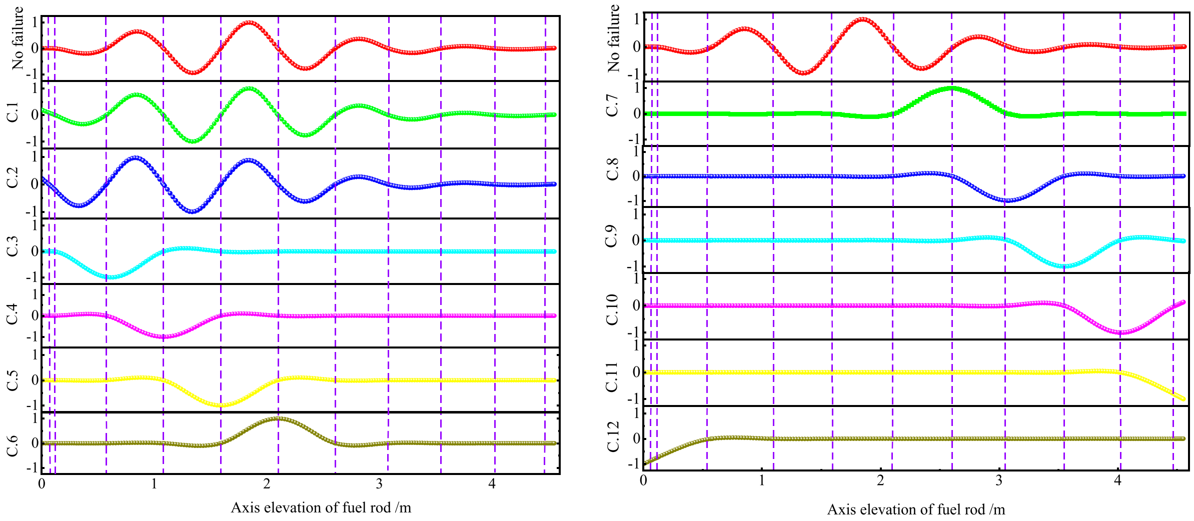

FIGURE 15
1-order vibration mode under clamping failure.

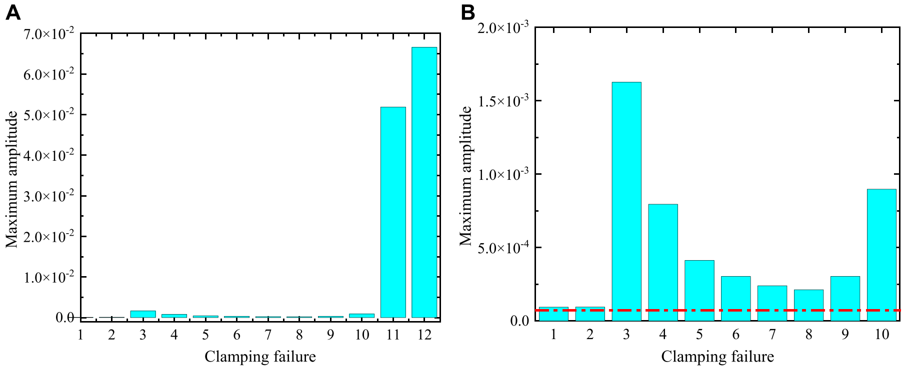

Under 12 failure working conditions

Under first 10 failure working conditions

FIGURE 16
Maximum amplitude under clamping failure. **(A)**: Maximum amplitude under 12 failure working conditions. **(B)**: Maximum amplitude under first 10 failure working conditions.

are different, and the influences of clamping failure on natural frequency are also different.

The grid failure at different positions has different effects on the natural frequencies. For the 1-order frequency, the failure of the 3-rd to 11-th grids has a great impact on the frequency. However, due to the close distance between the 1-st and 2-nd grids, the failure of the 1-st and 2-nd grids, respectively, has little effect on the frequency, but the failure of the 1-st and 2-nd grids at the same time has a great effect on the frequency. By observing the vibration mode of EPR fuel rods, it can be found that the amplitude of the 1-order vibration mode is mainly distributed behind the 3-rd grids, so clamping failure at these locations has the greatest impact on the 1-order natural frequency.

The influences of clamping failure on the vibration mode are further analyzed. Similarly, taking the vibration mode of fuel rods on the X-Y plane as an example. The dotted lines in Figure 15 represent the position of grids. The 1-order vibration mode of fuel rods under different failure working conditions is shown in Figure 15. Then, the 1-order vibration mode under clamping failure is compared with those without clamping failure.

It can be found from Figure 15 that, for the 1-order mode of fuel rods, the mode of failure of the 1-st and 2-nd grids is similar to the mode without grid failure. Except for the 1-st and 2-nd grids with close grid spacing, grid failure at other locations would cause the maximum amplitude to appear at the corresponding failure location. This is because the grid failure at these locations would make the spacing between adjacent grids longer, which would make the local stiffness decrease at these locations.

Finally, this article has calculated the maximum amplitude of fuel rods under different working conditions of clamping failure. Similarly, the maximum amplitude on the X-Y plane is shown in Figure 16. The dotted line in Figure 16B is the corresponding maximum amplitude when there is no clamping failure.

From Figure 16A, it can be found that under the failure working conditions 11 and 12, the maximum amplitude of fuel rods is much greater than that under other failure conditions. From Figure 16B, it can be found that the failure of one of the grids has little effect on the maximum vibration response of the fuel rods due to the close distance between the 1-st and 2-nd grids. From the 3-rd grid, the clamping failure has a great impact on the maximum vibration response of fuel rods.

Conclusion

Considering the fuel rod of EPR as an object, the natural frequency and vibration mode of the fuel rod are discussed in detail by combining numerical and theoretical equations in this article. The amplitude under different turbulent flow velocities is calculated, and the influences of clamping failure on the vibration response of the fuel rod are discussed. The following conclusions can be listed:

1) By comparing the vibration characteristics of EPR and M310, it can be found that compared with the fuel rod of M310, the fuel rod of EPR has a lower natural frequency in general. Under turbulent excitation, the vibration response of fuel rods of EPR is larger than that of M310.
2) The transverse vibration response under the transverse flow velocity is larger than that of axial flow velocity, so the influence of transverse flow velocity on vibration response is greater. The maximum transverse amplitude of the fuel rods would change more dramatically with the transverse velocity than it would change with the axial velocity.
3) Grid failure would reduce the natural frequency and increase the amplitude of fuel rods, and the grid failure at different positions has different effects on the natural frequencies. For the 1-order frequency, the failure of the 3-rd to 11-th grids has a great impact on the frequency. However, due to the close distance between the 1-st and 2-nd grids, the failure of the 1-st and 2-nd grids, respectively, has little effect on the frequency, but the failure of the 1-st and 2-nd grids at the same time has a great effect on the frequency. In addition, the failure of the 11-th grid has the greatest impact on the amplitude, followed by the 3-rd grid.
4) Compared with M310, the fuel rods of EPR are longer, and the core inlet flow of EPR is larger, so the vibration response of EPR is larger. However, it is an effective measure to reduce the vibration response of the fuel rod of EPR by increasing the number of grids and the stiffness of springs and dimples.

Data availability statement

The datasets presented in this study can be found in online repositories. The names of the repository/repositories and accession number(s) can be found below: https://data.mendeley.com/datasets/6ds6dtyywk/1.

Author contributions

NJ: designed the methodology, calculated some data, and revised the manuscript. GM: calculated some data, wrote the manuscript, and revised the manuscript. ZF: calculated some data. HQ: provided some parameters.

Funding

This study is financially supported by the National Natural Science Foundation of China (No. 11872060) and Special Project for Research and Development in Key Areas of Guangdong Province (No. 2021B0101250002).

Conflict of interest

The authors declare that the research was conducted in the absence of any commercial or financial relationships that could be construed as a potential conflict of interest.

Publisher's note

References

Ansari, S. A., Haroon, M., Sheikh, Z., and Kazmi, Z. (2008). Detection of flow-induced vibration of reactor internals by neutron noise analysis. *IEEE Trans. Nucl. Sci.* 55 (3), 1670–1677. doi:10.1109/TNS.2008.921490

Barbier, A., Cartier, O., Dolleans, P., Muller, T., Bellet, S., Fontes, J.-P., et al. (2009). "Experimental characterization of hydraulics in the EPR^{TM} lower plenum: Test performed on the JULIETTE mock-up," in *Proceedings of the 13th* international topical Meeting on nuclear reactor thermal hydraulics (NURETH-13*)* (Kanazawa, Japan). September 27-October 2.

Blevins, R. D. (1979). Flow-induced vibration in nuclear reactors: A review. *Prog. Nucl. Energy* 4 (1), 25–49. doi:10.1016/0149-1970(79)90008-8

Chen, S. S., and Wambsganss, M. W. (1972). Parallel-flow-induced vibration of fuel rods. *Nucl. Eng. Des.* 18 (2), 253–278. doi:10.1016/0029-5493(72)90144-6

Choi, Y., Park, J. B., Lee, S. J., Park, N. C., Park, Y. P., Kim, J. S., et al. (2016). Model reduction methods for cylindrical structures in reactor internals considering the fluid-structure interaction. *J. Nucl. Sci. Technol.* 53 (2), 204–222. doi:10.1080/00223131.2015.1035352

de Santis, D., and Shams, A. (2017). Numerical modeling of flow induced vibration of nuclear fuel rods. *Nucl. Eng. Des.* 320, 44–56. doi:10.1016/j.nucengdes.2017.05.013

Dutkiewicz, O., Marcinkiewicz, K. M., Madokoro, H., Shumski, S., Allison, C. M., and Hohorst, J. K. (2017). RELAP/SCDAPSIM/MOD3.5 analysis of KIT's QUENCH-14 experiment. *EPJ Nucl. Sci. Technol.* 3, 25. doi:10.1051/epjn/2017019

Ferrari, G., Franchini, G., Balasubramanian, P., Giovanniello, F., Le Guisquet, S., Karazis, K., et al. (2020). Nonlinear vibrations of a nuclear fuel rod supported by spacer grids. *Nucl. Eng. Des.* 361 (2020), 110503. doi:10.1016/j.nucengdes.2019.110503

Gorman, D. J. (1971). An analytical and experimental investigation of the vibration of cylindrical reactor fuel elements in two-phase parallel flow. *Nucl. Sci. Eng.* 44 (3), 277–290. doi:10.13182/NSE71-A20161

Gu, Z., Liu, C., and Fu, M. (2006). Strategic considerations on development of nuclear power and the associated fuel cycle in China. *J. Nucl. Sci. Technol.* 43 (9), 963–966. doi:10.1080/18811248.2006.9711183

Hassan, M. A., Weaver, D. S., and Dokainish, M. A. (2002). A simulation of the turbulence response of heat exchanger tubes in lattice-bar supports. *J. Fluids Struct.* 16 (8), 1145–1176. doi:10.1006/jfls.2002.0468

Ho, M. K., Hong, G., and Mack, A. N. (2004). "Experimental investigation of flow-induced vibration in a parallel plate reactor fuel-assembly," in *Australasian fluid mechanics conference* (Sydney, NSW 2006, Australia: The University of Sydney).

Jiang, N. B., Feng, Z. P., and Zang, F. G. (2018). *Theory and application of flow-induced vibration in nuclear engineering*. Shang Hai: SHANGHAI JIAO TONG University Press.

Jiang, N. B., Xiong, F. R., Zang, F. G., Zhang, Y. X., and Qi, H. H. (2017). Analysis on vibration response of U-tube bundles caused by two-phase cross-flow turbulence. *Ann. Nucl. Energy* 99, 328–334. doi:10.1016/j.anucene.2016.09.017

Kaneko, S., Nakamura, T., Inada, F., Kato, M., Ishihara, K., Nishihara, T., et al. (2014). *Flow-induced vibrations: Classifications and lessons from practical experiences*. Academic Press.

Kim, K. T. (2010). The effect of fuel rod supporting conditions on fuel rod vibration characteristics and grid-to-rod fretting wear. *Nucl. Eng. Des.* 240 (6), 1386–1391. doi:10.1016/j.nucengdes.2009.12.030

Liu, H., Chen, D., Hu, L., Yuan, D., and Gao, H. (2017). Numerical investigations on flow-induced vibration of fuel rods with spacer grids subjected to turbulent flow. *Nucl. Eng. Des.* 325, 68–77. doi:10.1016/j.nucengdes.2017.10.004

Mulcahy, T. M., Yeh, T. T., and Miskevics, A. J. (1980). Turbulence and rod vibrations in an annular region with upstream disturbances. *J. Sound Vib.* 69 (1), 59–69. doi:10.1016/0022-460X(80)90435-6

Paidoussis, M. P. (1981). Fluidelastic vibration of cylinder arrays in axial and cross flow: State of the art. *J. Sound Vib.* 76 (3), 329–360. doi:10.1016/0022-460X(81)90516-2

Pázsit, I., and Analytis, G. T. (1980). Theoretical investigation of the neutron noise diagnostics of two-dimensional control rod vibrations in a PWR. *Ann. Nucl. Energy* 7 (3), 171–183. doi:10.1016/0306-4549(80)90082-1

Peng, G., and Li, D. (2008). Design for fuel management of China integrated advanced NPP reactor core. *Nucl. Power Eng.* 29 (2), 39–42. doi:10.1088/0256-307X/25/2/069

Planchard, J. (1985). Vibrations of nuclear fuel assemblies: A simplified model. *Nucl. Eng. Des.* 86 (3), 383–391. doi:10.1016/0029-5493(85)90303-6

Puragliesi, R., Zhou, L., Zerkak, O., and Pautz, A. (2016). Steady-state CFD simulations of an EPR™ reactor pressure vessel: A validation study based on the juliette experiments. *Nucl. Eng. Des.* 300, 41–56. doi:10.1016/j.nucengdes.2015.12.025

Reavis, J. R. (1969). Vibration correlation for maximum fuel-element displacement in parallel turbulent flow. *Nucl. Sci. Eng.* 38 (1), 63–69. doi:10.13182/NSE69-A19354

Rubiolo, P. R. (2006). Probabilistic prediction of fretting-wear damage of nuclear fuel rods. *Nucl. Eng. Des.* 236 (14-16), 1628–1640. doi:10.1016/j.nucengdes.2006.04.023

Viebach, M., Bernt, N., Lange, C., Hennig, D., and Hurtado, A. (2018). On the influence of dynamical fuel assembly deflections on the neutron noise level. *Prog. Nucl. Energy* 104, 32–46. doi:10.1016/j.pnucene.2017.08.010

Wang, L., and Ni, Q. (2009). Vibration of slender structures subjected to axial flow or axially towed in quiescent fluid. *Adv. Acoust. Vib.* 2009, 1–19. doi:10.1155/2009/432340

Xiao, M., Zhang, H., Ma, C., Bai, C., Zhou, Z., Wang, L., et al. (2015). Practice and prospect of advanced fuel management and fuel technology application in PWR in China. *J. Nucl. Sci. Technol.* 52 (10), 1226–1231. doi:10.1080/00223131.2015.1029557

Yan, J., Yuan, K., Tatli, E., and Karoutas, Z. (2011). A new method to predict grid-to-rod fretting in a PWR fuel assembly inlet region. *Nucl. Eng. Des.* 241 (8), 2974–2982. doi:10.1016/j.nucengdes.2011.06.019

frontiers | Frontiers in Energy Research

ORIGINAL RESEARCH
published: 28 September 2022
doi: 10.3389/fenrg.2022.939712

Numerical Simulation and Experimental Study on Gas Flow in an Open Lattice Structure for an Advanced Space Nuclear Power System

Zhipeng Wang[1,2,3], *Jing Zhao*[1,2,3], *Zishen Ye*[1,2,3] *and Lei Shi*[1,2,3]*

[1]Institute of Nuclear and New Energy Technology, Tsinghua University, Beijing, China, [2]Collaborative Innovation Center of Advanced Nuclear Energy Technology, Tsinghua University, Beijing, China, [3]Key Laboratory of Advanced Reactor Engineering and Safety of Ministry of Education, Tsinghua University, Beijing, China

Helium flow in the rod bundle channel with an open lattice structure is an important phenomenon for the advanced gas-cooled nuclear core design. In this study, thermal analysis with helium flow in various channel designs is conducted based on CFD methods to determine a dimension-optimized rod bundle channel. An experimental study then follows in order to pick up an appropriate gas flow model in further numerical simulation. Finally, helium flow in the bundle channels consisting of 217 rods is simulated using this chosen flow model, which shows to satisfy the requirements of basic thermal analysis of a newly designed gas-cooled reactor with an open lattice structure. Generally, this work will contribute to the design and analysis of the future advanced space nuclear power system.

Keywords: gas-cooled reactor, dimension optimization, numerical simulation, thermal analysis, open lattice structure, space nuclear power system

Edited by:
Shichang Liu,
North China Electric Power University,
China

Reviewed by:
Ming Ding,
Harbin Engineering University, China
Xiang Chai,
Shanghai Jiao Tong University, China

***Correspondence:**
Lei Shi
shlinet@tsinghua.edu.cn

Specialty section:
This article was submitted to
Nuclear Energy,
a section of the journal
Frontiers in Energy Research

Received: *09 May 2022*
Accepted: *02 June 2022*
Published: *28 September 2022*

Citation:
Wang Z, Zhao J, Ye Z and Shi L (2022)
Numerical Simulation and
Experimental Study on Gas Flow in an
Open Lattice Structure for an
Advanced Space Nuclear
Power System.
Front. Energy Res. 10:939712.
doi: 10.3389/fenrg.2022.939712

1 INTRODUCTION

A high-temperature gas-cooled reactor combined with a closed cycle magnetohydrodynamic (CCMHD) power generation system is a promising technology for space applications (Litchford et al., 2001a; Harada et al., 2006; Kugeler and Zhang, 2018; She et al., 2021). It can meet the requirements in space tasks for high power and high efficiency.

The system mainly comprise a nuclear reactor, an MHD generator, a regenerator, compressors, and a radiator, whose schematic of working medium operation is shown in **Figure 1**. Helium is adopted as both the coolant and the power generation medium for its good ionization properties and chemical inertness (Kobayashi and Okuno, 2000; Litchford et al., 2001b).

The thermodynamic models and mass models of this system were established in the previous research (Wang et al., 2019), and a set of design parameters suitable for 1-MW thermal power system was given, including the reactor inlet and outlet temperature and the operating pressure. As for the elaborate reactor design, it remains to be a new challenge to match with the CCMHD system. MJ Wollman proposed a series of gas-cooled reactor designs that can match the Brayton dynamic conversion system in the Prometheus Research Program (Taylor, 2005; Wollman and Zika (Apr, 2006), including open lattice design, pin in block design, and modular cermet design, as shown in **Figure 2**, which can provide some references for the reactor design in the CCMHD system. The pin in block design not only shows great convective heat transfer characteristics in the preliminary study but also displays a large pressure drop with helium flow. The modular cermet design requires further research and experimental verification because CERMET fuel has not been tested for long-term ultra-high temperature, and the manufacturing process is also very difficult (An et al., 2015; Zhao et al., 2018).

Literally, the open lattice design has no flow block and provides the lowest mass geometry. Based on both the Prometheus open lattice structure and the Russian megawatt space reactor, Tao Meng designed a space gas-cooled reactor scheme composed of 534 fuel rods and 13 control rods. Through the flow and heat transfer simulation calculation of this scheme, conclusions were made that the reactor design had good thermal and hydraulic characteristics and can satisfy corresponding technical indexes (Meng et al., 2019; Meng et al., 2020).

Therefore, in this study, considering neutronics and thermal analysis, an initial feasible reactor core scheme based on the open lattice structure is presented without clarification in this first part. Sensibility analysis is then conducted to check the thermal hydraulic characteristics of the coolant flow in the open lattice structure, by means of changing the number of rods, the rod diameter, and the rod distance. After selecting a dimension-optimized rod bundle channel, an essential experiment concerning the open lattice structure is conducted, to pick up an appropriate gas flow model for further numerical simulation. In the last section, helium flow in the bundle channel with 217 rods is simulated using this determined flow model, to conduct more elaborate research on the new gas-cooled reactor with an open lattice structure.

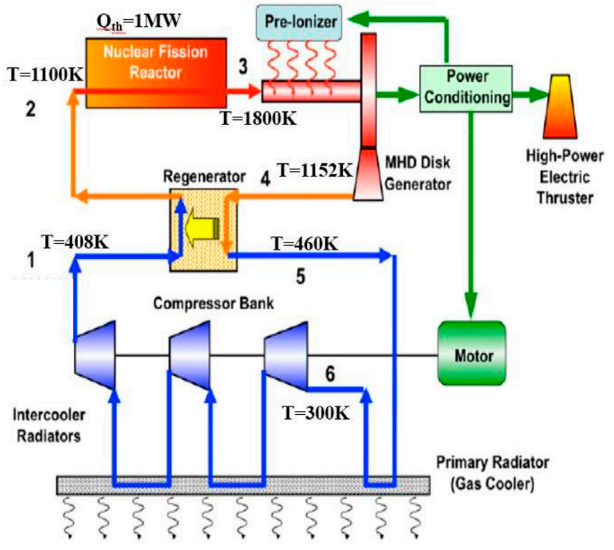

FIGURE 1 | Schematic of working medium operation in the CCMHD system (Harada et al., 2006).

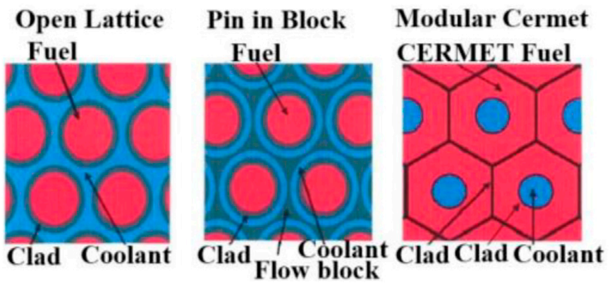

FIGURE 2 | Geometrical options mentioned in the Prometheus Research Program (Wollman and Zika (Apr, 2006)).

2 DIMENSION OPTIMIZATION

2.1 Preliminary Model

A preliminary model including a number of triangle-deposited rods is put forward, which combines both neutronics analysis and thermal considerations. The integral reactor design and the coolant flow path are illustrated in **Figure 3**, whose basic parameters are summarized in **Table 1**.

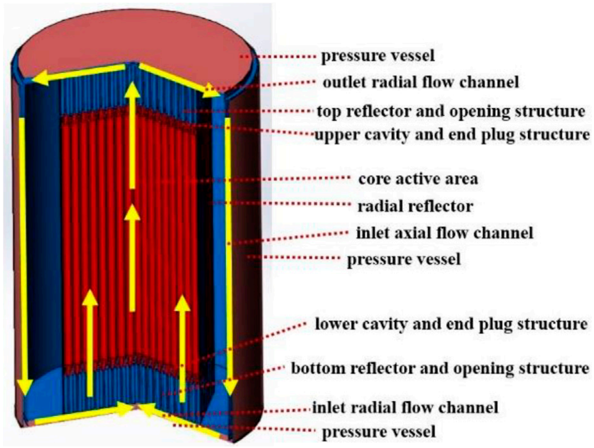

FIGURE 3 | Schematic of the coolant flow path.

TABLE 1 | Preliminary reactor design parameters.

Rod number	217
Reactor height/cm	72.5
Active area height/cm	50
Reactor diameter/cm	44
Axial reflector thickness/cm	8
Axial cavity height/cm	2
Annual channel height/cm	1
Rod distance/cm	1.75
Rod radius/cm	0.688
Clad inside radius/cm	0.69
Clad outside radius/cm	0.775
Pressure vessel thickness/cm	0.25

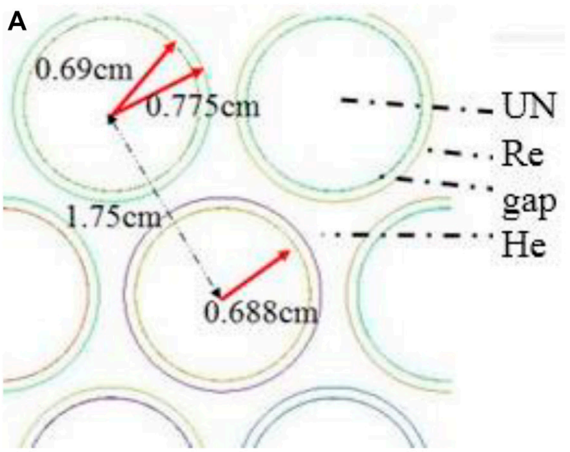

Schematic of preliminary core structure and size

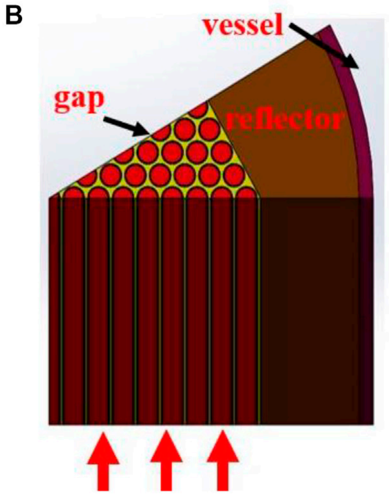

Schematic of 1/12 of the fuel layer

FIGURE 4 | (A) Schematic of preliminary core structures and size. **(B)** Schematic of 1/12 of the fuel layer.

In particular, the preliminary core structure and size are depicted in **Figure 4A**. Also, the diagram of 1/12 of the fuel layer among the reactor is shown in **Figure 4B**. Specifically, the fuel material is UN, the clad material is rhenium (Re), and the coolant is helium (He). The reflector material is BeO, and the pressure vessel material is a high temperature-resistant alloy MA-ODS956.

In the framework of given neutronics analysis, namely, fixing the reactor size and fuel installation, sensibility analysis is required to check thermal-hydraulic characteristics of the coolant flow in the open lattice structure, by means of changing the number of rods, the rod diameter, and the rod distance. Basic rules can be deduced qualitatively, while quantitative analysis is also indispensable in parameter optimization research. To simplify the calculation resources, in this section, only 1/12 of the individual channel is simulated and analyzed, as shown in **Figure 5**.

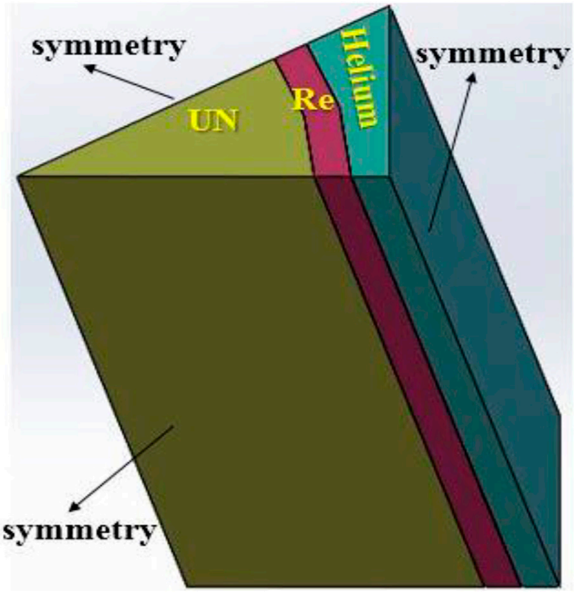

FIGURE 5 | Schematic of 1/12 of the individual channel.

As optimized in the previous system performance analysis research (Wang et al., 2019), the inlet temperature is set at 1100 K, and the outlet temperature is 1800 K. In addition, the outlet pressure is 0.4 MPa. Additionally, the gap structure which lies between the fuel and the clad and the radiation effects inside the reactor are neglected here, which will be considered in **Section 4**.

2.2 Numerical Approach

The governing equations conforming to the conservation of mass, momentum, and energy are established under the framework of incompressible Navier–Stokes equations, which can be written as

$$\frac{\partial \bar{u}_i}{\partial x_i} = 0, \tag{1}$$

$$\frac{1}{\rho}\frac{\partial\left(\bar{u}_i\bar{u}_j\right)}{\partial x_j} = -\frac{1}{\rho}\frac{\partial \bar{p}}{\partial x_i} + \frac{\partial}{\partial x_j}\left(\nu\left(\frac{\partial \bar{u}_i}{\partial x_j} + \frac{\partial \bar{u}_j}{\partial x_i}\right)\right) - \frac{\partial}{\partial x_j}\left(\overline{u_i' u'_j}\right) + g_i, \tag{2}$$

$$\frac{\partial\left(\rho \bar{u}_i c_p \bar{T}\right)}{\partial x_i} = \frac{\partial}{\partial x_i}\left(\lambda \frac{\partial \bar{T}}{\partial x_i}\right) - \frac{\partial}{\partial x_i}\left(\rho \overline{u'_i c_p T'}\right), \tag{3}$$

where the variables with over-bar are the mean parameters, while the variables with prime are fluctuated values. Furthermore, the unclosed parameters $-\rho\overline{u_i' u'_j}$ and $\rho\overline{u'_i c_p T'}$ are defined as Reynolds stress and turbulent heat flux, respectively, and will be treated by turbulence models. In this section, the SST k-w turbulence model is adopted for simulation, which is based on experience, and can be explained in a theoretical way. In fact, according to the ANSYS Fluent Theory Guide, the standard k-w model in ANSYS Fluent is

TABLE 2 | Summary of simulated rod bundle parameters in power density fixed analysis.

Rod number	271	217	169	127
Rod radius/cm	0.616	0.688	0.775	0.875
Rod distance/cm	1.556	1.75	2	2.334
Power density/MW/m^3	61.97	61.97	61.97	61.97
Mass flow rate/10^{4}kg/s	0.846	1.06	1.36	1.80
UN T_{max}/K	2016	2076	2165	2306
Re T_{max}/K	1989	2042	2121	2247
Pressure drop/kPa	13.88	8.53	5.27	3.17

TABLE 3 | Summary of simulated rod bundle parameters in mass flow rate fixed analysis.

Rod number	217	217	217	217
Rod radius/cm	0.683	0.688	0.693	0.698
Rod distance/cm	1.75	1.75	1.75	1.75
Power density/MW/m^3	62.88	61.97	61.08	60.21
Mass flow rates/10^{4}kg/s	1.06	1.06	1.06	1.06
UN T_{max}/K	2081	2076	2070	2064
Re T_{max}/K	2047	2042	2036	2031
Pressure drop/kPa	7.77	8.53	9.36	10.33

based on the Wilcox k-w model, which incorporates modifications for low-Reynolds number effects, compressibility, and shear flow spreading. One of the weak points of the Wilcox model is the sensitivity of the solutions to values for k and w outside the shear layer. The SST k-w model includes all the refinements of the BSL k-w model and in addition accounts for the transport of the turbulence shear stress in the definition of turbulent viscosity. These features make the SST k-w model more accurate and reliable for a wider class of flows than the standard and the BSL k-w models. In addition, flow model verification will also be conducted in **Section 3** in an experimental way.

2.3 Parametric Analysis

2.3.1 Power Density Fixed Analysis

The purpose of this section is to optimize the fuel parameters, such as the number of rods, the rod diameter, and the rod distance, in the framework of given neutronics analysis, namely, fixing the reactor size and fuel installation. The total power of the reactor is 1 MW.

If the power density of the fuel is kept constant at 61.97 MW/m^3, the fuel volume should be constant, which means the number of rods should be set inversely proportional to the square of the rod radius. Considering that the reactor size is fixed, the rod distance should be set inversely proportional to the number of rod turns. Mass flow rates can be deduced based on the conservation of energy. The calculation results of different number of rods are summarized in **Table 2**.

It can be concluded that when the number of rods decreases, the rod radius increases to keep the power density at a constant level. The actual heat exchange area decreases, leading to decreased heat exchange capabilities and decreased pressure drop. Overall, 217 rods prevail for medium temperature and pressure drop limitations.

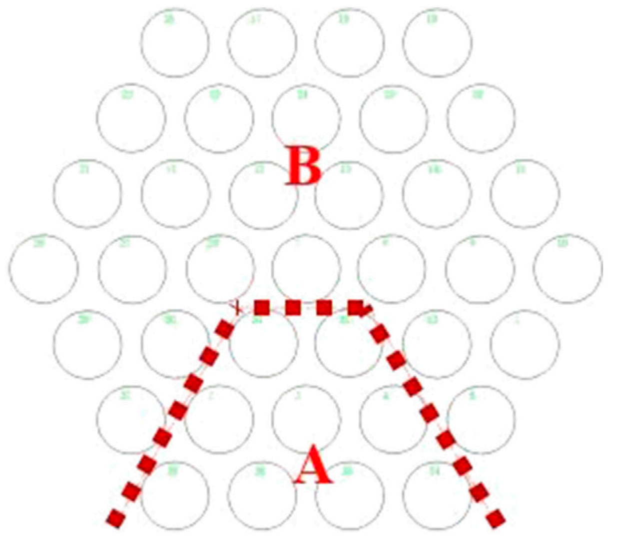

FIGURE 6 | Schematic of the arrangement and number of heating rods.

2.3.2 Mass Flow Rate Fixed Analysis

If the amount of the fuel is kept constant at 217, the rod distance should be constant to keep the reactor size constant. The power density should be set inversely proportional to the square of the rod radius, to keep the total power constant at 1 MW. Mass flow rates can be deduced based on the conservation of energy. The rod radius varies from 0.683 cm to 0.698 cm, which could hardly exercise effects on neutronics calculations. The calculation results of different rod radius are summarized in **Table 3**.

It can be concluded that when the rod radius increases, the total heat exchange area also increases, leading to the increased heat exchange capability. In addition, the velocity increases due to the decreased cross-sectional area, strengthening the heat exchange process as well. Therefore, temperature decreases and pressure drop increases during the process. A larger rod diameter is easy to cause rod contact, leading to heat transfer deterioration and even local melting, and also increasing the possibility of channel blockage. A smaller rod diameter will lead to higher fuel temperature and smaller safety temperature margin. In addition, the fuel parameter selection also considers the requirement of an MHD generator, which can be found in our previous research. The pressure of the reactor outlet is set at 0.4 MPa, and the inlet pressure of the reactor is supposed to be 0.41–0.43 MPa, so as to match the NFR/CCMHD generation system. In the scheme case of radius at 0.688 cm, the pressure drop is calculated to be 8.53 kPa, and the maximum temperature of all the materials are within the expected range, which meets the most design criteria. Overall, the rod radius of 0.688 cm prevails for appropriate temperature and pressure drop limitations.

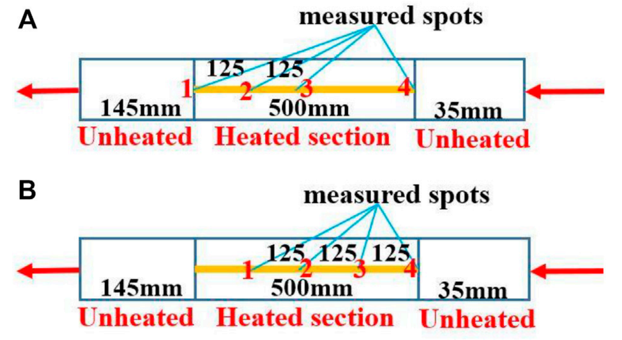

FIGURE 7 | Schematic of the specific structure of measured spots of Type **(A,B)**.

TABLE 4 | Five groups of working conditions under different mass flow rates and heating power distributions.

Exp no.	Expected mass rate	Power/W	Remark
2–100	48.68 kg/h	37*73	48.57 kg/h in reality
2–110	58.42 kg/h	37*73	High rates
2–120	48.68 kg/h	37*73/2	Low power
2–130	24.34 kg/h	37*73/2	Low power and rates
2–140	48.68 kg/h	/	Round-based power distribution

3 EXPERIMENTAL STUDY

3.1 Test Facility Description

After the preliminary analysis based on CFD methods, a dimension-optimized rod bundle channel is selected. The new challenge is to acquire a verified flow model in numerical simulation, which calls for further experimental research concerning the open lattice structure. After carefully performing similarity analysis, the linear geometry is kept almost the same, which adopts the same rod radius and rod distance as the optimized one in **Section 2**. The difference is that the experiment takes four-round heating rods rather than nine-round for saving the cost. Also, nitrogen is adopted as the experimental working medium. Details about the experiment are not the main concern in this study and can be found in other publications of our research team. In this section, the applicable turbulence model is obtained by using the temperature data of the rod cluster experimental section.

The arrangement and number of heating rods in the rod bundle test section are shown in **Figure 6**. The nine heating rods below the red dotted line are of type A, and the remaining 28 rods are of type B. Different types correspond to different specific structure of temperature-measured spots, as shown in **Figure 7**.

The temperature-measured spots of each heating rod are arranged as 1, 2, 3, and 4 in the order from top to bottom. Temperature measurement point 4 is taken as the height reference. It is clear that from the perspective of the entire rod bundle test section, there are five temperature measurement surfaces with relative heights of 0, 125, 250, 375, and 500 mm, respectively. Considering the arrangement of the two types of rods, it can be seen that there are 37 temperature measurement points at height 0, 28 temperature measurement points at height 125 mm, 37 temperature measurement points at height 250 mm, 37 temperature measurement points at height 375 mm, and 9 temperature measuring points at height 500 mm. In total, five groups of working conditions under different mass flow rates and heating power distributions are carried out by adjusting the control system. The conditions are summarized as follows in **Table 4**.

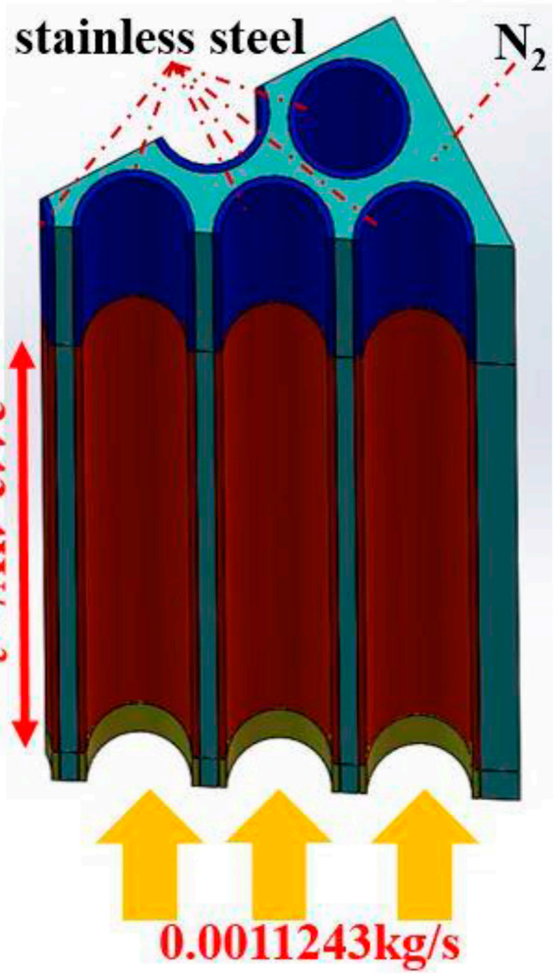

FIGURE 8 | Schematic of the simulation model of the test section.

3.2 Simulation Models

To analyze the data of measured temperature, numerical simulations are required based on some usual flow models including the laminar model, SST k-w model, RSM model, and standard k-ε with an enhanced wall model.

To simplify the calculation, 1/12 of the heating section is simulated, as shown in **Figure 8**. The housing material is stainless

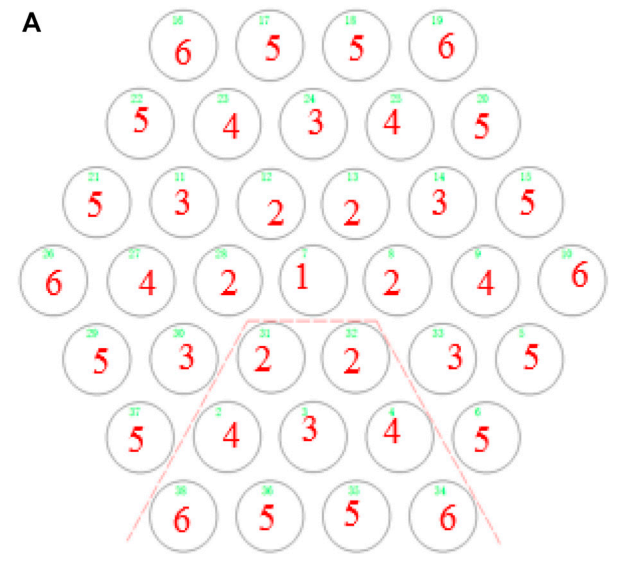

Experimental arrangement and number

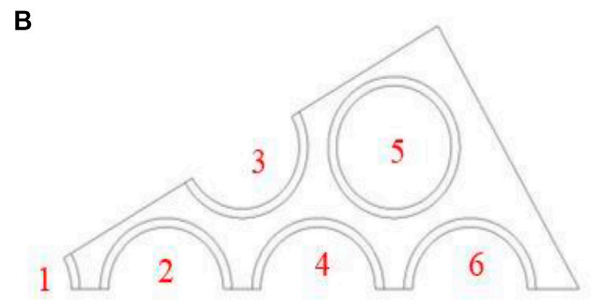

Simulated arrangement and number

FIGURE 9 | (A) Experimental arrangement and number. **(B)** Simulated arrangement and number.

steel. The heating surfaces are set to surface power heating conditions, i.e., 3443.4 W/m^2. The outer wall is set to be adiabatic because the heat-insulating material is adopted around the surface in the test rig. The inlet is set to be mass-flow-inlet with 0.0011243 kg/s in rates.

3.3 Test Data Analysis

3.3.1 Analysis Methods

As for the experiment, according to the relative positions of the rods, the rod bundle of 37 rods is divided into six different types of characteristic rods, as shown in **Figure 9A**. The measured values corresponding to each characteristic rod at the same height are counted and averaged, to obtain the average temperature of the cladding of the characteristic rod at that exact height. Here, we

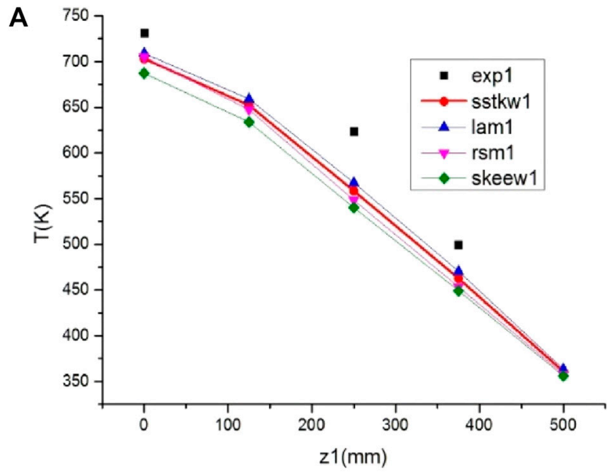

characteristic rod #1

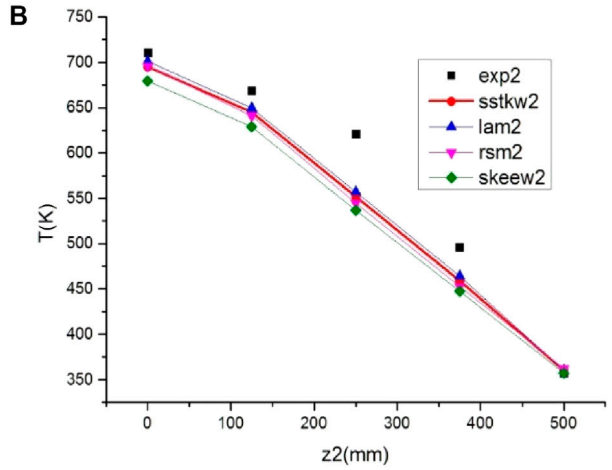

characteristic rod #2

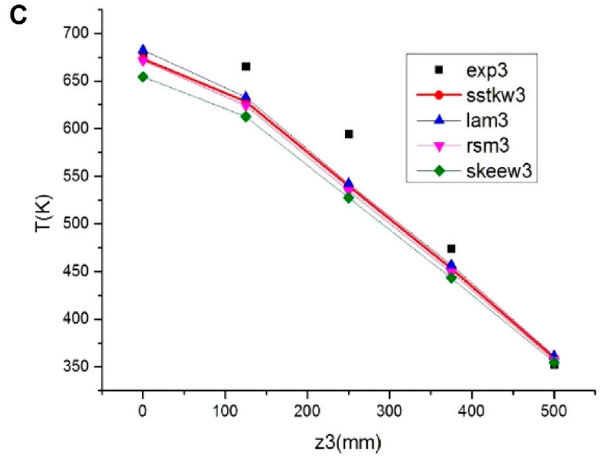

characteristic rod #3

FIGURE 10 | (Continued). Temperature distribution of the six characteristics rods along the axial height in the z-direction. **(A)** characteristic rod #1. **(B)** characteristic rod #2. **(C)** characteristic rod #3. **(D)** characteristic rod #4. **(E)** characteristic rod #5. **(F)** characteristic rod #6.

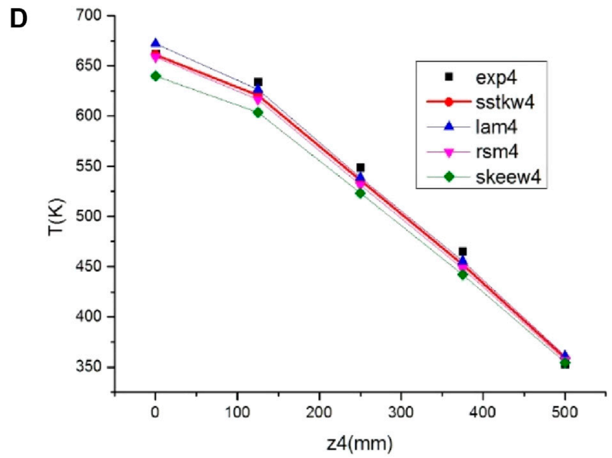

characteristic rod #4

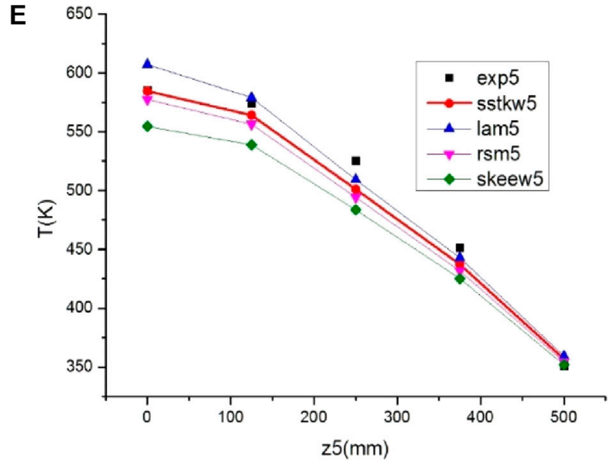

characteristic rod #5

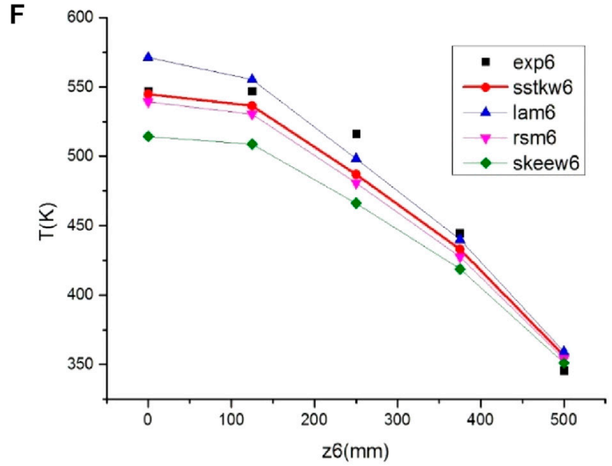

characteristic rod #6

FIGURE 10 | (Continued). Temperature distribution of the six characteristics rods along the axial height in the z-direction .

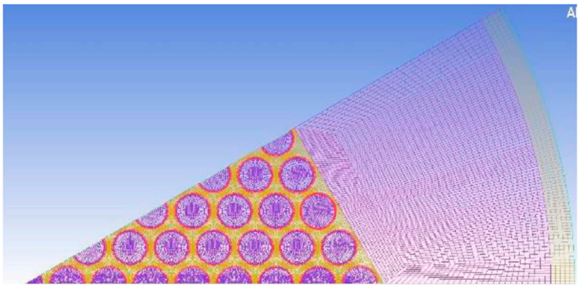

FIGURE 11 | Schematic diagram of the detailed mesh.

TABLE 5 | Main calculation results of different meshes.

Mesh number	Number of nodes	T_{max} reflector/K	Pressure drop/kPa
1	94e+4	1587	8.2
2	186e+4	1602	7.44
3	287e+4	1619	7.37
4	574e+4	1619	7.38
5	977e+4	1620	7.37

TABLE 6 | Main calculation results.

T_{max} fuel	2160 K
T_{max} cladding	2103 K
T_{max} gap	2123 K
T_{max} reflector	1619 K
T_{max} helium	2082 K
T_{max} vessel	1505 K
P_{max} inlet	7.373 kPa

should pay attention to eliminate unreasonable temperature measurement values.

As for the simulation, according to the thermal calculation results of 1 in 12 simulated parts, the area-weighted average temperature of the annular cladding surface of each rod at different heights is taken for reference, of which the arrangement and number are shown in **Figure 9B**.

3.3.2 Data Analysis

Taking the 2–100 reference condition as an example, the temperature distributions of the six characteristic rods in the z-direction along the axial height are depicted from **Figure 10A** to **Figure 10F**. In these figures, the experimental values are marked as points, and the calculated simulation values under the four flow models are marked as lines.

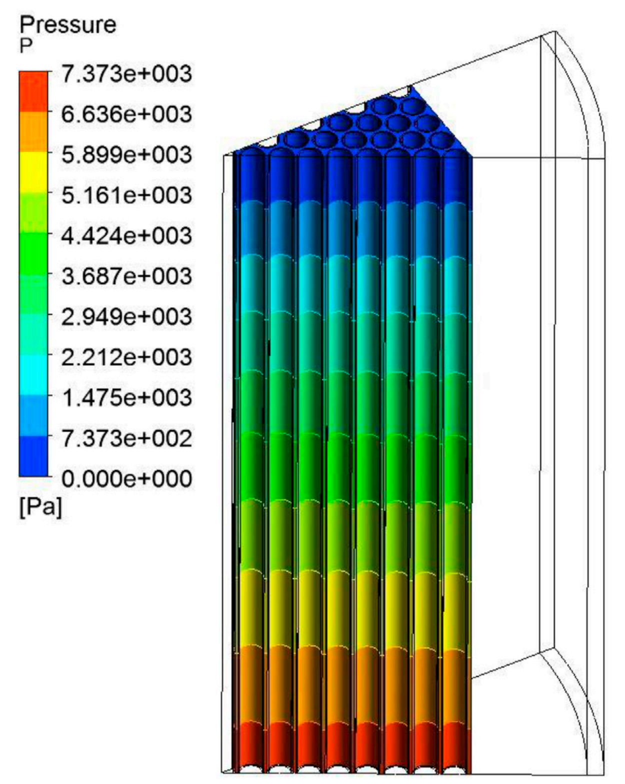

FIGURE 12 | Pressure contour of helium.

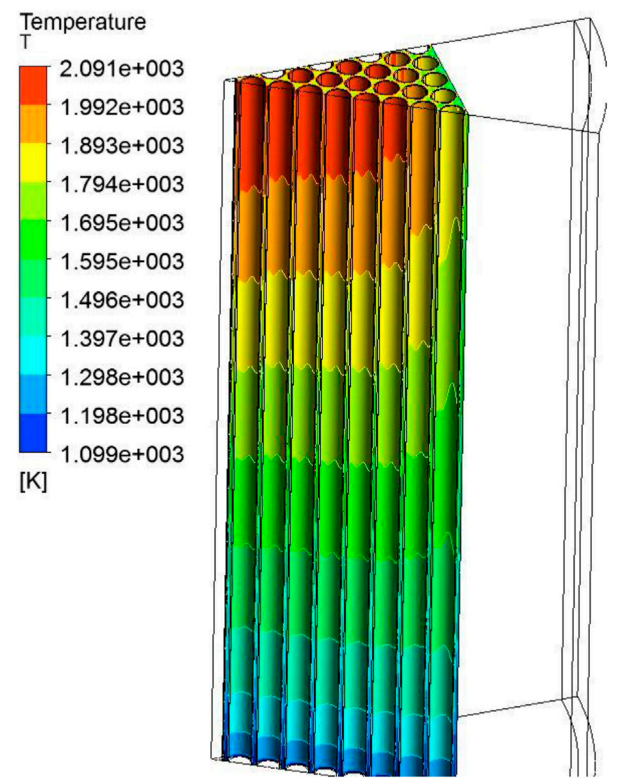

FIGURE 14 | Temperature contour of helium.

Considering the aforementioned six sets of data, the turbulence model SST k-w is relatively more consistent with the measured experimental data.

Applying this SST k-w turbulence model to all working conditions, it can be concluded that within the allowable error range, the simulated and experimental values are in good agreement.

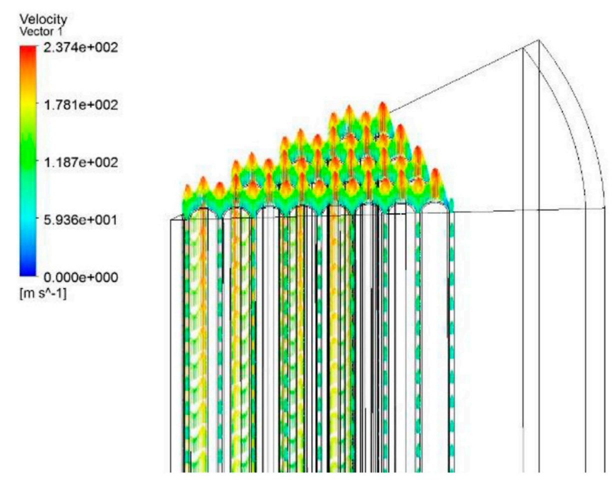

FIGURE 13 | Velocity vector of helium.

4 FURTHER ELABORATED NUMERICAL STUDY

Using the SST k-w turbulence model, it is achievable to simulate the heating section in a more elaborate way. Compared to **Section 2**, the gap structure, which lies between the fuel and the clad, the radial reflector and pressure vessel, and the radiation effects inside the reactor will all be considered in particular in this section.

4.1 Simulation Models

As for the fuel layer, simulation models consist of rods, rod claddings, the gap between the rod and the cladding, the coolant, the radial reflector, and the pressure vessel, as shown in **Figure 4B**. In addition to the turbulence model, the DO radiation model is also considered and calculated due to the overall high-temperature environment.

4.2 Boundary Conditions

The heating source item of the fuel is set at 6.19788e7W/m^3. The vessel boundary is set to radiation, where the outer space temperature is 200 K and the emissivity is 0.5. In addition, relevant surfaces that participate in the radiation are all set at

0.5 in the value of emissivity. Specifically, the radiation inside the flow channel is considered including the radiation between the fuel rods and the claddings, the radiation among the claddings, and the radiation between the reflector and the claddings. Also, since the coolant helium is a monatomic gas, there is no need to consider gas radiation.

4.3 Grid Independence Check

Details about the mesh are depicted in **Figure 11**. In order to find an appropriate mesh cell number and verify that the numerical results are not very sensitive to the mesh cell number, five cases with different mesh cell numbers are conducted. These cases have identical boundary conditions. The mesh cells and results for each case have been summarized in **Table 5**. According to the results, mesh 3 is chosen for further numerical calculation.

4.4 Result Analysis

After grid independence check, the mesh with 2.87 million nodes is proved to be sufficient to satisfy the calculation requirement. The main calculation results are summarized in **Table 6**. Compared to the original results in **Section 2**, the maximum temperature of rods rises by 4%, and the inlet maximum pressure drop decreases by approximately 13%. It can be concluded that the gap structure, the radial reflectors and pressure vessel structure, and the radiation effects inside the reactor cannot be neglected.

According to the pressure contour and velocity vector, as shown in **Figure 12** and **Figure 13**, helium flows into the open lattice structure and cools down the rods. The horizontal flow is relatively not obvious under this condition, leading to a horizontally uniform pressure distribution.

As shown in **Figure 14**, due to the non-uniformity of radial heating, the coolant has the highest temperature in the outlet near the center-rod. In addition, the coolant temperature distribution is also the most uneven at this height.

Overall, this design displays an acceptable result in the temperature field, velocity field, and pressure field and is appropriate for matching the CCMHD system. However, the axial and radial power profile and more elaborate reactor structures are also required to obtain more solid results.

5 CONCLUSION

The study presents numerical simulations and experimental study on gas flow in an open lattice structure for the advanced space nuclear power system. The conclusions are summarized as follows:

1. Given a certain neutronics limitation, a dimension-optimized rod bundle channel can be raised quantitatively, which requires to balance the maximum rod temperature, the pressure drop, and other factors in the design.
2. The experiment reveals that the SST k-w turbulence model is appropriate for further simulation in the open lattice structure.
3. Considering the gap structure, which lies between the fuel and the clad, the radial reflector and pressure vessel, and the radiation effects inside the reactor, the maximum temperature of rods rises by 4%, and the inlet maximum pressure drop decreases by approximately 13%.
4. This design displays an acceptable result in the temperature field, velocity field, and pressure field and is appropriate for matching the CCMHD system. Further research is also required to take the axial and radial power profile and more elaborate structures in the whole reactor into considerations.

DATA AVAILABILITY STATEMENT

The original contributions presented in the study are included in the article/Supplementary Material. Further inquiries can be directed to the corresponding author.

AUTHOR CONTRIBUTIONS

ZW: conceptualization, data curation, formal analysis, investigation, methodology, validation, writing—original draft, and writing—review and editing; JZ: conceptualization (supporting); ZY: data curation (supporting); and LS: conceptualization (lead), funding acquisition (lead), methodology (lead), project administration (lead), resources (lead), software (lead), and supervision (lead).

FUNDING

This work performed in Tsinghua University was financially supported by the National S&T Major Project of China (Grant No. ZX06901).

REFERENCES

An, W., Song, J., and Xie, J. (2015). Design of ultra-high temperature reactor core for magnetofluidic power generation [J]. *Atomic Energy Sci. Technol.* 49 (12), 5.

Harada, N., Le, C. K., and Hishikawa, M. (2006). in Basic Studies on Closed Cycle MHD Power Generation System for Space Application[C]//Aiaa Plasmadynamics and Lasers Conference.

Kobayashi, H., and Okuno, Y. (2000). Feasibility study on frozen inert gas plasma MHD generator. *IEEE Trans. Plasma Sci. IEEE Nucl. Plasma Sci. Soc.* 28 (4), 1296–1302. doi:10.1109/27.893319

Kugeler, K., and Zhang, Z. (2018). *Modular high-temperature gas-cooled reactor power plant[M]*. Springer.

Litchford, R. J., Bitteker, L. J., and Jones, J. E. (2001). *Prospects for nuclear electric propulsion using closed-cycle magnetohydrodynamic energy conversion, NASA TP-2001-211274[R]*. Washington D. C.: NASA.

Litchford, R. J., Bitteker, L. J., and Jones, J. E. (2001). *Prospects for nuclear electric propulsion using closed-cycle magnetohydrodynamic energy conversion, NASA TP-2001-211274[R]*. Washington D. C.: NASA.

Meng, T., Cheng, K., Zhao, F., Xia, C., and Tan, S. (2020). Computational flow and heat transfer design and analysis for 1/12 gas-cooled space nuclear reactor. *Ann. Nucl. Energy* 135, 106986. ISSN 0306-4549. doi:10.1016/j.anucene.2019.106986

Meng, T., Zhao, F., and Cheng, K. (2019). Numerical simulation of core flow and heat transfer in space gas cooled reactor [J]. *Atomic Energy Sci. Technol.* 053 (007), 1264–1271.

She, D., Xia, B., Guo, J., Wei, C-L., Zhang, , J., Li, F., et al. (2021). Prediction calculations for the first criticality of the HTR-PM using the PANGU code[J]. *Nucl. Sci. Tech.* 32 (9), 1–7. doi:10.1007/s41365-021-00936-5

Taylor, R. (2005). *Prometheus Project final report*.

Wang, Z., Sun, J., and Shi, L. Efficiency Analysis of Space Nuclear Reactor System Using Magnetic Fluid Power Generation [C]//The 16th National Academic Conference on Thermal Fluids for Reactors and the 2019 Academic Annual Conference of the Key Laboratory of Thermal and Hydraulic Technology for Nuclear Reactors in China. 2019 .

Wollman, M. J., and Zika (Apr, M. J. (2006). *Prometheus project reactor module final report*. United States. For Naval Reactors Information (SPP–67110-0008).

Zhao, Z., An, W., and Xie, J. (2018). Core design of 1MWth space reactor for closed-loop magnetic fluid power generation system [J]. *Sci. Technol. Innovation Her.* 15 (7), 4.

Conflict of Interest: The authors declare that the research was conducted in the absence of any commercial or financial relationships that could be construed as a potential conflict of interest.

frontiers | Frontiers in Energy Research

TYPE Original Research
PUBLISHED 19 October 2022
DOI 10.3389/fenrg.2022.1035797

OPEN ACCESS

EDITED BY
Jiankai Yu,
The University of Tennessee, Knoxville,
United States

REVIEWED BY
Yinan Cai,
Massachusetts Institute of Technology,
United States
Zhongchun Li,
Nuclear Power Institute of China (NPIC),
China

*CORRESPONDENCE
S. Xiao,
snrxs@nus.edu.sg

SPECIALTY SECTION
This article was submitted to Nuclear Energy,
a section of the journal Frontiers in Energy Research

RECEIVED 03 September 2022
ACCEPTED 30 September 2022
PUBLISHED 19 October 2022

CITATION
Than YR and Xiao S (2022), lp-CMFD acceleration schemes in multi-energy group 2D Monte Carlo transport.
Front. Energy Res. 10:1035797.
doi: 10.3389/fenrg.2022.1035797

lp-CMFD acceleration schemes in multi-energy group 2D Monte Carlo transport

Y. R. Than and S. Xiao*

Singapore Nuclear Research and Safety Initiative, National University of Singapore, Singapore, Singapore

The linear prolongation flux update scheme is extended to both regular CMFD acceleration, as well as partial CMFD acceleration in 2D multi energy group Monte Carlo *k*-eigenvalue neutron transport problems. The acceleration performance of these CMFD variants were investigated in simple 2D slab geometries, first with a monoenergetic case and then with a three group problem on the same geometry based on the monoenergetic cross sections. Flux convergence was determined *via* an on-the-fly convergence diagnostics developed by Ueki and Brown. It is found that on top of providing better acceleration in general, the linear prolongation scheme is also able to correct for instabilities in the CMFD scheme. Overall, the lp-pCMFD scheme employing a maximum history length is found to have the best performance across the cases presented.

KEYWORDS

CMFD variants, Monte Carlo, neutron transport, k-eigenvalue problem, acceleration performance

Introduction

In Monte Carlo (MC) calculations of the *k*-eigenvalue neutron transport problems, fission source iteration may have slow convergence in cases with high dominance ratios. Acceleration methods applied in MC calculations include the Coarse Mesh Finite Difference (CMFD) acceleration scheme, which was originally developed for the acceleration of deterministic neutron transport calculations. The CMFD acceleration scheme employs a diffusion-based calculation on a coarse mesh grid, for which the solution is used to update the transport flux. The use of coarse mesh is suitable efficient diffusion calculation in exceedingly fine mesh calculations or where the fine mesh geometry is complex. The effectiveness of the CMFD acceleration methods employed in MC transport calculations has been demonstrated (Lee et al., 2010; Hunter, 2014; Lee et al., 2014). CMFD variants include partial CMFD (pCMFD), where partial current drift coefficients, as opposed to net currents, are utilised in the diffusion calculation. pCMFD is also known to be unconditionally stable, unlike regular CMFD, though it has shown to be a bit slower in deterministic transport calculations for problems with small and intermediate optical thickness. Several works have also successfully incorporated

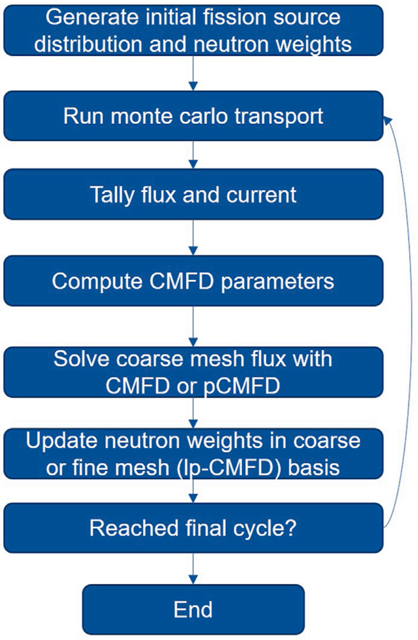

FIGURE 1
Overall flowchart of a Monte-Carlo k_{eff} calculation with CMFD-based acceleration.

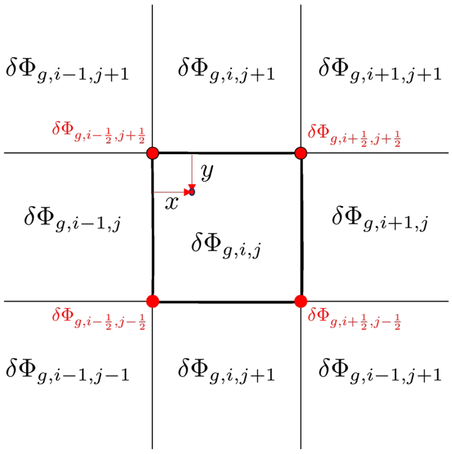

FIGURE 2
Illustration of linear interpolation scheme in lp-CMFD.

the pCMFD scheme in place of regular CMFD in continuous energy MC calculations (Yun and Cho, 2010; Jo and Cho, 2018a; Jo and Cho, 2018b).

Another CMFD variant is the linear prolongation CMFD (lp-CMFD) scheme, which is a method first proposed by Wang and Xiao (2018). Where regular CMFD updates the fine mesh flux in a coarse mesh basis after the diffusion step, lp-CMFD uses a linear additive approach from bilinear interpolation of the coarse mesh flux to update the fine mesh scalar flux, thereby resulting in a smoother transport flux update. Employing the linear prolongation in pCMFD results in a lp-pCMFD scheme, which can also be considered. The lp-CMFD scheme has been employed in deterministic transport problems with various spatial discretisation schemes, which demonstrated improved acceleration and stability (Chan and Xiao, 2019a; Chan and Xiao, 2019b; Chan and Xiao, 2019c; Chan and Xiao, 2020a; Chan and Xiao, 2020b). Following the results in deterministic calculations, lp-CMFD and lp-pCMFD schemes has also been employed in 1D slab MC transport calculations (Chan and Xiao, 2021), as well as in a 2D homogenous slab (Abdullatif and Wang, 2022; Than and Xiao, 2022), where its effectiveness relative to regular CMFD is once again demonstrated. Among the CMFD variants investigated in the aforementioned works, the most efficient scheme can vary depending on factors such as the total cross section values.

In this work, we further build on Monte-Carlo simulations of 2D geometries using lp-CMFD based acceleration schemes, with multi energy group and non-homogenous domains. A monoenergetic case will be first studied as a base line and then a three energy group problem based on the monoenergetic case will be investigated. Differences in the performance of each acceleration scheme going from single to multi-energy group will be discussed.

Theory and methodology

The neutron flux $\psi(\mathrm{r},\Omega,E)$ is typically split into discrete energy groups (as neutron flux $\psi_g(\mathrm{r},\Omega)$) in neutron transport, where r is the spatial coordinate, Ω is the direction of the neutron velocity, E is the neutron energy and g is the energy group index. The k-eigenvalue time-independent neutron transport equation is thus split into a system of coupled transport equations for each group:

$$\begin{aligned}&\boldsymbol{\Omega}\cdot\nabla\psi_g(\mathbf{r},\boldsymbol{\Omega})+\sigma_{tg}(\mathbf{r})\,\psi_g(\mathbf{r},\boldsymbol{\Omega})\\&=\frac{1}{4\pi}\sum_{g'}\sigma_{sg'g}(\mathbf{r})\,\phi_{g'}(\mathbf{r})+\frac{1}{4\pi}\sum_{g'}\chi_g\frac{\nu}{k}\sigma_{fg'}(\mathbf{r})\,\phi_{g'}(\mathbf{r})\end{aligned} \tag{1}$$

where $\phi_g(\mathrm{r})=\int\psi_g(\mathrm{r},\Omega')\mathrm{d}\Omega'$ is the scalar flux. σ_{tg}, $\sigma_{sg'g}$ and $\sigma_{fg'}$ are the group discretised total, scattering and fission cross sections respectively. ν is the average fission multiplicity. Xg is the fission energy spectrum. $keff$ is the multiplication factor.

CMFD acceleration schemes aim to solve a simpler diffusion based equation that is obtained by first integrating **Eq. 1** over Ω:

$$\begin{aligned}&\nabla\cdot\mathbf{J}_g(\mathbf{r})+\sigma_{tg}(\mathbf{r})\,\phi_g(\mathbf{r})\\&=\sum_{g'}\sigma_{sg'g}(\mathbf{r})\,\phi_{g'}(\mathbf{r})+\sum_{g'}\chi_g\frac{\nu}{k}\sigma_{fg'}(\mathbf{r})\,\phi_{g'}(\mathbf{r})\end{aligned} \tag{2}$$

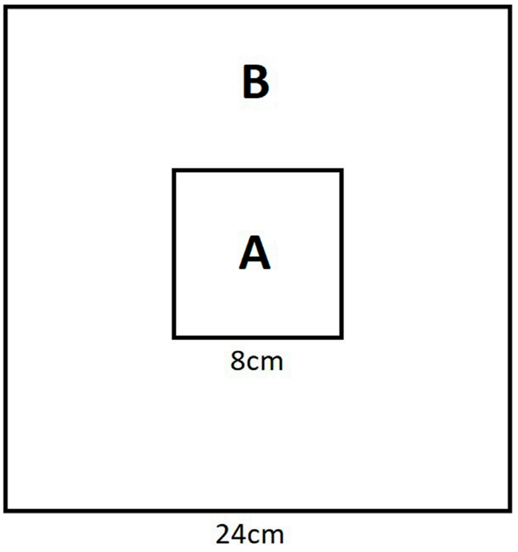

FIGURE 3
Illustration of the domain used in this work, consisting of two square regions of the indicated dimensions with fissile region A and non-fissile region B.

TABLE 1 Monoenergetic cross section values used in this work, indicated in units cm^{-1}.

Cross section	Region A	Region B
σ_t	5	5
$\nu\sigma_f$	0.5	0
σ_s	4.5	4.5

where J is the neutron current. Further integrating Eq. 2 over each coarse mesh gives the CMFD equations:

$$\sum_{m'\in N(m)} \frac{A_{mm'}}{V_m} J_{gmm'} + \sigma_{tgm}\phi_{gm} = \sum_{g'} \sigma_{sg'gm}\phi_{g'm} + \sum_{g'} \chi_g \frac{\nu}{k}\sigma_{f'gm}\phi_{g'm} \tag{3}$$

where m is the coarse mesh cell index with volume V_m, with $N(m)$ being the cells neighbouring cell m. $J_{gmm'}$ is the group neutron current from cell m to m' while $A_{mm'}$ adjoining surface area between cells m and m'.

Subsequently, a diffusion equation is obtained *via* Fick's law with a nonlinear correction term $\hat{D}$:

$$J_{gmm'} = \tilde{D}_{gmm'}\left(\phi_{gm} - \phi_{gm'}\right) + \hat{D}_{gmm'}\left(\phi_{gm} + \phi_{gm'}\right) \tag{4}$$

where

$$\tilde{D}_{gmm'} = \frac{2D_{gm}D_{gm'}}{h_{mm'}\left(D_{gm} + D_{gm'}\right)} \tag{5}$$

and

$$\hat{D}_{gmm'} = \frac{\bar{J}_{gmm'} - \tilde{D}_{gmm'}\left(\bar{\phi}_{gm} - \bar{\phi}_{gm'}\right)}{\bar{\phi}_{gm} + \bar{\phi}_{gm'}} \tag{6}$$

with $D_{gm} = \frac{1}{3\sigma_{tgm}}$. $h_{mm'}$ refers to the distance from the center of coarse mesh cell m to the m/m' surface and the overbars indicate values calculated from the most recent MC fine mesh transport flux.

pCMFD employs partial currents J^+ and J^- instead of the total current J, thus pCMFD equations equivalent to Eq. 4 will be

$$J_{gmm'} = \tilde{D}_{gmm'}\left(\phi_{gm} - \phi_{gm'}\right) + \hat{D}^+_{gmm'}\phi_{gm} - \hat{D}^-_{gmm'}\phi_{gm} \tag{7}$$

with

$$\hat{D}^+_{gmm'} = \frac{\bar{J}^+_{gmm'} - \tilde{D}_{gmm'}\left(\bar{\phi}_{gm} - \bar{\phi}_{gm'}\right)}{\bar{\phi}_{gm}} \tag{8}$$

and

$$\hat{D}^-_{gmm'} = \frac{\bar{J}^-_{gmm'} - \tilde{D}_{gmm'}\left(\bar{\phi}_{gm'} - \bar{\phi}_{gm}\right)}{\bar{\phi}_{gm'}} \tag{9}$$

The overall flowchart of a CMFD-based acceleration is given in Figure 1. After each Monte Carlo transport step, the flux and currents are tallied in the coarse mesh to compute the coefficients in the CMFD or pCMFD calculation. Following the CMFD or pCMFD solution, the MC fine mesh is then updated in either a coarse mesh or fine mesh basis. Updating the fine mesh flux *via* the linear prolongation method gives rise to the "lp" variant of the acceleration schemes (lp-CMFD and lp-pCMFD), which provides the 4 acceleration scheme variants to be investigated in this work. In regular or CMFD and pCMFD acceleration, the neutron weights w_n are updated according to

$$\tilde{w}_n = \frac{w_n N_p p_{M(n)}}{W_n} \tag{10}$$

where

$$W_n = \sum_{n':M(n')=M(n)} w_{n'} \tag{11}$$

to obtain the modified neutron weights $\tilde{w}_n$. N_p is the total neutron count, $M(n)$ refers to the coarse mesh cell index from with neutron n originates while

$$p_m = \sum_g \frac{\chi_g \nu\sigma_{fg}\phi_{mg}V_m}{\sum_{m'}\chi_g \nu\sigma_{fg}\phi_{m'g}V_{m'}} \tag{12}$$

is the neutron source fraction, where the scalar flux is updated according to

$$\phi^{new}_{g,fine} = \phi^{old}_{g,fine}\frac{\Phi^{new}_{g,coarse}}{\Phi^{old}_{g,coarse}} \tag{13}$$

In lp-CMFD and lp-pCMFD schemes, the CMFD flux is projected back on to the fine mesh flux according to the linear

TABLE 2 Three group cross section values used in this work, indicated in units cm^{-1}. Groups are labeled 1 to 3 in decreasing energy.

Cross section	Region A	Region B	Cross section	Region A	Region B
σ_{t1}	5	5	σ_{s11}	0.9	0.45
σ_{t2}	5	5	σ_{s12}	3.6	4.05
σ_{t3}	5	5	σ_{s22}	0.9	0.45
$\nu\sigma_{f1}$	0	0	σ_{s23}	3.6	4.05
$\nu\sigma_{f2}$	0	0	σ_{s33}	4.5	4.5
$\nu\sigma_{f3}$	0.5	0			

approach described by Wang and Xiao (Wang and Xiao, 2018) the weights are then updated on a fine mesh basis based on the updated fine mesh flux. Instead of **Eq. 13**, the update of scalar flux is achieved *via*

$$\phi_{g,fine}^{new} = \phi_{g,fine}^{old} + \Delta\phi_{g,fine} \tag{14}$$

where

$$\begin{aligned}\Delta\phi_{g,fine} = {} & \frac{x}{\Delta_x}\left(\delta\Phi_{g,i+\frac{1}{2},j-\frac{1}{2}} - \delta\Phi_{g,i-\frac{1}{2},j-\frac{1}{2}}\right) \\ & + \frac{xy}{\Delta_x\Delta_y}\Big(\delta\Phi_{g,i+\frac{1}{2},j+\frac{1}{2}} - \delta\Phi_{g,i-\frac{1}{2},j+\frac{1}{2}} \\ & + \delta\Phi_{g,i-\frac{1}{2},j-\frac{1}{2}} - \delta\Phi_{g,i+\frac{1}{2},j-\frac{1}{2}}\Big) \\ & + \frac{y}{\Delta_y}\left(\delta\Phi_{g,i-\frac{1}{2},j+\frac{1}{2}} - \delta\Phi_{g,i-\frac{1}{2},j-\frac{1}{2}}\right) + \delta\Phi_{g,i+\frac{1}{2},j-\frac{1}{2}}\end{aligned} \tag{15}$$

is the bilinear interpolation from the estimated corner node $\delta\Phi$ flux corrections as described in **Figure 2**.

$\delta\Phi$ is the difference between the CMFD (or pCMFD) solution and the pure Monte Carlo solution that is projected into the coarse mesh. The half integer index values of $\delta\Phi$ are the corner node flux corrections given by

$$\delta\Phi_{g,i+\frac{1}{2},j+\frac{1}{2}} = \frac{1}{4}\left[\delta\Phi_{g,i,j} + \delta\Phi_{g,i+1,j} + \delta\Phi_{g,i,j+1} + \delta\Phi_{g,i+1,j+1}\right] \tag{16}$$

The corner node flux corrections located at the boundary can be calculated in similar fashion according to boundary conditions. Following the fine mesh flux update, the neutron weights can then by updated in the same fashion as in **Eqs 10**, **12** in a fine mesh basis.

The initial MC iterations are considered to be inactive cycles, as the algorithm is still trying to converge to the true solution. The posterior relative entropy method (Ueki and Brown, 2005; Ueki, 2009) is used to determine the criteria for which the solution is sufficiently stable such that subsequent iterations may be classified as active cycles, from which statistical data such as variance and averages may be subsequently calculated. The Shannon entropy H at each cycle is calculated as

$$H = \sum_n \omega_n \log_2(\omega_n) \tag{17}$$

where

$$\omega_n = \frac{W_n}{\sum_{n'} W_{n'}} \tag{18}$$

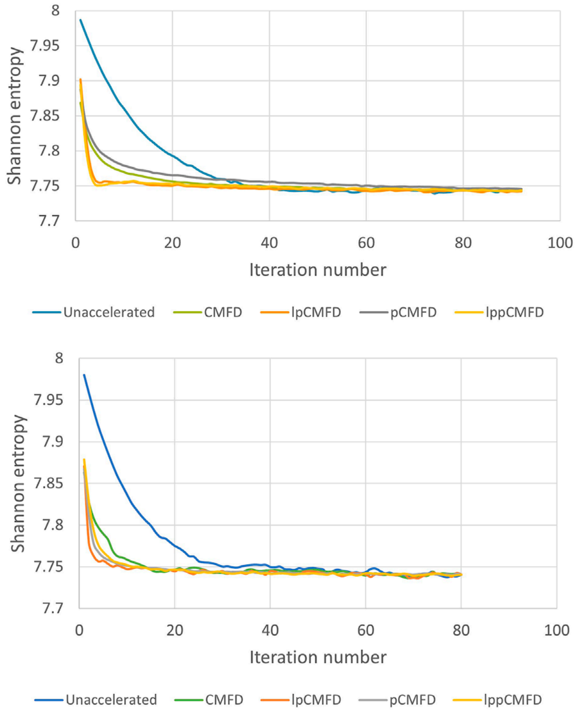

FIGURE 4
Shannon entropy progression in single group simulations (top) and multi group simulations (bottom) for each of the acceleration schemes employed, averaged over 10 independent simulations, for either a history length of 5 or maximum (whichever performs better).

The posterior relative entropy (PRE) is defined as

$$\begin{aligned}H_{pre}(\omega\|\omega^{\circ}) = {} & \sum_n \omega^{\circ}{}_n \log_2\left(\frac{\omega^{\circ}{}_n}{\frac{1}{2}(\omega^{\circ}{}_n + \omega_n)}\right) \\ & + \sum_n \omega_n \log_2\left(\frac{\omega_n}{\frac{1}{2}(\omega^{\circ}{}_n + \omega_n)}\right)\end{aligned} \tag{19}$$

where $\omega^{\circ}{}_n$ are the ω_n values at the start of cycle 1 (Ueki and Brown, 2005). H_{pre}). One advantage of this method is that additional simulations for a reference Shannon entropy stationary convergence is not required.

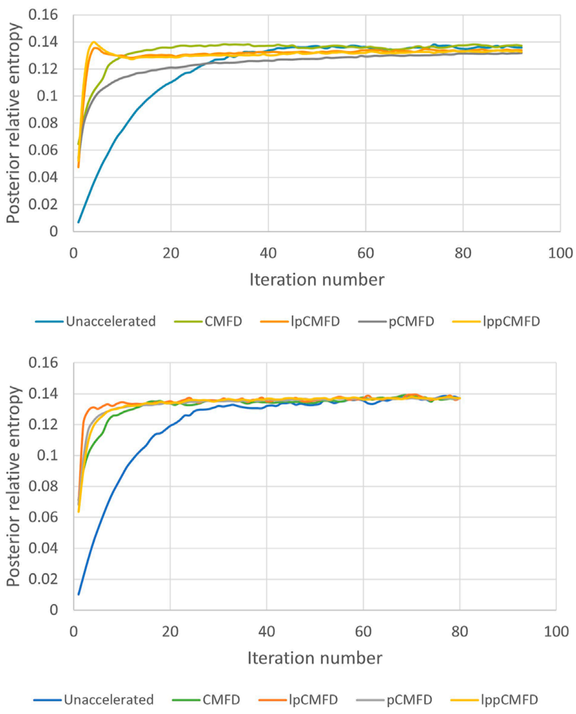

FIGURE 5
Posterior relative entropy progression in single group simulations (top) and multi group simulations (bottom) for each of the acceleration schemes employed, averaged over 10 independent simulations, for either a history length of 5 or maximum (whichever performs better).

As illustrated in Figure 3, we use a simple toy model following previous work in Ref. (Than and Xiao, 2022) with a central fissile zone (A) surrounded by a non-fissile zone (B) with vacuum boundary conditions. We study two cases based on this geometry, a monoenergetic case with cross sections listed in Table 1, as well as a three energy group case based on the monoenergetic case with cross sections listed Table 2. There are 500 neutrons per fine mesh for the monoenergetic case and 200 neutrons per fine mesh for the three energy group case in the fissile region A of the simulations, with a 48×48 fine mesh and a 24×24 coarse mesh for the whole domain. The MC neutron transport simulation codes are developed on the MATLAB platform and executed in parallel using 10 cores on the Intel Xeon W-2255 CPU @ 3.70GHz processor. 10 independent simulations are performed for each of the acceleration schemes: CMFD, pCMFD, lp-CMFD, lp-pCMFD with both a history length of 5 as well as using the full history starting from the first cycle.

Results and analysis

For each case, the k_{eff} values are recorded over 50 active cycles with an average k_{eff} of 0.974 ± 0.004 for the monoenergetic case and 0.744 ± 0.005 for the three energy group case. The k_{eff} is lower in the multi group case as the energy group structure poses as an additional barrier between the generated fission neutrons and the next thermal fission reaction. The suitability of the posterior relative entropy method as condition for the active cycle can be seen from Figures 4, 6. The active cycle flux is sufficiently converged in the sense that is suitable for recording statistical data. Figures 4, 6 further enforce this point, as it can be seen that the k_{eff} and entropy H values reach within fluctuation range of the stationary value well before the active cycle is declared.

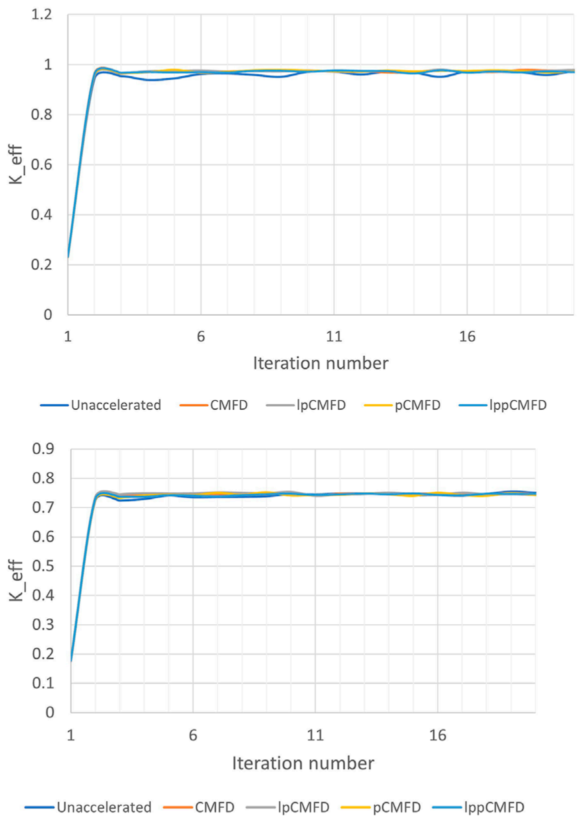

FIGURE 6
Estimated k_{eff} progression in single group simulations (top) and multi group simulations (bottom) for each of the acceleration schemes employed for the first 20 cycles, averaged over 10 independent simulations, for either a history length of 5 or maximum (whichever performs better).

Even with just 10 independent simulations for each scheme, the effectiveness of the CMFD-based acceleration methods is clear. From Table 3 it can be seen that CMFD schemes cut the number of inactive cycles by around half, though the base CMFD scheme is unstable when considering long history lengths for both the monoenergetic and multi group case. The CMFD flux did not always converge to the correct solution, thus causing the solution to diverge. This instability is corrected with the implementation of linear prolongation flux update, as

TABLE 3 Number of inactive cycles required in the single group simulations for each scheme averaged over 10 independent simulations for each acceleration history length. The standard deviation is indicated in the parenthesis. (*) CMFD with maximum history length did not converge.

Acceleration scheme	Last inactive cycle (history length 5)	Last inactive cycle (history length all)
Unaccelerated	93.9 ± 13.0	93.9 ± 13.0
CMFD	54.3 ± 10.4	*
lp-CMFD	47.6 ± 10.6	38.5 ± 4.8
pCMFD	57.1 ± 10.1	47.2 ± 5.8
lp-pCMFD	51.5 ± 10.1	34.7 ± 1.25

TABLE 4 Number of inactive cycles required in the multigroup simulations for each scheme averaged over 10 independent simulations for each acceleration history length. The standard deviation is indicated in the parenthesis. (*) CMFD with maximum history length did not converge.

Acceleration scheme	Last inactive cycle (history length 5)	Last inactive cycle (history length all)
Unaccelerated	83.7 ± 13.8	83.7 ± 13.8
CMFD	58.6 ± 8.6	*
lp-CMFD	55.8 ± 8.9	52.7 ± 8.5
PCMFD	63.8 ± 13.1	60.2 ± 8.5
lp-pCMFD	55.9 ± 6.36	53.1 ± 5.3

the lp-CMFD scheme consistently able to converge properly and yield the expected acceleration. It is however noted that the acceleration obtained in 1D MC transport calculations as reported by Chan and Xiao (2021) was much greater in terms of percentage decrease in inactive cycles required. It is clear that the linear prolongation schemes outperform the regular coarse mesh flux update in all cases investigated in this work. It is also interesting to note that while pCFMD schemes perform about equal or slightly worse than regular CMFD with lower history length, extending the history length yields significantly better results on top of being more stable as mentioned, though in all cases pCMFD is still significantly outperformed by lp-CMFD and lp-pCMFD. Having extended history lengths also resulted in a lower variance in the number of inactive cycles required. For the simple monoenergetic system investigated in this work, the lp-pCMFD acceleration proves to be most efficient, followed by the regular lp-CMFD scheme. For the multi energy group case, lp-CMFD and lp-pCMFD produce similar results.

The shannon entropy progression presented in **Figure 4** shows a similar picture. All CMFD-based schemes converge much faster to the stationary value, while lp-CMFD based schemes are even faster in the monoenergetic case. The speed of shannon entropy convergence appears to be primarily influenced by the flux update scheme employed rather the type of CMFD solver used. The posterior relative entropy progression used for on-the-fly convergence analysis presented in **Figure 5** mirrors the shannon entropy progression as expected for a diagnostic metric. The k_{eff} progression is presented **Figure 6**. There are a few differences in terms of the entropy of the three group problem. First is the pCMFD case, where the shannon entropy converges to the stationary value about as fast as the lp-pCMFD scheme, but interestingly does not reflect an earlier convergence according to the on-the-fly convergence analysis. In the three group case, the lp-CMFD shannon entropy is able to reach its stationary value the earliest, but as **Figures 4**, **5** show, the value shows fluctuation at first, thus does not result in an earlier active cycle according to the on-the-fly diagnostics. It is also noted in **Table 4** that the improvement due to the linear prolongation scheme is slightly more significant when applied to pCFMD versus regular CMFD. In contrast to what **Table 3** and **Figure 4** suggest, the unaccelerated calculation converges to the stationary k_{eff} just as quickly as the accelerated calculations. It is however noted that convergence in k_{eff} is not deemed to be sufficient for overall stationary solution convergence.

Conclusion

In this work, lp-CMFD based acceleration schemes (Wang and Xiao, 2018) are applied to monoenergetic and multi group 2D MC neutron transport calculations with on-the-fly convergence diagnostics (Ueki, 2009). Based on sets of 10 independent simulations, the acceleration given by the CMFD-based schemes in 2D MC neutron transport calculations reduce the inactive cycles required by around half, and is even more efficient with the use of the linear prolongation scheme for flux update. Further, the linear prolongation scheme is able to correct the instability of the CMFD solver at long history lengths. Overall, the linear prolongation-based schemes perform better in both single and multi-group calculations, which lp-pCMFD being the most efficient in single-group and both lp-CMFD and lp-pCMFD yielding similar acceleration in the multi-group simulations.

The shannon entropy of the accelerated schemes also converge much faster than that of the unaccelerated. While the k_{eff} values in the unaccelerated scheme do converge just as fast as in the accelerated calculations, the slower shannon entropy conversion shows that the overall flux is still much slower to converge without the CMFD-based acceleration schemes.

Data availability statement

The original contributions presented in the study are included in the article/Supplementary Material, further inquiries can be directed to the corresponding author.

Author contributions

YT and SX contributed to conception and design of the study. YT carried out the computational work. YT and SX contributed to writing the manuscript.

Funding

This work was supported by the National Research Foundation Singapore (A-0001360-06-00).

Acknowledgments

The authors thank Chan Yi Meng for the useful resources provided.

Conflict of interest

The authors declare that the research was conducted in the absence of any commercial or financial relationships that could be construed as a potential conflict of interest.

Publisher's note

References

Abdullatif, F., and Wang, D. (2022). "Acceleration of source convergence in Monte Carlo criticality calculation with cmfd schemes," in International conference on physics of reactors 2022 (PHYSOR 2022), Pittsburgh, PA, 3479–3488.

Chan, Y., and Xiao, S. (2019a). Convergence study of cmfd and lpcmfd acceleration schemes for k-eigenvalue neutron transport problems in 2-d cartesian geometry with Fourier analysis. *Ann. Nucl. Energy* 133, 327–337. doi:10.1016/j.anucene.2019.05.035

Chan, Y., and Xiao, S. (2020b). A linear prolongating coarse mesh finite difference acceleration of discrete ordinate neutron transport calculation based on discontinuous galerkin finite element method. *Nucl. Sci. Eng.* 194, 554–571. doi:10.1080/00295639.2020.1752045

Chan, Y., and Xiao, S. (2019b). Convergence study of variants of cmfd acceleration schemes for fixed source neutron transport problems in 2d cartesian geometry with Fourier analysis. *Ann. Nucl. Energy* 134, 273–283. doi:10.1016/j.anucene.2019.06.021

Chan, Y., and Xiao, S. (2020a). Implementation and performance study of lpCMFD acceleration method for multi-energy group k-eigenvalue neutron transport problem in hexagonal geometry. *Ann. Nucl. Energy* 139, 107220. doi:10.1016/j.anucene.2019.107220

Chan, Y., and Xiao, S. (2021). Implementation and performance study of the lp-cmfd acceleration scheme for Monte Carlo method based k-eigenvalue neutron transport calculation in 1d geometry. *Ann. Nucl. Energy* 163, 108562. doi:10.1016/j.anucene.2021.108562

Chan, Y., and Xiao, S. (2019c). Theoretical convergence study of lpcmfd for fixed source neutron transport problems in 2d cartesian geometry. *Trans. Am. Nucl. Soc.* 121, 788–791.

Hunter, J. L. (2014). *Improvements and applications of the uniform fission site method in Monte Carlo*. Massachusetts: Massachusetts Institute of Technology.

Jo, Y. G., and Cho, N. Z. (2018a). Acceleration and real variance reduction in continuous-energy Monte Carlo whole-core calculation via p-cmfd feedback. *Nucl. Sci. Eng.* 189, 26–40. doi:10.1080/00295639.2017.1373517

Jo, Y. G., and Cho, N. Z. (2018b). Inline critical boron concentration search with p-cmfd feedback in whole-core continuous-energy Monte Carlo simulation. *Ann. Nucl. Energy* 120, 402–409. doi:10.1016/j.anucene.2018.05.050

Lee, M. J., Joo, H. G., Lee, D., and Smith, K. (2014). Coarse mesh finite difference formulationfor accelerated Monte Carlo eigenvalue calculation. *Ann. Nucl. Energy* 65, 101–113. doi:10.1016/j.anucene.2013.10.025

Lee, M. J., Joo, H. G., Lee, D., and Smith, K. (2010). Investigation of cmfd accelerated Monte Carlo eigenvalue calculation with simplified low dimensional multigroup formulation. *Int. Conf. Phys. React. PHYSOR* 1, 578–590.

Than, Y. R., and Xiao, S. (2022). lp–cmfd acceleration schemes in 2d Monte Carlo transport. *Trans. Am. Nucl. Soc.* 126, 268–271.

Ueki, T., and Brown, F. B. (2005). Stationarity modeling and informatics-based diagnostics in Monte Carlo criticality calculations. *Nucl. Sci. Eng.* 149, 38–50. doi:10.13182/nse04-15

Ueki, T. (2009). Step-refined on-the-fly convergence diagnostics of Monte Carlo fission source distribution. *Nucl. Sci. Eng.* 163, 99–117. doi:10.13182/nse163-99

Wang, D., and Xiao, S. (2018). A linear prolongation approach to stabilizing cmfd. *Nucl. Sci. Eng.* 190, 45–55. doi:10.1080/00295639.2017.1417347

Yun, S., and Cho, N. Z. (2010). Acceleration of source convergence in Monte Carlo k-eigenvalue problems via anchoring with a p-cmfd deterministic method. *Ann. Nucl. Energy* 37, 1649–1658. doi:10.1016/j.anucene.2010.07.018

frontiers | Frontiers in Energy Research

TYPE Original Research
PUBLISHED 08 November 2022
DOI 10.3389/fenrg.2022.1002077

OPEN ACCESS

EDITED BY
Jingang Liang,
Tsinghua University, China

REVIEWED BY
Tengfei Zhang,
Shanghai Jiao Tong University, China
Qian Zhang,
Harbin Engineering University, China

*CORRESPONDENCE
Lou Lei,
371682011@qq.com
Wang Lianjie,
mcd2264@126.com

SPECIALTY SECTION
This article was submitted to Nuclear Energy,
a section of the journal
Frontiers in Energy Research

RECEIVED 24 July 2022
ACCEPTED 24 October 2022
PUBLISHED 08 November 2022

CITATION
Lei L, Lianjie W, Bingyan Z, Chen Z, Bin Z, Mingyu Y, Ce Z, Hongzhi X, Yun C, Xingbo W, Zifan Z, Nan Z and Jiayi L (2022), Research and analysis of the effect between the power level and economy on the lead-based modular nuclear power reactor.
Front. Energy Res. 10:1002077.
doi: 10.3389/fenrg.2022.1002077

Research and analysis of the effect between the power level and economy on the lead-based modular nuclear power reactor

Lou Lei*, Wang Lianjie*, Zhou Bingyan, Zhao Chen, Zhang Bin, Yan Mingyu, Zhang Ce, Xiang Hongzhi, Cai Yun, Wang Xingbo, Zhao Zifan, Zhou Nan and Liu Jiayi

Science and Technology on Reactor System Design Technology Laboratory, Nuclear Power Institute of China, Chengdu, China

The fast reactor is gradually being paid attention to in nuclear power due to a better breeding effect, and its economy is also directly followed. Due to the restriction of the core power density, the core power level is directly related to the volume of the core active area. When the power level and the volume of the core gradually increase, the mass of uranium and 235U in the core at the beginning of life will gradually increase on the basis of a critical uranium inventory. At the same time, due to the gradual increase in the breeding effect, the utilization rate of uranium resources at the end of life will gradually increase. Due to the characteristics of the large critical uranium mass and high breeding effect, the mass of uranium and 235U in the low power level core at the beginning of life cannot be further reduced because of the critical uranium inventory. The lifetime of the high power level core should be extended to use the wealthy reactivity of the core because of the improvement in the breeding effect. However, due to the requirements of the nuclear power refuel time and the limitation to fuel consumption, the breeding effect brought by the improvement in the core power level and the size of the active zone may be less effective. In this article, the power level and economy of lead-based modular nuclear power are analyzed, and the economy of different power level fast reactors with 2,000 EFPD lifetime such as 100 MWt, 300 MWt, 500 MWt, 700 MWt, and 1000 MWt thermal power is designed and analyzed. By analyzing the invention of uranium and 235U and the fuel utilization of different core schemes, the best economic analysis of the single reactor power of the current lead-based modular reactor is proposed and the foundation of the lead-based modular nuclear power is provided.

KEYWORDS

lead-based modular reactor, power level, economy, proliferation effect, fuel utilization

Introduction

As one of the fourth-generation nuclear energy system reactor types, the lead-based fast reactor is economical, secure, and sustainable. A lead-based coolant not only has the characteristics of high thermal conductivity in metals and the boiling point being higher than 1,000° under normal pressure but is also more chemically inert than some other lively metals such as sodium, and the lead-based coolant would hardly incur chemical reactions with water and air. The lead-based coolant can not only improve the inherent safety of the reactor core but can also use two circuit designs of the reactor system, so the lead coolant and water directly use the steam generator to use heat, which greatly improves the economy of the reactor (Zrodnikov et al., 2001; Zrodnikov et al., 2008).

The neutron spectrum of a fast reactor is harder than that of the thermal reactor. Fissile materials such as 235U and 239Pu have large fission cross sections in the thermal neutron zone but small fission cross sections in the fast neutron zone; however, the fertile material such as 238U is different; it has large capture cross sections in the fast neutron zone but relatively small capture cross sections in the thermal neutron zone, and the 238U material will capture fast neutrons and become 239Pu, which is the fissile material. The fast neutron spectrum can use 238U, so it can improve the utilization rate of uranium resources. At the same time, because the thermal neutron fraction of a fast reactor is much lower than that of a thermal reactor, so the critical uranium inventory of the fast reactor is far greater than that of the thermal reactor. Also, the analysis of the economy of the core must not only consider the utilization rate of uranium resources but also the inventory amount of uranium and 235U at the beginning of life.

At present, the fuel types of a lead-based fast reactor are commonly UO_2 and U-10Zr. UO_2 has rich experience and radiation data in PWR, and U-10Zr has the advantages of having more uranium amount in the unit volume. At the same time, the neutron spectrum of the core loaded with U-10Zr is relatively harder than that of UO_2, so the fuel breeding performance is better. Therefore, this article will also analyze the characteristics of the cores loaded with UO_2 and U-10Zr fuels at different power levels.

There are many factors that need to be considered in the installation capacity of the core in the nuclear power plant. Among them, from reactor's physical perspective, the economy about a single core power level should be considered and then, the conceptual design of a modular nuclear power plant is adopted according to multiple cores so as to fully improve its economy.

Based on the characteristics and needs of a lead-based modular nuclear power plant, this article conducts analysis and research on the core power levels and economy. It mainly analyzes the initial uranium inventory of different power levels and fuel utilization rate at the end of life. The characteristics of different power levels of the lead-based fast reactor core design are given, and recommended lead-based modular nuclear power levels are given.

Calculation program

Analyses of fast reactors can be accomplished by either deterministic methods or stochastic methods. Deterministic codes that are established on the neutron transport theory can provide both accurate and efficient solutions to fast reactor problems (Zhang et al., 2022). In addition, the Monte Carlo method is flexible in geometrical modeling and is suited for high-fidelity and accurate computations. The calculation of this article is completed by the reactor Monte Carlo code (RMC) (Wang et al., 2013) program, which was independently developed by the Department of Engineering Physics of Tsinghua University and is a three-dimensional transportation Monte Carlo program used for reactor core calculation analysis. The RMC program is developed in accordance with the basic needs of the reactor calculation analysis, such as complicated geometric structures and a complicated neutron spectrum in combination with the design of the new concept reactor system. Using continuous energy points to describe the complex energy spectrum and materials, it can be calculated based on the actual problems of a multiplier factor and fuel burnup problems.

Research route

In order to analyze the economics of lead-based modular nuclear power levels from the reactor physical perspective, this article will choose a fixed fuel assembly structure type, and five different power levels core schemes, such as 100 MWt, 300 MWt, 500 MWt, 700 MWt,, and 1000 MWt, are designed under the nearly same power density of the core and the lifetime of 2,000 equivalent full power day (EFPD) (Zrodnikov et al., 2009), as shown in Table 1. The lifetime of 2000EFPD refers to the Russian SVBR core (Zrodnikov et al., 2009) and the SLBR-50 core (Zhao et al., 2021) from the Nuclear Power Institute of China (NPIC). The core power is to analyze the economics of the core at different power levels. Therefore, several typical power points from 100 MWt to 1,000 MWt were selected for studies. The reason for choosing UO_2 in this paper is its rich operating experience and irradiation data, and the reason for choosing U-10Zr is it has a higher mass percentage of uranium; therefore, it has a higher fuel breeding performance. UN and UC are also compounds of uranium. Their characteristics when used as fuel are similar to UO_2 fuel. However, these two fuel types are less used in engineering than UO_2. Therefore, this paper only selects UO_2 as the representative of ceramic fuel for analysis. The amounts of 235U and uranium of cores with different power levels at the beginning and end of life will be given and analyzed.

TABLE 1 Main design parameters of 10 schemes.

Core scheme	Core power/MWt	Core life/EFPD	Fuel type
Scheme 1	100	≥2,000	UO_2
Scheme 2	100	≥2,000	U-10Zr
Scheme 3	300	≥2,000	UO_2
Scheme 4	300	≥2,000	U-10Zr
Scheme 5	500	≥2,000	UO_2
Scheme 6	500	≥2,000	U-10Zr
Scheme 7	700	≥2,000	UO_2
Scheme 8	700	≥2,000	U-10Zr
Scheme 9	1,000	≥2,000	UO_2
Scheme 10	1,000	≥2,000	U-10Zr

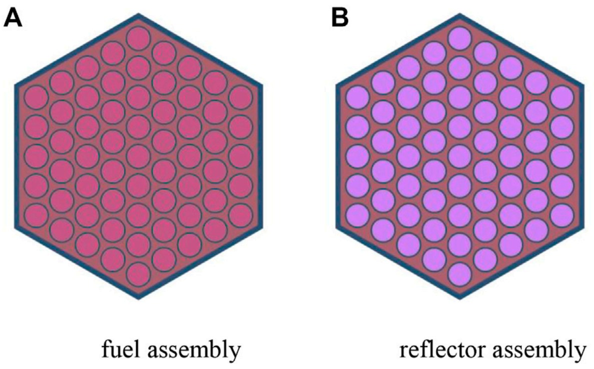

FIGURE 1
Schematic figure of assemblies: **(A)** fuel assembly and **(B)** reflector assembly.

Assembly design

The assembly type in the core is referred to as the assembly design of the lead-based research reactor SLBR-50 (Zhao et al., 2021) (small lead-based reactor—50 MWt) of the Nuclear Power Institute of China (NPIC). The assembly diagram is shown in Figure 1, and the main design parameters of the assembly are shown in Table 2.

Core design and calculation analysis

According to the research route and assembly design results, the assembly type selected previously is used for the core arrangement design with different power levels. In order to ensure that the core has a corresponding reactivity control ability, the corresponding control assembly positions are reserved during the core arrangement. In order to simplify the core design, the control rod assembly design is not performed and the core burn-up calculation is performed with all rods out of the core, and at the end of the life, k_{eff} of the core is greater than 1.005, which is the standard of judgment during core life. The arrangement diagrams of the 10 schemes are shown in Figures 2–6, and the design parameters of all the schemes are shown in Table 3. Here, the irradiation effect of the U-10Zr alloy is considered in its fuel density. The theoretical density of 75% is used in this paper, and the feasibility of metal fuel irradiation swelling is fully considered. Also, there are two main reasons why the height of the active section of the core is 1 m. One is to better compare the core performance under different core powers and

TABLE 2 Main design parameters of the assembly.

Parameter	Value	Parameter	Value
Fuel pin diameter/mm	8.0	Assembly center distance/mm	93.5
Air gap thickness/mm	0.1	Assembly box inner distance/mm	88.0
Clad thickness/mm	0.5	Assembly box outer distance/mm	93.0
Clad outer diameter/mm	9.2	Assembly box thickness/mm	2.5
Fuel rod center distance/mm	10.9	Assembly fuel rod number	61
Fuel effective temperature/K	900	Clad material	SS
Coolant temperature/K	700	Coolant material	Lead-based

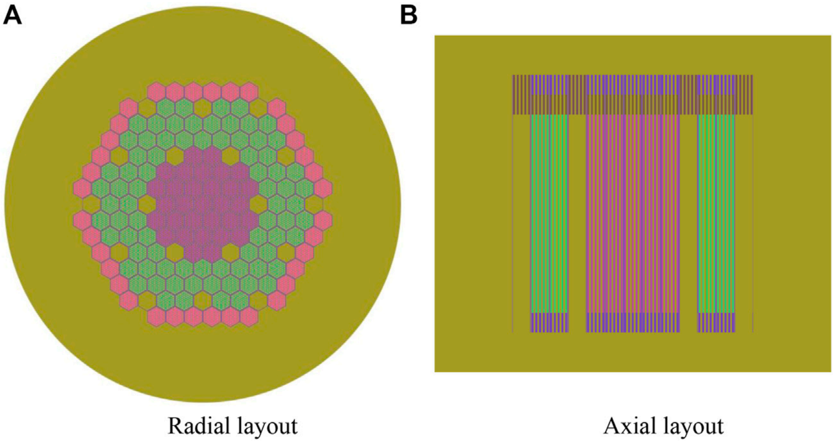

FIGURE 2
100-MWt core arrangement diagrams of UO_2 and U-10Zr: **(A)** radial layout and **(B)** axial layout.

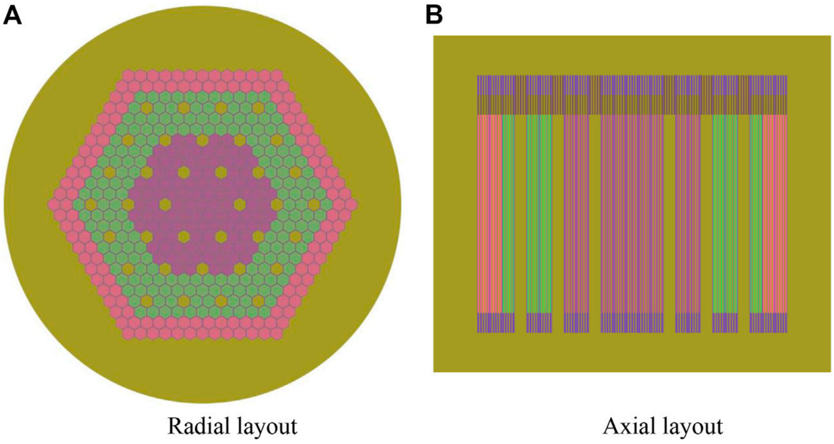

FIGURE 3
300-MWt core arrangement diagrams of UO_2 and U-10Zr: **(A)** radial layout and **(B)** axial layout.

core sizes, and the other is to obtain a relatively short and fat core design. The short and fat core design is beneficial to obtain a negative core feedback coefficient, so the core height should not be too high. To sum up, the core height is set to 1 m in this paper.

The amount of uranium and 235U of each core scheme changing along the core powers is shown in Figure 7. It can be seen that the amount of uranium and 235U have linear growth characteristics along the core powers. This is because each core scheme maintains a short and fat core design, and the overall leakage rates of the cores are not much different. The critical uranium inventory of each core scheme is basically the same. In order to maintain the energy output of a given power level and core life, they all need to increase the corresponding uranium and 235U amounts on the basis of critical uranium inventory. So the amount of uranium and 235U of all the core schemes with different power levels but the same fuel assembly structure presents a linear growth trend.

Fuel utilization rates of all the schemes are shown in Table 3, from which it can be seen that, with the increase in the power level of the schemes, the fuel utilization rate of the schemes with the same fuel type is linearly increased. This is because the fuel utilization rate is similar to the ratio of fuel consumption and the sum of fuel consumption and critical fuel mass, and with the increase in the power level of the core, the amount of fuel

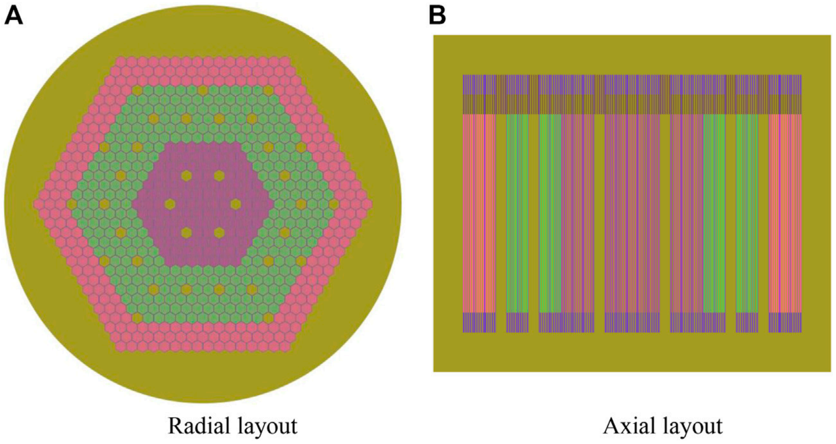

FIGURE 4
500-MWt core arrangement diagrams of UO_2 and U-10Zr: **(A)** radial layout and **(B)** axial layout.

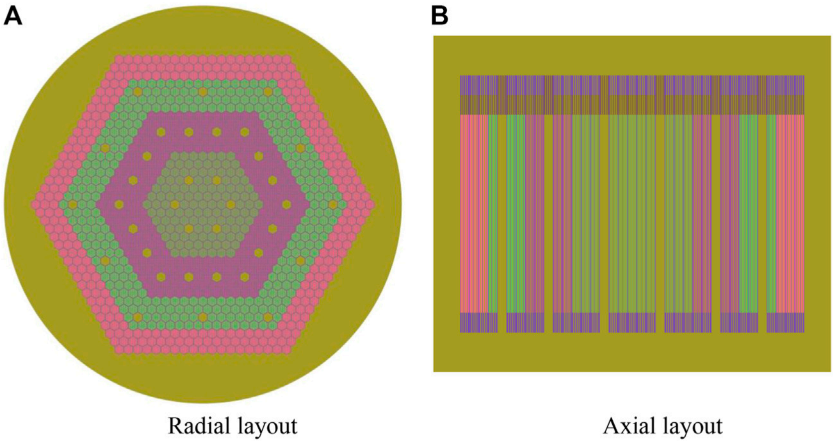

FIGURE 5
700-MWt core arrangement diagrams of UO_2 and U-10Zr: **(A)** radial layout and **(B)** axial layout.

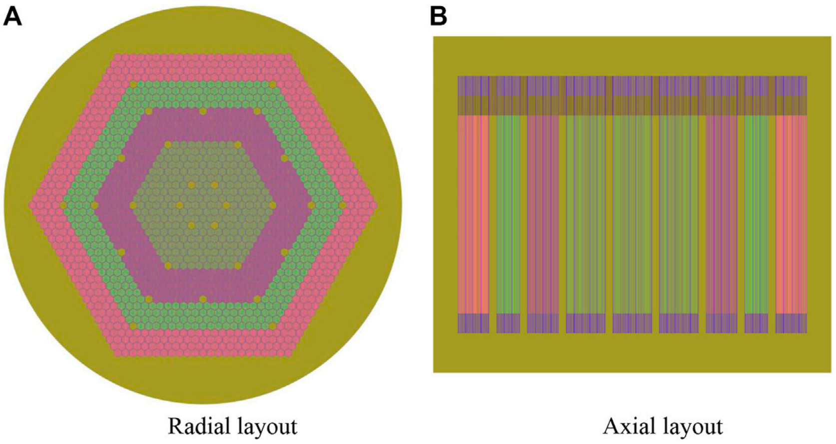

FIGURE 6
1000-MWt core arrangement diagrams of UO_2 and U-10Zr: **(A)** radial layout and **(B)** axial layout.

TABLE 3 Design parameters of all the schemes.

Core scheme	Scheme 1	Scheme 2	Scheme 3	Scheme 4	Scheme 5	Scheme 6	Scheme 7	Scheme 8	Scheme 9	Scheme 10
Core thermal power/MWt	100	100	300	300	500	500	700	700	1,000	1,000
Core life/EFPD	2,000	2,000	2,000	2,000	2,000	2,000	2,000	2,000	2,000	2,000
Fuel pin density/(g/cm^3)	10.38	11.94	10.38	11.94	10.38	11.94	10.38	11.94	10.38	11.94
Fuel type	UO_2	U-10Zr	UO_2	U-10Zr	UO_2	U-10Zr	UO_2	U-10Zr	UO_2	U-10Zr
Mass of 235U at BOL/kg	873	882	2,151	2025	3,276	2,930	4,459	4,143	6,320	5,952
Mass of 238U at BOL/kg	3,194	3,895	9,993	12,242	15,964	19,673	23,335	28,510	35,273	42,912
Mass of 235U at EOL/kg	646	668	1,498	1,425	2,211	1970	2,969	2,782	4,199	3,955
Mass of 238U at EOL/kg	3,067	3,762	9,514	11,714	15,125	18,711	22,117	27,008	33,473	40,605
Mass of 239Pu at EOL/kg	92	94	346	372	596	667	877	964	1,303	1,441
Utilization rate of 235U/%	25.94	24.32	30.36	29.64	32.49	32.77	33.42	32.85	33.56	33.55
Utilization rate of 238U/%	3.96	3.42	4.79	4.32	5.26	4.89	5.28	5.27	5.30	5.38
Fuel enrichment/%	22.50	19.50	19.75	15.00	19.75	14.00	19.75	14.00	18.00	13.50
	21.50	18.50	17.50	14.00	16.00	12.50	16.00	13.00	16.00	12.50
	20.50	17.50	15.50	13.50	14.00	12.00	14.50	12.00	14.00	11.50
	—	—	—	—	—	—	10.00	10.00	10.00	10.00
Number of fuel assemblies	145	344	433	433	686	686	991	991	1,483	1,483
Number of control assemblies	18	18	36	36	35	35	36	36	30	30
Active core height/mm	1,000	1,000	1,000	1,000	1,000	1,000	1,000	1,000	1,000	1,000
Outer reflector diameter/mm	≈1,300	≈1,300	≈2,200	≈2,200	≈2,700	≈2,700	≈3,300	≈3,300	≈3,900	≈3,900
Average fuel enrichment/%	18.92	16.62	15.61	12.77	15.00	11.67	14.14	11.42	13.39	10.96
Core line power density/(W/cm)	11.31	11.31	11.36	11.36	11.95	11.95	11.58	11.58	11.05	11.05
Core body power density/(W/cm^3)	91.09	91.09	91.51	91.51	96.27	96.27	93.30	93.30	89.06	89.06
k_{eff} at BOL	1.084353	1.059786	1.065428	1.027194	1.067185	1.009590	1.059138	1.012693	1.062321	1.012008
k_{eff} at EOL	1.008247	1.008881	1.006127	1.005588	1.008295	1.009543	1.005208	1.017490	1.008250	1.023341

consumption increased during the core life and the critical fuel mass has basically maintained, so the fuel utilization rate is increasing linearly.

Core k_{eff} curves of all the schemes with UO_2 and U-10Zr fuel along with the core life are shown in Figures 8, 9. The k_{eff} curves of all the UO_2 schemes have no big difference except for that of the 100 MWt core. This is because all the schemes adopt a short and fat core design, and the ratio of height and diameter of all the schemes is far less than 1 except that of the 100 MWt core is nearly 1. Although the size of the UO_2 fuel core increases the fuel utilization rate, the breeding performance has not changed much, so the trends of the k_{eff} have basically remained unchanged. The k_{eff} cures of U-10Zr schemes show increasing trend along the increases of the core size, such as the cores with 500 MWt, 700 MWt, and 1000 MWt. In the 500 MWt core, k_{eff} reaches the maximum value at 1,000 EFPD, and then, it gradually decreases along the increasing fuel burn-up, and at the end of life, k_{eff} is basically the same as the beginning of life. In the 700 MWt and 1,000 MWt cores, k_{eff} increases from the beginning of life and does not reach the maximum value at 2,000 EFPD. From the perspective of evaluating the reactivity of the core, it can be seen that the core has not reached the end of life, and it is estimated that it can also operate more than 2,000 EFPD or more, and the life period will reach 4,000 EFPD or longer.

The main reason why the breeding performance of U-10Zr is greater than that of UO_2 is that U-10Zr fuel has a larger proportion of uranium per unit volume than UO_2, and at the same time, there is no oxygen element in metal fuel and the energy spectrum is harder. All these reasons make the breeding performance of U-10Zr fuel stronger.

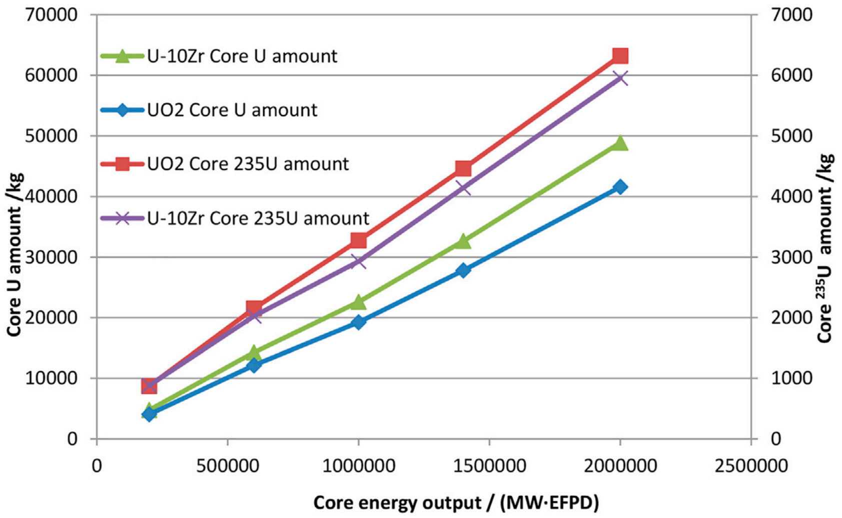

FIGURE 7
Amounts of uranium and 235U of each core scheme changes along the core powers.

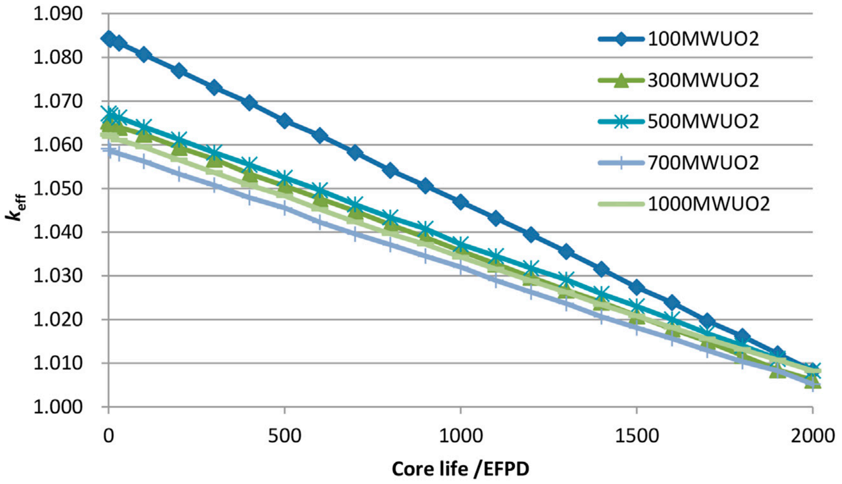

FIGURE 8
Core k_{eff} curves of all the schemes with UO_2 fuel along with core life.

It can be seen by comparing the core schemes with UO_2 and U-10Zr fuels at the same power level that, at low power levels, because the total energy output of the core is relatively small, the size of the core and the amount of uranium are relatively small, which saves uranium resources and more economical.

The breeding performance and the fuel utilization rate of the UO_2 core will gradually enhance with the increase in the core power level and core size, so the high power level core, such as 700 MWt and 1,000 MWt, is more suitable for loading with the UO_2 fuel.

The breeding performance of the U-10Zr core is far higher than that of the UO_2 fuel core with the increase in the core power level and core size. For example, k_{eff} of the 700 MWt core shows the upward trend, and the core life period of 2,000 EFPD is not long enough to release the breeding capacity of the core. Therefore, it is necessary to appropriately reduce the power level and size of the core to make the breeding effect of the core match the core life period. So uranium fuel is suitable for the core of the 500 MWt class power level.

The utilization rates of 235U and 238U along with the core power level are shown in Figures 10, 11. It can be seen that the core fuel utilization rate gradually increases with the increase in

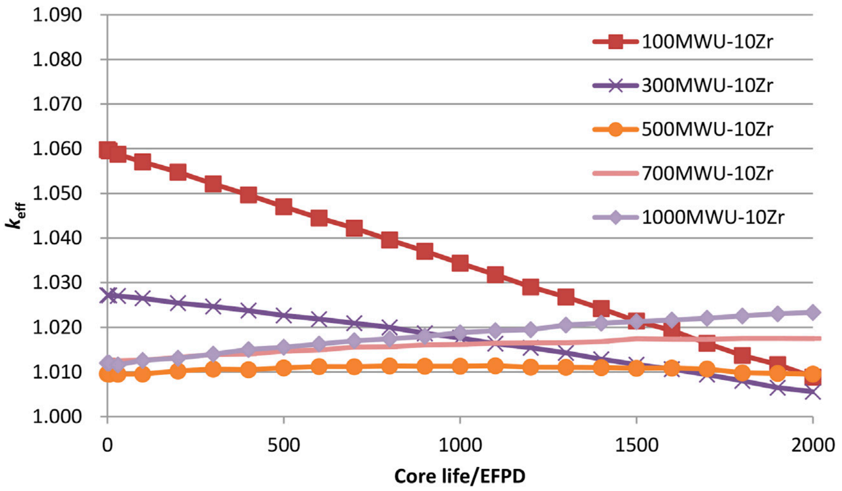

FIGURE 9
Core k_{eff} curves of all the schemes with U-10Zr fuel along with core life.

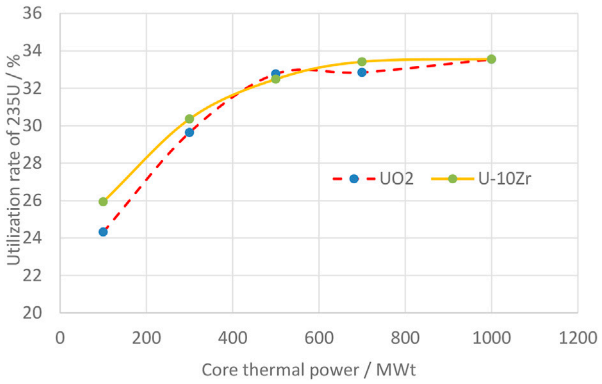

FIGURE 10
Utilization rate of 235U along with the core power level.

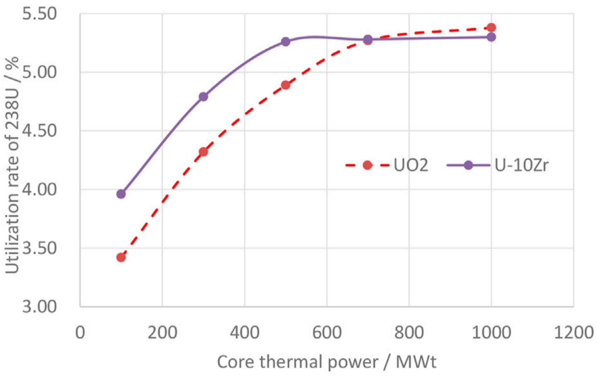

FIGURE 11
Utilization rate of 238U along with the core power level.

core power, but with the increase in the core power level to a certain extent and the core size being increased to a certain degree, the increase rate of the core fuel utilization rate will gradually become gentle. At the same time, the fuel utilization rate of the UO_2 core is generally slightly lower than that of the U-10Zr fuel core.

It should be noted that the main reason for pursuing an approximate level of the reactivity curve of the modular core is to reduce the difficulty of reactivity control. In a fast reactor, the reactivity value of a single control rod is generally small in order to avoid a prompt supercritical accident, and the low residual reactivity of the core can be used to reduce the number of control rods in the core. On the other hand, the flatter reactivity curve of the core means that the reactivity loss during the core burn-up matches with the reactivity increase in the breeding so that the breeding performance of the core can be more fully utilized.

Conclusion

This article is based on the same fuel assembly structure type to design core schemes with different power levels and different fuel types and analyzes the amount of uranium and 235U of each core scheme and the fuel utilization rate at the end of life. The following conclusion can be obtained:

(1) In the case of maintaining the leakage and life of the core, the amount of uranium linearly increases with the power level of the core, and the fuel utilization rate increases with the increase in the power level and size of the core.
(2) The UO_2 fuel type is more suitable for the core arrangement of the low power level such as 100 MWt and high power level such as 1000 MWt. As in the low power level core, the amount of uranium with UO_2 fuel is less, and in the high power level core, the core breeding performance matches the core energy output, which is more suitable for the core reactivity control.
(3) The U-10Zr fuel type is more suitable for the core arrangement of the middle power level such as 500 MWt. As in the middle power level core, the core breeding performance nearly matches the core energy output, which can give full play to the breeding performance of U-10Zr fuel.

The aforementioned conclusion is applicable to the power density, life period, and the ratio of grid distance and rod diameter specified in this article. If the aforementioned parameters change, the core power level of different fuel types will be appropriately shifted, but the basic laws will be constant and appropriate.

Data availability statement

The raw data supporting the conclusion of this article will be made available by the authors, without undue reservation.

Author contributions

LL: conceptualization, methodology, and software. WL: conceptualization. ZuB: methodology and conceptualization. ZCh: methodology and conceptualization. ZgB: visualization and investigation. YM: funding acquisition and conceptualization. ZCe: funding acquisition and supervision. XH: funding acquisition and supervision. CY: methodology and visualization. WX: visualization and software. ZZ: funding acquisition and supervision. ZN: funding acquisition and supervision. LJ: funding acquisition and supervision.

Conflict of interest

The authors declare that the research was conducted in the absence of any commercial or financial relationships that could be construed as a potential conflict of interest.

Publisher’s note

References

Wang, K, Li, Z G, She, D, Liang, J., Xu, Q., Qiu, A., et al. (2013). RMC-A Monte Carlo code for reactor physics analysis [C], Joint International Conference on Supercomputing in Nuclear Applications and Monte Carlo. Paris: France.

Zrodnikov, A. V., Toshinskii, G. I., Grigor’ev, O. G., Dragunov, Y. G., Stepanov, V. S., Klimov, N. N., et al. (2001). SVBR-75/100 multipurpose modular low-power fast reactor with lead–bismuth coolant. *At. Energy* 91 (6), 528–533. doi:10.1023/b:aten.0000047677.16291.f2

Zrodnikov, A.V., Toshinsky, G.I., Komlev, O.G., Stepanov, V.S., Klimov, N.N., Kudryavtseva, A.V., et al. (2009, Fuel Cycle of Reactor SVBR-100 [J], Proceedings of GlobalSeptember, May 2009).. Paris, France. 6-11.

Zrodnikov, A.V., Toshinsky, G., Komlev, O., Dragunov, Y., Stepanov, V., Klimov, N., et al. (2008). Innovative nuclear technology based on modular multi-purpose lead–bismuth cooled fast reactors. *Progress in Nuclear Energy* 50, 170–178. doi:10.1016/j.pnucene.2007.10.025

Zhao, C, Lou, L., Peng, X., Zhang, B., and Wang, L. (2021). Application of the Spectral-Shift Effect in the Small Lead-Based Reactor SLBR-50. *Front. Energy Res.* 9, 756106. doi:10.3389/fenrg.2021.756106

Zhang, T, Xiao, W, Han, Y, Sun, Q, and Liu, X (2022). VITAS: A multi-purpose simulation code for the solution of neutron transport problems based on variational nodal methods. *Annals of Nuclear Energy* 178 (2022), 109335. doi:10.1016/j.anucene.2022.109335

frontiers | Frontiers in Energy Research

TYPE Original Research
PUBLISHED 14 November 2022
DOI 10.3389/fenrg.2022.1036142

OPEN ACCESS

EDITED BY
Jingang Liang,
Tsinghua University, China

REVIEWED BY
Zhongchun Li,
Nuclear Power Institute of China (NPIC), China
Yang Liu,
Argonne National Laboratory (DOE), United States
Chen Wang,
University of Illinois at Urbana-Champaign, United States

*CORRESPONDENCE
Sicong Xiao,
snrxs@nus.edu.sg

SPECIALTY SECTION
This article was submitted to Nuclear Energy,
a section of the journal
Frontiers in Energy Research

RECEIVED 04 September 2022
ACCEPTED 26 October 2022
PUBLISHED 14 November 2022

CITATION
Guo Z, Xiao S and Chung KY (2022), Steady-state thermal hydraulic modelling and turbine trip transient simulation of the NuScale integral pressurised water reactor using the ASTEC code.
Front. Energy Res. 10:1036142.
doi: 10.3389/fenrg.2022.1036142

Steady-state thermal hydraulic modelling and turbine trip transient simulation of the NuScale integral pressurised water reactor using the ASTEC code

Zhexi Guo, Sicong Xiao* and Keng Yeow Chung

Singapore Nuclear Research and Safety Initiative, National University of Singapore, Singapore, Singapore

A steady state model of the NuScale reactor has been built using the thermal hydraulic module CESAR of the severe accident code ASTEC. Construction of the model was achieved through iterations based on convergence towards data provided by NuScale pertaining to important operating properties—core temperatures, coolant mass flow rate and secondary steam temperature—at 100% power (160 MW) and also at lower power levels. Good agreement with reference values was achieved to within 3% deviation. With a similar methodology, the previous model was adjusted to give a second steady state model meant to provide conservative initial conditions from which a turbine trip transient simulation would be performed. Sound agreement with literature was achieved, with maximum deviations of less than 1.8% for monitored parameters. Lastly, a turbine trip transient was simulated and compared to reference data from analyses performed with NRELAP5 and RELAP5/SCDAPSIM. The most important system behaviors and event timings are well captured and reproduced, with discrepancies arising from inevitable estimates made due to lack of information.

KEYWORDS

ASTEC, NuScale, SMR, system code, thermal hydraulics, natural circulation

1 Introduction

Classification of small modular reactors (SMRs) often includes reactors with a power rating within 10–300 MWe, a range sufficient for practical applications and adequately low to reap the advantages of convenient production and implementation. The modular design means the nuclear steam supply system could be assembled from smaller components possibly of standardized designs manufactured in fixed locations before being transported to the desired site of construction. In contrast, the equivalent process for conventional large reactors is often performed on-site, leading to larger upfront costs and longer deployment periods.

One class of SMRs being developed comprises pressurized water reactors (PWRs), essentially scaled-down versions of conventional PWRs, that are able to utilize existing knowledge of such systems and phenomena concerning two-phase water flow. A particular design of such SMRs known as integral PWRs (iPWRs) has garnered much interest for the fact that the steam generators (SGs) fit into the reactor pressure vessel (RPV) and remove heat from the primary coolant without need for U-tubes external to the overall cylindrical RPV geometry like in traditional PWRs, thereby reducing the dimensions of the system and contribute to the compactness of the design. Another prominent characteristic is the use of natural circulation *versus* forced convection to drive primary coolant flow. Natural circulation is a well-recognized physical process with regards to reactor passive safety which has become part of the design philosophy of newer systems. A comprehensive summary of the major ongoing pressurized water SMR projects in the world is provided in various literature (IAEA, 2020; Ingersoll and Carelli, 2021).

The subject of study in this work is the NuScale iPWR that produces 160 MW of thermal power and 50 MW electrical power (thermal efficiency ~31%). Reactor dimensions are small since all main components are housed in one RPV. Helical SG tubes are "integrated" into the RPV of the primary circuit, coiling around the riser and removing heat from primary coolant within the downcomer region. More information is presented in the cited certification application documents published by NuScale Power LLC. Due to the integral design, possibility of large-break loss-of-coolant accidents (LOCAs) is effectively eliminated, leaving small-break LOCAs to be adequately dealt with by passive safety systems. Core damage frequency is deemed to be lower than existing light water reactors (LWRs) (NuScale Power LLC 2020a).

Passive safety is a prominent feature highlighted by the manufacturer. In accordance with regulations by the Nuclear Regulatory Commission (NRC), the NuScale design has been demonstrated to be capable of performing safety-related functions without relying on AC power for 72 h after the initiating event, of which a station blackout (SBO) is a typical example scenario (NuScale Power LLC 2020d). Each NuScale power module is placed in a large water pool that serves as the ultimate heat sink (UHS) in design basis accidents (DBAs) where a complete loss of AC power occurs. Heat is extracted from the core by the SG secondary coolant as usual, flowing through the valve-actuated decay heat removal system (DHRS) *via* natural circulation, and finally exchanging heat with the UHS through condenser tubes. Existence of the large UHS water inventory is key to ensuring integrity of the core by continuous cooling through boil-off for more than 30 days without operator action, electric power or makeup water (NuScale Power LLC 2020e).

With a vast amount of information available on public domain, NuScale serves as a suitable subject of study and benchmark of different codes. Numerous studies have been performed, ranging from overall steady-state and transient characteristics using system codes (Yan et al., 2016; Skolik et al., 2021) to specific phenomena related to natural circulation, helical SG coils, boiling instabilities etc. with CFD methods (Che et al., 2020), and combinations of these (Hoffer et al., 2011; Kim et al., 2020).

CESAR has been used extensively for numerous PWRs such as the French PWRs (Foucher et al., 2014), German KONVOI (Gómez-García-Toraño et al., 2017), and for validation of specific CESAR models (Gómez-García-Toraño et al., 2018; Gómez-García-Toraño and Laborde, 2019), but full ASTEC models of iPWRs are scarce. One such model had been validated based on the IRIS reactor (Di Giuli 2014; Di Giuli et al., 2015) but only the two-phase five-equation rather than six-equation model had been applied. Compared to RELAP5 used by multiple other works (Ricotti et al., 2002; Freitag 2018; Johnson 2021; Skolik 2021), the application of the relatively new ASTEC code in the modelling of natural circulation in full systems, in particular thermal hydraulics (TH) of primary coolant, has not yet been examined extensively. The aim of this work is to conduct a code-to-code comparison with RELAP5 and NRELAP5 (a RELAP5-based code developed by NuScale) in order to have a preliminary assessment of the ASTEC model from a user's point of view. This initial step lays the foundation for subsequent construction of the full ASTEC NuScale model.

This paper is structured as follows. Section 2 introduces the basic features of the ASTEC code and of the numerical model of CESAR most relevant to this work, and subsequently how these tools are used to build the steady-state and turbine trip transient models. Section 3 lays out the parameters to yield the optimized steady-state model and how it was validated. Finally, the main results of the turbine trip transient simulation are discussed in Section 4, ultimately showing that the ASTEC-CESAR model is indeed comparable to reference data obtained with other system codes.

2 Methodology

2.1 The ASTEC code and CESAR module

The most widely used system codes today are RELAP5 (RELAP5 Development Team 1995), TRACE (NRC, U.S., 2010), ATHLET (Burwell et al., 1989) and CATHARE (Bestion 1990), all of which were originally developed specifically for LWRs to simulate and predict accident phenomena therein. Concise descriptions and summaries of these codes are available in literature (Petruzzi et al., 2008; Bestion 1990; Bestion 2008; Bestion 2017). 1-D system codes have the advantage of being computationally fast in simulating large-scale processes up to the entire plant but naturally lose intricate 3-D effects that may be crucial. These issues are inherent in severe accident (SA) codes such as MELCOR and ASTEC (Accident Source Term Evaluation Code) as well, the latter of which is used in the present work.

SA codes are made up of several modules (or "packages" in MELCOR terminology), each responsible for simulating a particular phase or group of coupled physical processes within the long and complex sequence of events from normal operation to core-melt and subsequent release of radionuclides. Development of ASTEC was originally carried out by Institut de Radioprotection et de Sûreté Nucléaire (IRSN, France) and Gesellschaft für Anlagen und Reaktorsicherheit mbH (GRS, Germany). The latest version is V2.2 released in 2021, with a clear overview based on V2.1 available in public literature (Chatelard et al., 2016).

2.2 Basic equations in CESAR

The ASTEC-CESAR module is responsible for simulation of two-phase TH in PWR coolant systems, very much like the above system codes. Its TH model is governed by the well-known conservation equations of mass, momentum, and energy for two-phase flow. Spatial discretization is done with the finite volume method using a staggered grid approach, where scalar variables are defined at the center of each control volume while vector quantities are determined at *volume* interfaces or *junctions*, using the donor cell (or upwind) principle to calculate advective terms. Time discretization is carried out with the first-order backward difference scheme. This implicit time discretization strategy enhances the numerical stability and yields a system that is unconditionally stable for any time step Δt. Solution of equations is performed with the Newton-Raphson method (Zambaux 2021). This work uses the six-equation approach for all cells in preparation for more complex transient simulations. The basic conservation equations for each phase k (liquid, gas) are described below.

The mass conservation equation reads

$$\frac{\partial}{\partial t}(\alpha_k\rho_k) + \frac{\partial}{\partial z}(\alpha_k\rho_k\vec{u}_k) = \Gamma_k \tag{1}$$

where α_k, ρ_k, $\vec{u}_k$ and Γ_k are phasic void fraction, density, velocity, and mass transfer rate respectively.

The momentum conservation equation reads

$$\frac{\partial}{\partial t}(\alpha_k\rho_k\vec{u}_k) + \frac{\partial}{\partial z}(\alpha_k\rho_k\vec{u}_k\vec{u}_k) = -\frac{\partial}{\partial z}(\alpha_k p_k) + \alpha_k\rho_k g + f_{wall,k} + M_k \tag{2}$$

where p_k, g, $f_{wall,k}$ and M_k are respectively pressure, gravitational acceleration, wall forces and additional terms that include contributions from interfacial forces, pumps and virtual mass. The wall forces comprise the commonly known friction and form loss terms as follows:

$$f_{wall,k} = \frac{1}{2}\left(\frac{L_J P_J}{S_J}\zeta_{fric,k} + \alpha_k K_{\mathrm{form}}\right)\rho_k\vec{u}_k|\vec{u}_k| \tag{3}$$

where L_J, P_J, S_J, $\zeta_{fric,k}$ and K_{form} (hereafter simplified as K) are junction length, wetted perimeter, junction flow area, friction loss coefficient and form loss coefficient respectively. The K coefficients are often tuned to converge towards the desired operating conditions, a long iteration process that is necessary to capture the complex 3-D geometric effects in this 1-D averaged approach. This problem is aggravated by the lack of design details in this case.

The energy conservation equation reads

$$\frac{\partial}{\partial t}(\alpha_k\rho_k h_k) + \frac{\partial}{\partial z}(\alpha_k\rho_k h_k\vec{u}_k) = \frac{\partial}{\partial t}(\alpha_k p_k) + \phi_{wall,k} + \phi_{int,k} + \Gamma_k h_k \tag{4}$$

where h_k, $\phi_{wall,k}$ and $\phi_{int,k}$ are enthalpy, wall heat transfer and interfacial heat transfer respectively.

Heat exchange is described by solid *wall* components comprising two half-walls, each for which the temperature at the center is calculated. The temperature gradient between the two temperature nodes leads to a diffusive flux through the surface common to both half-walls. The other surface of each half-wall has a flux contribution that could originate from an external source φ_{ext} such as fuel, which implies a defined boundary condition, or fluid $\varphi_{\mathrm{wall\text{-}fluid}}$ such as the SG primary and secondary sides. The energy balance equation is then

$$\frac{1}{2}(V\rho c_{\mathrm{p}})_{\mathrm{wall}}\frac{\partial T_i}{\partial t} = -A_{\mathrm{wall}}\lambda_{\mathrm{wall}}\left.\frac{\partial T}{\partial x}\right|_i - \varphi_{\mathrm{wall-fluid},i} + \varphi_{\mathrm{ext},i} \tag{5}$$

where V, ρ, c_{p}, A and λ are respectively the volume, density, specific heat capacity, surface area and thermal conductivity. The temperature gradient is assumed linear from the external surface of half-wall i to that of half-wall j as follows

$$\left.\frac{\partial T}{\partial x}\right|_i = \frac{T_i - T_j}{\text{wall thickness}} \tag{6}$$

and x has been used in the equation to emphasize that it is perpendicular to flow in the z-axis. The wall-fluid flux is derived from complex models correlating heat transfer coefficients with void fraction, phase thermal conductivities, and flow properties characterized by the Reynolds, Grashof, Nusselt and Prandtl numbers. Based on these properties, a heat transfer coefficient is calculated corresponding to one of the four flow types: laminar natural convection, turbulent natural convection, laminar forced convection, and turbulent forced convection. Specific equations are not provided but the reader may refer to a largely representative description provided in the CATHARE models (Bestion 1990).

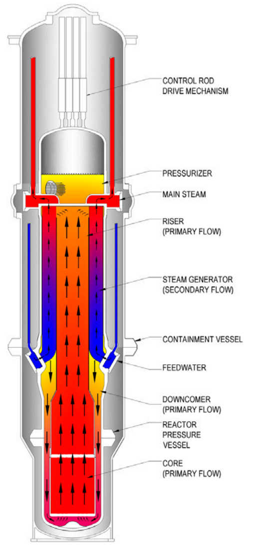

FIGURE 1
Schematic of one NuScale power module (NuScale Power LLC 2020a).

TABLE 1 Main properties of the NuScale reactor at full nominal power (NuScale Power LLC 2020b).

Reactor property		
Core thermal output	160	MWth
Nominal electrical output	50	MWe
No. of fuel assemblies (FAs)	37	
FA configuration	17 × 17	
No. of fuel rods (FRs) per FA	264	
FR pitch	0.0126	m
FA height	2.44	m
No. of spacer grids per FA	5	
Active fuel height	2.00	m
Primary operating pressure	12.8	MPa
Hot leg temperature	583	K
Cold leg temperature	531	K
Primary coolant mass flow rate	587	kg/s
SG type	vertical helical tube	
Secondary inlet temperature	422	K
Secondary outlet temperature	580	K
Secondary outlet pressure	3.45	MPa
Secondary coolant mass flow rate	67.1	kg/s

2.3 NuScale reactor model nodalization

Preservation of coolant fluid dimensions was of priority when nodalizing the system, carried out based on the individual component heights, flow areas and fluid volumes, adhering as closely as possible to reference values (NuScale Power LLC 2020b; Guo et al., 2022). It is important to ensure that component heights are consistent since they significantly influence pressure differences due to gravity and resultant natural circulation. In heated sections such as the core and SG region, fluid volume is crucial as well, since it directly impacts the temperature changes corresponding to total enthalpy transferred.

Figure 1 from NuScale documentation (NuScale Power LLC 2020a) is a schematic of the RPV and flow of coolant under normal operating conditions included in Table 1, while Figure 2 illustrates the CESAR nodalization where the primary circuit follows the flow in Figure 1 and the secondary circuit with the reactor pool for DHRS operation. Natural circulation in the primary loop is initiated by fuel rods generating 160 MW at 100% nominal power along the 2.0-m-tall active core region, represented by red wall components and red single-headed arrows in the figure.

The blue arrows (junctions) show heated coolant rising through the respective volumes to the upper plenum before turning downwards through the SG region and downcomer, and finally re-entering the core after turning through the lower plenum. In normal operation, the primary loop is cooled *via* heat exchange (red double-headed arrows) through the SG wall with the secondary loop, which comprises a pumped feedwater source whose flow rate is a boundary condition to the problem, and superheated steam enters the turbine through the main steam isolation valve (MSIV) where the outlet pressure is another boundary condition. Two actuation valves connect the secondary line to the DHRS, in order to simulate accident scenarios where the system is available to provide passive cooling.

Primary pressure is maintained by the pressurizer, which is modelled by CESAR as a fluid volume of water and steam at saturation with a spray system to remove enthalpy and raise the water level when pressure and void fraction exceed an upper limit, and a heater system to provide enthalpy and lower the water level when pressure and void fraction drop below a lower limit. Reactor safety valves (RSVs) serve as an overpressure protection, like in the NuScale design. For each valve the user defines the maximum flow area, activation pressure and pressure range over which the valve is gradually opened. No flow arrow is included in Figure 2 between the Pressurizer and Upper Plenum Turn volumes because heat exchange is intentionally limited—just as in the actual design where a baffle plate with holes separates the two regions—while allowing pressure changes to be communicated quickly from the pressurizer to the entire system. In CESAR, two form loss coefficients are defined for each junction in both forward and reverse directions. Defining a large value for this junction achieves the intended pressurizer function described above.

2.4 Turbine trip transient model setup

As an initial test among the multiple possible design basis events (DBEs), a turbine trip transient was simulated to assess the accuracy

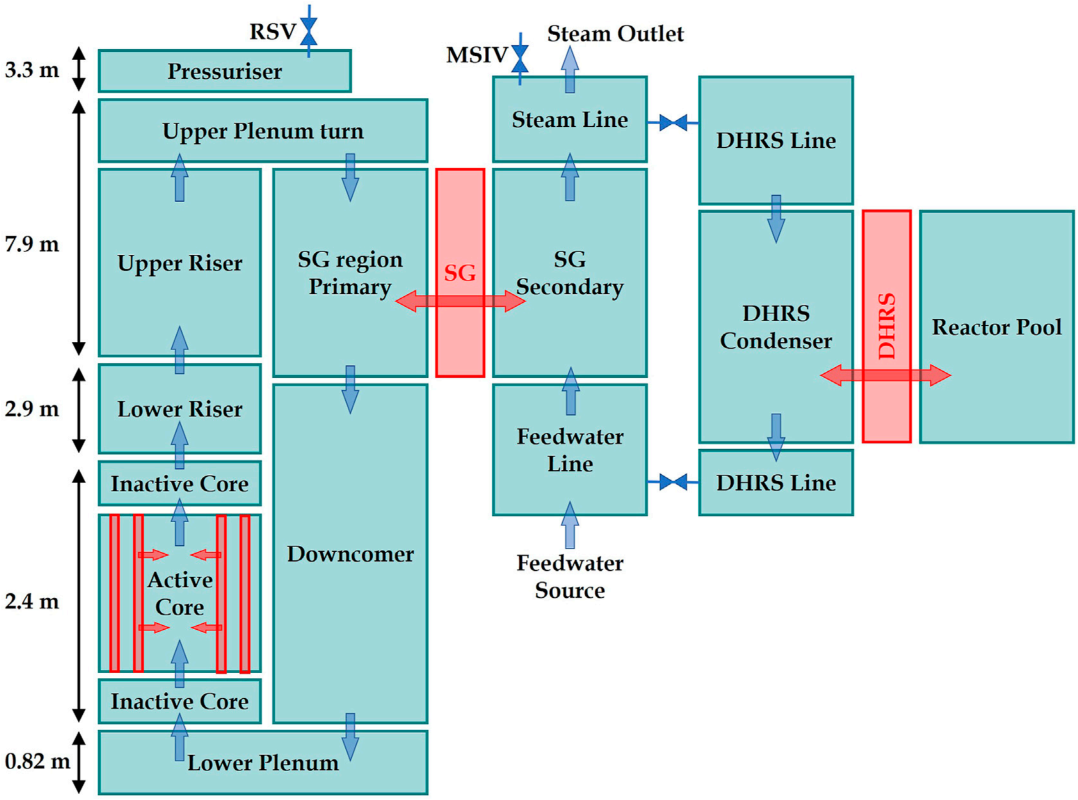

FIGURE 2
CESAR nodalization diagram of the NuScale system. Blue arrows show the expected coolant flow path under normal conditions; red arrows represent heat transfer from the fuel in the active core and heat exchange through the SG and DHRS condenser tubes. Opening the DHRS actuation valves forms a flow circuit cooled by the reactor pool *via* natural circulation.

and performance of the model. This transient was chosen for several reasons. Firstly, its simplicity compared to other transients would allow better identification of problems in the model. Secondly, it involves operation of the crucial DHRS that is supposed to maintain integrity of the plant for a long duration without human action, making the test highly relevant to subsequent transient analyses. Thirdly, a number of studies using system codes had already been performed, including reference results published by NuScale (Skolik et al., 2018a; Skolik et al., 2018b; NuScale Power LLC 2020f), which can be used for comparison as well.

The turbine trip transient falls under the "decrease in heat removal by the secondary system" group of DBEs and for it NuScale had performed transient analysis based on a set of conservative initial conditions. The first step was to modify the steady-state CESAR model to converge towards these conservative conditions. This means some of the form loss coefficients and feedwater pump flow rate obtained in the 160 MW steady state described in Section 3 had to be adjusted to cope with the increased input power of 163.2 MW (2% higher). The process is largely similar to that for the original steady state other than the exclusion of the lower power cases, reducing the number of parameters to be considered during iteration.

3 Steady state simulation

Several existing works using RELAP5 (Skolik et al., 2018a; Hosseini et al., 2021) have achieved good agreement with reference values at 100% power. However, data for lower powers at 75%, 50% and 15% are also available in the safety analysis report (NuScale Power LLC 2020c). To have an improved confidence of the constructed CESAR steady-state model, this work applies the optimization process to all four power levels. The procedure taken was to adjust the form loss coefficients K of each component. The final set of parameters was selected through an iterative approach, based on two criteria: 1) it has the lowest sum of root-mean-square deviations of major reactor operating quantities from reference values, i.e., core inlet temperature, primary SG region inlet (hot leg) temperature, core inlet-outlet temperature difference (ΔT), primary coolant

TABLE 2 Form loss coefficients, secondary feedwater MFR and SG heat exchange area used in the optimized steady state model.

Form loss coefficients K

Core	Bypass	Riser	SG primary	Downcomer
3.5	0.16	0.1	1.6	0.2

Modified operating parameters

	Feedwater MFR [kg/s]	SG area [m^2]
References	67.07	1,666
Model	68.95 (+2.8%)	2,165 (+30%)

mass flow rate (MFR), and secondary steam outlet temperature; 2) each deviation should not exceed 3%.

Summarized in Table 2 are the values obtained at the end of the optimization process to achieve the final reactor operating conditions in Table 3. Larger deviations at 160 and 24 MW exemplify the difficulty of achieving convergence at all powers. In addition, a similar difficulty is shown by the decreasing MFR and increasing ΔT deviations in with reduction in power. This can be expected given the balance between the volumetric heat generation rate $\dot{q}'''$ and the product of coolant MFR $\dot{m}$, specific heat capacity c_p and ΔT at steady state

$$\dot{q}''' = \dot{m}c_p\Delta T \tag{7}$$

The SG heat exchange area had to be drastically modified from the stated physical value. Other works using RELAP5 (Hoffer et al., 2011; Skolik et al., 2021) had also found this increase of 30% to be necessary for overall reactor quantities to fit correct values. Severe deviation in this heat exchange region is attributed to the need to compensate for 1-D simplification by system codes of the complex geometry, flow, and heat exchange in the once-through helical-coil SG region.

Adjustment of the secondary feedwater pump MFR had to be made but was kept minimal. One reason is that uncertainties of the pump MFR are expected to be small since it is a relatively standard component, and its operation should not evolve drastically under normal conditions. Furthermore, changing the pump MFR leads to large deviations especially at lower powers.

Minimization of errors in regions like the core and SG require higher-resolution CFD modelling to better reflect local flow and consequent energy exchange phenomena, instead of arbitrary adjustment of the above system parameters to fit the desired results. It is important to note that changing the value of one parameter shifts the optimal values of others. In fact, applying all ideal values does not produce overall results that lie within 3% deviation. Covering a large span of operating powers is hence critical for examining natural circulation systems and for future work on accident scenarios that usually involve inadvertent or intentional power losses.

4 Turbine trip transient simulation

4.1 Conservative initial steady state conditions

The final converged values for the steady state are recorded in Table 4. Core power, feedwater temperature, reactor pool temperature and RSV setpoint are boundary conditions defined by the user in the code and hence should

TABLE 3 Deviation of core inlet (cold leg), primary SG region inlet (hot leg) and secondary steam temperatures, primary coolant mass flow rate, and core inlet-outlet temperature difference from reference values at four power levels. Calculations are done in SI units, i.e., K for temperatures and kg/s for MFR.

Power [MW]		Cold leg T [K]	Hot leg T [K]	Steam T [K]	Pri. MFR [kg/s]	Core ΔT [K]
160	References	531.3	583.2	574.8	587.0	55.4
	Model	535.0	585.1	575.1	600.1	54.1
	Error [%]	+0.70	+0.32	+0.045	+2.2	−2.4
120	References	535.3	579.2	—	521.6	47.0
	Model	534.3	577.6	—	530.6	47.0
	Error [%]	−0.19	−0.27	—	+1.7	−0.031
80	References	539.9	574.5	—	443.7	36.9
	Model	539.4	574.2	—	440.2	37.7
	Error [%]	−0.10	−0.048	—	−0.80	+2.1
24	References	549.0	565.5	—	280.2	17.5
	Model	556.8	573.2	—	271.8	17.7
	Error [%]	+1.4	+1.4	—	−3.0	+0.66

TABLE 4 Steady-state initial conditions for turbine trip transient generated by the CESAR model in comparison to reference NuScale values.

	References (NuScale)	ASTEC-CESAR	Error [%]
Core power [MW]	163.2	163.2	0.0
Feedwater temperature [K]	427.6	427.6	0.0
Reactor pool temperature [K]	366.5	366.5	0.0
RSV lift setpoint [MPa]	14.73	14.73	0.0
Average RCS temp [K]	563.7	573.3	1.7
Primary coolant MFR [kg/s]	535.2	536.4	0.22
Pressurizer pressure [MPa]	13.24	13.38	1.1
SG pressure [MPa]	3.69	3.69	0.0

TABLE 5 Form loss coefficients, secondary feedwater MFR and SG heat exchange area used in the conservative steady state from which the transient will be simulated. *The reference feedwater MFR here is not provided by NuScale but increased by 2% from the steady-state value of 67.07 kg/s, scaled linearly with the higher input power.

Form loss coefficients K				
Core	Bypass	Riser	SG primary	Downcomer
5.88	0.27	0.17	2.7	0.34
Modified operating parameters				
	Feedwater MFR [kg/s]		SG area [m^2]	
References	*68.41		1,666	
Model	71.01 (+3.8%)		2,165 (+30%)	

not differ from the reference values. From the table, the adjusted model has generated sufficiently accurate conditions, showing only small deviations in the average primary coolant temperature, pressurizer pressure and primary coolant MFR.

Corresponding to Table 4, the parameters used to attain the desired initial transient model are listed in Table 5. Because of the considerably lower primary MFR of 535.2 kg/s required (8.8% decrease from 587.0 kg/s for steady state at 160 MW), the form loss coefficients had to be raised significantly to provide adequate pressure drops along the loop. All K values for primary-side components were increased significantly by 68% from steady-state values. This general scaling was done, instead of tuning each K as before, to preserve the overall proportionality since the MFR cannot be expected to be lower at a higher core power of 163.2 MW under natural circulation given the same geometries unchanged from normal steady state. The feedwater MFR was raised by 5.9%–71.01 kg/s, but this includes the increase that would have been expected by design to account for the 2% higher input power, which would otherwise be 68.41 kg/s and lower the deviation to 3.8%. On the other hand, the SG heat exchange area was kept the same as earlier.

4.2 Simulation results

From the conservative steady-state conditions obtained earlier, simulation of the turbine trip transient was initiated by closing the MSIV at $t = 0$. The immediate effect is an increase in secondary pressure since the steam outlet is closed, reducing its heat removal ability, and leading to increased primary pressure. The reactor trip signal is triggered when primary pressure exceeds 13.79 MPa, with a 2-s delay before the trip is physically activated, followed by a sharp drop in core thermal power described by Figure 3, start of feedwater pump coast-down, and start of the 30-s wait before the DHRS actuation valves are opened as shown by the sudden rise in DHRS flow rate in Figure 4. The time taken for the feedwater pump to be completely shut off was set to 14.0 s.

Table 6 shows the sequence of events reflecting the set delays mentioned and the events dependent on evolution of physical phenomena such as the time taken to reach the reactor trip high-primary-pressure trigger and maximum primary pressure attained during the transient. Comparison of the timings with references in Table 7 shows no large differences. In fact, the ASTEC model appears to reproduce the NRELAP5 data more closely with regards to the time taken for the high primary pressure that triggers the reactor trip signal to be reached, and also the timing at which the maximum primary pressure is reached is closer to the NRELAP5 time of 10.0 s at 13.8 s compared to 15.0 s in the RELAP5 model.

To enable direct comparison with the other two reference curves, the vertical axis has been limited to 10 kg/s, cutting off part of the peak. The maximum MFR reached is about 45.8 kg/s, in stark contrast to 5 kg/s and 8.5 kg/s in the RELAP5/SCDAPSIM and NRELAP5 studies respectively. However, if one considers that the peak width measured at 4 MW is about 50 s in the NRELAP5 analysis and less than 6 s in this CESAR model, mass flowing through in both peaks is very similar. This discrepancy could arise from the need to estimate information such as the secondary component flow areas and DHRS actuation valve orifice dimensions since they directly impact the consequent maximum and stable DHRS MFR calculated.

Figures 5–8 display the evolution of main quantities during the transient. Progression of the quantities calculated using RELAP5/

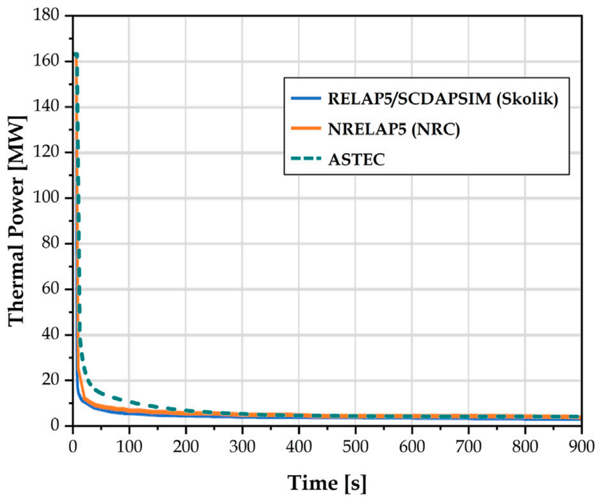

FIGURE 3
Turbine trip transient: Evolution of core thermal power after transient initiation. After reactor trip has been triggered, a 2.0-s delay is implemented before the actual sharp power reduction begins. Compared to the other two references, the thermal power in the first 200 s in this work is set higher, before reaching the same decay heat level.

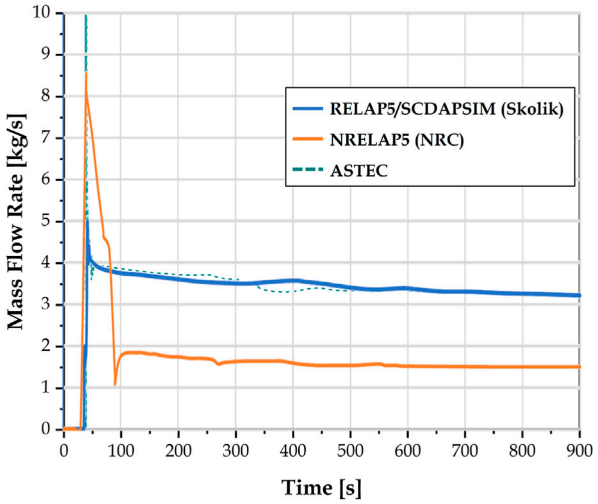

FIGURE 4
Turbine trip transient: DHRS total mass flow rate of both liquid and vapor phases. This figure zooms in on values below 10 kg/s for direct comparison with references. Refer to text for detailed discussion on the peak excluded from this figure.

TABLE 6 Sequence of events in the turbine trip transient simulated. The initiating event occurs at time t = 0.0 s, causing a rise in primary pressure sufficient to trigger the reactor trip. Events labelled 'dependent' are physical processes whose timing depend on the system evolution, whereas the other events have user-defined durations or delays relative to earlier events.

Time [s]	Event
0.0	• Turbine trip initiated by closing the steam outlet and by turning the pressurizer heater and spray systems off • Feedwater pump MFR starts decreasing gradually over the next 14.0 s
5.0 (dependent)	• High pressurizer pressure limit of 13.79 MPa exceeded • Reactor trip signal with 2.0-s delay triggered (but not received yet)
7.0	• Reactor trip signal received • Core thermal power starts decreasing to decay heat level, following the References time profile; Power drops from 163.2 MW to 39.5 MW within the first 5.0 s, then reaches decay heat level ~4.2 MW by ~840 s • DHRS actuation valves completely open 30.0 s later
12.7 (dependent)	• Peak pressurizer pressure of 14.49 MPa reached
14.0	• Feedwater pump completely off
37.0	• DHRS actuation valves completely open abruptly (i.e., from 0% to 100%)

TABLE 7 Timing of events in the turbine trip transient simulated by RELAP5/SCDAPSIM (Skolik et al., 2018b), NRELAP5 (NuScale Power LLC 2020f) and ASTEC.

Event	RELAP5/ SCDAPSIM [s]	NRELAP5 [s]	ASTEC [s]
Turbine trip initiated	0.0	0.0	0.0
Feedwater flow starts to drop	0.0	0.0	0.0
Reactor trip triggered by high pressurizer pressure	6.0	5.0	5.0
Reactor trip signal received	8.0	7.0	7.0
Peak primary pressure	15.0	10.0	13.8
Feedwater pump off	14.0	14.0	14.0
DHRS actuation valves open	36.0	35.0	37.0

SCDAPSIM (Skolik et al., 2018b; Skolik 2021), NRELAP5 (NuScale Power LLC 2020f) and ASTEC in this work generally agree. Primary pressure (Figure 5) shows a steeper negative gradient than reference, with the initially higher pressure dropping below reference values after about 350 s, whereas secondary pressure (Figure 6) is consistently higher than reference. Investigation of different parameters (e.g., power-time profile, duration over which the feedwater pump coasts down, starting time of feedwater pump coast-down, DHRS actuation valve size) yield no simple way to reconcile both pressures since events that tend to raise primary pressure would have a similar effect on secondary pressure as well. The ideal method would involve the exact component designs,

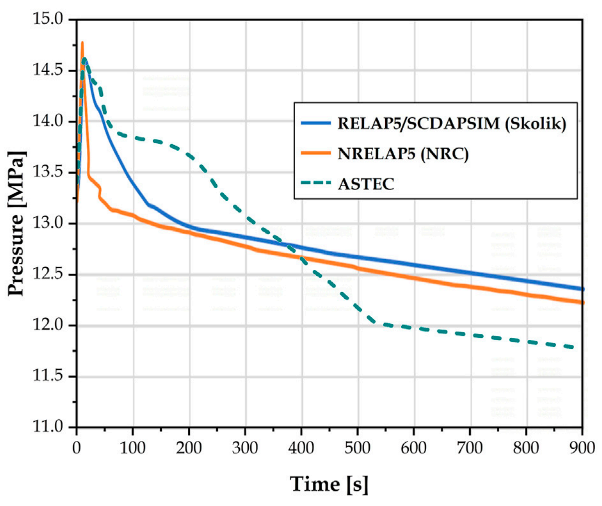

FIGURE 5
Turbine trip transient: Primary pressure.

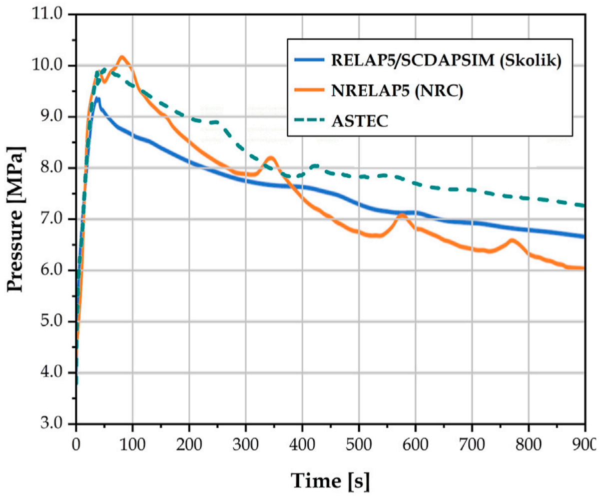

FIGURE 6
Turbine trip transient: Secondary pressure.

especially the heat exchange components like the SG that couples the two separate coolant circuits and also the DHRS condenser that couples the secondary side to the ultimate heat sink.

The primary coolant mass flow rate calculated with ASTEC exhibits the same behavior as that with NRELAP5, most prominent of which are the two large peaks followed by low-frequency oscillations at a stable level, as plotted in Figure 7. This was not well captured by the RELAP5/SCDAPSIM simulation. On the other hand, both peaks in this work occur about 80 s earlier than the NRELAP5 ones. The initial sharp drop also does not reach close to zero as was exhibited by the reference analyses. This is related to the slightly slower drop in power implemented in this study, as previously described with Figure 3. Even though using a more drastic power reduction would reproduce the initial MFR drop better, the peaks would correspondingly be shifted to the left and the stable MFR attained earlier as well. The final flow rate calculated in all three studies show great agreement around 150 kg/s.

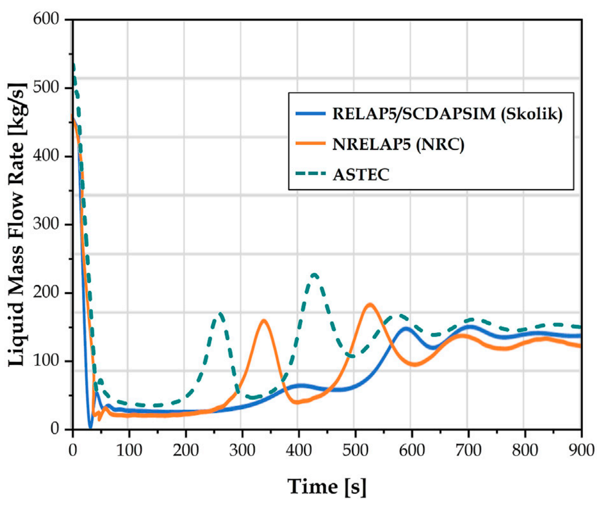

FIGURE 7
Turbine trip transient: Primary coolant mass flow rate. CESAR result generally follows that of NRELAP5 but appears shifted earlier by approximately 80 s.

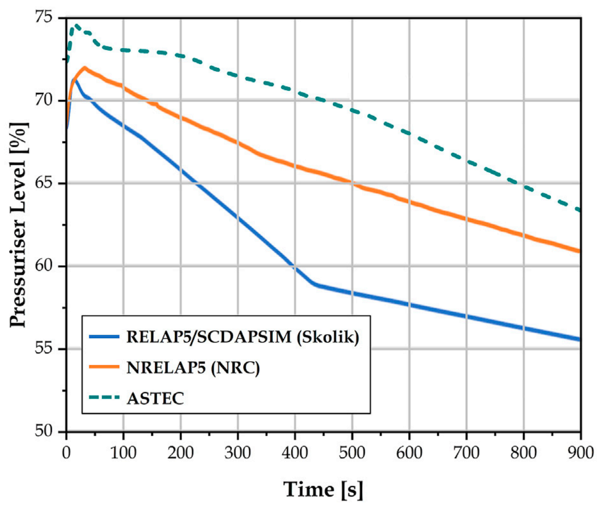

FIGURE 8
Turbine trip transient: Pressurizer water level.

Lastly, the pressurizer level undergoes largely the same absolute changes as reference, with the difference being the fact that the initial level was slightly higher, as shown in

Figure 8. As compared to the RELAP5/SCDAPSIM result, discrepancies are within 5% of the NRELAP5 results. It should be noted that the pressurizer level is heavily dependent upon the control volume setup from the beginning since the exact position of the heaters and spray MFR need to be estimated from limited information as well. As such, it is possible for the pressurizer level to exhibit large differences without affecting its modelling function of maintaining primary system pressure. The only time it can pose problems is when trying to replicate the real system where the spray has a minimum MFR even when pressure is on the low end of the acceptable range. This means that if the simulation is run long enough, the pressurizer becomes completely filled and eventually the system pressure reaches critical temperature and pressure. To circumvent this, the minimum spray MFR is set to zero and pressure limits modified to prevent unrealistic over-filling of the pressurizer.

5 Conclusion

A steady state model of the NuScale iPWR has been set up with the TH module of the ASTEC code. An improvement to existing works has been made with regards to its accuracy from low (15%) to full nominal power, results of which served as a guide for iteration towards a best-fitting model and could be used in modelling of similar reactor designs. Good agreement of reactor operating conditions at all power levels with reference data to within 3% deviation was deemed sufficient to verify the accuracy of the model. With largely the same methodology, a second steady state model was constructed by modifying the previous one to generate conservative initial conditions from which a turbine trip transient simulation would be performed. Deviations from reference data were small, with those of primary coolant average temperature and mass flow rate reaching 1.7% and 0.22% respectively, while pressurizer pressure differed by only 1.1%.

The second steady state model enables subsequently a range of transient scenarios to be studied. This steady state was then used for simulation of a turbine trip transient, and results showed good agreement with NuScale NRELAP5 analyses pertaining mainly to evolution of system pressures and mass flow rates. Further work remains to be done as inherent uncertainties of such system models in complex regions like the core and SG rely on CFD modelling to be minimized, and simulation of other DBEs to validate the applicability of this model.

Data availability statement

The original contributions presented in the study are included in the article/Supplementary Material, further inquiries can be directed to the corresponding author.

Author contributions

ZG: Modelling, analysis, writing, editing; SX: Concept, research, editing, supervision; KC: Project funding, overall supervision.

Funding

This work was supported by the National Research Foundation Singapore (A-0001360-06-00).

Acknowledgments

The authors would like to acknowledge the Institut de Radioprotection et de Sûreté Nucléaire (IRSN, France) as developers of the ASTEC code and for making technical support available when needed.

Conflict of interest

The authors declare that the research was conducted in the absence of any commercial or financial relationships that could be construed as a potential conflict of interest.

Publisher's note

References

Bestion, D. (1990). The physical closure laws in the CATHARE code. *Nucl. Eng. Des.* 124 (3), 229–245. doi:10.1016/0029-5493(90)90294-8

Bestion, D. (2008). "System code models and capabilities," in *THICKET 2008*. (Pisa, Italy: OECD/NEA).

Bestion, D. (2017). System thermal hydraulics for design basis accident analysis and simulation: Status of tools and methods and direction for future R&D. *Nucl. Eng. Des.* 312, 12–29. doi:10.1016/j.nucengdes.2016.11.010

Burwell, M. J., Lerchl, G., Miro, J., Teschendorff, V., and Wolfert, K. (1989). "The thermalhydraulic code ATHLET for analysis of PWR and BWR systems," in *4th international topical meeting on nuclear reactor thermal-hydraulics (NURETH-4)*. Editors: U. Mueller, K. Rehme, and K. Rust. Karlsruhe, Germany.

Chatelard, P., Belon, S., Bosland, L., Carénini, L., Coindreau, O., Cousin, F., et al. (2016). Main modelling features of the ASTEC V2.1 major version. *Ann. Nucl. Energy* 93, 83–93. doi:10.1016/j.anucene.2015.12.026

Che, S., Breitenmoser, D., Infimovskiy, Y. Y., Manera, A., and Petrov, V. (2020). CFD simulation of two-phase flows in helical coils. *Front. Energy Res.* 8 (65), 1–15. doi:10.3389/fenrg.2020.00065

Di Giuli, M. (2015). *PhD dissertation: Severe accident simulation in small modular reactor*. Bologna, Italy: Università di Bologna.

Di Giuli, M., Sumini, M., and Bandini, G. (2014). "Pressurized water small modular reactor (SMR), design basis accident analysis using the ASTEC code," in *23rd international conference nuclear energy for new Europe*. (Portorož, Slovenia: Nuclear Society of Slovenia).

Foucher, L., Cousin, F., Fleurot, J., and Brethes, S. (2014). Assessment on 900-1300 MWe PWRs of the ASTEC-based simulation tool of SGTR thermal-hydraulics for the IRSN emergency technical centre. *Nucl. Eng. Des.* 272, 287–298. doi:10.1016/j.nucengdes.2013.07.041

Freitag, P. (2018). *Master thesis: Transient thermal-hydraulic simulation of a small modular 365 reactor in RELAP 5*. Kingston, RI: University of Rhode Island.

Gómez-García-Toraño, I., Sánchez-Espinoza, V. H., Stieglitz, R., and Queral, C. (2017). Analysis of primary bleed and feed strategies for selected SBLOCA sequences in a German Konvoi PWR using ASTEC V2.0. *Ann. Nucl. Energy* 110, 818–832. doi:10.1016/j.anucene.2017.08.003

Gómez-García-Toraño, Ignacio, and Laborde, L. (2019). Validation of selected cesar friction models of the ASTECV21 code based on moby dick experiments. *J. Nucl. Eng. Radiat. Sci.* 5 (2). doi:10.1115/1.4042119

Gómez-García-Toraño, Ignacio, Laborde, L., and Zambaux, J. A. (2018). Overview of the CESAR thermalhydraulic module of ASTEC V2.1 and selected validation studies. Proceedings of the 18th Int. Youth Nucl. Congr. Bariloche, Argentina, March 2018, 2, 2–5.

Guo, Z., Xiao, S., and Chung, K. Y. (2022). "Preliminary steady-state thermal hydraulic modelling of the NuScale integral pressurised water reactor using the CESAR module of ASTEC," in *Advances in thermal hydraulics (ATH 2022)*. (Anaheim, CA, USA: American Nuclear Society).

Hoffer, N. V., Sabharwall, P., and Anderson, N. A. (2011). *Modeling a helical-coil steam generator in RELAP5-3D for the next generation nuclear plant*.

Hosseini, S. A., Akbari, R., Shirani, A. S., and D'Auria, F. (2021). Analysis of the natural circulation flow map uncertainties in an integral small modular reactor. *Nucl. Eng. Des.* 378, 111156. doi:10.1016/j.nucengdes.2021.111156

IAEA (2020). *Advances in Small Modular Reactor Technology developments*. Austria: IAEA.

Ingersoll, D., and Carelli, M. (2021). *Handbook of Small Modular Nuclear Reactors*. Second Edition. Elsevier.

Johnson, K. P. (2021). *Master Thesis: Transient Analysis of the NuScale Power Helical-Coil Steam 387 Generator Tube Rupture Using RELAP5-3D*. Kingston, RI: University of Rhode Island.

Kim, M. S., and Jeong, Y. H. (2020). Conceptual design of small modular reactor driven by natural circulation and study of design characteristics using CFD & RELAP5 code. *Nucl. Eng. Technol.* 52, 2743–2759. doi:10.1016/j.net.2020.05.014

NRC, U.S. (2008). *TRACE V5.0 theory manual*. Washington, DC: U.S. NRC.

NuScale Power LLC (2020a). NuScale standard plant design certification application. *Chapter 01: Introduction. and General Description of the Plant*. Washington, DC: U.S. NRC.

NuScale Power LLC (2020b). NuScale standard plant design certification application. *Chapter 04: Reactor*. Washington, DC: U.S. NRC.

NuScale Power LLC (2020c). NuScale standard plant design certification application. *Chapter 05: Reactor Coolant System and Connecting Systems*. Washington, DC: U.S. NRC.

NuScale Power LLC (2020d). NuScale standard plant design certification application. *Chapter 08: Electric Power*. Washington, DC: U.S. NRC.

NuScale Power LLC (2020e). NuScale standard plant design certification application. *Chapter 09: Auxiliary Systems*. Washington, DC: U.S. NRC.

NuScale Power LLC (2020f). NuScale Standard Plant Design Certification Application. *Chapter 15: Transient and Accident Analyses*. Washington, DC: U.S. NRC.

Petruzzi, A., and D'Auria, F. (2008). Thermal-hydraulic system codes in nulcear reactor safety and qualification procedures. *Sci. Technol. Nucl. Installations* 2008 (460795), doi:10.1155/2008/460795

RELAP5 Development Team (1995). *RELAP5/MOD3 code manual vol. 1: Code structure, system models, and solution methods*. Idaho falls, ID: Idaho National Engineering Laboratory.

Ricotti, M. E., Cammi, A., Cioncolini, A., Cipollaro, A., Oriolo, F., Lombardi, C., et al. (2002). "Preliminary safety analysis of the IRIS reactor," in *International conference on nuclear engineering (ICONE10)*. (Arlington, VA, USA: ASME). doi:10.1115/ICONE10-22398

Skolik, K., Allison, C., Hohorst, J., Malicki, M., Perez-Ferragut, M., Pieńkowski, L., et al. (2021). Analysis of loss of coolant accident without ECCS and DHRS in an integral pressurized water reactor using RELAP/SCDAPSIM. *Prog. Nucl. Energy* 134, 103648. doi:10.1016/j.pnucene.2021.103648

Skolik, Katarzyna (2021). *PhD dissertation: Thermal-hydraulic analysis of severe accident progress in pressurized light water reactor according to its scale*. AGH University of Science and Technology. Kraków, Poland.

Skolik, K., Trivedi, A., Perez-Ferragut, M., and Allison, C. (2018a). "Assessment of RELAP/SCDAPSIM for turbine trip transient in NuScale-SMR," in *26th international conference on nuclear engineering (ICONE26)*. (London, UK: ASME). doi:10.1115/ICONE26-81861

Skolik, K., Trivedi, A., Perez-Ferragut, M., and Allison, C. (2018b). "Integrated uncertainty analysis of the turbine trip transient in NuScale SMR using RELAP/SCDAPSIM," in *12th international conference of the Croatian nuclear society*. (Zadar, Croatia: Croatian Nuclear Society).

Yan, Y., Shi, S., and Ishii, M. (2016). "Scaling analysis and facility design for stability investigation during accidents in a PWR-type SMR," in *24th international conference on nuclear engineering (ICONE24)*. (Charlotte, NC: ASME). doi:10.1115/ICONE24-60476

Zambaux, J.-A. (2021). *ASTEC V2.2: CESAR physical and numerical modelling*. France: IRSN: Fontenay-aux-Roses.

frontiers | Frontiers in Energy Research

TYPE Original Research
PUBLISHED 06 January 2023
DOI 10.3389/fenrg.2022.1036063

OPEN ACCESS

EDITED BY
Qingming He,
Xi'an Jiaotong University, China

REVIEWED BY
Yuxuan Liu,
University of Michigan, United States
Hongbo Zhang,
Nuclear Power Institute of China (NPIC),
China

*CORRESPONDENCE
Song Li,
lisong_ls@foxmail.com
Yongfa Zhang,
zhangyf@163.com

SPECIALTY SECTION
This article was submitted to Nuclear Energy,
a section of the journal
Frontiers in Energy Research

RECEIVED 03 September 2022
ACCEPTED 30 November 2022
PUBLISHED 06 January 2023

CITATION
Li S, Zhang Q, Liu L, Zhang Y, Hao J, Wang X, Jiang L and Liu X (2023), Analysis of the fine-mesh subgroup method and its feasible improvement. *Front. Energy Res.* 10:1036063.
doi: 10.3389/fenrg.2022.1036063

Analysis of the fine-mesh subgroup method and its feasible improvement

Song Li[1]*, Qian Zhang[2], Lei Liu[3], Yongfa Zhang[1]*, Jianli Hao[1], Xiaolong Wang[1], Lizhi Jiang[1] and Xiaoya Liu[1]

[1]College of Nuclear Science and Technology, Naval University of Engineering, Wuhan, China, [2]Laboratory for Advanced Nuclear Energy Theory and Applications Zhejiang Institute of Modern Physics, Department of Physics Zhejiang University, Hangzhou, China, [3]College of Electrical Engineering, Naval University of Engineering, Wuhan, China

The fine-mesh subgroup method (FSM) is proposed to treat the significant resonance self-shielding effect both effectively and accurately. Similar to the ultra-fine group method, the fine-mesh subgroup method adopts a fine group structure on the resonance energy range to avoid the extra resonance interference effect correction. To improve the efficiency, on the one hand, the one-group micro-level optimization is adopted, so the subgroup fixed-source equations will be only calculated on a certain number of pre-determined subgroup levels, and an interpolation process is employed to obtain the actual subgroup flux. On the other hand, the slowing-down calculation is carried out for group condensation for multigroup transport calculation. The main theory and feasible improvements of the fine-mesh subgroup method are analyzed in this paper. Several pin cell and lattice problems are applied to test the performance of the fine-mesh subgroup method, and the particle swarm optimization method is adopted to find the better group structure. The numerical results indicate a good performance both for accuracy and efficiency.

KEYWORDS

resonance self-shielding, subgroup method, resonance interference effect, particle swarm optimization, fine group structure

1 Introduction

With the development of nuclear energy, the demand for accurate calculation of reactor physics has become increasingly higher. Since the resonance self-shielding calculation provides the effective material cross-sections for all processes of the core simulation, handling the resonance effect accurately and effectively has been the research hotspot in recent years. There are three main resonance treatment methods applied in reactor physics, namely, the equivalence theory (Askew et al., 1966; Hebert et al., 1991), ultra-fine group method (Ishiguro et al., 1971; Sugimura et al., 2007; Kim et al., 2011; Zhang et al., 2020), and subgroup method (Nikolaev et al., 1971; Cullen, 1977; Hebert, 2009; Joo et al., 2009; Downar et al., 2016; Li et al., 2019). The equivalence method uses the neutron's first escape probability from absorption to develop the equivalence relation between the homogeneous and heterogeneous systems, and the effective resonance cross-section is obtained by interpolating the resonance integrals. The equivalence method is simple and efficient but is difficult to apply to conditions such as irregular geometry and complicated material compositions. The ultra-fine group method is the most direct approach for the resonance effect as it has hundreds of thousands of groups to capture the severe fluctuation of cross-sections in the resonance energy range. Since the resonance peaks would be reproduced accurately enough by extremely detailed energy structure, this method has the same level of accuracy as the Monte Carlo method. However, the efficiency of the ultra-fine group method is unacceptable as too many groups sharply increase the calculation burden, so it is not suitable for use in large-scale problems. The subgroup method is another widely used method for resonance treatment. Different from the traditional group structure divided by energy discretion, the subgroup structure is determined by the level of the cross-section. The variations of resonance peaks are described by subgroup parameters, including subgroup levels and subgroup weights. The former represents the magnitude of the cross-section level, and the latter indicates the probability that a neutron locates in the corresponding subgroup. In this method, the traditional resonance group will be further divided into several subgroups, and the calculation accuracy would be comparable with that of ultra-fine groups. In addition, the subgroup method has the ability to be coupled with any kind of transport solver such as the method of characteristics (MOC), so that it can handle complex geometry configurations. However, the subgroup theory is derived on the basis that only one resonant nuclide exists in the system. For conditions with the resonance interference effect between different resonant nuclides, the accuracy of the subgroup method would decrease and extra correction is needed, such as the Bondarenko method (Bondarenko, 1964) or the resonance interference factor (RIF) method (Williams, 1983; Peng et al., 2013; Sohail et al., 2015). However, the Bondarenko method has been proven to be inaccurate, and the RIF method will cause a great increase in calculation burden. In recent years, there are other new resonance treatment methods proposed, such as the embedded self-shielding method (Williams et al., 2012; Liu et al., 2015; Zhang et al., 2015; Kim et al., 2019), pseudo resonance isotope method (Liu et al., 2018; Zhang et al., 2018), or pin-based slowing-down method (Choi et al., 2017), which all have relatively high accuracy. However, the first method treated the fuel rod as a whole system, so the resonance effect inside the fuel pin is unknown, while the latter two still need the ultra-fine group slowing-down equations, which is time-consuming.

From the theory of the ultra-fine group and the subgroup method, a compromise proposal could be found by coupling the two methods' advantages, so the fine-mesh subgroup method (FSM) was proposed by the author (Li et al., 2020). In the coupling assumption, as the energy group mesh is further divided by the subgroup, the fine energy mesh could be much coarser than the ultra-fine group method. Different from the traditional subgroup method, the fine-mesh energy structure could be considered so that the resonance interference effect is avoided. To obtain the proper fine energy mesh, the SHEM-361 group structure (Hfaiedh et al., 2005; Hébert et al., 2008) is adopted and modified. The resonance energy range has been extended from 1.855 to 9,118 eV, and the energy group number in this range is 289 and the total group number is 408. Compared with the original SHEM-361 structure, the new 408 group structure has a finer mesh between 1.855 and 100 eV, while the energy structure of the other energy range remains the same. To reduce the number of subgroup fixed-source equations, the one-group micro-level optimization, which is modified based on the macro-level grid optimization (Park et al., 2019), is adopted and the 289 resonance groups are averaged to be one group and each resonant nuclide only needs to solve fixed-source problems for eight subgroup levels. Then, an interpolation of the background cross-section would be carried out to reproduce the original subgroup fluxes in actual subgroups in each resonance group. Furthermore, as the fine-mesh structure would inevitably lead to the increase in calculation burden for the transport module, the group condensation procedure is carried out in this work and the 47-group structure library of the Helios-1.11 program (Stamm'ler, 2008), which has 16 resonance groups, is adopted. The 16 resonance groups' cross-sections are calculated by collapsing the fine group, while those of fast and thermal groups are provided by the NJOY code (Macfarlane et al., 2016). The neutron slowing-down equation is used in this work for group condensation, which is handled group by group. The source item for the slowing-down equation is obtained by only down-scattering since the upper scattering effect and fission source could be neglected for the resonance range.

In this work, more detailed analyses or the FSM are carried out, especially for the procedure of making the fine-mesh group structure and sensitivity analysis of selecting the interpolation cross-section of one-group micro-level approximation for the subgroup fixed source problem. In addition, there are also some promisingly improvable aspects of the FSM. The 47-group structure will still cause too much burden for the whole calculation, and a coarser structure with fewer total group numbers is necessary. The particle swarm optimization method (PSO) (Kennedy et al., 1995) is a feasible approach for this issue.

The remaining sections of this paper are arranged as follows. Section 2 gives an introduction to the fine-mesh subgroup method which is combined with the traditional subgroup method and ultra-fine method first; then, the process of choosing the group structure and finding the micro-level of the subgroup fixed-source problem is discussed. Finally, the feasible improvement in the group structure by PSO is introduced. Section 3 demonstrates the numerical verification of the FSM compared with traditional methods and presents a further discussion of possible improvements for the FSM. Section 5 provides the summary of this paper.

2 Methodological model

2.1 Basic theory of the subgroup method

Instead of defining the group structure by energy range, the subgroup method further divides the resonance group into several subgroups by the magnitude of the cross section. In this way, the variation of resonance peaks could be described by subgroup parameters, namely, subgroup levels and subgroup weights. According to the defining process, the subgroup level represents the magnitude of the cross section, and the subgroup weight indicates the width of the energy range of each subgroup. The subgroup method uses the subgroup parameters and subgroup flux to obtain the effective resonance cross section, which is shown in Eq. 1.

$$\sigma_{x,g} = \frac{\int_{\Delta E_i} dE \sigma_{x,i}(E)\varphi_i(E)}{\int_{\Delta E_i} dE \varphi_i(E)} = \frac{\sum_i^I \frac{\Delta E_i}{E_g}\sigma_{x,\mathrm{g},i}\phi_i}{\sum_i^I \frac{\Delta E_i}{E_g}\phi_i} = \frac{\sum_i^I \omega_i \sigma_{x,\mathrm{g},i}\phi_i}{\sum_i^I \omega_i \phi_i}. \tag{1}$$

In Eq. 1, E represents the energy, σ represents the micro cross-section, x represents the reaction type, g is the group index, i is the subgroup index, ϕ represents the scalar flux for a subgroup, ω_i is subgroup weight for subgroup i, and $\sigma_{x,g,i}$ represents the subgroup level.

In the actual calculation process, the subgroup parameters could be calculated according to the relationships among the effective resonance cross-section, the subgroup parameters, and the subgroup fluxes shown in Eq. 1, and they could be stored in the multigroup library or calculated on-the-fly. The subgroup parameters used in this work are physical probability tables, and the methods for calculating them are also a research hotspot, which could be referenced by many papers (Joo et al., 2009; Zu et al., 2019; He et al., 2020; Li et al., 2021), so in this work, this process would not be illustrated in detail. Once the subgroup parameters are obtained, the subgroup fixed-source equation could be established, which is in the same formation as the Boltzmann transport equation and could be solved by a transport module such as MOC. As the overwhelming majority of the fission neutrons have energy above the upper limit of the resonance energy range, the fission source could be neglected for the subgroup fixed-source equations. Moreover, the upper scattering phenomenon is also negligible. Therefore, through the intermediate resonance approximation, the source item for the subgroup could be described just as a constant. In this case, the subgroup fixed-source equation is shown in Eq. 2.

$$\begin{aligned}\Omega \cdot \nabla\phi_{g,i}(r,\Omega) + \Sigma_{t,g,i}(r)\phi_{g,i}(r,\Omega) \\ = \frac{1}{4\pi}\left[\left(1-\lambda_g\right)\Sigma_{s,g,i}\phi_{g,i}(r) + \lambda\Sigma_{p,g}\right].\end{aligned} \tag{2}$$

In Eq. 2, $\Sigma_{t,g,i}$ and $\Sigma_{s,g,i}$, respectively, indicate the macro subgroup total and scattering cross-section for group g and subgroup i. λ is the intermediate resonance approximation factor, and Σ_p is the macro potential cross-section. For the resonant nuclides, items for Eq. 2 are calculated according to the subgroup parameters. For the non-resonant nuclides, since their absorption and resonance scattering effects are small, $\Sigma_{t,g,i}$ and $\Sigma_{s,g,i}$ could be both replaced by $\lambda\Sigma_p$. Through the aforementioned approximations, the subgroup transport equation could be easily solved by any type of transport program to obtain the subgroup flux, so the final effective resonance cross section could be obtained by Eq. 1.

2.2 Fine-mesh subgroup method

The basic idea of the FSM is to establish a finer mesh of the resonance range so that the implementation of the subgroup method no longer needs to consider the subsequent resonance interference correction calculation. To relieve the increasing calculation burden of the subgroup fixed-source equation brought by the fine mesh, the one-group micro-level approximation is adopted. Subsequently, the slowing-down equation for the fine-mesh resonance energy structure is solved to condense the effective resonance cross-section to a broader group structure, which is finally applied to the multigroup transport equation calculation. This section will focus on two main topics, namely, the determination process of the fine-mesh structure and the sensitivity of the subgroup calculation with one-group micro-level optimization.

2.2.1 Analysis of the fine-group structure

Since the conventional subgroup method only considers one resonant nuclide in the deduction process, the overlapping phenomenon for resonance peaks of different resonant nuclides could not be described accurately. Conventionally, by adopting a finer multigroup structure, the resonance peak inside a coarse resonance group could be impaired and make the results more precise. Therefore, if the subgroup method is carried out based on a fine enough energy structure, the calculation accuracy would be assumed to be the same level as that of the ultra-fine group method. However, selecting the fine group structure is the key issue to handle.

Compared with the commonly used multigroup structure such as WLUP-69 (Aldama, 2003) or HELIOS-47 structure (Stamm'ler, 2008), there are also some finer meshes proposed internationally, such as WLUP-172 (Aldama, 2003) and SHEM-

TABLE 1 Distributions of main resonance peaks of typical actinide nuclides.

Nuclide	Location of the resonance peak/eV
^{235}U	2.0、2.8、3.6、4.8、5.4、6.4、7.1、8.8、9.3、11.7、12.4、14.0、16.1、16.7、19.3、21.1、23.42
^{238}U	6.67、20.9、36.7、66.0、80.7、102.6、116.9、165.3、189.7、237.4、291.0、347.8、937.3、958.8、991.8、1140
^{238}Pu	18.6
^{239}Pu	7.8、10.9、11.9、14.3、14.7、17.7、22.3、65.9
^{240}Pu	20.5、38.3、41.6、66.6、72.8、90.8、92.5、105.1、121.7、151.9、162.7、170.1、185.8、239.3、287.1、405.0、596.8、665.0
^{241}Pu	4.3、8.6、13.4、14.8、17.9
^{242}Pu	2.7、53.46
^{241}Am	5.4、5.9

281 (Hfaiedh, 2005). In Hébert et al. (2008), the energy range between 22.5 and 11.4 keV is optimized based on the SHEM-281 group structure, and the finer SHEM-361 group structure is proposed. The authors of this paper pointed out that by adopting SHEM-361, the subgroup method would not need the extra correction for the resonance interference effect, since the resonance cross section inside each energy group is flat enough for the subgroup method to handle. Then, the DRAGON5 program further modified the SHEM-361 structure to the SHEM-295 structure to increase the calculation efficiency but the accuracy is relatively sacrificed (Canbakan et al., 2015). Meanwhile, DRAGON5 put forward a 2-level scheme based on the subgroup method. In this method, the subgroup method is carried out based on the SHEM-295 structure, and then, the interface current method is used to get the fine-mesh flux to condense the group structure from 295 to 26 groups. Finally, the MOC is used for the 26-group structure for eigenvalue calculation.

The fine-mesh subgroup method (FSM) of this paper is proposed based on the aforementioned research, and the SHEM-361 group structure is optimized in this work for the fine-mesh calculation. For the optimized structure, the resonance range is adjusted and the resonance group number is increased. Different from the DRAGON which calculates the fine-mesh flux for the whole group structure, the FSM only calculates the flux for the fine-mesh resonance group by solving the neutron slowing-down equation, and the group condensation is also only carried out for resonance groups. Cross-sections for fast and thermal groups of the coarse mesh are provided by the pre-produced multigroup library.

The resonance range of the conventional multigroup structure such as WLUP-69 is 4–9,118 eV, which is accurate for typical UO_2 problems. However, since actinide nuclides such as ^{242}Pu also have significant resonance peaks near the thermal range, the lower limit of the resonance range in this work is extended to 1.8554 eV, which is the same as that of the HELIOS-47 group structure. Moreover, since resonance peaks of ^{238}U play the most important role in the resonance interference effect, the fine mesh should make modifications, especially toward the distribution of ^{238}U resonance peaks. Table 1 displays the energy points where the resonance peaks of typical actinide nuclides are. It could be found that ^{238}U has resonance peaks nearly all over the resonance range, while other nuclides mainly focus on the energy range below 100 eV. Therefore, the overlap effect for smaller energy ranges is relatively more severe. In Hfaiedh et al. (2005) and Hébert (2009), the resonance peaks of common reactor component materials, such as ^{152}Sm, ^{109}Ag, ^{177}Hf, and ^{155}Gd, are also provided.

It could be found from Table 1 that most of the resonant peaks of different resonant nuclides are around a relatively low energy range. Figure 1 shows the resonance peaks of ^{235}U, ^{238}U, and ^{239}Pu near 6.7 eV. It is evident that ^{238}U has a highly significant resonance peak in this range, so the effective cross-section would change sharply with the background cross-section. Under this condition, the space self-shielding and energy self-shielding effects would be very severe. However, the calculation process of subgroup parameters of the physical probability table does not consider the influence of background cross-section to each subgroup, so extra deviation may be raised. To address this issue, the energy between 1.8554 and 100.6 eV of the SHEM-361 structure is optimized in this work.

On the one hand, to get a precise effective cross-section around significant resonance peaks, a further discrete of the energy group between 22.5 and 100.6 eV is carried out. The resonance peaks in this range are divided into multiple resonance groups, and the key nuclide taken into consideration is ^{238}U. In this way, the deviation trend of the resonance cross-section with background cross-section is weakened to be similar to that of the un-resolved resonance range, so that only 2–3 subgroups would be accurate enough to describe the self-shielding effect of the new resonance group. On the other hand, the SHEM-361 structure deploys a very meticulous discrete below 22.5 eV, and the resonance calculation is not conducted in this range. Since the lower limit of the resonance range is extended to 1.8554 eV in

TABLE 2 Optimized group structure for the energy range of 1.8554–100 eV.

Energy range/eV	Nuclides with the significant resonance peak	Group number	
		Original	Optimized
1.8554–2.38	^{235}U、^{243}Cm、	6	2
2.38–3.93	^{235}U、^{242}Pu、^{153}Eu、^{115}In、^{177}Hf、^{155}Gd	14	14
3.93–6.43	^{235}U、^{241}Am、^{133}Cs、^{147}Pm、^{145}Nd、^{109}Ag、^{177}Hf、^{167}Er	22	9
6.43–8.31	^{235}U、^{238}U、^{239}Pu、^{152}Sm、^{176}Hf、^{177}Hf、^{178}Hf	26	14
8.31–22.5	^{235}U、^{238}U、^{239}Pu、^{240}Pu、^{241}Pu、^{131}Xe、^{177}Hf、^{157}Gd	56	30
22.5–47.9	^{238}U、^{240}Pu、^{95}Mo	20	60
47.9–78.9	^{238}U、^{239}Pu、^{240}Pu、^{242}Pu	20	60
78.9–100.6	^{238}U、^{240}Pu	6	16

this work, the SHEM-361 structure between 1.8554 and 22.5 eV could be merged. In addition, for energy ranges around 2.7 and 6.7 eV where the resonance peaks are widely distributed, the original fine structure is reserved to ensure the calculation accuracy. Finally, compared with the SHEM-361 structure, the newly optimized structure between 1.8554 and 100.6 eV is shown in Table 2.

In general, the process of energy structure optimization mainly follows two principles. First, the distribution of resonance peaks should be described in detail. Second, the group boundary should be set to be feasible for group condensation to commonly used coarse group structures such as WLUP-69 or HELIOS-47. By introducing the subgroup calculation to the energy range of 1.8554–22.5 eV, the group number of this range is reduced from 124 to 81. For energy between 22.5 and 100.6 eV, further discreteness makes the group number increase from 46 to 136. The resonance range of this work is 1.8554–9,118 eV. The SHEM-361 structure has 242 groups in total in this range, while the optimized structure has 289 groups. Meanwhile, the fast group and thermal group still adopt the original SHEM-361 group, so the total group number of the new structure is 408.

To enhance the efficiency of the multigroup transport calculation, the resonance fine-mesh cross-section needs to be condensed. According to Kim et al. (2011) and Li et al. (2020), for the neutron slowing-down equation, the source item of the resonance group could be simplified as the down-scattering source. As the lethargy width of the FSM is not as narrow as the ultra-fine group, the down-scattering source will be calculated by the scattering matrix, and the slowing-down equation of the FSM is shown in Eq. 3. Similar to the ultra-fine slowing-down equation, the flux of Eq. 3 could be solved group by group and the flux of the fast groups could be considered as the asymptotic flux. Finally, the effective multigroup resonance cross section is calculated by Eq. 4.

$$\Omega \cdot \nabla \varphi_g + \sum_m^M \Sigma_{m,t,g} \varphi_g = \sum_m^M \sum_{g'}^{g-1} \Sigma_{m,s,g' \to g} \varphi_{g'}, \tag{3}$$

$$\sigma_x = \frac{\sum_g^G \sigma_{x,g} \varphi_g}{\sum_g^G \varphi_g}. \tag{4}$$

2.2.2 Analysis of one-group micro-level optimization

The subgroup method used in this work is the physical subgroup approach, and the subgroup parameters are generated by preserving resonance integrals. The subgroup parameters of this work are in the form of the probability table, which is obtained by fitting the resonance integrals for different background cross-sections. The commonly used fitting methods include the Pade approximation method and the least square method. However, during the calculation process of subgroup parameters, there is a notable shortcoming in the negative subgroup parameters that may occur for certain selections of resonance integrals. The traditional multigroup library only has 10 background cross-sections for resonance integrals, which is not enough to select the optimal combination that meets the accuracy requirement. To avoid this situation, the multigroup library used for the FSM is adapted to have 40 sets of background cross-sections from 10 bar to 10^{10} bar, which is shown in Table 3. In addition, the resonance tables used in this work are homogeneous ones that are generated by the NJOY-2016 code.

The subgroup group number used in this work is limited from 2 to 5, and each resonance group is calculated starting from two subgroups. If the relative error shown in Eq. 5 is too large for all combinations of background cross-sections, the number of subgroups will be added by one and the calculation procedure will be repeated for the new subgroup number. If the subgroup number is increased to the maximum, then the criterion will be added by 0.1%.

TABLE 3 Background cross sections of resonance integral.

Background cross-section range/b	Number	Background cross-section/b
$10\sim10^2$	9	10、20、30、40、50、60、70、80、90
$10^2\sim10^3$	11	100、120、150、160、200、250、300、500、750、800、900
$10^3\sim10^4$	9	1,000、2,000、3,000、4,000、5,000、6,000、7,000、8,000、9,000
10^4~10^5	7	10,000、20,000、30,000、40,000、50,000、75,000、90,000
$10^5\sim10^{10}$	4	10^5、10^6、10^7、10^{10}
Total	40	\

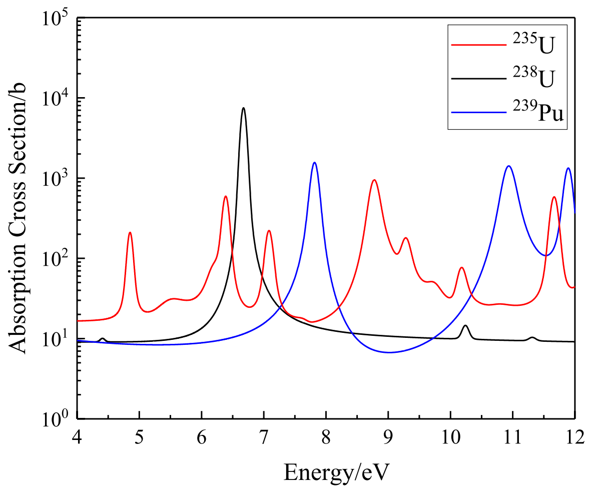

FIGURE 1
Variation curve of the absorption cross-section for ^{235}U, ^{238}U, and ^{239}Pu around 6.7 eV.

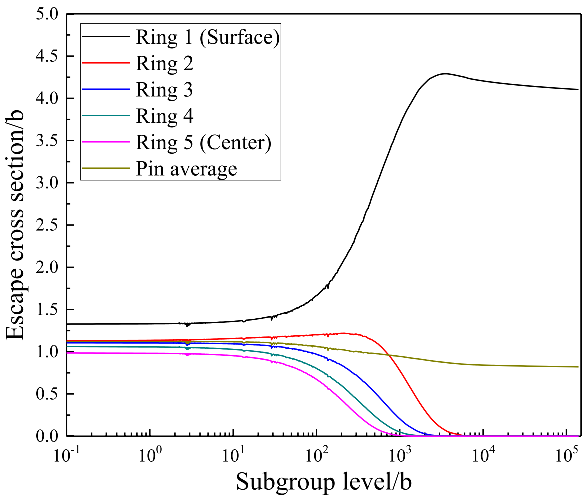

FIGURE 2
Variation trend of the escape cross-section by the subgroup level in different regions (Li et al., 2020)

$$RE = \frac{\left| \frac{\sum_{i}^{I} \omega_i \sigma_{x,i} \frac{\sigma_b}{\left[\sigma_{a,i} + \lambda\left(\sigma_{s,i} - \sigma_{p,i}\right) + \sigma_b\right]}}{\sum_{i}^{I} \omega_i \frac{\sigma_b}{\left[\sigma_{a,i} + \lambda\left(\sigma_{s,i} - \sigma_{p,i}\right) + \sigma_b\right]}} - \sigma_x\left(\sigma_b\right) \right|}{\sigma_x\left(\sigma_b\right)} \times 100\%. \tag{5}$$

For conventional subgroup methods, the subgroup fixed-source problems would be solved for all subgroups in all resonance groups. However, it would result in a large amount of computation once the number of the resonance group increases. To avoid this phenomenon, the one-group micro-level optimization is adopted in this work. All resonance groups are averaged as one effective group by Eq. 6.

$$\sigma_x = \frac{\sum_{g}^{G} \sigma_{xg} RI_{g,\infty} \Delta u_g}{\sum_{g}^{G} RI_{g,\infty} \Delta u_g}. \tag{6}$$

In Eq. 6, $RI_{g,\infty}$ is the infinite absorption resonance integral and Δu is the lethargy width. The subgroup level of the effective one group is calculated by sensitivity analysis, and the subgroup fixed-source problem is carried out only for these subgroup levels. The actual subgroup flux of each resonance group could be obtained by interpolating $ln(\sigma_{t',i})$, where $\sigma_{t',i} = \sigma_{t,i} - (1-\lambda)\sigma_{s,i}$. However, according to the author's previous work (Li et al., 2020), to avoid numerical instability, the actual interpolating process of the subgroup flux is carried out by the subgroup level and escape cross-section defined by Eq. 7, where R indicates the resonant nuclide, while L indicates all the nuclides in the calculation system. For a typical single pin cell divided by five equal rings, the variation trend of the escape cross section with subgroup levels is shown in Figure 2.

$$\sigma_{e,i,R} = \frac{1}{N_R}\left(\frac{\Sigma_{t',i,R}\phi_i}{1-\phi_i} - \sum_{l}^{L}\lambda_l \Sigma_{p,l}\right). \tag{7}$$

TABLE 4 Design of the single-cell cases.

Case no.	Description
1	Base case
2–8	Number density of H_2O is gradually reduced to 0.01368×10^{24} cm^{-3}
8–15	Number density of^{238}U is gradually reduced to 0.01824×10^{24} cm^{-3}
15–20	Radius of the fuel pin is gradually increased to 0.50 cm

According to Figure 2, it could be found that the subgroup level influences the escape cross-section at the surface area most. Therefore, to analyze the interpolation accuracy for the subgroup flux and find the best choice of interpolating subgroup levels, the following procedure is carried out.

1) Between the subgroup level range of 1~10^5 b where the value of the escape cross-section dramatically changes, 500 subgroup levels are selected by an equal proportion.
2) A series of single-cell problems are designed according to Table 4. The base case is a fuel pin surrounded by light water, which is shown in Figure 3. For simplification, the clad and gas gap are neglected. The number density and geometry parameters are referenced from the JAEA benchmark (Yamamoto et al., 2002). For the base case, the fuel pin radius is 0.4095 cm, the half pitch of the cell is 0.63 cm, and the fuel is composed of ^{238}U and ^{16}O, of which the number density is 0.0204×10^{24} cm^{-3} and 0.046×10^{24} cm^{-3}, respectively. The moderator is composed of light water whose number density is 0.03315×10^{24} cm^{-3}. The system temperature is 300 K with the reflective boundary condition.
3) All the subgroup levels defined in step (1) are used in the geometry defined in step (2), and the fuel pin is divided into 5, 10, and 15 rings, respectively. Then, the MOC transport module (Song et al., 2019) is used to solve the subgroup fixed source equation shown in Eq. 2 of these problems, so the subgroup fluxes for different subgroup levels in different regions are obtained.
4) Several subgroup levels are chosen between 1~10^5 b from step (1), and then step (2) is repeated only for chosen subgroup levels to calculate the subgroup flux. For other unchosen subgroup levels, the subgroup fluxes are obtained by interpolating among the chosen ones. In this work, the number of chosen subgroup levels is 4–13, and the value range of the subgroup levels for each condition is shown in Table 5.
5) The interpolated subgroup fluxes of step (4) were compared with those directly calculated by step (5), and the interpolating bias was analyzed. The root-mean-square (RMS) deviation of all regions and all subgroup levels is shown in Figure 4. Apparently, the interpolating bias decreases sharply with the increase in the interpolating number, and the RMS tends to remain stable after eight interpolating subgroup levels. In this way, the subgroup level used in the one-group subgroup-level fixed-source equation is chosen as 10, 100, 200, 300, 500, 1,000, 2,000, and 10,000 b, respectively.

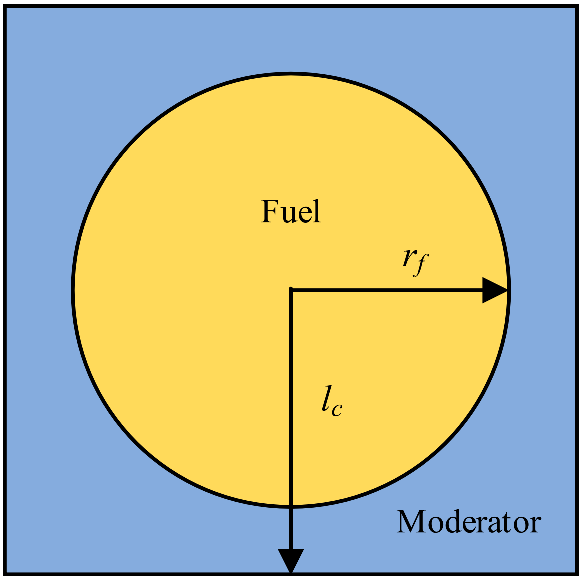

FIGURE 3
Structural configuration of the single-cell case.

2.3 Feasible improvement of the FSM

The FSM still has some aspects for possible improvement, and one of the most dominant parts is the group number of the multigroup transport problems. As this process accounts for the most calculation time, it is useful to reduce the final group number. Since the FSM has 408 group meshes, any combination of energy points could establish a new multigroup structure, and it is necessary to find the best selection. In this paper, the particle swarm optimization method (PSO) (Kennedy et al., 1995) is adopted for group structure optimization.

The main theory of PSO is shown later (Kennedy et al., 1995; Li et al., 2021). PSO defines a series of particles with different positions and velocities and uses the fitness function to describe

TABLE 5 Subgroup-level values chosen for each interpolating condition.

Subgroup-level value range/b	Subgroup-level number									
0~10^2	1	1	1	1	1	2	3	3	3	4
10^2~10^3	1	2	2	3	4	4	4	4	4	4
10^3~10^4	1	1	2	2	2	2	2	3	4	4
10^4~10^5	1	1	1	1	1	1	1	1	1	1
Total	4	5	6	7	8	9	10	11	12	13

the error between the aim value and the current value. There are two parameters to describe the condition of a particle, namely, the particle position X and the flying velocity V. The position of the particle indicates the relevant parameters of the calculation problems. In this work, the position coordinate of the particle could represent the group energy boundary of the coarse group structure. The particle would update the position generationally to get the target. For the i^{th} particle of the t^{th} generation, the particle position is $X_i(t) = [x1/i(t), x2/i(t), \ldots xD/i(t)]$, and the flying velocity of the particle could be written as $V_i(t) = [v1/i(t), v2/i(t), \ldots vD/i(t)]$. The distance from the particle to the destination is expressed by the fitness function $f_i(t)$, so the computing purpose is to find the minimum value of f. All particles would fly over the domain of definition and find the best position independently. When the i^{th} particle has searched for t generations, it would have recorded t positions and the one with the minimum f would be defined as the personal best value P, which is expressed as $P_i(t) = [p1/i(t), p2/i(t), \ldots pD/i(t)]$. The particles would share with each other their personal best values and positions, and the global best value G indicates the best position among all personal best values, which is obtained by $G(t) = min[P_1(t), P_2(t), \ldots P_D(t)]$. During the generations, each particle would adjust its individual position and velocity according to its own $P_i(t)$ and the global best $G(t)$, which could be shown in Eq. 8–9.

$$v_i^j(t+1) = wv_i^j(t) + c_1 r_1\left[P_{best,i}^j(t) - x_i^j(t)\right] + c_2 r_2\left[G_{best}^j(t) - x_i^j(t)\right], \tag{8}$$

$$x_i^j(t+1) = x_i^j(t) + v_i^j(t+1). \tag{9}$$

In Eq. 8–9, i is the particle index; j represents the dimension of the particle; t is the generation index; w is the inertia weight; c is the acceleration constant, which gives random values between 0 and 2; and r is the random value between 0 and 1. In addition, the velocity and position should be limited to the pre-determined value range.

Since the particle position is composed of a multidimensional variable, each dimension represents an energy mesh in this work. In this way, different particles indicate the different energy structures. As the particle moves in a certain velocity, the position would be changed and the energy structure is changed accordingly. After one step of movement, the particles would communicate with each other about each individual group structure and the error of eigenvalue calculations. Afterward, all particles would move to the best position particle with each certain velocity and the aforementioned process would be repeated until the error reaches the requirement. In addition, there are also some existing research studies relevant to energy structure optimization based on PSO (Akbari et al., 2012; Yi et al., 2013; Edgar et al., 2015), which could provide a useful reference for this work. Overall, the process of searching for the optimized group structure is shown as follows:

1) The particle position $xj/i = X_{min} + r(X_{\max} - X_{\min})$ and velocity $vj/i = V_{\min} + r(V_{\max} - V_{\min})$ are initialized, where r is the random value from 0 to 1. The value of xj/i is the group index of the 408 mesh, so the domain of definition of xj/i is [1, 408]. The velocity should also have top and bottom limitations to avoid the non-sensical value, so in this work, we chose the velocity between 1 and 5. Also, the number of particles is set to 1,000, and the maximum particle generation is limited to under 300. The dimension J of x_i, which indicates the coarse group number, is chosen from 10 to 30.
2) Since the particle coordinate value represents a series of group boundaries, so the group condensation is carried out for each particle. For total absorption and fission cross-section, the condensation formula follows Eq. 4. For the scattering matrix, the condensation rule is shown as in Eq. 10.

$$\sigma_{l,h'\to h=}\frac{\sum\limits_{g=h_1}^{h_2}\ \sum\limits_{g'=h_1'}^{h_2'}\ \sigma_{l,g'\to g}\varphi_g'}{\sum\limits_{g'=h_1'}^{h_2'}\ \varphi_g'}. \tag{10}$$

In Eq. 10, h’ and h are the group indexes of the coarse mesh and g’ and g are those of the fine mesh. h_1 and h_2 are the upper and lower limit of fine-mesh group index corresponding to the group h of the coarse mesh, respectively. h_1 and h_2 are the upper and lower limits of fine-mesh group index corresponding to the group h of the coarse mesh, respectively. l is the Legendre order number.

3) The effective multiplication factor k_{eff} was calculated using the coarse mesh cross-section obtained previously. The calculation results were offered as the fitness function

$f_i(t)$ of each particle, and P_{best} of all the previous generations was obtained. P_{best} would be shared among all the particles to find the G_{best}. Then, the particle position x and velocity v were modified based on P_{best} and G_{best}, which are shown in Eq. 8–9.

4) The G_{best} of the current generation was checked for convergence criterion. In this work, we define the convergence criterion as under 50 pcm between the coarse mesh and fine mesh. If the accuracy is not satisfied, then steps (2) and (3) would be repeated until the optimized position is obtained or the upper limit of the particle generation number is reached.

3 Numerical verification

To analyze the accuracy of the resonance cross sections, the FSM adopts the multigroup library format of the HELIOS-1.11 code, of which the number of the fast, resonance, and thermal group is 9, 16, and 22, respectively. The fine mesh of the FSM has 289 resonance groups from 1.8554 to 9,118 eV. A series of benchmarks containing UO_2, MOX, Gd-bearing problems, and control rod problems are used to test the performance of the FSM, and the reference value is provided by the continuous energy Monte Carlo code MCNP5 (X-5 Monte Carlo Team, 2003). The ultra-fine group method (UFG) and the traditional subgroup method with the Bondarenko iteration method (BIM) for the resonance interference effect are applied to compare the calculation results of the FSM. The group structure of the BIM is the HELIOS-47 structure, which is the same as the second group mesh of the FSM. The UFG method has 34,000 groups for the resonance range. After the effective resonance cross-sections are obtained, the UFG would condense the group structure to the HELIOS-47 structure to carry out the eigenvalue calculation. The MCNP code has 100,000 particles for each problem, and 300 iterations excluding the first 50 are adopted to obtain the reference results. The library type of all the methods in this work is ENDF/VII.0. The MOC parameters of the FSM, BIM, and UFG are set as three polar angles and 16 azimuthal angles per octant, 0.01 cm ray spacing Tabuchi–Yamamoto quadrature (Yamamoto et al., 2007) for single-cell problems, and 0.03 for lattice problems. Moreover, the transport correction method in this work is the inflow correction method, which is referenced from Choi et al. (2015). Given the limited space of this study, the transport correct method will not be discussed in detail.

The contents of numerical verification are arranged as follows: Section 3.1 gives a brief induction to the BIM and UFG. Section 3.2 displays the calculation results of the single cell and 17 × 17 lattice problems consisting of typical UO_2. To analyze the calculation capability for complex conditions, Section 3.3 and Section 3.4 show the results of the Gd-bearing problem and problems with strong absorbers, respectively. Section 3.5 analyze the calclating efficiency. Finally, Section 3.6 gives the further discussion of feasible improvement by PSO group structure optimization.

3.1 Brief induction for the BIM and UFG

3.1.1 BIM

BIM is the classical approach for the resonance interference effect. If there is more than one type of resonant nuclide, the BIM will solve the subgroup transport equations using each resonant nuclide. When handling the current resonant nuclide, the resonance cross-sections of other resonant nuclides in Eq. 2 are still unclear. Therefore, the BIM gives all the resonant nuclides an initial effective resonance cross-section before the subgroup calculation. In this case, when carrying out the subgroup transport calculation of the current resonant nuclide, the other resonant nuclides will be regarded as non-resonant nuclides, and the macro total cross section of Eq. 2 is obtained by Eq. 11:

$$\Sigma_{t,g,i} = N_R\sigma_{t,g,i,R} + \sum_{m=1}^{M} N_{R_m}\sigma_{t,g,\infty,R_m} + \sum_{l=1}^{L} N_l\lambda_l\sigma_{p,l}, \qquad (11)$$

where R indicates the current resonant nuclide, M indicates the total number of non-resonant nuclides, and L is the total number of all nuclides.

First, the initial effective resonance cross-section is used to solve the subgroup transport equations to obtain the effective resonance cross-section of the current resonant nuclide. Once this process is completed for all resonant nuclides, the newly obtained resonance cross- section will replace the initial effective resonance cross-section and the aforementioned calculation process will be carried out again until the iterating bias of the effective resonance cross-section converges.

3.1.2 UFG

The UFG method applied in this section is referenced from Kim et al. (2011) and Zhang et al. (2020). If the total number of all nuclides in the calculation system is L, the slowing-down equation for the resonance energy range is shown as follows:

$$\begin{aligned}\boldsymbol{\Omega}\cdot\nabla\varphi(\boldsymbol{r},u,\boldsymbol{\Omega}) + \sum_{l=1}^{L}\Sigma_{t,l}(\boldsymbol{r},u)\varphi(\boldsymbol{r},u,\boldsymbol{\Omega}) \\ = \sum_{l=1}^{L}\int_{u-\Delta_l}^{u}\frac{\Sigma_{s,l}(\boldsymbol{r},u')\varphi(\boldsymbol{r},u')}{(1-\alpha_l)}e^{u'-u}du',\end{aligned} \qquad (12)$$

where α is obtained by $(A-1)^2/(A+1)^2$; A is the atom mass; u is the lethargy; and $\Delta_l = \ln(1/\alpha)$, which indicates the maximum lethargy increase after one collision. The ultra-fine group number is 34,000 in this work. For group g, the source item of Eq. 12 is shown as

$$Q_g = \sum_{l=1}^{L}\sum_{n=1}^{N_l} P_{n,l}\Sigma_{s,g-n,l}\phi_{g-n}\Delta u_f, \qquad (13)$$

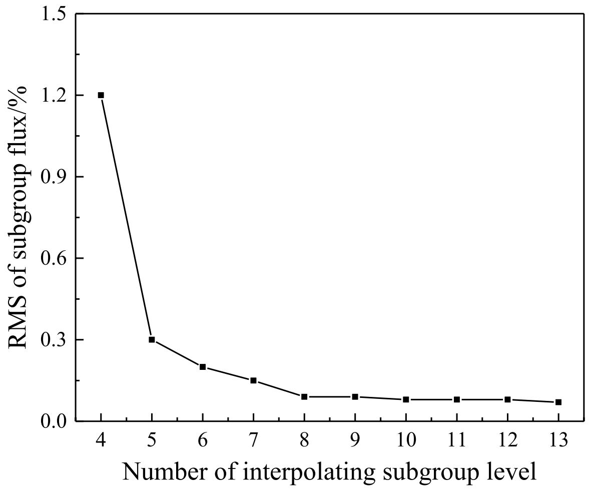

FIGURE 4
Variation trend of RMS for the subgroup flux by the interpolating number of subgroup levels.

where $P_{n,l}$ is the probability for a neutron scatters over n ultra-fine groups and finally locates in group g after a collision with nuclide l. Δu_f is the lethargy width. N_l is the maximum number of ultra-fine groups covered by down-scattering. Kim et al. (2011) and Zhang et al. (2020) give the recursive calculation method for $P_{n,l}$, which is shown in Eq. 14.

$$\begin{aligned} P_{n+1} &= \frac{1}{\Delta u_f(1-\alpha)}\left(1-e^{-\Delta u_f}\right)^2 e^{-n\Delta u_f} \\ &= e^{-\Delta u_f}\frac{1}{\Delta u_f(1-\alpha)}\left(1-e^{-\Delta u_f}\right)^2 e^{-(n-1)\Delta u_f} = e^{-\Delta u_f}P_n. \end{aligned} \quad (14)$$

Therefore, according to Eq. 14, the scattering source could be expressed as follows:

$$\begin{aligned} Q_g = \; & P_1\Sigma_{g-1}\phi_{g-1} + (P_2\Sigma_{g-2}\phi_{g-2} + P_3\Sigma_{g-3}\phi_{g-3} + \cdots \\ & + P_{L-1}\Sigma_{g-L+1}\phi_{g-L+1} + P_L\Sigma_{g-L}\phi_{g-L} \\ & + P_{L+1}\Sigma_{g-L-1}\phi_{g-L-1}) - P_{L+1}\Sigma_{g-L-1}\phi_{g-L-1}. \end{aligned} \quad (15)$$

By comparing Eqs. 14, 15, the recursive expression for the scattering source could be derived as

$$Q_g = e^{-\Delta u_f}Q_{g-1} + P_1\Sigma_{g-1}\phi_{g-1} - e^{-\Delta u_f}P_L\Sigma_{g-L-1}\phi_{g-L-1}. \quad (16)$$

In this work, the fission source and up-scattering effect are neglected in the resonance energy range. In addition, the scattering source for the first resonance group could be calculated by asymptotic flux, which could be expressed as 1/E for the pressurized water reactor. Therefore, the neutron flux of the first ultra-fine resonance group can be obtained by solving a fixed source equation. Subsequently, the flux of the first group could be used to obtain the scattering source of the second group by Eq. 16, and the same procedure will be repeated for all the following groups until the flux of the last group is obtained. Since the ultra-fine group structure is not suitable for eigenvalue calculation, the group condensation process is adopted, which is similar to the FSM. The final effective multigroup resonance cross-section is also calculated by Eq. 4.

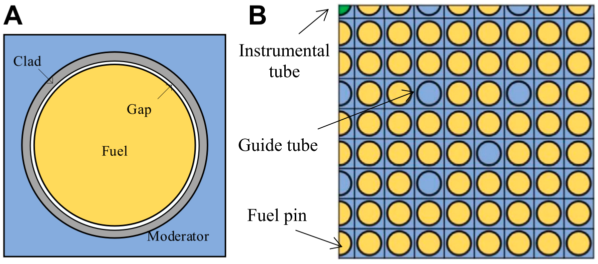

FIGURE 5
Structural configuration of the VERA benchmark: **(A)** single cell and **(B)** 1/4 lattice.

3.2 Typical UO_2 problem

3.2.1 Single cell

The VERA benchmark (Godfrey et al., 2013) released by the Ork Ridge National Laboratory is adopted in this section. The geometry configurations of the single cell and 17 × 17 lattice are shown in Figure 5. The detailed material and geometry parameters can be found in the previous benchmark reference and are not repeated in this work. The UO_2 single cell and lattice are both calculated for four cases, and the results are shown as follows.

For single-cell problems, VERA 1A~1D cases are calculated. The enrichment of these problems is 3.1 wt%, the fuel density is 10.257 g cm^{-3}, and the boron concentration is 1,300 ppm. These four problems have different fuel temperature, moderator temperature, and density, so it could be a test for the FSM to treat the resonance effect under different conditions. In addition, to test the performance of highly enriched UO_2 fuel simulations, two UO_2 pin cell problems of which the enrichment is 20 wt% and 75 wt% are also analyzed in this section. The latter two highly enriched fuels are referenced from the cold-stated UO_2 problem of Yamamoto et al. (2002), but the enrichment is adjusted to 20 and 75 wt%, respectively. It should be noted that the highly enriched fuel is not commonly used for commercial nuclear reactors, so this is only a calculating capability test for the FSM. Table 6 gives the calculation results of k_{eff}. For conventional VERA cases, it was found that the k_{eff} error of the FSM is within ±50 pcm for all problems, while that of the traditional BIM is more than 200 pcm. For highly enriched

TABLE 6 Calculation results of k_{eff} for VERA single-cell problems.

Case	Temperature/K		Moderator density/(g·cm^{-3})	Reference k_{eff}	k_{eff} error/pcm		
	Fuel	Moderator			FSM	UFG	BIM
VERA 1A	565	565	0.743	1.18704	−46	−20	254
VERA 1B	600	600	0.661	1.18215	−26	2	292
VERA 1C	900	600	0.661	1.17172	29	56	228
VERA 1D	1200	600	0.661	1.16260	44	−55	257
20 wt%	300	300	1.000	1.63521	69	−82	324
75 wt%	300	300	1.000	1.76976	130	99	457

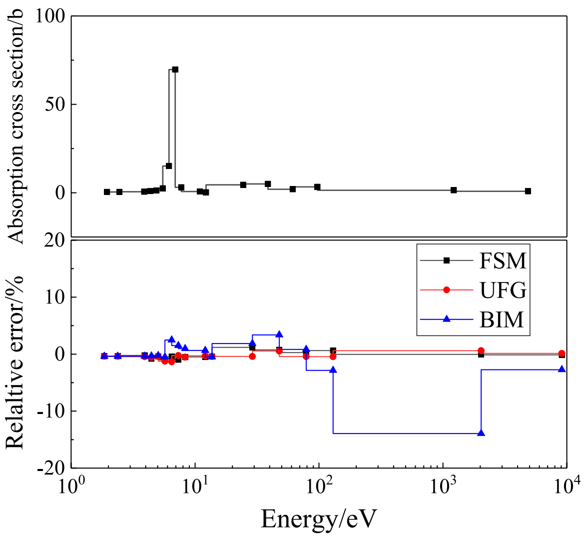

FIGURE 6
Relative deviation of the absorption cross-section for ^{238}U for the VERA 1B case.

problems, the error of k_{eff} increases to some extent for all methods, while the FSM still has a relatively satisfactory accuracy.

Taking the 1B case as an example, Figure 6 displays the calculation results for pin-averaged absorption cross-section of ^{238}U, and Figure 7 gives the results for absorption and fission production of ^{235}U. It was observed that the FSM and UFG could keep the relative error within ±1% nearly for all groups, while the variation of the BIM is not acceptable. The maximum error, average, and root-mean-square relative error of cases 1B and 1C are shown in Table 7.

For the high-enriched fuel problems, taking the 75 wt% case as an example, Figure 8 displays the calculation results for pin-averaged absorption cross-section of ^{238}U, and Figure 9 gives the results for absorption and fission production of ^{235}U. The FSM and UFG could keep the relative error nearly within ±1.5% for all groups, while the variation of the BIM is much larger. Due to the strong self-shielding effect of the highly rich fuel, the error increased slightly compared with the conventional fuel. The maximum error, average, and root-mean-square relative error of cases 1B and 1C are shown in Table 8, of which the accuracy is still acceptable.

3.2.2 17 × 17 lattice

In this section, VERA 2A~2D are selected to verify the capability of the FSM to lattice problems. These lattices have 264 fuel pins, 24 guide tubes, and one instrumental tube, which are shown in Figure 5. Taking 2B and 2C problems as examples, the distribution of normalized pin power calculated by the FSM is shown in Figures 10, 11, respectively. It could be observed that the relative error of normalized pin power is less than 0.5% for most fuel pins. The largest relative error of VERA 2B and 2C problems is 0.67 and 0.65%, respectively, which indicates an accurate performance for the FSM.

In addition, it could be observed that the maximum deviation was always observed at the lower right corner. There are two main reasons why the maximum deviation is always observed at the lower right corner. First, the power value of the corner is always the smallest one in the lattice, so the relative error may rise to some extent. The second one is that for the original VERA benchmark, there is a very small inter-assembly gap that exists between all assemblies containing the core moderator, and the half-gap thickness is 0.04 cm Due to the limit of the modeling capability, the transport module in this work could not directly consider the inter-assembly gap. To make up for this limit, the inter-assembly gap is homogenized to the outermost cell of the lattice. This homogenization process may cause the calculation bias to the outermost cell, so the maximum deviation is always observed at the lower right corner. Since the relative error is still small enough, this deviation is acceptable for lattice calculation.

The overall calculation results of pin power and effective multiplication factor for VEAR 2A~2D are shown in Table 9. The

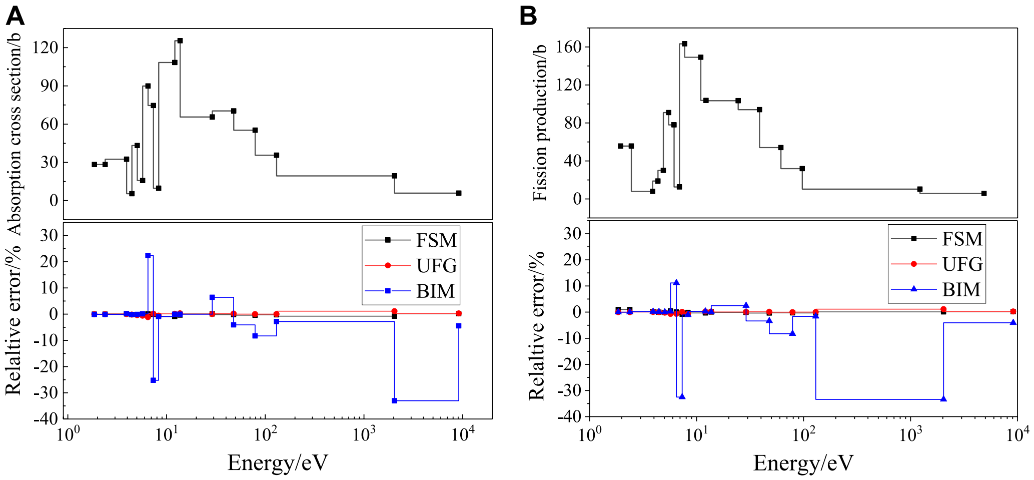

FIGURE 7
Relative deviation of the cross-section for ^{235}U for the VERA 1B case: **(A)** absorption; **(B)** fission production.

TABLE 7 Calculation results of the resonance cross section for VERA 1B and 1C cases.

Relative error value	^{235}U absorption		^{235}U fission production		^{238}U absorption	
	VERA 1B	VERA 1C	VERA 1B	VERA 1C	VERA 1B	VERA 1C
Maximum	−0.87%	1.12%	1.00%	1.03%	−1.19%	0.95%
Average	−0.22%	−0.10%	0.03%	0.05%	−0.20%	−0.17%
RMS	0.32%	0.37%	0.43%	0.46%	0.60%	0.53%

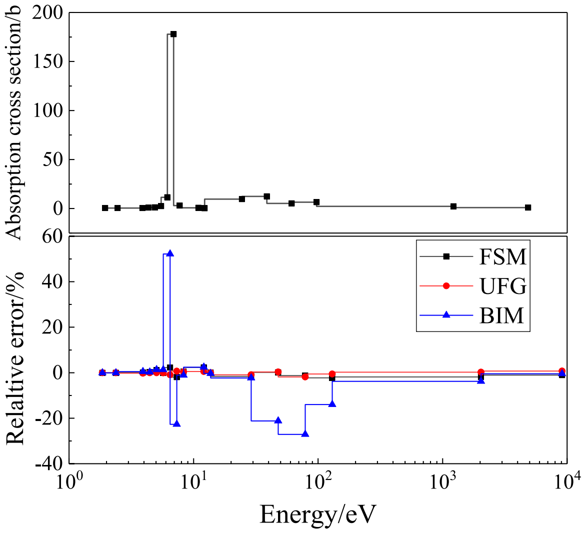

FIGURE 8
Relative deviation of the absorption cross-section for ^{238}U for the 75 wt% case.

maximum, average, and root-mean-square relative error of normalized pin power all meet the precision requirement. For the effective multiplication factor, the maximum error is 74 pcm for the 2B problem, which is still accurate. To sum up, the FSM has excellent performance both for UO_2 single-cell and lattice problems.

3.3 Gd-bearing problem

To control the reactivity, burnable poison such as Gd_2O_3 could be added to the fuel pin. Gd isotopes have strong absorption characteristics and significant resonance peaks, so the Gd-bearing problem is a challenging issue for resonance calculation. Figure 12 gives the geometry configuration of the BWR 4 × 4 lattice (Hong et al., 1998), VERA 2O, and 2P lattice. The BWR lattice has two pins consisting of 3wt% UO_2 and Gd_2O_3, and the others are 3wt% UO_2. VERA 2O and 2P have 12 and 24 Gd-bearing fuel pins, respectively, which are located in the region marked by O andP in Figure 12. Since the flux in the Gd pin changes

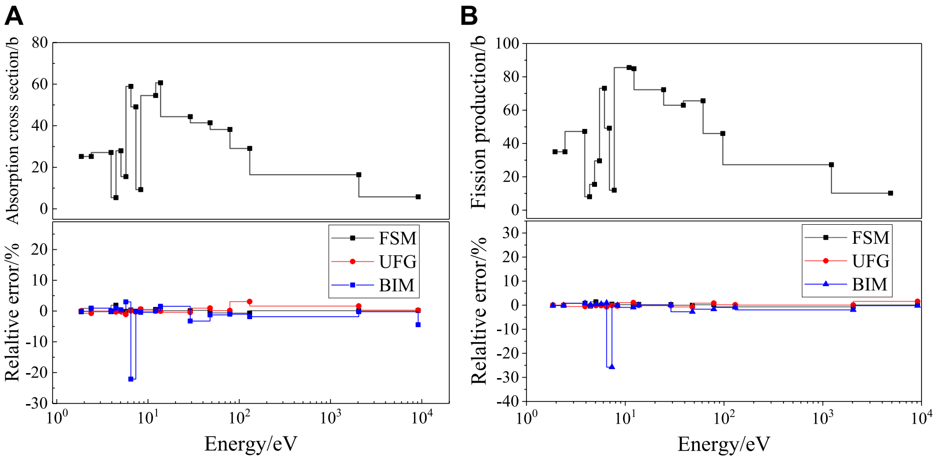

FIGURE 9
Relative deviation of the cross-section for ^{235}U for the 75 wt% case: **(A)** absorption; **(B)** fission production.

TABLE 8 Calculation results of the resonance cross section for 20 and 75wt% cases.

Relative error value	^{235}U absorption		^{235}U fission production		^{238}U absorption	
	20 wt%	75 wt%	20 wt%	75 wt%	20 wt%	75 wt%
Maximum	1.03%	1.69%	1.15%	1.38%	2.15%	2.29%
Average	−0.10%	0.18%	−0.09%	0.07%	0.70%	−0.22%
RMS	0.28%	0.46%	0.32%	0.37%	0.78%	0.89%

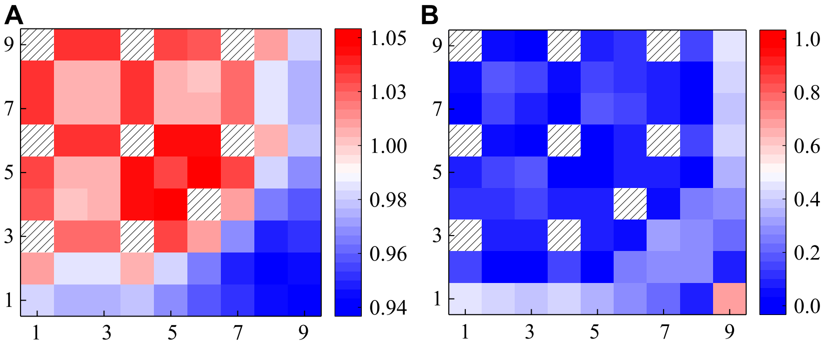

FIGURE 10
Calculation results of pin power of the VERA 2B lattice: **(A)** referenced normalized pin power; **(B)** absolute value of relative deviation/%.

dramatically along the radius direction, the Gd pin is divided by 10 equal-volume rings, while the UO_2 pin is divided by three rings. Moreover, each ring is further divided into eight equal-volume sectors.

The calculation results of the ^{238}U resonance absorption cross-section of ^{238}U for UO_2 pin 1 and Gd-bearing pin 2 are shown in Figure 13A. The largest relative error of pin 1 and pin 2 is 0.91% and −2.24%, respectively. Compared with the

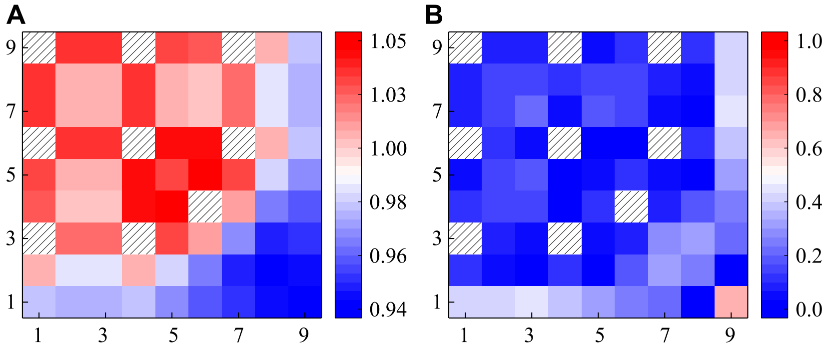

FIGURE 11
Calculation results of pin power of VERA 2C lattice: **(A)** referenced normalized pin power; **(B)** absolute value of relative deviation/%.

TABLE 9 Calculation results for VERA lattice problems.

VERA 17 × 17 lattice	Relative error of normalized pin power			k_{eff}		k_{eff} error/pcm
	Maximum (%)	Average (%)	RMS (%)	Reference	FSM	
2A	0.97	0.20	0.27	1.18218	1.18147	−71
2B	0.67	0.17	0.23	1.18336	1.18410	74
2C	0.65	0.17	0.22	1.17375	1.17331	−44
2D	0.69	0.17	0.23	1.16559	1.16496	−63

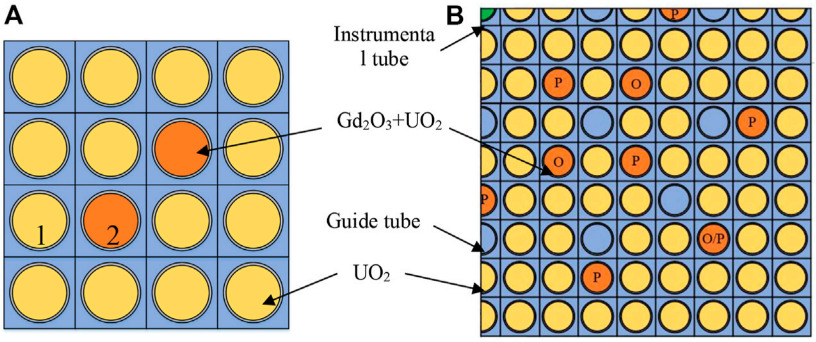

FIGURE 12
Structural configuration of the lattice with gadolinium pins: **(A)** BWR 4 × 4; **(B)** VERA 2O/2P.

conventional UO_2 pin, the calculation bias for the Gd-bearing pin is increased to some extent. Figure 13B gives the resonance absorption cross-section of ^{155}Gd and ^{157}Gd in pin 2, and the largest error is −1.59% and 2.13%, respectively. The calculation on the whole is shown in Table 10. The strong resonance absorption of Gd isotopes makes the precision of the Gd-bearing pin has a relatively larger error compared with conventional problems, but is still acceptable on the whole. The reference k_{eff} of 4 × 4 lattice is 1.08589, the calculation result is 1.08652, and the error is 63 pcm.

Figures 14, 15, respectively, show the calculation results of the normalized pin power of VERA 2O and 2P. For most of the regions, the absolute value of the relative error of pin power is less than 0.5%. The error near the Gd-bearing pins would

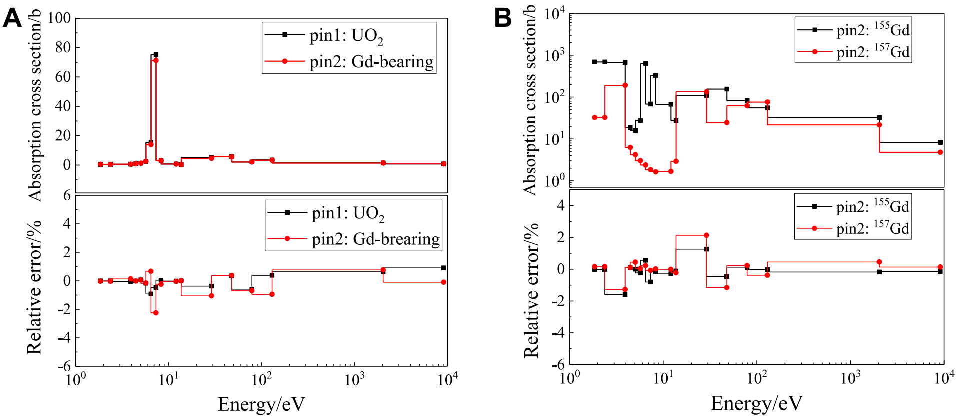

FIGURE 13
Relative deviation of absorption cross section for the 4 × 4 lattice: **(A)** ^{238}U; **(B)** ^{155}Gd and ^{157}Gd.

TABLE 10 Calculation results of the resonance cross-section of pins 1 and 2 of 4 × 4 lattice.

Absorption cross-section	UO$_2$ pin1		Gd-bearing pin2					
	^{235}U (%)	^{238}U	^{235}U (%)	^{238}U	^{155}Gd	^{156}Gd (%)	^{157}Gd (%)	^{158}Gd (%)
Maximum	1.15	0.91%	1.57	−2.24%	−1.59%	1.24	2.13	1.08
Average	0.06	−0.02%	0.13	−0.21%	−0.12%	0.24	0.06	0.03
RMS	0.35	0.32%	0.68	0.65%	0.57%	0.41	0.68	0.38

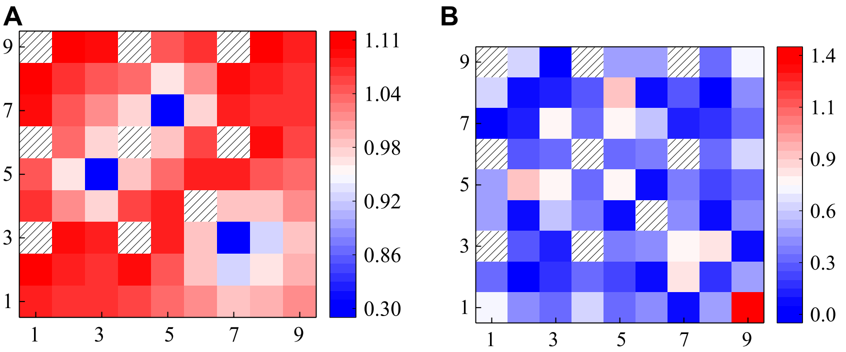

FIGURE 14
Calculation result of pin power of the VERA 2O lattice: **(A)** referenced normalized pin power; **(B)** absolute value of relative deviation/%.

increase a little, but the largest error of 2O and 2P are still acceptable, which are 1.43% and 1.91%, respectively. The general calculation results of pin power and k_{eff} are shown in Table 10, which indicates that FSM could handle the Gd-bearing problems accurately.

3.4 Strong absorber problem

In addition to the Gd-bearing rod, the reactivity could also be controlled by inserting strong absorbers into the guide tubes, such as the Pyrex rod or control rod, which are shown in

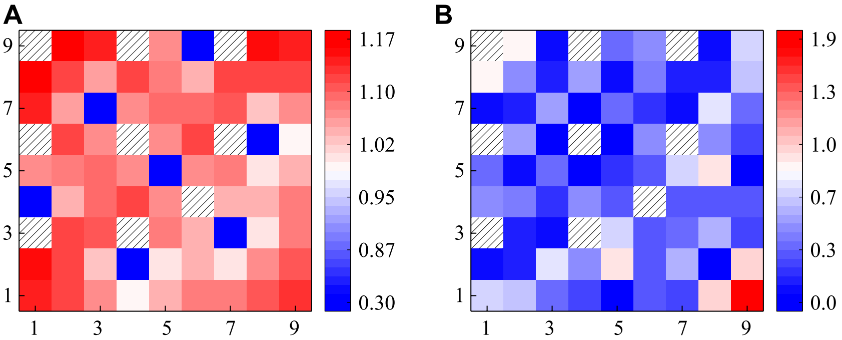

FIGURE 15
Calculation result of pin power of the VERA 2P lattice: **(A)** referenced normalized pin power; **(B)** absolute value of relative deviation/%.

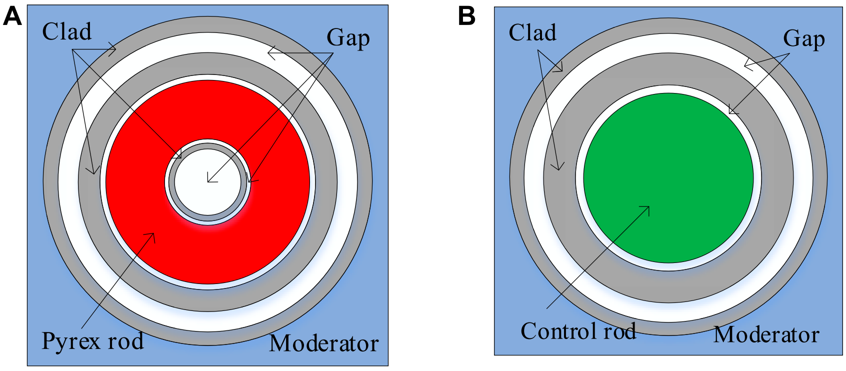

FIGURE 16
Structural configuration of the rod with strong absorber: **(A)** Pyrex rod; **(B)** control rod.

Figure 16. The strong absorber would dramatically influence the neutron flux and raise challenges to the resonance calculation. In this section, VERA 2F, 2G, and 2H problems are selected to verify the capability of the FSM to strong absorber problems. The geometry configuration of these two problems is similar to Figure 5B, and the only difference is the guide tubes that are inserted by Pyrex rods, AIC control rods, and B_4C control rods for 2F, 2G, and 2H, respectively. The Pyrex or control rod is divided by 10 equal-volume rings, while the UO_2 pin is divided by three rings. Moreover, each ring is further divided into eight equal-volume sectors.

Figures 17–19 display the calculation results of normalized pin power of VERA 2F, 2G, and 2H, respectively. The distribution of pin power tends to be flat in the lattice center but increases evidently near the lattice surface area. The fuel pin beside the guide tubes with a strong absorber has the lowest pin power. For 2F and 2H, the FSM has satisfactory calculation results for both two problems and the relative error for most fuel pins is less than 0.5%. For 2G, the average error increases to 0.74%. The largest relative error of 2F, 2G, and 2H is 0.75, 1.47, and 1.07%, respectively. Since AIC has a very strong absorption effect, the error of VERA 2G is relatively larger than that of the others, but the precision on the whole is still acceptable. The general calculation results of pin power and k_{eff} are shown in Table 11, which indicates that the FSM could handle the strong absorber problems accurately.

3.5 Analysis of calculation efficiency

Compared with the conventional subgroup method, the group structure of the FSM is optimized to fine mesh according to the basic idea of the ultra-fine group method. The two-level discrete with fine mesh and subgroup structure makes the FSM capable of handling more complex resonance interference effects accurately. In essence, the FSM is the

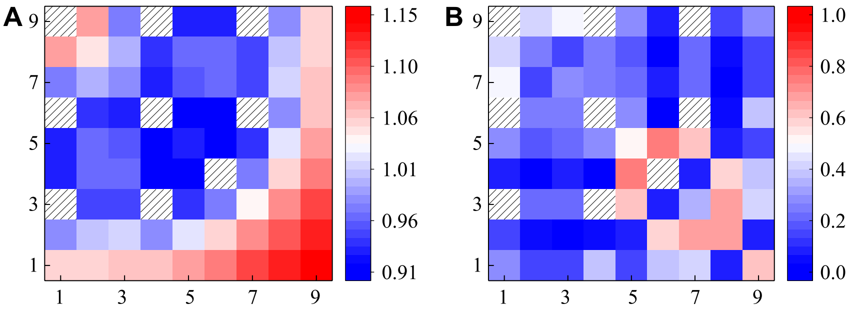

FIGURE 17
Calculation results of pin power of the VERA 2F lattice: **(A)** referenced normalized pin power; **(B)** absolute value of relative deviation/%.

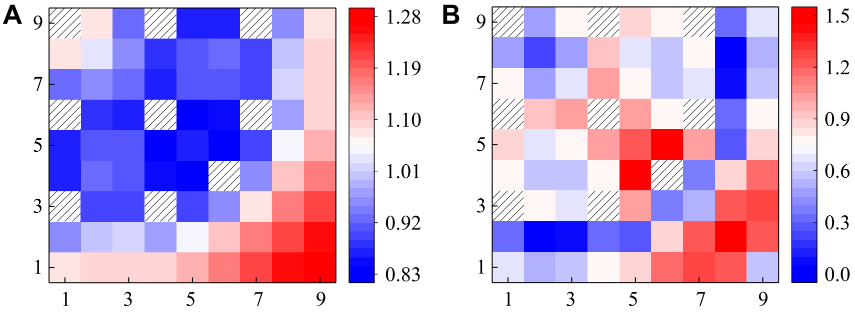

FIGURE 18
Calculation results of pin power of the VERA 2G lattice: **(A)** referenced normalized pin power; **(B)** absolute value of relative deviation/%.

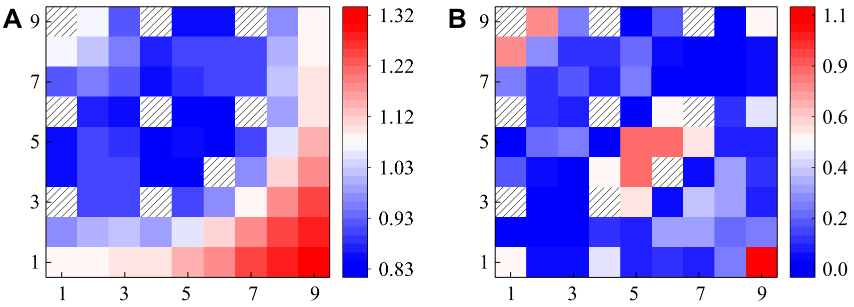

FIGURE 19
Calculation results of pin power of VERA 2H lattice: **(A)** referenced normalized pin power; **(B)** absolute value of relative deviation/%.

compromise between precision and efficiency. It has the same level of accuracy as the UFG and addresses the limitations that the conventional subgroup method does not have the capability for complex problems. In general, the FSM sacrifices part of the calculation efficiency reasonably to achieve higher accuracy.

The calculation efficiency could be reflected by the number of subgroup fixed-source equations and slowing-down equations. Taking the fresh UO_2 problem and its depletion condition as examples, Table 12 shows the calculation burden for different resonance treatment methods. It could be observed that the UFG needs to solve the 34,000 ultra-fine group slowing-down equation for all problems, so the calculation efficiency is the worst. The BIM needs to solve the subgroup fixed-source equation of each resonant nuclide. Iteratively, the total calculation burden increases linearly by the number of resonant nuclides. The

TABLE 11 Calculation results for VERA 2F, 2G, and 2H lattice problems.

VERA 17 × 17 lattice	Relative error of normalized pin power			k_{eff}		k_{eff} error/pcm
	Maximum (%)	Average %)	RMS (%)	Reference	FSM	
2F: 24 Pyrex rods	0.75	0.30	0.36	0.97602	0.97557	-45
2G: 24 AIC rods	1.47	0.74	0.35	0.84769	0.84885	116
2H: 24 B_4C rods	1.07	0.27	0.38	0.78822	0.78843	21

TABLE 12 Calculation burden for different resonance treatment methods.

Depletion condition	FSM			BIM (subgroup fixed-source equation)	UFG (slowing-down equation)
	Subgroup fixed-source equation	Slowing-down equation	Total		
Fresh UO_2	16	289	305	106	34,000
60 GWd/t	56	289	345	346	34,000

FSM adopts the one-group micro-level optimization, so the burden of the subgroup fixed-source equation is far less than that of BIM. Moreover, the FSM has 289 slowing-down equations to solve, and it is independent of the problem condition. Therefore, for the fresh UO_2 problem, the total calculation burden of the FSM is more than that of BIM. However, for the depletion condition, since the number of resonant nuclides increases, seven resonant nuclides are treated as resonant nuclides. Under this condition, the calculation burden of the FSM and BIM is almost the same. If the resonant nuclide number continues to increase, the efficiency of the FSM would be better while the accuracy is also higher. The CPU information in this section is AMD Ryzen7 4800H 2.90 GHz 1 CPU is used. For the fresh UO_2 problem, the calculation time consumed by the FSM, BIM, and UFG is 4.85 s, 2.76 s, and 347.5 s, respectively. For the depletion condition, the calculation time consumed by the FSM, BIM, and UFG is 7.67, 7.26, and 527.1 s, respectively On the whole, compared with the conventional BIM and UFG method, the FSM proposed in this work could handle the resonance effect accurately and efficiently.

3.6 Further discussion of feasible improvement

Based on the PSO theory introduced in Section 2.3, a new energy structure with 19 groups in total is proposed. Compared with the original FSM, the improved FSM has four fast groups, 11 resonance groups, and four thermal groups. The fine resonance mesh would be condensed to 11 groups, while the data of the fast and thermal regions are provided by the NJOY code. Since the PSO is carried out before the eigenvalue calculation, its results are stored in the multigroup library as the input information. Therefore, although the PSO method may suffer from the inefficiency problem, it is a “one-off” work. Once it has been conducted, the optimized group structure could be used for all problems without further burden.

To test the performance of the new structure, six problems consisted of JAEA UO_2 and MOX of three temperatures, respectively. The calculation results of two versions of the FSM are shown in Table 13.

From Table 13, the new FSM has an acceptable difference in eigenvalue accuracy but has far fewer group numbers for transport calculation, which would make a significant improvement in efficiency. However, it should be noticed that the fine-mesh structure of the FSM also accounts for plenty of calculation burden. The PSO method could also be applied to searching for the optimized fine structure with as few groups as possible. In addition, it could be found that the UO_2 problems in Table 13 have more deviations than MOX cases. The errors of MOX and UO_2 cases mainly result from the following reasons:

First, the group condensation process inevitably enlarges the deviation since the coarse group structure would make the self-shielding effect not comprehensively considered. The group structure selected may not be the proper one for all problems. Second, the fitness function in this work only considered the accuracy of k_{eff}, while the other important parameters, such as reaction rate and neutron flux, are not taken into account. This thoughtlessness might cause unexpected errors in practical application. Third, the fitness function selected several typical problems as the calculation samples. In other words, the G_{best} is found according to a finite number of fuel conditions, so the extension to all conditions may cause deviations.

TABLE 13 Calculation results for UO_2 and MOX problems with the optimized FSM.

Case	Description	k_{eff}		k_{eff} error/pcm
		Original FSM	Optimized FSM	
1	UO_2 300K	1.531156	1.531736	−58
2	UO_2 600K	1.432500	1.433590	−109
3	UO_2 900K	1.417656	1.418866	−121
4	MOX 300K	1.264269	1.264199	7
5	MOX 600K	1.241725	1.241725	0
6	MOX 900K	1.233390	1.233380	1

Therefore, further research is still needed for the amendment of the new FSM based on PSO optimization.

4 Conclusion

The fine-mesh subgroup method (FSM) and its feasible improvement are illustrated in this paper. The FSM adopts the two-level discretion consisting of the fine mesh and the subgroup to guarantee the accuracy of the resonance cross-section and the resonance interference correction could be avoided. In addition, the FSM uses the one-group micro-level optimization and the subgroup fixed-source equations are only solved eight times for each resonant nuclide. Afterward, the neutron slowing-down equation is applied to get the spectrum for group condensation. To find the proper group structure for the multigroup transport calculation, the particle swarm optimization method (PSO) is used and the 19-group structure is proposed. Similarly, PSO could also be applied to find the optimized fine-mesh structure of the FSM and further work is needed.

Data availability statement

The raw data supporting the conclusion of this article will be made available by the authors, without undue reservation.

Author contributions

SL, QZ, and LL proposed the research point, conducted the program coding and manuscript writing. YZ and JH supervised this study. XW, LJ, and XL participated in the work of the formula derivation. All the authors contributed to the manuscript's supervision and revision.

Funding

This work is supported by China Postdoctoral Science Foundation grant 2022M48884, the National Natural Science Foundation of China grant 12105063, the Science and Technology on Reactor System Design Technology Laboratory grant HT-KFKT-24-2021011, the Stability Support Fund for Key Laboratory of Nuclear Data grant JCKY2021201C154, and the project of Young Talents of China National Nuclear Corporation.

Conflict of interest

The authors declare that the research was conducted in the absence of any commercial or financial relationships that could be construed as a potential conflict of interest.

Publisher's note

References

Akbari, M., Minuchehr, A., Zolfaghari, A., and Khoshahval, F. (2012). An investigation for an optimized neutron energy-group structure in thermal lattices using Particle Swarm Optimization. *Ann. Nucl. Energy* 47, 53–61. doi:10.1016/j.anucene.2012.02.016

Aldama, D., Leszczynski, F., and Trkov, A. (2003). *WIMS-D library update*. Austria: International Atomic Energy Agency.

Askew, J., Fayers, F., and Kemshell, P. (1966). A general description of lattice code WIMS. *J. Br. Nucl. Energy Soc.* 5, 546–585.

Bondarenko, I. I. (1964). *Group constants for nuclear reactor calculations*. New York, USA: Consultants Bureau.

Canbakan, A., and Hebert, A. (2015). Accuracy of a 2-level scheme based on a subgroup method for pressurized water reactor fuel assembly models. *Ann. Nucl. Energy* 81, 164–173. doi:10.1016/j.anucene.2015.03.034

Choi, S., Smith, K., Lee, H. C., and Lee, D. (2015). Impact of inflow transport approximation on light water reactor analysis. *J. Comput. Phys.* 299, 352–373. doi:10.1016/j.jcp.2015.07.005

Choi, S., Lee, C., and Lee, D. (2017). Resonance treatment using pin-based pointwise energy slowing-down method. *J. Comput. Phys.* 330, 134–155. doi:10.1016/j.jcp.2016.11.007

Cullen, D. (1977). *Calculation of probability table parameters to include intermediate resonance self-shielding*. Livermore, USA: Lawrence Livermore National Laboratory. UCRL-79761.

Downar, T., Kochunas, B., and Collins, B. (2016). "Validation and verification of the MPACT code," in Proceedings of the PHYSOR 2016. Sun valley January 2016, (USA: Idaho).

Edgar, C. A., Yi, C., and Sjoden, G. (2015). Automatically optimized collapsed neutron energy group structure using particle swarm optimization, Proceedings of the Joint international conference on mathematics and computation (M&C), supercomputing in nuclear applications (SNA) and the Monte Carlo. USA: MC) Method. NashvilleTN.

Godfrey, A. T. (2013). *VERA core physics benchmark progression problem specifications*. Oak Ridge, USA: Oak Ridge National Laboratory, 793.

He, Q., Chen, J., Liu, Z., Cao, L., and Wu, H. (2020). The on-the-fly subgroup method capable of treating spatial self-shielding, resonance interference and temperature distribution effects. *Prog. Nucl. Energy* 119 (), 103173. doi:10.1016/j.pnucene.2019.103173

Hebert, A. (2009). Development of the subgroup projection method for resonance self-shielding calculations. *Nucl. Sci. Eng.* 162, 56–75. doi:10.13182/nse162-56

Hébert, A., and Marleau, G. (1991). Generalization of the stamm'ler method for the self-shielding of resonant isotopes in arbitrary geometries. *Nucl. Sci. Eng.* 108 (3), 230–239. doi:10.13182/nse90-57

Hébert, A., and Santamarina, A. (2008). "Refinement of the Santamarina-Hfaiedh energy mesh between 22.5 eV and 11.4 keV," in Proceedings of the International conference on reactor physics (Switzerland: Interlaken).July 2008,

Hfaiedh, N., and Santamarina, A. (2005). *M&C: International conference on mathematics and computational methods applied to nuclear science and engineering*. France: Avignon.Determination of the optimized shem mesh for neutron transport calculations

Hong, S. G., and Cho, N. Z. (1998). Crx: A code for rectangular and hexagonal lattices based on the method of characteristics. *Ann. Nucl. Energy* 25 (8), 547–565. doi:10.1016/s0306-4549(97)00113-8

Ishiguro, Y., and Takano, H. (1971). *Peaco: A code for calculation of group constant of resonance energy region in heterogeneous systems*. Ibaraki, Japan: Atomic Energy Research Institute. No.JAERI-1.

Joo, H. G., Kim, G. Y., and Pogosbekyan, L. (2009). Subgroup weight generation based on shielded pin-cell cross section conservation. *Ann. Nucl. Energy* 36 (7), 859–868. doi:10.1016/j.anucene.2009.03.017

Kennedy, J., and Eberhart, R. (1995). "Particle swarm optimization," in *Proceedings of IEEE international conference on neural networks*, 1942–1948.

Kim, K. S., and Hong, S. G. (2011). The method of characteristics applied to solving slowing down equation to estimate the self-shielded resonance cross sections with an explicit geometrical effect. *Ann. Nucl. Energy* 38 (2–3), 438–446. doi:10.1016/j.anucene.2010.09.022

Kim, K. S., and Williams, M. L. (2019). Spatially dependent embedded self-shielding method for nonuniform temperature distribution. *Ann. Nucl. Energy* 132, 563–575. doi:10.1016/j.anucene.2019.06.043

Li, S., Zhang, Q., Zhang, Z., Zhao, Q., and Liang, L. (2021). Improved subgroup method coupled with particle swarm optimization algorithm for intra-pellet non-uniform temperature distribution problem. *Ann. Nucl. Energy* 153, 108070. doi:10.1016/j.anucene.2020.108070

Li, S., Zhang, Z., Zhang, Q., Hao, C., and Zhao, Q. (2019). Analysis of categorical subgroup method for resonance self-shielding treatment. *Front. Energy Res.* 7 (48), 1–12. doi:10.3389/fenrg.2019.00048

Li, S., Zhang, Z., Zhang, Q., and Zhao, Q. (2020). Improvements of subgroup method based on fine group slowing-down calculation for resonance self-shielding treatment. *Ann. Nucl. Energy* 136, 106992. doi:10.1016/j.anucene.2019.106992

Liu, Y., Martin, W., Williams, M., and Kim, K. (2015). A full-core resonance self-shielding method using a continuous-energy quasi-one-dimensional slowing-down solution that accounts for temperature-dependent fuel subregions and resonance interference. *Nucl. Sci. Eng.* 180, 247–272. doi:10.13182/nse14-65

Liu, Z., He, Q., Zu, T., Cao, L., Wu, H., and Zhang, Q. (2018). The pseudo-resonant-nuclide subgroup method based global–local self-shielding calculation scheme. *J. Nucl. Sci. Technol.* 55 (2), 217–228. doi:10.1080/00223131.2017.1394232

Macfarlane, R., Muir, D. W., Boicourt, R. M., Kahler, A. C., III, and Conlin, J. L. (2016). *The NJOY nuclear data processing system, version 2016*. LA-UR: Los Alamos National Laboratory, 19–33.

Nikolaev, M., Ignatov, A., Isaev, N., and Khokhlov, V. (1971). The method of subgroups for considenring the resonance structure of the cross sections in neutron calculations. *Sov. A. T. Energy* 30, 426–430.

Park, H., and Joo, H. G. (2019). Effective subgroup method employing macro level grid optimization for LWR applications. *Ann. Nucl. Energy* 129, 461–471. doi:10.1016/j.anucene.2019.02.005

Peng, S., Jiang, X., Zhang, S., and Wang, D. (2013). Subgroup method with resonance interference factor table. *Ann. Nucl. Energy* 59, 176–187. doi:10.1016/j.anucene.2013.04.005

Sohail, M., and Kim, M. H. (2015). Estimation of self-shielded cross section by employing interference correction factors in subgroup method. *Prog. Nucl. Energy* 79, 150–157. doi:10.1016/j.pnucene.2014.11.008

Song, P., Zhang, Z., Liang, L., Zhang, Q., and Zhao, Q. (2019). Implementation and performance analysis of the massively parallel method of characteristics based on GPU. *Ann. Nucl. Energy* 131, 257–272. doi:10.1016/j.anucene.2019.02.026

Stamm'ler (2008). *HELIOS methods*. Nyköping, Sweden: Studsvik Scandpower.

Sugimura, N., and Yamamoto, A. (2007). Resonance treatment based on ultra-fine-group spectrum calculation in the AEGIS code. *J. Nucl. Sci. Technol.* 44 (7), 958–966. doi:10.1080/18811248.2007.9711335

Williams, M. L. (1983). Correction of multigroup cross sections for resolved resonance interference in mixed absorbers. *Nucl. Sci. Eng.* 83, 37–49. doi:10.13182/nse83-2

Williams, M. L., and Kim, K. S. (2012). *The embedded self-shielding method, Proc. PHYSOR 2012*. KnoxvilleUSA: Tennessee.

X-5 Monte Carlo Team (2003). *Mcnp - a general N-particle transport code, version 5 - volume I: Overview and theory. LA-UR-03-1987*. Los Alamos, USA: Los Alamos National Laboratory.

Yamamoto, A., Ikehara, T., Ito, T., and Saji, E. (2002). Benchmark problem suite for reactor physics study of LWR next generation fuels. *J. Nucl. Sci. Technol.* 39 (8), 900–912. doi:10.1080/18811248.2002.9715275

Yamamoto, A., Tabuchi, M., Sugimura, N., Ushio, T., and Mori, M. (2007). Derivation of optimum polar angle quadrature set for the method of characteristics based on approximation error for the bickley function. *J. Nucl. Sci. Technol.* 44 (2), 129–136. doi:10.1080/18811248.2007.9711266

Yi, C., and Sjoden, G. (2013). Energy group structure determination using particle swarm optimization. *Ann. Nucl. Energy* 56, 53–56. doi:10.1016/j.anucene.2012.12.020

Zhang, Q., Qin, S., Zhao, Q., Liang, L., Wu, H., and Cao, L. (2020). Improvements on the method of ultra-fine-group slowing-down solution coupled with method of characteristics on irregular geometries. *Ann. Nucl. Energy* 136, 107017. doi:10.1016/j.anucene.2019.107017

Zhang, Q., Wu, H., Cao, L., and Zheng, Y. (2015). An improved resonance self-shielding calculation method based on equivalence theory. *Nucl. Sci. Eng.* 179 (3), 233–252. doi:10.13182/nse13-108

Zhang, Q., Zhao, Q., Yang, W. S., Wu, H., Zhang, Q., Zhao, Q., et al. (2018). Modeling of resonance-interference effect in depleted fuel compositions by pseudo resonant isotopes. *Nucl. Sci. Eng.* 191 (1), 46–65. doi:10.1080/00295639.2018.1429174

Zu, T., Xia, F., and Wu, H. (2019). An improved fitting method for subgroup parameters based on the heterogeneous cells. *J. Nucl. Sci. Technol.* 56 (2), 179–192. doi:10.1080/00223131.2018.1545609

frontiers | Frontiers in Energy Research

TYPE Original Research
PUBLISHED 09 January 2023
DOI 10.3389/fenrg.2022.1010482

OPEN ACCESS

EDITED BY
Shichang Liu,
North China Electric Power University,
China

REVIEWED BY
Qingquan Pan,
Shanghai Jiao Tong University, China
Jiankai Yu,
The University of Tennessee, Knoxville,
United States

*CORRESPONDENCE
Guanbo Wang,
wgb04dep@hotmail.com

SPECIALTY SECTION
This article was submitted to Nuclear Energy,
a section of the journal Frontiers in Energy Research

RECEIVED 03 August 2022
ACCEPTED 20 September 2022
PUBLISHED 09 January 2023

CITATION
Guo X, Wang G and Wang K (2023), Convergence characteristics and acceleration of the transient fixed source equation solved by Monte Carlo method.
Front. Energy Res. 10:1010482.
doi: 10.3389/fenrg.2022.1010482

Convergence characteristics and acceleration of the transient fixed source equation solved by Monte Carlo method

Xiaoyu Guo[1], Guanbo Wang[1]* and Kan Wang[2]

[1]Institute of Nuclear Physics and Chemistry, China Academy of Engineering Physics, Mianyang, China, [2]Department of Engineering Physics, Tsinghua University, Beijing, China

The safety analysis of nuclear systems such as nuclear reactors requires transient calculation. The Monte Carlo (MC) method has grown rapidly in recent years because of its high-fidelity modelling and simulation capability. The predictor-corrector quasi-static (PCQS) MC method has been investigated for kinetic calculation. However, the approach to shorten the computational time required to solve the transient fixed source equation (TFSE) is still under development. The convergence characteristic of the neutron source iteration algorithm of the PCQS MC method is analyzed in this study with a simplified model. It is found that the convergence rate of the iteration algorithm is governed by the effective spectral radius (ESR). The lower the ESR is, the faster the convergence is. In order to reduce the ESR, the asymptotic superhistory method (ASM) is developed for the PCQS MC method in the RMC code. The performance of ASM is evaluated by the C5G7-TD benchmark. Results show that the reduction in the number of inactive cycles is more than 85%, and over 15% of computational time including active cycles is saved. It is demonstrated how ASM speeds up the iterations using the Wasserstein distance measure.

KEYWORDS

PCQS, Monte Carlo, fixed-source equation, asymptotic superhistory method, convergence

1 Introduction

High-fidelity simulations for nuclear systems such as nuclear reactors and spent fuel reprocessing solutions have been developed rapidly in the last decade. In particular, the exponential increase of high-performance computing accelerates the implementation of high-fidelity simulations in engineering fields. Among many high-fidelity simulation methods, the Monte Carlo (MC) method is widely regarded as the most accurate method and is usually used for validations of other methods. The MC method has two major advantages: one is the usage of accurate continuous-energy cross-sections, and another is the precise 3-dimensional (3D) geometry modeling based on constructive solid geometry (CSG) or computer-aided design (CAD) geometry (Wilson et al., 2010; Davis et al., 2020; Deng et al., 2022). MC codes such as MCNP

(Goorley et al., 2012), Serpent (Leppänen et al., 2015), OpenMC (Romano et al., 2015), and RMC (Wang et al., 2015) are widely used in new reactor designs, which have disparate features from normal nuclear reactors in geometry, material, and spectra.

Typically, the MC method is capable of steady state simulations, including criticality calculation and shielding calculation, etc. Kinetic simulation functions are not as well-developed as steady state simulation functions for many MC codes. However, transient behaviors are fundamental and essential in the safety analysis of nuclear systems. The lack of kinetic simulation functions severely limits MC codes' further applications. Therefore, many studies concerning kinetic simulation methods are under development.

Generally, kinetic MC methods could be divided into two kinds: one is the direct MC kinetic simulation method, and another is the hybrid MC kinetic simulation method with deterministic methods. The direct MC kinetic simulation method includes Dynamic Monte Carlo (DMC) method (Sjenitzer and Hoogenboom, 2013; Jia et al., 2022) and similar methods which implement acceleration skills such as quasi-static treatments (Trahan, 2019). The direct method simulates the neutron flight and delayed neutron precursors variation with a continuous-in-time model, which is very accurate but causes massive computational consumption. The hybrid MC kinetic simulation method with deterministic methods include the time-dependent coarse mesh finite difference method (TD-CMFD) based on the multi-group cross-sections tallied from a MC solver (Shaner, 2018; Kreher et al., 2022), the transient fission matrix method (TFM) (Heuer et al., 2015), the time-dependent response matrix (TDRM) method (Mickus et al., 2020), and the predictor-corrector quasi-static (PCQS) method (Jo et al., 2016). Among the above methods, the TD-CMFD, TFM and TDRM methods require extra treatment on space meshing before calculation. As a result, the suited geometries are limited. By comparison, the PCQS method is still based on continuous-energy cross-sections and arbitrary complex geometries, and thus has an advantage in modelling flexibility.

A complete PCQS MC calculation consists of a series of single MC calculations at successive time steps. Every single MC calculation solves a transient fixed-source equation (TSFE), except for the first time step at which the eigenvalue equation is solved. Usually, solving the fixed-source equation by MC method does not need any iteration algorithm, but the neutron tracking may not terminate when calculating transient supercritical problems with a large time step (Jo et al., 2016). Therefore, the neutron source iteration algorithm is used to solve both the TFSEs and the eigenvalue equation. **Figure 1** shows the flow chart of a complete PCQS MC calculation. Consequently, the computational cost of a complete PCQS MC calculation is tens of or even hundreds of times of a single MC criticality calculation, depending on the number of time steps. It is necessary then to accelerate the calculation, especially to reduce iterations for fission source and external source convergence.

Jo et al. (2016) proposed a partial current-based CMFD (p-CMFD) acceleration method, which has been the only acceleration method for PCQS MC calculation. As mentioned before, the CMFD method requires space meshing, which limits the capability to solve problems with irregular geometries.

Many previous studies have proposed methods to accelerate neutron source iterations. There are two kinds of acceleration methods. The first kind uses space meshing, including the fission matrix method (Kuroishi and Nomura, 2003; Dufek and Gudowski, 2009), the CMFD method (Lee et al., 2010; Yun and Cho, 2010), the functional Monte Carlo (FMC) method (Larsen and Yang, 2011), etc. These methods are all sensitive to the meshing methods, which are highly dependent on the users' experience. Besides, some methods need a vast footprint, and some are only suited for nuclear systems with regular shapes, which eliminates the MC method's advantage in free 3D modeling. The second kind is independent of space meshing, including the Wielandt's method (Yamamoto and Miyoshi, 2004; Brown, 2007; She et al., 2015; Pan et al., 2022c), the superhistory method (Brissenden and Garlick, 1986; She et al., 2015; Mickus and Dufek, 2018; Pan et al., 2022c), the neutron population growth method (Mickus and Dufek, 2018; Pan et al., 2022a), and the source extrapolation method (Pan et al., 2022b). Wielandt's method is based on the shifted inverse power method (Bronson et al., 2013). Other methods are based on the property that iteration computational cost is directly proportional to the neutron history number while the statistical error is in reverse proportion to the square root of the neutron history number. However, the above methods have only been applied to criticality problems where the eigenvalue equation is solved.

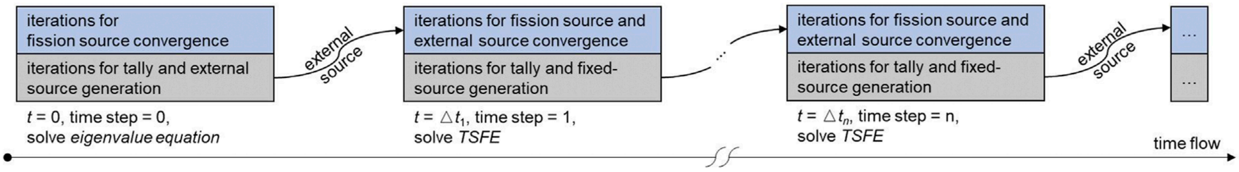

FIGURE 1
Flow chart of the PCQS MC calculation.

In this study, the asymptotic superhistory method (ASM) is developed to accelerate the neutron source iterations in solving TFSE. The basic theory is introduced in Section 2. Section 3 shows the numerical simulations and performance. Section 4 makes the conclusion.

2 Methodology

2.1 Transient fixed source equation of the predictor-corrector quasi-static method and the neutron source iteration algorithm

Before introducing the asymptotic superhistory method for TFSE, the deduction of TFSE is provided herein, and the iteration algorithm is discussed.

The TFSE is the key equation of the PCQS method. The fundamental equations of the PCQS method were firstly developed for deterministic codes (Dulla et al., 2008). The PCQS equations are derived from the time-dependent Boltzmann neutron transport equation:

$$
\begin{aligned}
&\frac{1}{v}\frac{\partial \Phi(\boldsymbol{r},\boldsymbol{\Omega},E,t)}{\partial t}+L\Phi(\boldsymbol{r},\boldsymbol{\Omega},E,t)+T\Phi(\boldsymbol{r},\boldsymbol{\Omega},E,t)\\
&\quad=S\Phi(\boldsymbol{r},\boldsymbol{\Omega},E,t)+\frac{\chi_p(E)}{4\pi}\left(1-\sum_{i=1}^{d}\beta_i\right)F\Phi(\boldsymbol{r},\boldsymbol{\Omega},E,t)\\
&\qquad+\sum_{i=1}^{d}\frac{\chi_i(E)}{4\pi}\lambda_i C_i(\boldsymbol{r},t),
\end{aligned}
\tag{1}
$$

and the delayed precursor transport equation:

$$
\frac{\partial C_i(r,t)}{\partial t}=\beta_i F\Phi(\boldsymbol{r},\boldsymbol{\Omega},E,t)-\lambda_i C_i(\boldsymbol{r},t),
\tag{2}
$$

where $\boldsymbol{r}$ is the neutron position, $\boldsymbol{\Omega}$ is the neutron flying angle, E is the neutron energy, t is the time, Φ is the neutron flux, v is the neutron speed, χ_p is the prompt neutron energy spectra, i is the delayed neutron family, χ_i is the delayed neutron energy spectra of family i, β_i is the delayed neutron fraction of family i, λ_i is the delayed constant of family i, C_i is the delayed neutron precorsor concentration of family i. $L\Phi$ is the leakage operator, $T\Phi$ is the collision operator, $S\Phi$ is the scattering operator, and $F\Phi$ is the fission operator. Definitions of the operators in Eqs. 1, 2 could be found in Rao et al. (2019).

In the PCQS method, the implicit backward difference time discretization strategy is applied. At time step t_{n+1}, the partial differential terms in Eqs. 1, 2 are expressed as follows:

$$
\begin{aligned}
\frac{\partial \Phi(\boldsymbol{r},\boldsymbol{\Omega},E,t)}{\partial t}&\approx\frac{\tilde{\Phi}(\boldsymbol{r},\boldsymbol{\Omega},E,t_{n+1})-\Phi(\boldsymbol{r},\boldsymbol{\Omega},E,t_n)}{\Delta t_{n+1}},\\
\frac{\partial C_i(\boldsymbol{r},t)}{\partial t}&\approx\frac{\tilde{C}_i(\boldsymbol{r},t_{n+1})-C_i(\boldsymbol{r},t_n)}{\Delta t_{n+1}},
\end{aligned}
\tag{3}
$$

where $\Delta t_{n+1}=t_{n+1}-t_n$.

Replace all t in Eqs. 1, 2 with t_{n+1} except the partial item, substituting Eq. 3 into Eqs. 1, 2, and rearranging gives the predicted neutron flux equation:

$$
\begin{aligned}
&L\tilde{\Phi}(\boldsymbol{r},\boldsymbol{\Omega},E,t_{n+1})+T'\tilde{\Phi}(\boldsymbol{r},\boldsymbol{\Omega},E,t_{n+1})-S\tilde{\Phi}(\boldsymbol{r},\boldsymbol{\Omega},E,t_{n+1})\\
&\quad=\left[\frac{\chi_p(E)}{4\pi}\left(1-\sum_{i=1}^{d}\beta_i\right)+\sum_{i=1}^{d}\frac{\chi_i(E)}{4\pi}\frac{\lambda_i\Delta t_{n+1}}{1+\lambda_i\Delta t_{n+1}}\beta_i\right]\\
&\qquad\times F\tilde{\Phi}(\boldsymbol{r},\boldsymbol{\Omega},E,t_{n+1})+S_n(\boldsymbol{r},\boldsymbol{\Omega},E,t_{n+1}),
\end{aligned}
\tag{4}
$$

where $T'\Phi$ is the PCQS leakage operator and S_n is the external source (PCQS source). Denote that

$$
\begin{aligned}
M\tilde{\Phi}_{n+1}=&\,L\tilde{\Phi}(\boldsymbol{r},\boldsymbol{\Omega},E,t_{n+1})+T'\tilde{\Phi}(\boldsymbol{r},\boldsymbol{\Omega},E,t_{n+1})\\
&-S\tilde{\Phi}(\boldsymbol{r},\boldsymbol{\Omega},E,t_{n+1}),
\end{aligned}
\tag{5}
$$

and

$$
\begin{aligned}
F\tilde{\Phi}_{n+1}=&\left[\frac{\chi_p(E)}{4\pi}\left(1-\sum_{i=1}^{d}\beta_i\right)+\sum_{i=1}^{d}\frac{\chi_i(E)}{4\pi}\frac{\lambda_i\Delta t_{n+1}}{1+\lambda_i\Delta t_{n+1}}\beta_i\right]\\
&\times\int\!\!\int v\Sigma_f(\boldsymbol{r},E',t_{n+1})\tilde{\Phi}(\boldsymbol{r},\boldsymbol{\Omega}',E',t_{n+1})\,\mathrm{d}E'\mathrm{d}\boldsymbol{\Omega}',
\end{aligned}
\tag{6}
$$

and then Eq. 4 becomes:

$$
M\tilde{\Phi}_{n+1}=F\tilde{\Phi}_{n+1}+S_n,
\tag{7}
$$

which is obviously a fixed-source equation. Therefore, Eq. 4 is the TFSE of the PCQS method.

The MC codes usually use a direct method to solve Eq. 7:

$$
\tilde{\Phi}_{n+1}=(M-F)^{-1}S_n,
\tag{8}
$$

however, there are several problems to use Eq. 8 to solve TFSE:

- As Jo et al. (2016) stated, the neutron history may not terminate when Δt_{n+1} is not sufficiently small, which means that Eq. 8 does not have solutions. This characteristics will also be shown in Section 2.2.
- Code users cannot control statistical errors conveniently. Due to the variation of the geometries or materials during the transient process, the neutron multiplication characteristics differs at each time step. Consequently, the simulated neutron history number varies at different time steps. The estimated statistical errors may be significant in deep sub-critical conditions and minor in super-critical states.

Thus, the neutron source iteration algorithm is used instead, which is similar to that used in deterministic methods (Turinsky et al., 1994):

$$
\tilde{\Phi}_{n+1}^{(j+1)}=M^{-1}F\tilde{\Phi}_{n+1}^{(j)}+M^{-1}S_n,
\tag{9}
$$

where (j) is the serial number of iterations. $F\tilde{\Phi}_{n+1}^{(j)}$ are fission neutron sources generated at (j)th iteration at t_{n+1}. Mixing the external sources S_n generated at t_n with the fission neutron sources $F\tilde{\Phi}_{n+1}^{(j)}$ by the ratio of the external source strength to the total source strength yields the neutron sources prepared for the next $(j+1)$th iteration, and track the neutrons sampled from the neutron sources to obtain $\tilde{\Phi}^{(j+1)}$. The iteration stops at the total cycle set by the code users. The tally starts at the end of the inactive cycle. The process is just the same as that of the criticality calculation.

2.2 Convergence characteristics of the neutron source iteration algorithm

Before developing the acceleration algorithm, it is necessary to analyze the convergence characteristics of **Eq. 9**. Because **Eq. 9** is closely related to the model complexity and does not have a common analytical solution, a 0-dimensional and mono-energy model with single family delayed neutron precorsor is used herein, which can also reveal the essence.

For the simplified model, **Eqs. 1**, **2** become:

$$\frac{1}{v}\frac{\mathrm{d}\Phi(t)}{\mathrm{d}t} + \Sigma_a(t)\Phi(t) = (1-\beta)\nu\Sigma_f(t)\Phi(t) + \lambda c(t), \tag{10}$$

and

$$\frac{\mathrm{d}c(t)}{\mathrm{d}t} = \beta\nu\Sigma_f(t)\Phi(t) - \lambda c(t). \tag{11}$$

To obtain the PCQS fixed source equation corresponding to **Eqs.10**, **11** the implicit difference strategy is implemented:

$$\begin{aligned}\frac{\mathrm{d}\Phi(t)}{\mathrm{d}t} &= \frac{\Phi_{n+1}-\Phi_n}{\Delta t_{n+1}},\\ \frac{\mathrm{d}c(t)}{\mathrm{d}t} &= \frac{c_{n+1}-c_n}{\Delta t_{n+1}}.\end{aligned} \tag{12}$$

Substituting **Eq. 12** into **Eqs. 10**, **11** and rearranging gives:

$$\Phi_{n+1} = g_{n+1}\Phi_{n+1} + s_n, \tag{13}$$

where s_n is the external source:

$$s_n = \frac{1}{1+v\Delta t_{n+1}\Sigma_{a,n+1}}\left(\Phi_n + \frac{v\Delta\lambda t_{n+1}}{1+\lambda\Delta t_{n+1}}c_n\right), \tag{14}$$

and g_{n+1} is a coefficient:

$$g_{n+1} = \left(1-\frac{\beta}{1+\lambda\Delta t_{n+1}}\right)\frac{k_{\mathrm{eff},n+1}}{1+\dfrac{1}{v\Delta t_{n+1}\Sigma_{a,n+1}}}, \tag{15}$$

where $k_{\mathrm{eff},n+1}$ is the effective multiplication factor of the simplified model at $t = t_{n+1}$ without external sources:

$$k_{\mathrm{eff},n+1} = \frac{\nu\Sigma_{f,n+1}}{\Sigma_{a,n+1}}. \tag{16}$$

Eq. 13 is the TFSE of this simplified model. When solving **Eq. 13** using the fixed-point iteration method, the iteration format is:

$$\Phi_{n+1}^{(j+1)} = g_{n+1}\Phi_{n+1}^{(j)} + s_n, \tag{17}$$

Therefore, this paper called g_{n+1} the equivalent spectral radius (ESR) of the TFSE. The condition that **Eq. 17** is converged is:$|g_{n+1}| < 1$. Obviously, $g_{n+1} > 0$, and thus the convergence condition is:

$$g_{n+1} < 1. \tag{18}$$

Besides, the closer to 1 the g_{n+1} is, the lower the convergence rate is.

It is found that $k_{\mathrm{eff},n+1} \le 1$ sets up **Eq. 18**, which means that the iteration is converged if the model at $t = t_{n+1}$ is critical or subcritical without external sources. When the model is supercritical, substituting **Eq. 15** into **Eq. 18** and rearranging yields a quadratic inequality:

$$a\Delta^2 t_{n+1} + b\Delta t_{n+1} - 1 < 0, \tag{19}$$

where

$$a = \lambda v\left(\nu\Sigma_{f,n+1} - \Sigma_{a,n+1}\right) \tag{20}$$

and

$$b = (1-\beta)v\nu\Sigma_{f,n+1} - \left(v\Sigma_{a,n+1} + \lambda\right). \tag{21}$$

Because $k_{\mathrm{eff},n+1} > 1$, $a > 0$, and thus $b^2 + 4a > 0$. Therefore, the quadratic fucntion

$$h\left(\Delta t_{n+1}\right) = a\Delta^2 t_{n+1} + b\Delta t_{n+1} - 1 \tag{22}$$

is a parabola going upwards, and **Eq. 19** has analytical solution:

$$0 < \Delta t_{n+1} < \frac{-b+\sqrt{b^2+4a}}{2a}. \tag{23}$$

Eq. 23 shows that when the model is supercritical without external sources, the time step should be sufficiently small to make sure that the iteration is converged. Besides, direct solution by $\Phi_{n+1} = s_n/(1-g_{n+1})$ will give meaningless results that $\Phi_{n+1} < 0$ when $g_{n+1} > 1$, which is consistent with the discussion in Section 2.1.

Extrapolating from the study of the simplified model, the time step should be small enough when the model is supercritical, and the neutron source iteration is unconditional convergence when the model is subcritical or critical without external sources. The convergence rate can be increased by a lower ESR, which can be used to speed up TFSE iterations. The asymptotic superhistory approach is used in this paper to reduce ESR.

2.3 The asymptotic superhistory acceleration method

The superhistory method was proposed by Brissenden and Garlick (1986) to accelerate the MC criticality calculation. The

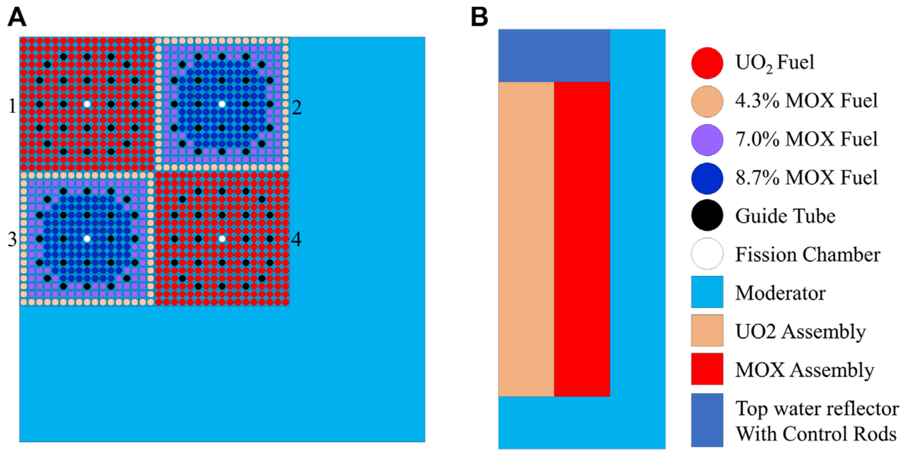

Horizontal cross-section of the C5G7-TD model.

Vertical cross-section of the C5G7-TD model.

FIGURE 2
Geometry configuration of the C5G7-TD benchmark. **(A)** Horizontal and **(B)** vertical cross-section of the C5G7-TD model.

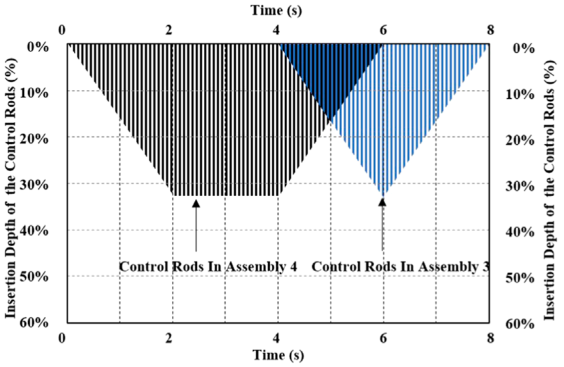

FIGURE 3
Control rod movement in TD4-4.

MC criticality calculation solves the eigenvalue equation by neutron source iterations:

$$\Phi^{(j+1)} = \frac{1}{k_{\mathrm{eff}}} M^{-1} F \Phi^{(j)}. \tag{24}$$

The convergence rate of Eq. 24 is determined by the dominance ratio $dr(M^{-1}F)$ which is less than 1. Reducing $dr(M^{-1}F)$ can speed up the iteration. The superhistory method modify the eigenvalue equation to:

$$\Phi^{(j+1)} = \frac{1}{k_{\mathrm{eff}}^{N}} \left(M^{-1}F\right)^{N} \Phi^{(j)}, \tag{25}$$

and the dominance ratio is reduced to $dr\left[\left(M^{-1}F\right)^{N}\right] = dr^{N}\left(M^{-1}F\right)$. Accordingly, the fission sources are tracked through N generations in one cycle.

Similarly, the superhistory method is applied to the TFSE as follows:

$$\begin{aligned}\Phi^{(j+1)} &= \left(M^{-1}F\right)^{N} \Phi^{(j)} \\ &\quad + \left(I + M^{-1}F + \cdots + \left(M^{-1}F\right)^{N-1}\right) S_n,\end{aligned} \tag{26}$$

and the ESR $\rho(M^{-1}F)$ is reduced to $\rho\left[\left(M^{-1}F\right)^{N}\right]$. Accordingly, the fission sources and the external sources are tracked and mixed through N generations in one cycle.

Note that the Wielandt method is not applicable, because the Wielandt method is based on the shifted inverse power method, which is only suitable for solving the eigenvalue problems. However, the TFSE is a nonhomogeneous equation and thus only the ASM method is suitable.

Based on the effective DR measure, a metric of the computational burden, She et al. (2015) proved, however, that the superhistory method could not shorten the calculation time because every cycle requires additional time. The ASM (She et al., 2015), which lowers each generation's neutron history number by a set of predetermined factors, is suggested as a remedy, and used in this paper:

1) Given the neutron population of each cycle m.
2) Input the asymptotic factors $N_1, N_2, \ldots, N_n$ and asymptotic period p. Notably, $N_1 > N_2 > \cdots > N_n$.
3) Starting from the first cycle, the neutron population is changed to m/N_1. Then, one cycle consists of N_1 generations.
4) After p cycles, change the neutron population to m/N_2 and run p cycles.
5) Repeat until finishing $n \times p$ cycles.
6) Change the neutron population back to m and execute the simulation as usual.

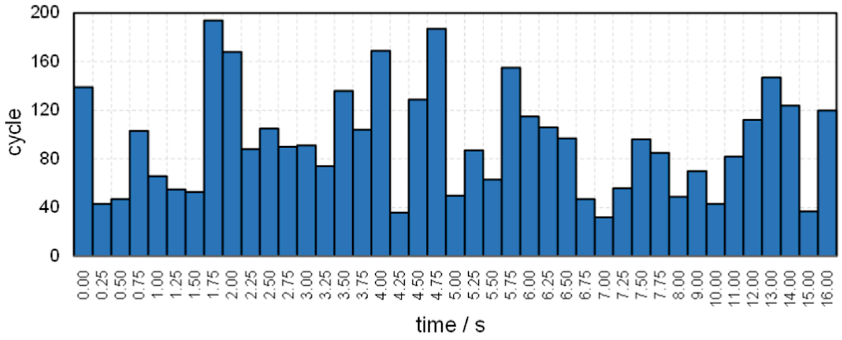

FIGURE 4
The convergence cycles of TD4-4, given by **Eq. 28**.

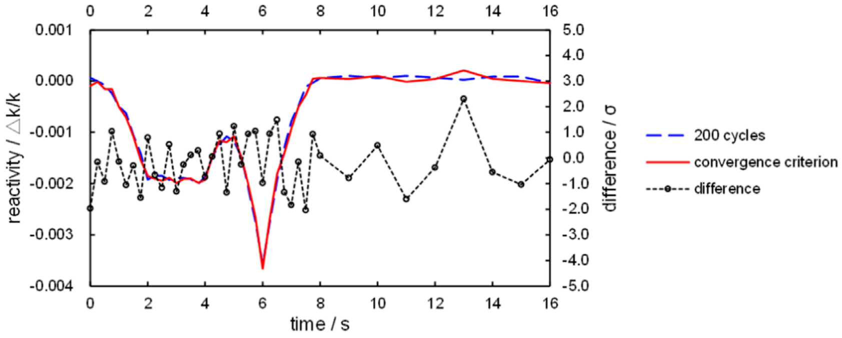

FIGURE 5
Comparison of reactivity profiles, obtained by setting 200 inactive cycles and using **Eq. 28**.

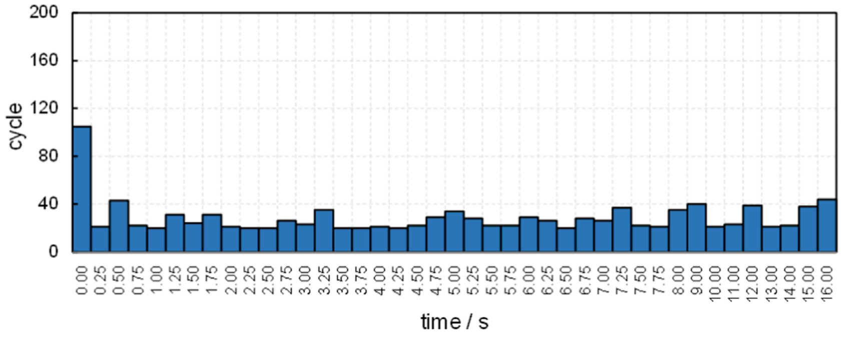

FIGURE 6
The convergence cycles given by **Eq. 28**, after accelerating TD4-4's transient calculation by ASM.

The algorithm is implemented in the RMC code (Wang et al., 2015). The asymptotic factors are $16, 8, 4, 2$ and the asymptotic periods are 5, by default, and thus the acceleration lasts for 20 cycles. Default asymptotic parameters are used in **Section 3**, however user-defined parameters are also allowed.

3 Results and discussion

The ASM's performance is evaluated in this section. In order to more effectively compare the convergence characteristic with and without the superhistory method, this work uses the Wasserstein distance (WD) measure (Guo et al., 2022) as defined

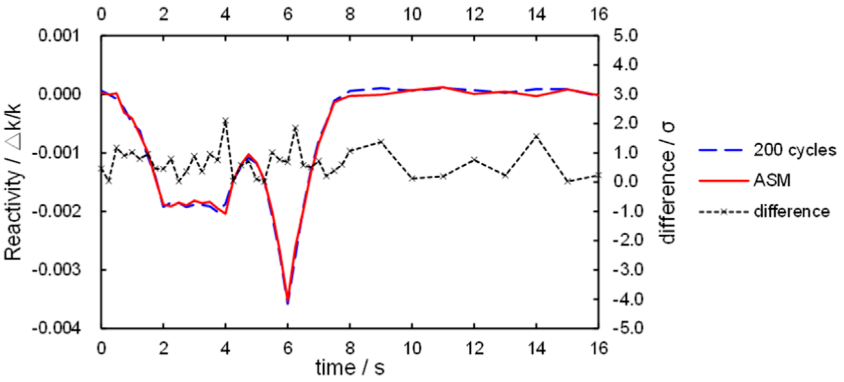

FIGURE 7
Comparison of reactivity profiles, obtained by setting 200 inactive cycles and using ASM.

TABLE 1 Performance of ASM.

Parameter	200 inactive cycles	Convergence cycle accelerated by ASM
Total simulation cycles	24600	17572
Total computational time (CPU hours)	856	722
Speed up ratio		1.19

by Eq. 27, which is similar to the progress relative entropy but performs better:

$$\mathrm{WD}_{r,j} = \frac{1}{m}\sum_{i}^{m} |d^*_{i,j} - d^*_{i,2}|, j \geq 2, \tag{27}$$

where $\mathrm{WD}_{r,j}$ is WD of cycle j in the r direction (r can be x, y or z), i is the neutron index, and $d^*_{i,j}$ is the coordinate of neutron i after sorting. The Wasserstein distance's physical meaning is the average distance between neutrons in cycle j and cycle 2.

Besides, an experience-based convergence criterion is employed:

$$j - j_{\min} > \frac{j_{\max}}{\ln j}, \tag{28}$$

where $j_{\max} = \max(\mathrm{WD}_{r,2}, \mathrm{WD}_{r,3}, \ldots, \mathrm{WD}_{r,j})$ and $j_{\min} = \min(\mathrm{WD}_{r,j_{\max}}, \mathrm{WD}_{r,j_{\max}+1}, \ldots, \mathrm{WD}_{r,j})$. This convergence criterion make use of the property that WD has a monotonically increasing trend. The meaning of Eq. 28 is that WD fluctuates within the range $(\mathrm{WD}_{r,j_{\max}}, \mathrm{WD}_{r,j_{\min}})$ over an experience-based number of cycles, $j_{\max}/\ln j$. $j_{\max}$ is larger as the convergence rate is lower, and the fluctuation process to reach convergence is longer since $j_{\max}/\ln j$ is larger. The validity of this convergence criterion is provided below, based on the test case from the C5G7-TD benchmark (Hou et al., 2017).

3.1 The C5G7-TD benchmark and the TD4-4 case

The C5G7-TD benchmark consists of a set of kinetic and transient test cases. Figure 2 depicts a quarter of its geometry model, with Figures 2A,B showing the 2-dimensional (2D) geometry and the 3D geometry's expansion down the z-axis, respectively. Guo et al. (2021) simulated all subcritical kinetic cases using the RMC code.

The C5G7-TD benchmark has 28 subcritical kinetic cases. The TD4-4 case is a 3D transient, driven by the control rod (CR) movement shown in Figure 3. Initially, the CRs in assembly 4 are inserted. After 2 s the insertion stops at one-third depth of the assembly, and then the CRs stay in the position. At the end of 4 s, the CRs in assembly 4 are withdrawn, meanwhile the CRs in assembly 3 are inserted. After 2 s, the CRs in assembly 4 are fully out of the core, and the CRs in assembly 3 stops insertion and are withdrawn until the end of 8 s.

3.2 Validation of the convergence criterion

The previous study (Guo et al., 2021) employed 200 inactive cycles and 400 active cycles for TD4-4's convergence at all time steps, and the results showed good agreement with other codes. The reason for a global inactive cycle configuration throughout the transient is that the convergence is unknown in advance, and

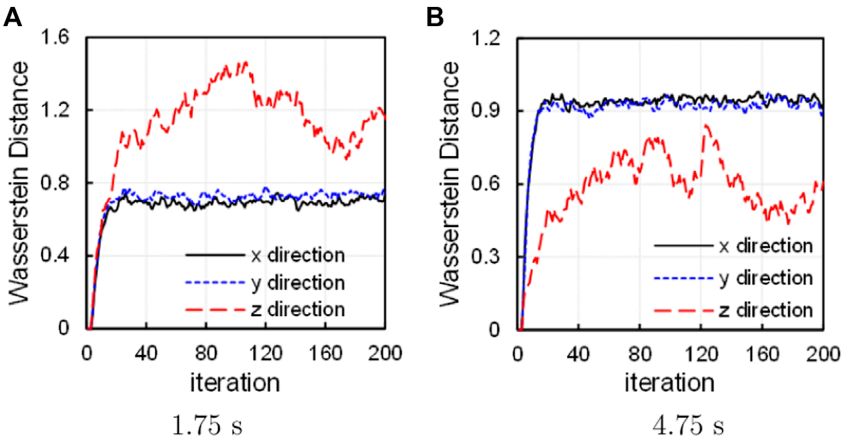

FIGURE 8
WD curves at **(A)** 1.75 s and **(B)** 4.75 s, without ASM.

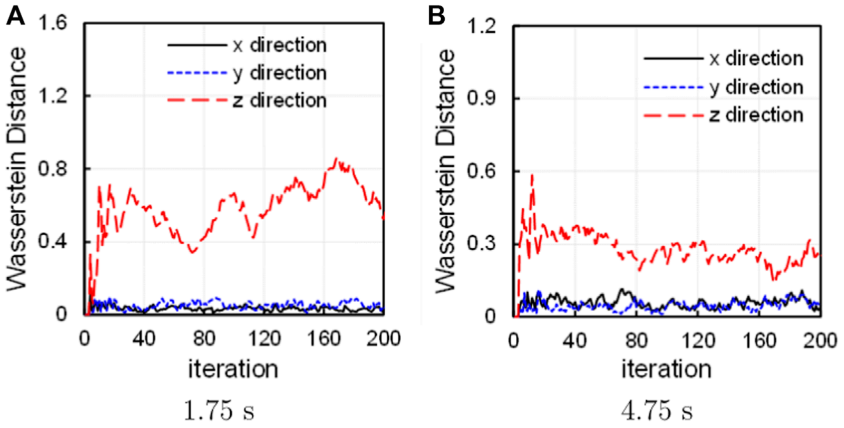

FIGURE 9
WD curves at **(A)** 1.75 s and **(B)** 4.75 s, with ASM.

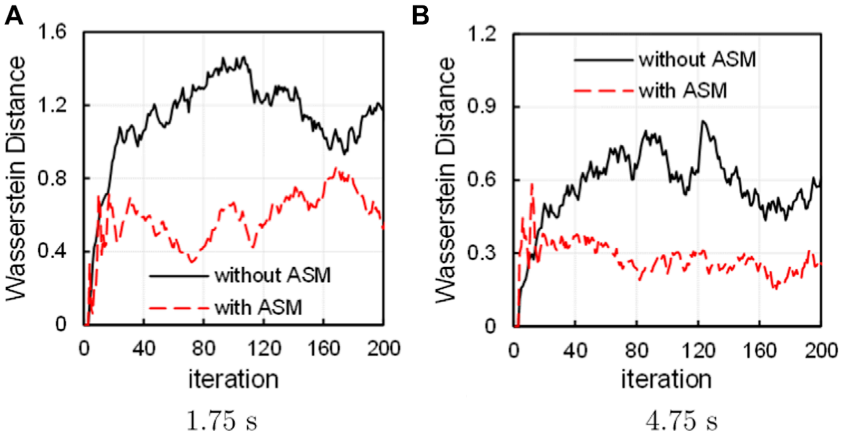

FIGURE 10
Comparison of Wasserstein distance curves in the *z* direction at **(A)** 1.75 s and **(B)** 4.75 s.

thus a conservative value is required. Using **Eq. 28**, the cycles at which the neutron source iteration achieves convergence are displayed in **Figure 4**.

Nearly half of the time steps require over 100 iterations to converge. Especially, time step $t = 1.75$ s requires a maximum of 194 iterations, and time step $t = 4.75$ s requires a second maximum of 187 iterations. Both are close to but still less than 200. Therefore, the convergence criterion demonstrates the conservatism of the previous configuration.

A comparative calculation is performed to further validate the convergence criterion, in which the inactive cycle configurations are set as the declared convergence iterations shown in **Figures 4**, **5** compares the reactivity results. It is found that the reactivity profile obtained by fewer iterations given by **Eq. 28** is in good agreement with that obtained by 200 iterations, with all time-steps' deviation less than 3 times the standard deviation. Therefore, the convergence criterion can be used to determine the convergence iteration. At least, it is valid for the TD4-4 case.

3.3 Performance of the asymptotic superhistory method

To accelerate the entire TD4-4 transient calculation, the ASM is used. After acceleration, the convergence iterations given by **Eq. 28** are shown in **Figure 6**. When compared to **Figure 4**, the asymptotic super history method significantly speeds up the neutron source iteration. Notably, the convergence cycles are reduced at every time step.

Figure 7 provides the comparison of reactivity profiles obtained with and without ASM. It is observed that two reactivity curves agree well statistically. Therefore, implementation of ASM does not reduce the accuracy of the result.

The whole TD4-4 transient consists of 41 time steps, and the previous study used a total of 8,200 inactive cycles. Applying the asymptotic super history method reduces the number of inactive cycles to 1,172, a reduction of more than 85%. Considering that a complete MC calculation consists of both inactive and active cycles, the total simulation cycles and the total computational time are compared, and the results are listed in **Table. 1**. It is found that over 15% of the total computational cost is saved.

3.4 Inspection of the convergence process

A detailed inspection into the convergence process is studied using WD curves. Since the slowest convergence occurs at $t = 1.75$ s and $t = 4.75$ s as **Figure 4** shows, the two time steps are selected to apply WD diagnostics. The Wasserstein diagnostics curves are depicted in **Figures 8A,B** at the two time steps.

In the x and y direction, the WD curves exhibit steep rising edge and rapidly reaches stable after less than 20 cycles. However, in the z direction, the WD curves rise slowly, which slows down the convergence. Besides, the WDz curves show distinct fluctuation, which indicates that the neutron source distribution is oscillating along the z direction. One of the reason is that the length of the active region along the z direction is 128.52 cm, three times of that along the x and y directions (42.84 cm). Another reason is that this study uses a quarter core model, in which the left and up boundary conditions in **Figure 2A** are reflective along x and y directions, while the up and down boundary conditions in **Figure 2B** are crossing along z directions. Therefore, the neutron source distribution trends to oscillate around the axis of symmetry along the z direction.

It is also noted that the WDz curve is higher than the WDx and WDy curves at $t = 1.75$ s, while the WDz curve is lower at $t = 4.75$ s. Only the CRs in assembly 4 is moving vertically at $t = 1.75$ s, which causes larger changes of the neutron source distribution along the z direction. However, at $t = 4.75$ s the CRs in both assembly 3 and 4 are moving oppositely, and thus the neutrons are flowing from assembly 3 into assembly 4, causing larger changes in the horizontal direction.

After applying ASM, the WD curves exhibit significant changes, as shown in **Figure 9**. The curves in the x and y direction stable at much faster speed and lower level ($WD < 0.1$) than the curves in **Figure 8**. Considering the first asymptotic factor is 16, the neutron source distribution in the x and y direction is accelerated by 16 times the original convergence speed as revealed by **Eq. 26**. Because the neutron source distribution along the x and y directions converges at less than 20 cycles in **Figure 8**, the curves in the x and y direction after applying the ASM method stable after 2 cycles theoretically. Because WD uses the second cycle as the reference, the WDx and WDy values are as small as their fluctuation range.

In the z direction, however, the WD curves stable at a little higher level than those in the x and y direction. **Figure 10** compares the WD_z curves with and without ASM. It is found that the WD_z curves obtained with ASM are lower than those without ASM, which indicates that the convergence is accelerated in the first cycle because the neutrons of next cycles become closer to those of the second cycle. Therefore, the WD results also proves the acceleration capability of ASM.

4 Conclusion

The acceleration problem in the MC PCQS calculation is studied in this paper. TFSE and the corresponding neutron source iteration algorithm are introduced, as well as the reason to use iterations. A simplified model is used to analyze the iteration convergence features of TFSE. It is found that reducing ESR is capable of accelerating the iteration convergence. Therefore, ASM is developed for MC PCQS to decrease inactive cycle numbers and lower the computational cost. The performance is tested with the TD4-4 case of the C5G7-TD benchmark. Results show that the number of inactive cycles is reduced by more than 85% compared with the previous study, and over 15% of the total computational cost is saved. Using the Wasserstein distance measure, it is found that ASM considerably speeds up the convergence of the neutron source distributions along the x and y directions. The iteration is also accelerated along the z direction. As predicted by the convergence characteristic analysis using the simplified model, the time step affects the convergence, which will be studied in the future.

Data availability statement

The original contributions presented in the study are included in the article/Supplementary Material, further inquiries can be directed to the corresponding author.

Author contributions

XG: Conceptualization, Modeling, Formal Analysis, Writing-original draft and revising. GW: Conceptualization, Supervision, Writing-review and editing. KW: Funding Acquistion.

Funding

This work was supported by the National Key Research and Development Project of China (Grant No: 2020YFB1901700).

Conflict of interest

The authors declare that the research was conducted in the absence of any commercial or financial relationships that could be construed as a potential conflict of interest.

Publisher's note

References

Brissenden, R. J., and Garlick, A. R. (1986). Biases in the estimation of keff and its error by Monte Carlo methods. *Ann. Nucl. Energy* 13, 63–83. doi:10.1016/0306-4549(86)90095-2

Bronson, R., Costa, G. B., and Saccoman, J. T. (2013). *Linear algebra: Algorithms, applications, and techniques*.

Brown, F. B. (2007). *Wielandt acceleration for mcnp5 Monte Carlo eigenvalue calculations*.

Davis, A., Shriwise, P., and Zhang, X. (2020). "Dag-openmc: Cad-based geometry in openmc," in Transactions - 2020 Virtual Conference.

Deng, L., Li, G., Zhang, B.-Y., Li, R., Zhang, L.-Y., Wang, X., et al. (2022). A high fidelity general purpose 3-d Monte Carlo particle transport program jmct3. 0. *Nucl. Sci. Tech.* 33, 108–118. doi:10.1007/s41365-022-01092-0

Dufek, J., and Gudowski, W. (2009). Stability and convergence problems of the Monte Carlo fission matrix acceleration methods. *Ann. Nucl. Energy* 36, 1648–1651. doi:10.1016/j.anucene.2009.07.020

Dulla, S., Mund, E. H., and Ravetto, P. (2008). The quasi-static method revisited. *Prog. Nucl. Energy* 50, 908–920. doi:10.1016/j.pnucene.2008.04.009

Goorley, T., James, M., Booth, T., Brown, F., Bull, J., Cox, L., et al. (2012). Initial mcnp6 release overview. *Nucl. Technol.* 180, 298–315. doi:10.13182/nt11-135

Guo, X., Li, Z., Huang, S., and Wang, K. (2022). Convergence diagnostics for Monte Carlo fission source distributions using the wasserstein distance measure. *Nucl. Eng. Des.* 389, 111675. doi:10.1016/j.nucengdes.2022.111675

Guo, X., Shang, X., Song, J., Shi, G., and Wang, K. (2021). Kinetic methods in Monte Carlo code rmc and its implementation to c5g7-td benchmark. *Ann. Nucl. Energy* 151, 107864. doi:10.1016/j.anucene.2020.107864

Laureau, A., Aufiero, M., Rubiolo, P. R., Merle-Lucotte, E., Heuer, D., et al. (2015). Transient fission matrix: Kinetic calculation and kinetic parameters beta(eff) and lambda(eff) calculation. *Ann. Nucl. energy* 85, 1035–1044.

Hou, J. J., Ivanov, K. N., Boyarinov, V. F., and Fomichenko, P. A. (2017). Oecd/nea benchmark for time-dependent neutron transport calculations without spatial homogenization. *Nucl. Eng. Des.* 317, 177–189. doi:10.1016/j.nucengdes.2017.02.008

Jia, C., Jian, L., Guo, X., Wang, K., Huang, S., and Liang, J. (2022). Development of an improved direct kinetic simulation capability in rmc code. *Ann. Nucl. Energy* 173, 109110. doi:10.1016/j.anucene.2022.109110

Jo, Y., Cho, B., and Cho, N. Z. (2016). Nuclear reactor transient analysis by continuous-energy Monte Carlo calculation based on predictor-corrector quasi-static method. *Nucl. Sci. Eng.* 183, 229–246. doi:10.13182/nse15-100

Kreher, M. A., Shaner, S., Forget, B., and Smith, K. (2022). Frequency transform method for transient analysis of nuclear reactors in Monte Carlo. *Nucl. Sci. Eng.* 2022, 1–12. doi:10.1080/00295639.2022.2067739

Kuroishi, T., and Nomura, Y. (2003). Development of fission source acceleration method for slow convergence in criticality analyses by using matrix eigenvector applicable to spent fuel transport cask with axial burnup profile. *J. Nucl. Sci. Technol.* 40, 433–440. doi:10.1080/18811248.2003.9715377

Larsen, E. W., and Yang, J. (2011). A functional Monte Carlo method for k-eigenvalue problems. *Nucl. Sci. Eng.* 159, 107–126. doi:10.13182/nse07-92

Lee, M. J., Joo, H. G., Lee, D., and Smith, K. (2010). "Investigation of cmfd accelerated Monte Carlo eigenvalue calculation with simplified low dimensional multigroup formulation," in PHYSOR 2010.

Leppänen, J., Pusa, M., Viitanen, T., Valtavirta, V., and Kaltiaisenaho, T. (2015). The serpent Monte Carlo code: Status, development and applications in 2013. *Ann. Nucl. Energy* 82, 142–150. doi:10.1016/j.anucene.2014.08.024

Mickus, I., and Dufek, J. (2018). Optimal neutron population growth in accelerated Monte Carlo criticality calculations. *Ann. Nucl. Energy* 117, 297–304. doi:10.1016/j.anucene.2018.03.046

Mickus, I., Roberts, J. A., and Dufek, J. (2020). Stochastic-deterministic response matrix method for reactor transients. *Ann. Nucl. Energy* 140, 107103. doi:10.1016/j.anucene.2019.107103

Pan, Q., An, N., Zhang, T., Liu, X., Cai, Y., Wang, L., et al. (2022a). Single-step Monte Carlo criticality algorithm. *Comput. Phys. Commun.* 279, 108439. doi:10.1016/j.cpc.2022.108439

Pan, Q., Cai, Y., Wang, L., Zhang, T., Liu, X., and Wang, K. (2022b). Source extrapolation scheme for Monte Carlo fission source convergence based on rmc code. *Ann. Nucl. Energy* 166, 108737. doi:10.1016/j.anucene.2021.108737

Pan, Q., Zhang, T., Liu, X., Cai, Y., Wang, L., and Wang, K. (2022c). Optimal batch size growth for wielandt method and superhistory method. *Nucl. Sci. Eng.* 196, 183–192. doi:10.1080/00295639.2021.1968223

Rao, J., Shang, X., Yu, G., and Wang, K. (2019). Coupling rmc and cfd for simulation of transients in treat reactor. *Ann. Nucl. Energy* 132, 249–257. doi:10.1016/j.anucene.2019.04.039

Romano, P. K., Horelik, N. E., Herman, B. R., Nelson, A. G., Forget, B., and Smith, K. (2015). Openmc: A state-of-the-art Monte Carlo code for research and development. *Ann. Nucl. Energy* 82, 90–97. doi:10.1016/j.anucene.2014.07.048

Shaner, S. C. (2018). *Development of high fidelity methods for 3d Monte Carlo transient analysis of nuclear reactors*.

She, D., Wang, K., and Yu, G. (2015). Asymptotic wielandt method and superhistory method for source convergence in Monte Carlo criticality calculation. *Nucl. Sci. Eng.* 172, 127–137. doi:10.13182/NSE11-44

Sjenitzer, B. L., and Hoogenboom, J. E. (2013). Dynamic Monte Carlo method for nuclear reactor kinetics calculations. *Nucl. Sci. Eng.* 175, 94–107. doi:10.13182/nse12-44

Trahan, T. J. (2019). A quasi-static Monte Carlo algorithm for the simulation of sub-prompt critical transients. *Ann. Nucl. Energy* 127, 257–267. doi:10.1016/j.anucene.2018.11.055

Turinsky, P. J., Al-Chalabi, R. M., Engrand, P., Sarsour, H. N., Faure, F. X., and Guo, W. (1994). "NESTLE: Few-group neutron diffusion equation solver utilizing the nodal expansion method for eigenvalue, adjoint, fixed-source steady-state and transient problems," in *Tech. rep.* (Idaho Falls, Idaho: Idaho National Lab., USA).

Wang, K., Li, Z., She, D., Xu, Q., Qiu, Y., Yu, J., et al. (2015). Rmc–a Monte Carlo code for reactor core analysis. *Ann. Nucl. Energy* 82, 121–129. doi:10.1016/j.anucene.2014.08.048

Wilson, P., Tautges, T. J., Kraftcheck, J. A., Smith, B. M., and Henderson, D. L. (2010). Acceleration techniques for the direct use of cad-based geometry in fusion neutronics analysis. *Fusion Eng. Des.* 85, 1759–1765. doi:10.1016/j.fusengdes.2010.05.030

Yamamoto, T., and Miyoshi, Y. (2004). Reliable method for fission source convergence of Monte Carlo criticality calculation with wielandt's method. *J. Nucl. Sci. Technol.* 41, 99–107. doi:10.1080/18811248.2004.9715465

Yun, S., and Cho, N. Z. (2010). Acceleration of source convergence in Monte Carlo k-eigenvalue problems via anchoring with a p-cmfd deterministic method. *Ann. Nucl. Energy* 37, 1649–1658. doi:10.1016/j.anucene.2010.07.018

frontiers | Frontiers in Energy Research

TYPE Original Research
PUBLISHED 11 January 2023
DOI 10.3389/fenrg.2022.1013004

EDITED BY
Jingang Liang,
Tsinghua University, China

REVIEWED BY
Wenbin Wu,
Sun Yat-sen University, China
Chen Hao,
Harbin Engineering University, China

*CORRESPONDENCE
Li Qing,
email@uni.edu

SPECIALTY SECTION
This article was submitted to Nuclear Energy,
a section of the journal
Frontiers in Energy Research

RECEIVED 06 August 2022
ACCEPTED 05 September 2022
PUBLISHED 11 January 2023

CITATION
Hongbo Z, Wenbo Z, Chen Z, Bo W, Zhang C, Xingjie P, Qing L, Yingrui Y, Zhaohu G and Wei Z (2023), Study on the calculational framework development of the advanced numerical reactor neutronics code SHARK.
Front. Energy Res. 10:1013004.
doi: 10.3389/fenrg.2022.1013004

Study on the calculational framework development of the advanced numerical reactor neutronics code SHARK

Zhang Hongbo, Zhao Wenbo, Zhao Chen, Wang Bo, Chen Zhang, Peng Xingjie, Li Qing*, Yu Yingrui, Gong Zhaohu and Zeng Wei

Science and Technology on Reactor System Design Technology Laboratory, Nuclear Power Institute of China, Chengdu, China

The SHARK program (Simulation-based High-fidelity Advanced Reactor physics Kit) is a high-fidelity heterogeneous neutronics code for the numerical reactor system being developed at the Nuclear Power Institute of China (NPIC). The program uses a Constructive Solid Geometry (CSG) framework to model various complex geometries. To enhance the flexibility and robustness during continuous development process, SHARK program attempts to support a rich set of methods, tools and library options within a unified general framework as a “toolkit”. For the multi-core clustered supercomputer architectures that are commonly used today, the SHARK program adopts a hybrid parallel strategy of MPI and OpenMP to achieve complementary advantages between them. In addition, the framework of SHARK program is designed with a true object-oriented manner. Through reasonable abstraction, inheritance and encapsulation, the maintainability and extensibility of the code are improved, and long-term team development is facilitated. Up to now, key modules for cross-section generation, heterogeneous transport calculation and microscopic depletion have been developed under the general frameworks. The main features of SHARK’s “resonance-transport-depletion” coupling system are elaborated in this paper, and some verification and validation (V&V) results in the current phase are presented and discussed.

KEYWORDS

numerical reactor, neutronics code, framework design, resonance self-shielding, neutron transport, microscopic depletion, V&V

1 Introduction

The innovative numerical reactor concept has been proposed for several years and is continuously developed and refined. Today, numerical reactors in a general sense are often considered as a combination of key elements such as high performance computing platforms, high fidelity and high resolution modeling and simulation, multi-physics and multi-scale coupled analysis. As the core component for the digital twin of nuclear reactors, numerical reactor will play a key role in improving design, exploiting margins, exploring mechanisms, and reducing costs. It will have far-reaching influence on both existing reactors and newly developed reactors.

For numerical reactor systems with multi-physics coupling simulation, high-fidelity neutronics programs for simulating neutron/photon field distribution in the reactor are undoubtedly one of the core engines. Depending on the underlying principles, high-fidelity neutronics computational techniques can be simply divided into Monte Carlo route and deterministic theory route. In recent years, with the rising of numerical reactor, a number of excellent high-fidelity neutronics calculation programs have emerged internationally for application in this field, such as MCNP (Cardoni, 2011), MC21 (Aviles et al., 2016), RMC (Liu et al., 2018), and JMCT (Deng et al., 2018) based on Monte Carlo theory, and MPACT (Kochunas et al., 2013), NECP-X (Chen et al., 2018), DeCART (Joo et al., 2014), nTRACER (Jung, 2013), STREAM (Choi et al., 2019) based on deterministic theory. Excellent work has been done by researchers around the development and application of all these programs.

At the same time, today's high-fidelity neutronics codes still face various challenges to some degrees. First, different types of reactors often have different fuel and structural designs, core arrangements, and control/operation modes. This requires neutronics codes to be adaptable. In terms of geometry modeling, it is worthwhile to investigate how to model complex geometries easily and intuitively, and how to partition and map different levels of meshes efficiently. Sometimes, this can also be solved partly with the help of various advanced multi-physics coupling platforms, such as SALOME, and MOOSE. In terms of fuel simulations, different designs including enrichments and dispersion manners occurs in conventional type fuel and accident resistant fuel (ATF), which can pose a variety of problems on numerical simulations. In terms of the reactor core as a whole, different spectrum characteristic, flux levels and gradients, and dynamic properties place higher demands on the cross-section library and resonance data processing, the fuel depletion chain and algorithms, and also require a more stable and powerful transport solver to support them.

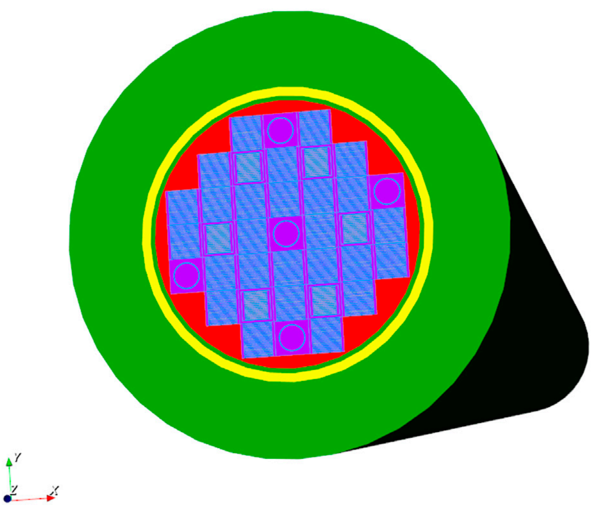

FIGURE 1
CSG modeling function in SHARK program.

Second, high-fidelity neutron transport calculation is always an extremely memory and computation intensive scientific computing task. Therefore, it is necessary to take full advantage of today's rapidly developing high-performance computing platforms. The software parallelism strategies and their implementation techniques should be improved. On the one hand, the parallelizability of specific neutronics algorithms needs to be analyzed in depth. On the other hand, the architecture characteristics of the High Performance Computing (HPC) platform should also be fully considered.

In addition, from the point of view on software engineering, maintainability, scalability, and teamwork development are also key considerations in the software framework design and code development process for such a large-scale scientific computing software.

The SHARK program (Simulation-based High-fidelity Advanced Reactor physics Kit) is a high-fidelity heterogeneous neutronics code for numerical reactor systems being developed at the Nuclear Power Institute of China (NPIC). Like other similar programs, the team is trying to achieve a step-by-step exploration and solution of the aforementioned problems during the development. It uses the popular Constructive Solid Geometry (CSG) strategy for geometric modeling, and an ordered hierarchical structure for grid management and mapping between modules of neutronics calculations. Thus, a wide range of complex problem geometries can be described through text cards or visualization tools under development. The SHARK program attempts to enhance the adaptability and robustness as a "toolkit" by supporting a rich and flexible set of methods, tools and library options within a unified overall framework. For the multi-core clustered supercomputer architectures that are commonly used today, it adopts a hybrid parallelism strategy of MPI and OpenMP to achieve complementary advantages. In addition, the framework of SHARK program is designed with a true object-oriented philosophy. Through reasonable abstraction, inheritance and encapsulation, it improves the maintainability and extensibility of the code and facilitates long-term collaborative team development.

SHARK program is currently being developed continuously according to the above concepts. Up to now, the parts that have been developed or integrated include the main framework, the cross-section library and resonance module, the heterogeneous

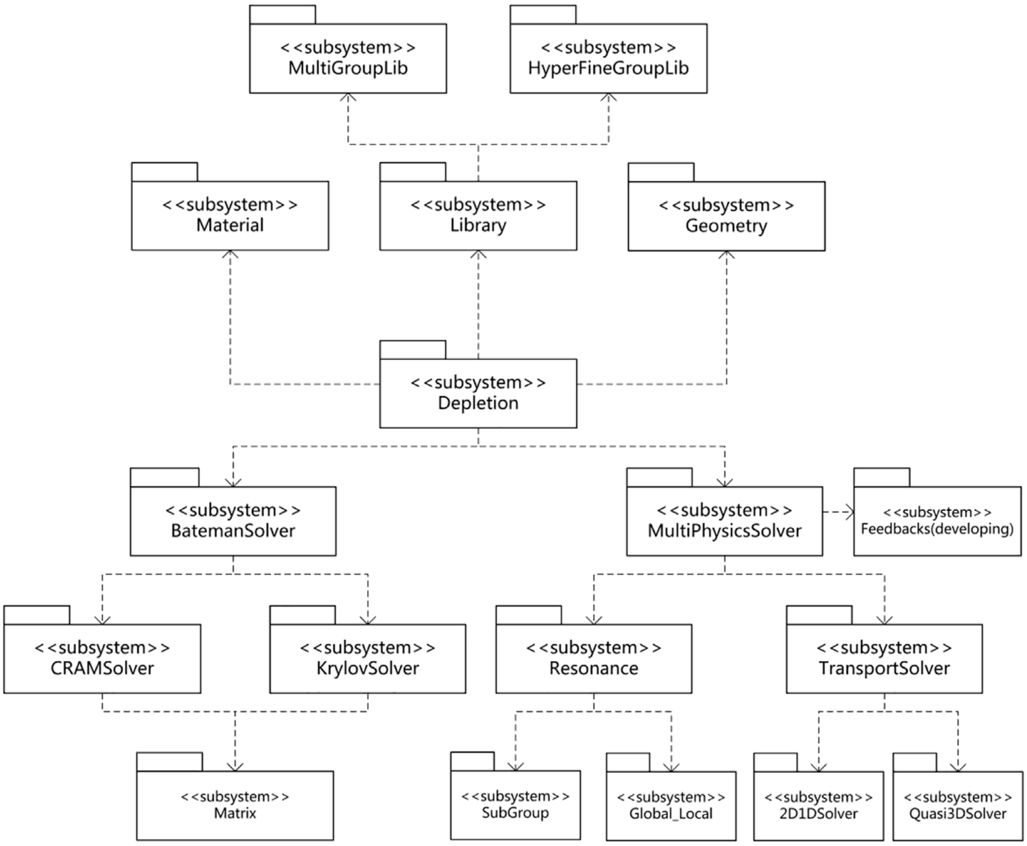

FIGURE 2
Design of the SHARK program framework for depletion.

transport module, the high-fidelity depletion module and relevant utilities. The numerical simulation capability of steady-state and dynamic depletion for heterogeneous neutron transport problems at the microscopic cross-section level has been basically established. For the treatment of resonance self-shielding effects, the SHARK framework currently offers the option of improved subgroup methods (Zhang et al., 2022a) with corresponding cross-section library, and other options like global-local method (He et al., 2018) are also being integrated. For heterogeneous transport calculations, the SHARK program uses the method of characteristics (MOC) and prepares two-dimensional/one-dimensional (2D/1D), quasi-three-dimensional (Quasi-3D) (Zhao et al., 2021) and three-dimensional (3D) options. For the high-fidelity simulation of burnup, the SHARK program supports both power and pure decay modes and considers the burnup characteristics of poisons with rapid reaction rate changes. While using a refined burnup chain, the SHARK program is also designed to support easy switching of the depletion chain and library in order to meet the potential needs of different application scenarios. In addition, the development of functions such as multi-physics coupling, transient calculation, engineering calculation sequences, and output visualization are also underway or forthcoming.

This paper presents the establishment of the “resonance-transport-depletion” coupling calculation system of SHARK, and gives some V&V results of the current phase. The remaining of this paper can be divided into three parts. In Section 2, we present the general framework of the SHARK program, the methodology and technical solutions of the main computational modules. In Section 3, we give some staging results and data analysis of the program. In the last section, we conclude the paper and give some discussions.

2 Methodologies

2.1 General framework

CSG strategies are well known in computer industrial design. In the field of neutronics computing, CSG was first applied in various Monte Carlo software and has recently been applied in deterministic neutron transport software (Boyd et al., 2014). The

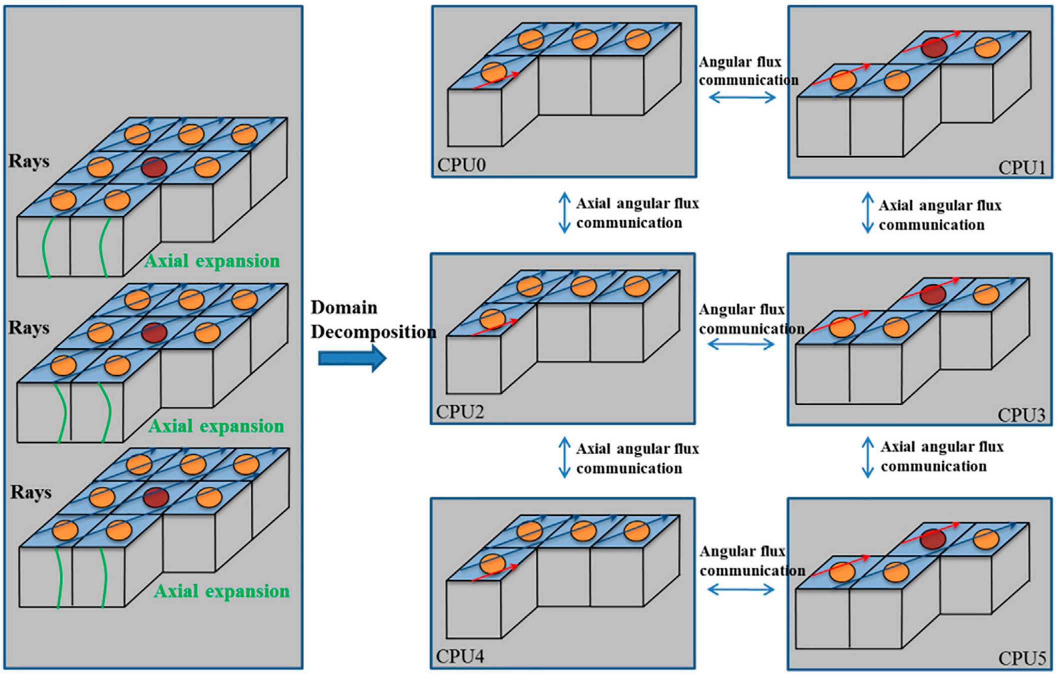

FIGURE 3
Domain decomposition parallel strategy in SHARK program.

SHARK program uses the CSG strategy to describe complex geometric models including two-dimensional and three-dimensional problems. In the CSG model, various surfaces are the most basic constructive elements and they are represented by equations. The geometric modeling module currently used by SHARK supports a variety of planes and quadratic surfaces. By defining surfaces, a number of halfspaces can be partitioned. By performing Boolean operations such as intersection, union, and complement to the halfspaces, the basic unit cell of the CSG geometry is obtained. The entity cells can be filled with material or geometric units. A large number of solid cells form universes by Boolean operations. In addition, repeated structures in the reactor can be easily and quickly defined by means of lattices. In conclusion, hierarchical geometry framework of CSG strategy is highly universal and extensible, which can effectively enhance the front-end geometry modeling capability of the program. At this stage, the SHARK program has successfully tried to model reactor geometry in the form of square and hexagonal lattices with fuel rods or plates (Figure 1).

The logic flow of the high-fidelity neutronics calculation program is relatively complex and has a large number of program modules and coupling interfaces. Therefore, in order to facilitate the integration of different models within the SHARK program framework, we strictly follow the object-oriented programming ideas. In the process of building the main calculational framework, the basic principle of “high cohesion - low coupling” is used to cut the key modules. At the same time, a large number of utility modules are provided to help program developers reuse them. For the different method implementations in the same computational stage, the concept of inheritance between parent and child classes is implemented. For example, “Resonance” class is the parent class of resonance self-shielding computation, which defines the abstraction process, basic data and methods in resonance calculations. “SubGroup” class, “Global-Local” class and other specific resonance methods are the child classes of “Resonance”. They inherit the basic features of the “Resonance” class, but also define different implementation details in an individualized way by static or dynamic polymorphism. The different child classes can be developed, extended and maintained independently under a unified framework. Figure 2 shows a simple illustration of this design philosophy, where a mix of C++ and Python programming is used in the development of SHARK program. In particular, C++ is used to develop the calculational kernel, which facilitates stable and efficient numerical computation. The application interface, on the other hand, is written in Python, which is more user-friendly and extensible.

MPI and OpenMP hybrid parallel strategies are known to perform well in today’s commonly adopted distributed-shared memory supercomputer platforms. MPI technology is used to handle process-level parallelism for distributed memory with

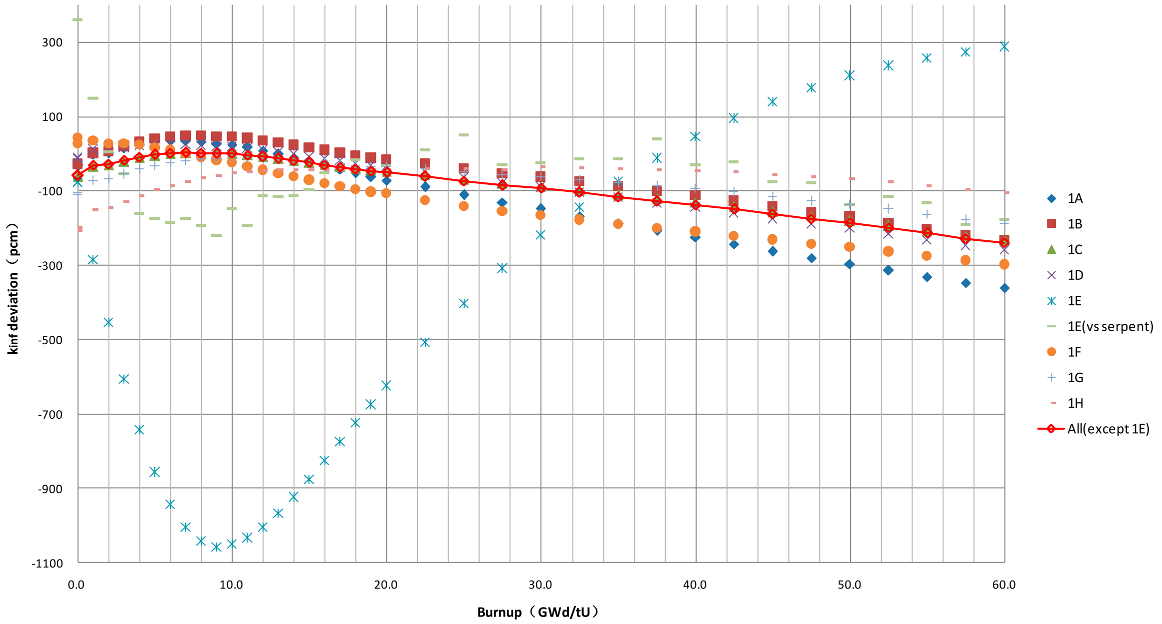

FIGURE 4
Deviation of infinite multiplication factor for VERA1 depletion problem.

good scalability. OpenMP technology is used to handle thread-level parallelism for shared memory with simple implementation and almost without communication latency and load balancing issues. On high performance computing, the SHARK program provides this hybrid parallel architecture. Specifically, the MPI technique is used to handle spatial domain decompositions, with each domain independently performing ray tracing and communicating with neighboring domains on the inner boundary (Figure 3); the OpenMP technique is used to parallelize the sweep of rays, meshes and energy groups. This hybrid parallel strategy can effectively distribute the computation and storage load with good parallel efficiency.

In SHARK program, data is carefully classified and encapsulated. Data inside a class is only available for manipulation by trusted classes. Various pointers are also used in the program implementation to improve data manipulation efficiency and save memory cost. In addition, for some special data, linked lists, binary trees, hash tables and the corresponding sorting and searching algorithms are used effectively.

To ensure compatibility, the programming language standard is used as the basic programming principles. This minimizes the dependence on specific compilers and compilation environments. Some settings that may be related to the system environment are handled using conditional compilation. In addition, common tools for version control and automatic testing are also essential in the code development.

2.2 Cross-Section generation

Cross-section generation plays an important role in neutronics calculations. Especially for a program like SHARK, which is based on the one-step heterogeneous transport theory, the largest source of error and uncertainty in the system comes from the multi-group cross-section generation. It directly affects the accuracy and applicability of the program. The cross-section generation module mainly consists of two parts: resonance calculation and the corresponding nuclear data library. In addition to accuracy and efficiency, the SHARK program imposes other requirements on the resonance effect treatments. On the one hand, it has to be able to provide spatially dependent high-resolution results for multi-physics coupling within the fuel element. On the other hand, it has to be highly geometrically adaptable to meet the application requirements of different reactor types. The subgroup resonance option inside the SHARK program is illustrated (Zhang et al., 2022a).

In the subgroup approach, the effective resonance cross section σ_x is expressed in the form of

$$\sigma_x = \frac{\sum_n w_{x,n}\sigma_{x,n}\phi_n}{\sum_n w_{a,n}\phi_n} \tag{1}$$

where $(w_{x,n}, \sigma_{x,n})$ is the x-type subgroup parameter; ϕ_n is the subgroup flux.

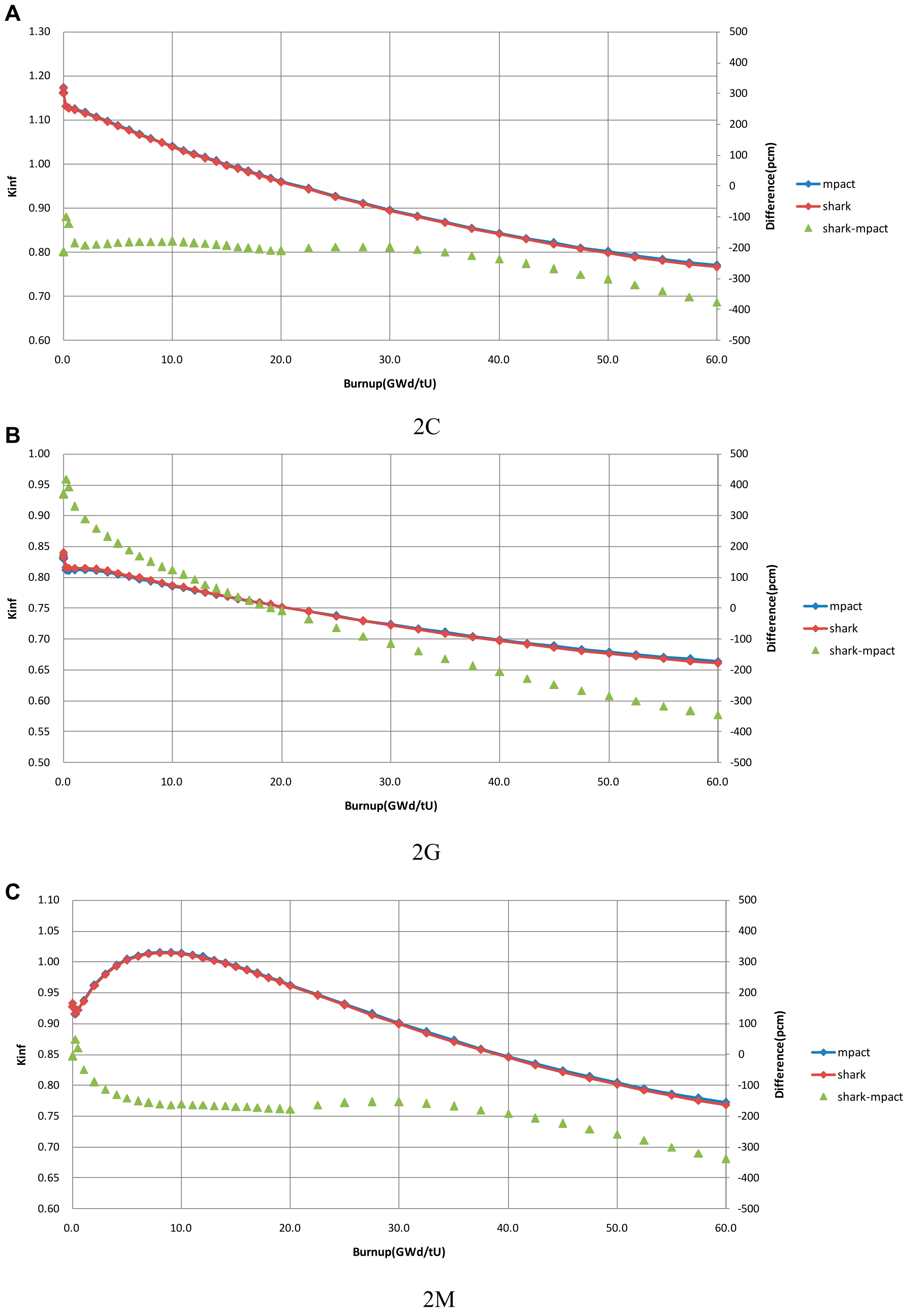

FIGURE 5
Infinite multiplication factors and deviations for the VERA2 problems.

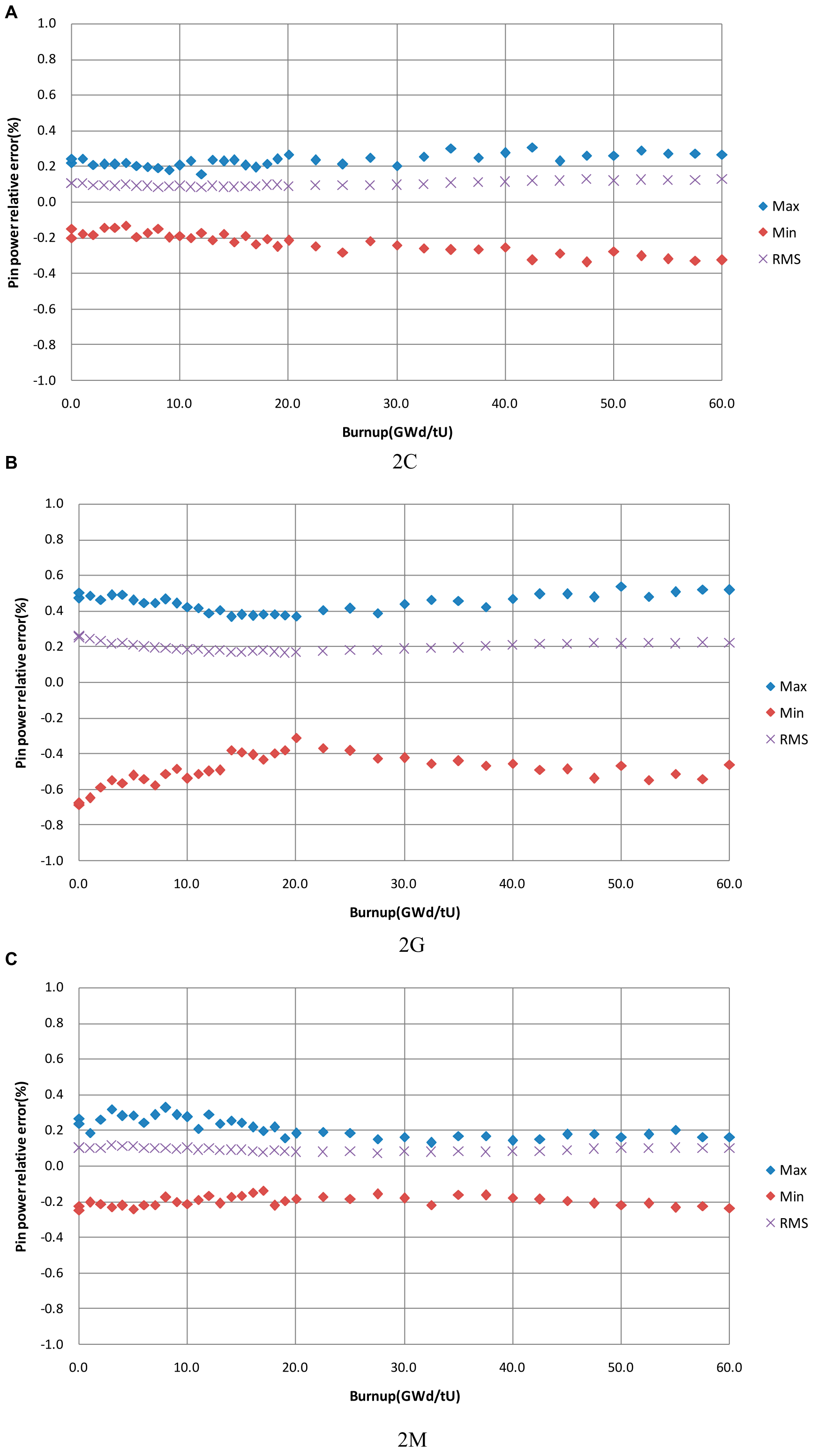

FIGURE 6
Deviations of pin power distributions in the VERA2 problems.

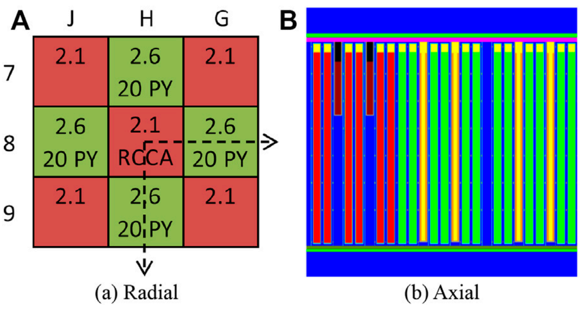

(a) Radial (b) Axial

FIGURE 7
Configurations of the VERA4 3D problem.

In Eq. 1, if it is required to take σ_x, the subgroup equations with the form of transport equations must be solved to obtain the subgroup fluxes. To improve the efficiency of the core-level resonance calculation, the approximate solution (Stamm'ler, 2001) of the slowing down equation is introduced to rewrite Eq. 1 as

$$\sigma_x \approx \frac{\sum_n w_{x,n}\sigma_{x,n}\frac{\sigma_{b,n}}{\sigma_{a,n}+\sigma_{b,n}}}{\sum_n w_{a,n}\frac{\sigma_{b,n}}{\sigma_{a,n}+\sigma_{b,n}}} \tag{2}$$

$$\sigma_{b,n} = \frac{\lambda\Sigma_p + \Sigma_{e,n}}{N} \tag{3}$$

$$\Sigma_{e,n} = \Sigma_{b,n} - \lambda\Sigma_p = N\left(\frac{\phi_n}{1-\phi_n}\right)\sigma_{a,n} - \lambda\Sigma_p \tag{4}$$

where $\sigma_{b,n}$ is the subgroup background cross section; $\lambda\Sigma_p$ is the product of the intermediate resonance factor and the macroscopic potential scattering cross section; Σ_e is the macroscopic equivalent cross section; and N is the resonant nuclide number density.

The key to calculate the effective resonance cross section using Eqs. 2–4 is to obtain $\Sigma_{e,n}$, which is also uneconomical to solve directly. Since Σ_e and σ_a present a relatively smooth monotonic relationship, a linear logarithmic interpolation table of $\Sigma_e(\sigma_a)$ can be constructed to reduce the frequency of solving the subgroup equations.

The interpolation table of subgroup equivalent cross sections $\Sigma_e(\sigma_a)$ is related to resonance energy groups and resonant nuclides. According to the distribution of the resonance peaks, two strategies, " resonant nuclide classification" and "resonance energy segmentation", can be used to reduce the computational cost.

Based on the above simplification, the subgroup equations as Eq. 5 are solved by MOC to obtain the subgroup fluxes and complete the tabulation.

$$\mathbf{\Omega}\cdot\nabla\psi_m(\mathbf{r},\mathbf{\Omega}) + \left(\Sigma_{a,m}+\Sigma_p\right)\psi_m(\mathbf{r},\mathbf{\Omega}) = \lambda\Sigma_p + (1-\lambda)\Sigma_p\phi_m(\mathbf{r}),\quad m = 1,\ldots,M \tag{5}$$

where, $\mathbf{\Omega}$ is the direction vector; $\mathbf{r}$ is the position vector; ψ_m is the subgroup m angular flux.

When multiple resonant nuclides are contained in the same material region, the iterative idea is used to deal with the multi-nuclide resonance interference effect.

The effective resonance absorption integral after convergence of the Bondarenko iteration can be used to obtain the background cross section by the binary search method, and the effective resonance scattering cross section is calculated accordingly.

For non-resonant nuclides, the slowing down effect of light nucleus is relatively accurately treated by correction factor to take

TABLE 1 Calculation results for the VERA #4 problem.

Cases	Withdraw (%)	DRW (pcm)		IRW (pcm)		Axial Offset (%)	
		MPACT	SHARK	MPACT	SHARK	MPACT	SHARK
257.9 cm	-	-	-	−240	−241	−35.3	−34.1
0 steps	0	−134	−135	−2975	−2978	−6.9	−5.9
23 steps	10	−596	−568	−2842	−2843	−20.9	−18.6
46 steps	20	−794	−793	−2245	−2275	−56.5	−53.5
69 steps	30	−541	−552	−1451	−1482	−71.6	−69.7
92 steps	40	−344	−354	−910	−929	−70.9	−69.6
115 steps	50	−230	−233	−566	−576	−62.0	−60.8
138 steps	60	−153	−158	−336	−343	−45.8	−44.6
161 steps	70	−103	−104	−183	−185	−28.5	−27.4
184 steps	80	−58	−63	−80	−81	−13.6	−12.7
207 steps	90	−22	−18	−22	−18	−3.0	−3.1
230 steps	100	-	-	-	-	0.0	−0.1

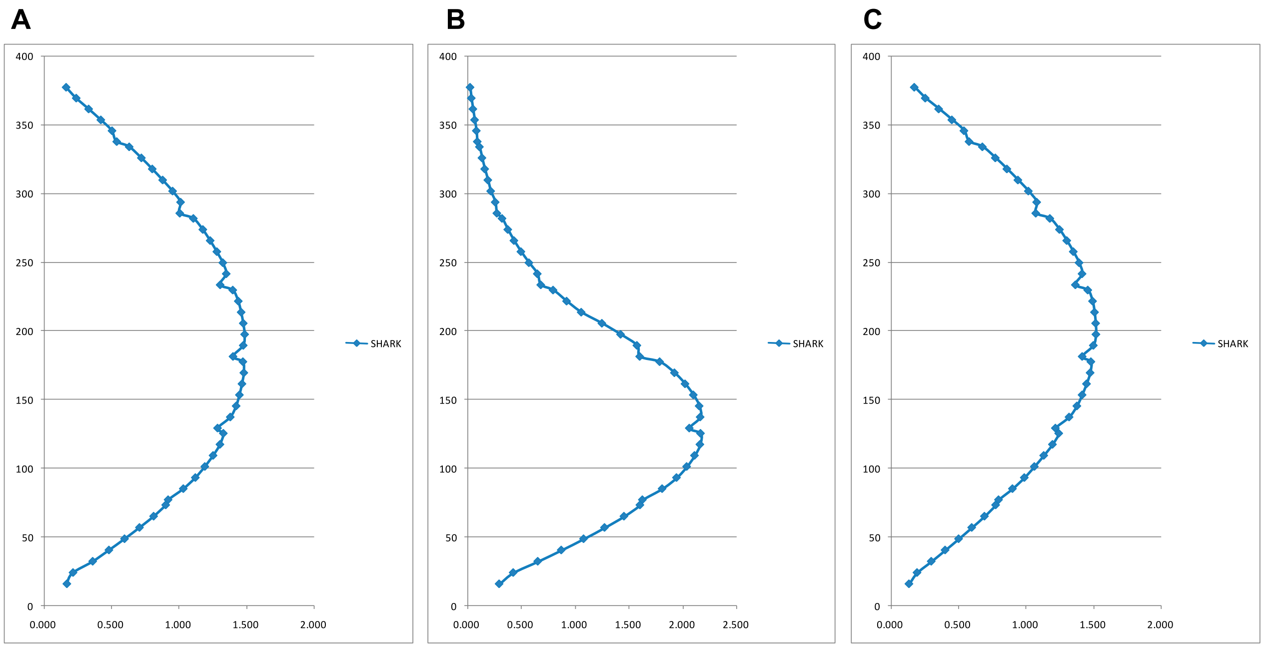

ARI

Half insertion

ARO

FIGURE 8
Axial power distributions at different control rod positions.

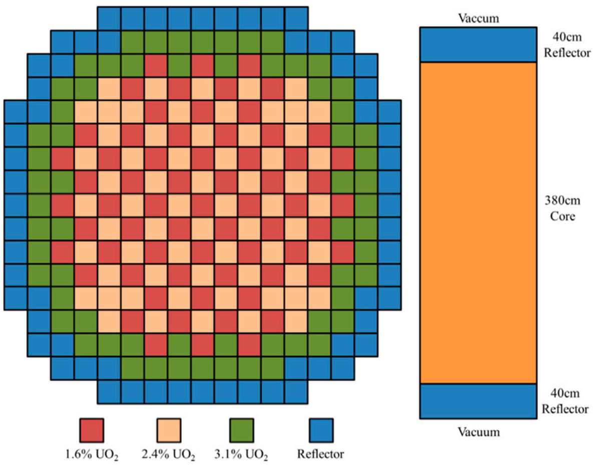

FIGURE 9
Configurations of the BEAVRS core.

into account resonance spectrum effects on the scattering cross section of claddings and moderators.

The subgroup parameters and multigroup cross sections corresponding to the subgroup module are provided by the accompanying cross section library (Chai et al., 2017). At present, the library contains more than 280 nuclides in total, considering the main reaction types such as fission, capture, (n, 2n)/(n, 3n), and decay. The number of its energy groups will also cover a varying range to meet the application needs of different scenarios.

2.3 Transport calculation

Using the generated multigroup cross sections as input, the transport solver completes the calculation and provides the flux distributions for a specific condition. The SHARK program uses MOC with powerful heterogeneous neutron transport capability as the solver. Besides direct 3D MOC, 2D/1D MOC and Quasi-3D MOC (Zhao et al., 2021) have been developed. In general, both of them transform the 3D transport problem into a 2D MOC problem with several layers coupled to each other in the axial direction.

In 2D/1D MOC, the 3D neutron transport equations are integrated axially and radially to obtain the basic coupling equation as

$$\begin{aligned}\xi_m \frac{\partial \psi^L_{g,m}(x,y)}{\partial x} + \eta_m \frac{\partial \psi^L_{g,m}(x,y)}{\partial y} + \Sigma^L_{t,g}(x,y)\psi^L_{g,m}(x,y) \\ = Q^L_{g,m}(x,y) - TL^{Axial}_{g,m,L}(x,y)\end{aligned} \tag{6}$$

TABLE 2 Calculation results of macroscopic BEAVRS core problem.

Method/Codes	k_{eff}	k_{eff} error (pcm)	Pin power errors (%)		Assembly power errors (%)		Time (h)
			MAX	RMS	MAX	RMS	
RMC (Ref)	1.26726	±0.3	-	-	-	-	-
2D/1D	1.26735	9	2.9	0.5	1.2	0.4	0.79

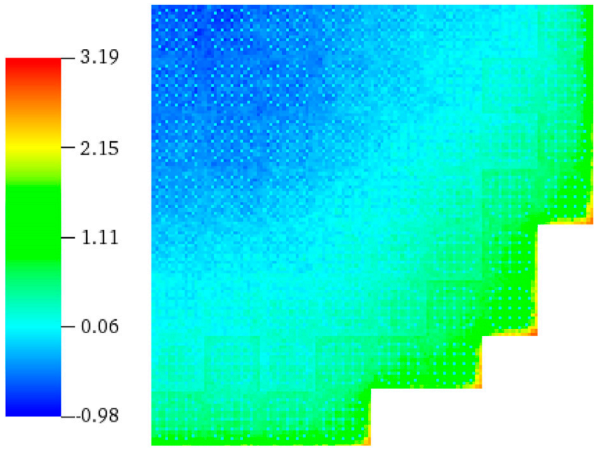

FIGURE 10
Radial pin power deviations in Macroscopic BEAVRS core problem.

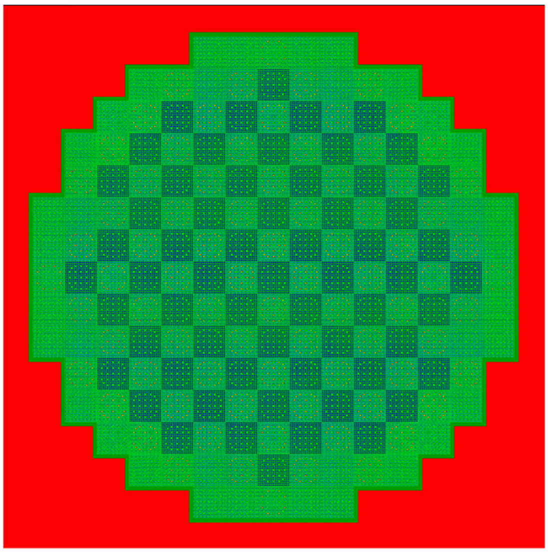

FIGURE 11
Configurations of advanced PWR whole-core problem.

TABLE 3 Calculation results of HuaLong whole-core problem.

Code	k_{eff}	Assembly power errors (%)			
		MAX	MIN	AVG	RMS
RMC	0.99668	-	-	-	-
SHARK	0.99756	2.28	−2.56	0.85	1.03

$$\mu_m \frac{d\psi_{g,m}^{p}(z)}{dz} + \Sigma_{t,g}^{p}(z)\psi_{g,m}^{p}(z) = Q_{g,m}^{p}(z) - TL_{g,m,p}^{Radial}(z) \tag{7}$$

where, $\psi_{g,m}^{L}(x,y)$ is the angular flux of the direction m energy group g at the position of (x,y) on the axial Lth layer; $\psi_{g,m}^{p}(z)$ is the angular flux of the direction m energy group g in the radial mesh p at the axial position of z; $TL_{g,m,L}^{Axial}(x,y)$ and $TL_{g,m,p}^{Radial}(z)$ is the axial leakage term and radial leakage term, respectively; the rest of the symbols are in common notation.

The SHARK program uses a discrete-ordinates method (S_n) in finite difference format to solve the 1D Eq. 7 in order to fully consider the heterogeneous transport effects in the axial direction.

For the potential numerical instability problem in 2D/1D MOC calculation, the isotropic leakage approximation and leakage splitting methods (Zhao et al., 2018) are used.

And in the Quasi-3D MOC, the 3D neutron transport equation is transformed into the 2D coupling equation by introducing the axial differential format approximation as follows.

$$\begin{aligned} &\varepsilon \frac{\partial \psi_{g,m}^{L}(x,y)}{\partial x} + \eta \frac{\partial \psi_{g,m}^{L}(x,y)}{\partial y} + \left(\Sigma_{t,g}^{L}(x,y) + \frac{2\mu}{\Delta z_L}\right)\psi_{g,m}^{L} \\ &(x,y) = Q_{g,m}^{L}(x,y) + \frac{2\mu}{\Delta z_L}\psi_{g,m}^{L-1/2}(x,y)\mu > 0 \\ &\varepsilon \frac{\partial \psi_{g,m}^{L}(x,y)}{\partial x} + \eta \frac{\partial \psi_{g,m}^{L}(x,y)}{\partial y} + \left(\Sigma_{t,g}^{L}(x,y) - \frac{2\mu}{\Delta z_L}\right)\psi_{g,m}^{L} \\ &(x,y) = Q_{g,m}^{L}(x,y) - \frac{2\mu}{\Delta z_L}\psi_{g,m}^{L+1/2}(x,y)\mu < 0 \end{aligned} \tag{8}$$

$$\psi_{g,m}^{L}(x,y) = \frac{\psi_{g,m}^{L+1/2}(x,y) + \psi_{g,m}^{L-1/2}(x,y)}{2} \tag{9}$$

where $\psi_{g,m}^{L\pm 1/2}(x,y)$ is the angular flux of the direction m energy group g at the positions (x,y) on the top and bottom surfaces of the Lth layer; the rest of the symbols are in common notation.

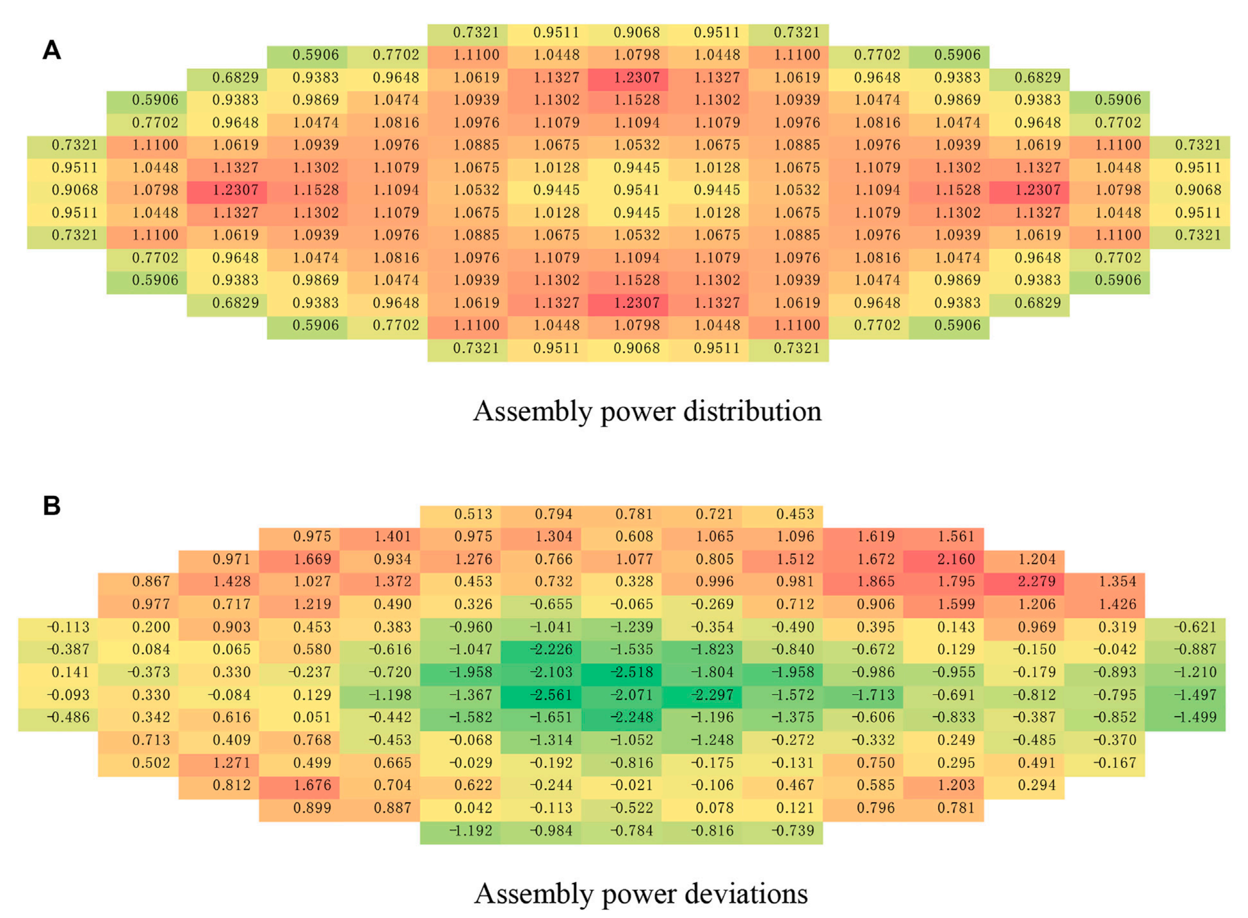

					0.7321	0.9511	0.9068	0.9511	0.7321					
			0.5906	0.7702	1.1100	1.0448	1.0798	1.0448	1.1100	0.7702	0.5906			
		0.6829	0.9383	0.9648	1.0619	1.1327	1.2307	1.1327	1.0619	0.9648	0.9383	0.6829		
	0.5906	0.9383	0.9869	1.0474	1.0939	1.1302	1.1528	1.1302	1.0939	1.0474	0.9869	0.9383	0.5906	
	0.7702	0.9648	1.0474	1.0816	1.0976	1.1079	1.1094	1.1079	1.0976	1.0816	1.0474	0.9648	0.7702	
0.7321	1.1100	1.0619	1.0939	1.0976	1.0885	1.0675	1.0532	1.0675	1.0885	1.0976	1.0939	1.0619	1.1100	0.7321
0.9511	1.0448	1.1327	1.1302	1.1079	1.0675	1.0128	0.9445	1.0128	1.0675	1.1079	1.1302	1.1327	1.0448	0.9511
0.9068	1.0798	1.2307	1.1528	1.1094	1.0532	0.9445	0.9541	0.9445	1.0532	1.1094	1.1528	1.2307	1.0798	0.9068
0.9511	1.0448	1.1327	1.1302	1.1079	1.0675	1.0128	0.9445	1.0128	1.0675	1.1079	1.1302	1.1327	1.0448	0.9511
0.7321	1.1100	1.0619	1.0939	1.0976	1.0885	1.0675	1.0532	1.0675	1.0885	1.0976	1.0939	1.0619	1.1100	0.7321
	0.7702	0.9648	1.0474	1.0816	1.0976	1.1079	1.1094	1.1079	1.0976	1.0816	1.0474	0.9648	0.7702	
	0.5906	0.9383	0.9869	1.0474	1.0939	1.1302	1.1528	1.1302	1.0939	1.0474	0.9869	0.9383	0.5906	
		0.6829	0.9383	0.9648	1.0619	1.1327	1.2307	1.1327	1.0619	0.9648	0.9383	0.6829		
			0.5906	0.7702	1.1100	1.0448	1.0798	1.0448	1.1100	0.7702	0.5906			
					0.7321	0.9511	0.9068	0.9511	0.7321					

					0.513	0.794	0.781	0.721	0.453					
			0.975	1.401	0.975	1.304	0.608	1.065	1.096	1.619	1.561			
		0.971	1.669	0.934	1.276	0.766	1.077	0.805	1.512	1.672	2.160	1.204		
	0.867	1.428	1.027	1.372	0.453	0.732	0.328	0.996	0.981	1.865	1.795	2.279	1.354	
	0.977	0.717	1.219	0.490	0.326	-0.655	-0.065	-0.269	0.712	0.906	1.599	1.206	1.426	
-0.113	0.200	0.903	0.453	0.383	-0.960	-1.041	-1.239	-0.354	-0.490	0.395	0.143	0.969	0.319	-0.621
-0.387	0.084	0.065	0.580	-0.616	-1.047	-2.226	-1.535	-1.823	-0.840	-0.672	0.129	-0.150	-0.042	-0.887
0.141	-0.373	0.330	-0.237	-0.720	-1.958	-2.103	-2.518	-1.804	-1.958	-0.986	-0.955	-0.179	-0.893	-1.210
-0.093	0.330	-0.084	0.129	-1.198	-1.367	-2.561	-2.071	-2.297	-1.572	-1.713	-0.691	-0.812	-0.795	-1.497
-0.486	0.342	0.616	0.051	-0.442	-1.582	-1.651	-2.248	-1.196	-1.375	-0.606	-0.833	-0.387	-0.852	-1.499
	0.713	0.409	0.768	-0.453	-0.068	-1.314	-1.052	-1.248	-0.272	-0.332	0.249	-0.485	-0.370	
	0.502	1.271	0.499	0.665	-0.029	-0.192	-0.816	-0.175	-0.131	0.750	0.295	0.491	-0.167	
		0.812	1.676	0.704	0.622	-0.244	-0.021	-0.106	0.467	0.585	1.203	0.294		
			0.899	0.887	0.042	-0.113	-0.522	0.078	0.121	0.796	0.781			
					-1.192	-0.984	-0.784	-0.816	-0.739					

FIGURE 12
Assembly power distribution and deviations in advanced PWR whole-core problem.

As seen in Eqs. 8, 9, the Quasi-3D MOC does not contain a transverse leakage term and the right term of the equation is always positive, thus providing better numerical stability than the 2D/1D MOC. All these transport solvers are accelerated by the Coarse Mesh Finite Difference (CMFD) method.

2.4 Depletions

The depletion calculation is used to track the nuclides over time and predict the dynamic behavior of the core during burnup. It is important for fuel management, breeding and transmutation, spent fuel reprocessing, and multi-physics coupling analysis of the core. In the framework design of the high-fidelity transport software, the depletion function is not only responsible for completing the burnup calculation, but also driving the solvers of resonance, transport, and multi-physics to complete the coupling analysis of each burnup point (Figure 2).

The SHARK program adopts an internally coupled framework for depletion calculations (Zhang et al., 2022b), with the following features reserved.

1) Support for both neutron reaction depletions with multiple burnup steps and pure decay calculations during the cooling down stage on the reactor shutdown.
2) Support replacement for different depletion libraries and chains. As mentioned earlier, different application scenarios in various reactor types may have different requirements for depletion accuracy and efficiency. The implementation of many codes is usually tied to a specific chain, which makes it difficult to achieve easy replacement of depletion data. The SHARK program is designed to load the depletion chain and depletion data as external library files for "plug-and-play" scalability.
3) Several "transport-depletion" coupling schemes and point depletion solver options are reserved. For common fuels, a conventional predictor-corrector (PC) with sub-steps strategy is used. For fuels containing special poisons such as Gd, a

combination of PC and log-linear reaction rate (LLR) (Carpenter and WOLF, 2010) is used. Also, options such as Semi-PC plus LLR are considered for future multi-physics coupling. Solvers for point depletion equations with good performance, such as CRAM (Pusa and Leppanen, 2009) and Krylov subspace methods (Yamamoto et al., 2007), are also available to program developers and users in the form of different child classes in Bateman solver parent class.

4) With the ability of mapping transport meshes to depletion meshes of different sizes, the parallel capability based on domain decomposition to improve the computational efficiency of large-scale high-fidelity depletion is adopted.
5) Provide engineering analysis functions related to depletions, including settings for power, control rods, core inlet coolant temperatures. Functions of xenon mode, soluble boron depletion, and restart calculation are also presented.
6) The depletion matrix is processed in a proper manner to avoid redundant matrix generation and excessive storage, improving the data access efficiency. In the matrix utilities, the sparse matrix storage format and operation methods suitable for different point depletion solvers are provided.

3 Preliminary V&V results

At present, the main framework of SHARK program has been established, and the first batch of key calculation modules have been developed and embedded into it. The program has the initial capability to perform the "resonance-transport-depletion" calculation, and preliminary verifications have been carried out. Due to space limitation, some of the results are shown in this paper. More details can be found in published or forthcoming articles. All the numerical results are calculated with the option of "subgroup-2D/1D". Accordingly, a 45-group cross-section library and out-flow transport correction (Stamm'ler and Abbate, 1983) are used.

3.1 VERA depletion benchmark problems

The series of VERA progression benchmarks is one of the most authoritative benchmark problems for validating heterogeneous transport calculation codes (Godfrey, 2014; Kang, 2015). Among them, the VERA1/2 series are for commercial Pressurized Water Reactor (PWR) pins and lattices. They consider heterogeneous effects from fuel enrichment, temperature, burnable poisons (IFBA/WABA/gadolinium rods), control rods (AIC/B_4C), and spacer grids. We have already completed the steady-state verifications in our previous study and obtained good results (Zhang et al., 2022c). In this paper, we focus on verifying the newly developed depletion functions, where the reference solution (Wen, 2022) is obtained from the advanced high-fidelity transport calculation program MPACT. For the single pin problems, the calculation scheme of 10-6-0.01 (10 azimuthal and 6 polar angles in [0,π] with 0.01 cm ray width) is used. The scheme of 16-6-0.01 is used in the single lattice problems.

The deviations of the infinite multiplication factor (k_{inf}) with depletion for the single pin problems are shown in Figure 4. As can be seen, all the results agree well with the reference solution, except for the 1E calculation. For different enrichments and temperatures, the overall deviation falls within the range of -300 pcm to +100 pcm and varies smoothly with the burnups. For the 1E problem (IFBA pin with 3.1w/o enrichment), the SHARK program shows a large abnormal deviation from the reference solution; however, after comparing with the Monte Carlo program Serpent (Leppänen, 2013), it is found that SHARK and Serpent agree well and the trend of deviations with burnups is normal.

For the single lattice problems, the k_{inf} and its deviation with burnups for 2C (3.1 w/o enrichment), 2G (24 AIC control rod insertion), and 2M cases (128 IFBA) are given in Figure 5. As can be seen from the figure, for the lattices with and without absorbers, the calculation results of the SHARK program agree well with the reference solutions.

Figure 6 shows the deviation statistics of the pin power distributions during depletion. The deviation of pin powers does not exceed 0.4% in the case without control rod, and does not exceed 0.8% in the case with inserted control rods. Moreover, the deviations are stable even in deep burnups.

3.2 VERA4 3-D colorset benchmark problem

The problem is a 3-D multi-assembly one for PWR in a 3 × 3 arrangement (Godfrey, 2014). It takes into account different enrichments, burnable poisons (Pyrex), different AIC/B_4C control rod insertions, and structural details such as end plugs, springs, nozzles, and spacer grids, which can truly reflect the software's ability to simulate radial and axial heterogeneous effects (Figure 7).

The results of SHARK are given in Table 1 with the reference from MPACT, which are obtained by the scheme of 16-6-0.03 with about 50 planes in the active zone. Both the Differential Rod Worth (DRW) and Integrated Rod Worth (IRW) are very close to the reference solutions. In general, the maximum deviation is +28pcm for DRW and -31pcm for IRW.

The AO values also match well in Table 1. The axial power distributions at different insertions are given in Figure 8. It can be seen that the spacer grid effect and the axial power shift due to the insertion of control rods are well represented.

3.3 Macroscopic BEAVRS core problem

The problem is adapted from a large commercial PWR core loaded with 193 UO_2 assemblies (Zhang et al., 2022c). The core is arranged with fuel assemblies of 1.6 w/o, 2.4 w/o, and 3.1 w/o enrichments. The core has simplified geometry with an active zone of 380 cm high and 40 cm reflectors at both axial end (Figure 9).

The reference solution of the problem is obtained from the famous Monte Carlo program RMC (Wang et al., 2013). In the calculations, the scheme of 16-6-0.02 with 26 planes is used. The convergence criteria of eigenvalue and source term are 1 pcm and 10-4 respectively. A summary of the results is shown in Table 2, and the pin power distribution deviations are shown in Figure 10. The simulation takes about 0.88 h with 578 CPU cores, in which the time partitions of track generation, MOC solution and CMFD solution are about 10%: 80%: 10%.

3.4 Advanced PWR whole-core problem

This whole-core problem is from the third-generation million-kilowatt-level commercial PWR HuaLong (Figure 11). The active zone of this core consists of 177 AFA3G fuel assemblies with three different enrichments, and Pyrex is used as burnable absorbers. The SHARK program is used to simulate the three-dimensional core under the Hot Full Power (HFP), ARO condition. The heterogeneous pins with different compositions are modelled; the radial and axial reflectors outside the active zone are considered explicitly in the simulation. The scheme of 16-6-0.03 with 26 planes is used. There are tens of millions of meshes in total and 578 CPU cores are used. Using the Monte Carlo program RMC as the reference, the statistical results are given in Table 3. Assembly power distribution and their deviations are shown in Figure 12. As can be seen, SHARK has good calculation results for the initial state core of the real nuclear power plant. Only 88 pcm deviation exists for k_{eff}. The power distribution maintains symmetry and has a Max/Min deviation no more than ±2.6%. The improved subgroup resonance computation takes less than 20% of the total resonance-transport solution time.

4 Conclusion

This paper presents the design and development of the high-fidelity neutronics calculation program SHARK with main technical features, and gives a series of stage verification results from pin to whole-core level. The results show that the SHARK program has the initial computational capability to obtain accurate and reasonable results for microscopic problems in the commercial PWRs. In the future work, the improvement and expansion of functional modules will be carried out continuously for better adaptability to different application targets and scenarios under the unified frameworks. In addition, further V&V based on measurements of nuclear power plants will move on.

Data availability statement

The original contributions presented in the study are included in the article/supplementary material, further inquiries can be directed to the corresponding author.

Author contributions

ZH: Framework design; resonance module, depletion module, utilities development; VERA verifications. ZW: Team leader, technical advisor. ZC: transport module development; BEAVRS verifications. WB: PWR Core verifications, utilities development. CZ: Project management, technical advisor. PX: Project management, technical advisor. LQ: Project management, technical advisor. YY: Project management, technical advisor. GZ: Project management, technical advisor. ZW: Project management, technical advisor.

Funding

This work is supported by National Natural Science Foundation of China (Grant No. 11905214, 12005214) and China Association for Science and Technology (Young Elite Scientists Sponsorship Program 2019QNRC001).

Acknowledgments

The first author would like to thank Wen Xingjian for sharing reference solutions in VERA depletion verifications.

Conflict of interest

The authors declare that the research was conducted in the absence of any commercial or financial relationships that could be construed as a potential conflict of interest.

Publisher’s note

References

Aviles, B., Kelly, D., and Aumiller, D. (2016). “Coupled MC21 and COBRA-IE solution to VERA core physics benchmark problem# 6[C],” in PHYSOR 2016, Sun Valley, Idaho, USA, May 1, 2016 - May 5, 2016.

Boyd, W., Shaner, S., Li, L., Forget, B., and Smith, K. (2014). The OpenMOC The OpenMOC method of characteristics neutral particle transport codeethod of characteristics neutral particle transport code. *AnnAnn. Nucl. Energy Nucl. Energy* 68, 43-52. doi:10.1016/j.anucene.2013.12.012

Cardoni, J. N. (2011). “Nuclear reactor multi-physics simulations with coupled MCNP5 and STAR-CCM+[D],” in M&C 2011: International conference on mathematics and computational methods applied to nuclear science and engineering, Rio de Janeiro, Brazil, 8-12 May 2011 (Illinois, USA: University of Illinois at Urbana-Champaign).

Carpenter, D. C., and Wolf, J. H. (2010). “The log linear rate constant power depletion method [C],” in PHYSOR 2010, Pittsburgh, PA, 9-14 May 2010.

Chai, X., Tu, X., Guo, F., Yin, Q., Shi, H., Wei, L., et al. (2017). Development and preliminary V&V for advanced neutron transport lattice code KYLIN-2 [J]. *High Power Laser Part. Beams (in Chinese)* 29 (01), 016016. doi:10.11884/HBLPB201729.160306

Chen, J., Liu, Z. Y., Zhao, C., He, Q., Zu, T., Cao, L., et al. (2018). A new high-fidelity neutronics code NECP-X. *Annals of Nuclear Energy* 116, 417-428. doi:10.1016/j.anucene.2018.02.049

Choi, S., Choe, J., Nguyen, K., Lee, W., Kim, W., Kim, K., et al. (2019). “Recent development status of neutron transport code STREAM,” in Transactions of the Korean Nuclear Society Spring Meeting, Jeju, Korea, May 23-24, 2019.

Deng, L., Li, G., Zhang, B. Y., Shangguan, D., Hu, Z., Li, R., et al. (2018). “JMCT v2.0 Monte Carlo code with integrted nuclear system feedback for simulation of BEAVRS model[C],” in PHYSOR 2018, Cancun, Mexico, April 22-26, 2018.

Godfrey, A. T. (2014). VERA core physics benchmark progression problem specifications, revision 4[R]. CASL, CASL-U-2012-0131-004.

He, Q., Cao, L., and Liu, Z. (2018). Research of global-local resonance self-shielding calculation method based on NECP-X[J]. *Nuclear Power Engineering* 39 (2), 124–128. doi:10.13832/j.jnpe.2018.02.0124

Joo, H. G., Cho, J., Kim, K., Lee, C., and Zee, S. (2014). “Methods and performance of a three-dimensional whole-core transport code DeCART,” in PHYSOR 2004, Chicago, Illinois, April 25-29, 2004.

Jung, Y. S. (2013). “Development of practical numerical nuclear reactor for high fidelity core analysis[D],” (Korea: Seoul National University). Thesis(Dr. Eng.).

Kang, S. (2015). Specification for the VERA depletion benchmark suite, revision 0 [R]. CASL, CASL-X-2015-1014-000.

Kochunas, B., Collins, B., Jabaay, D., Downar, T., and Martin, W. (2013). “Overview of development and design of MPACT: Michigan parallel characteristics transport code,” in M and C 2013: 2013 International Conference on Mathematics and Computational Methods Applied to Nuclear Science and Engineering, Sun Valley, Idaho, May 5-9,2013.

Leppänen, J. (2013). *Serpent – a continuous-energy Monte Carlo reactor physics burnup calculation code[R]*. Espoo, Finland: VTT Technical Research Centre of Finland.

Liu, S. C., Luo, Z., Guo, X. Y., Yu, G., Li, Z., and Kan, W. (2018). “RMC/CTF multiphysics solutions to VERA benchmark problem 6 and 7[C],” in PHYSOR 2018, Cancun, Mexico, April 22-26, 2018.

Pusa, M., and Leppanen, J. (2009). Computing the Computing the Matrix Exponential in Burnup Calculationsatrix exponential in burn-up calculations[R]. *Nucl. Sci. Eng.* 164, 140. 150. doi:10.13182/NSE09-14

Stamm’ler, R. (2001). *HELIOS methods[R]*. Nyköping, Sweden: Studsvik Scandpower.

Stamm’ler, R. J., and Abbate, M. J. (1983). *Methods of steady-state reactor physics in nuclear design*. London: Academic Press.

Wang, K., Li, Z., and Liang, J. (2013). *Rmc – a Monte Carlo code for reactor core analysis[J]*. La Grange Park (United States): American Nuclear Society - ANS.

Wen, X. (2022). *Numerical reactor high-fidelity cycle depletion and source term calculation method development and application[D]*. Xi’An, Shaanxi, China: Xi’an Jiaotong University. In Chinese.

Yamamoto, A., Tatsumi, M., and Sugimura, N. (2007). Numerical Numerical Solution of Stiff Burnup Equation with Short Half Lived Nuclides by the Krylov Subspace Methodolution of stiff bumup equations with short Half lived nuclides by the Krylov subspace method[J]. *J. Nucl. Sci. Technol.* 44 (2), 147. 154. doi:10.1080/18811248.2007.9711268

Zhang, H. B., Peng, X. J., and Zhao, C. (2022). Subgroup method for the high fidelity neutronics code SHARK and preliminary benchmarking[J]. *Nuclear Engineering and Design*. under review.

Zhang, H. B., Zhao, C., Peng, X. J., and Zhao, W. B. (2022c). Numerical reactor high-fidelity neutronics program SHARK development[J]. *Atomic Energy Science and Technology* 56 (2), 2022. In Chinese. doi:10.7538/yzk.2021.youxian.0902

Zhang, H. B., Zhao, W. B., and Zhao, C. (2022). “Technical features of the depletion framework in the digital reactor neutronics code SHARK [C],” in Pacific Basin Nuclear Conference, Chengdu, China, Oct 31-Nov 4, 2022. under review.

Zhao, C., Liu, Z., Liang, L., Chen, J., Cao, L., and Wu, H. (2018). Improved leakage splitting method for the 2D/1D transport calculation. *Progress in Nuclear Energy* 105 (5), 202-210. doi:10.1016/j.pnucene.2018.01.007

Zhao, C., Peng, X. J., Zhang, H. B., Zhao, W., Li, Q., and Chen, Z. (2021). Analysis and comparison of the 2D/1D and quasi-3D methods with the direct transport code SHARK. *Nuclear Engineering and Technology* 54, 19. 29. doi:10.1016/j.net.2021.07.038

frontiers | Frontiers in Energy Research

TYPE Methods
PUBLISHED 26 January 2023
DOI 10.3389/fenrg.2022.1055405

EDITED BY
Jingang Liang,
Tsinghua University, China

REVIEWED BY
Jinsen Xie,
University of South China, China
Chenglong Wang,
Xi'an Jiaotong University, China

*CORRESPONDENCE
Lianjie Wang,
wanglianjie@npic.ac.cn

SPECIALTY SECTION
This article was submitted to Nuclear Energy,
a section of the journal
Frontiers in Energy Research

RECEIVED 27 September 2022
ACCEPTED 28 November 2022
PUBLISHED 26 January 2023

CITATION
Zhang B, Wang L, Lou L, Zhao C, Peng X, Yan M, Xia B, Zhang C, Qiao L and Wu Q (2023), Development and verification of lead-bismuth cooled fast reactor calculation code system Mosasaur.
Front. Energy Res. 10:1055405.
doi: 10.3389/fenrg.2022.1055405

Development and verification of lead-bismuth cooled fast reactor calculation code system Mosasaur

Bin Zhang, Lianjie Wang*, Lei Lou, Chen Zhao, Xingjie Peng, Mingyu Yan, Bangyang Xia, Ce Zhang, Liang Qiao and Qu Wu

Science and Technology on Reactor System Design Technology Laboratory, Nuclear Power Institute of China, Chengdu, Sichuan, China

Lead-bismuth cooled fast reactor calculation code system named MOSASAUR has been developed to meet the simulation requirements from LBFR engineering design. An overview of MOSASAUR developments is provided in this paper, four main functional modules and their models are introduced: cross-sections generation module, flux spectrum correction module, core simulation module and sensitivity and uncertainty analysis module. Verification and validation results of numerical benchmark calculations, code-to-code comparisons with the Monte-Carlo code and critical experimental calculations shown in this paper prove the capabilities of MOSASAUR in dealing with lead-bismuth cooled fast reactor analysis problems with good performances. Numerical results demonstrate that compared with the Monte-Carlo code, the relative errors of eigenvalues are smaller than 350pcm when the calculations were carried out with the same nuclear data file. Compared with the measured values, the errors will increase due to the simulation details and the measurement accuracy.

KEYWORDS

lead-bismuth cooled fast reactor, cross-sections generation, flux spectrum correction, core simulation, sensitivity and uncertainty, verification and validation

1 Introduction

Due to the hard neutron spectrum, fast reactors have significant advantages in utilization rate of the nuclear energy resources and incineration of long-lived nuclear waste (Bouchard and Bennett, 2008). The fast reactors play an important role among the six candidate types of the fourth generation of nuclear power. Lead-based cooled advanced reactor, a fourth-generation nuclear reactor system, uses liquid metal as coolant. The excellent performances of lead-bismuth which is used as the reactor coolant in Lead-bismuth cooled fast reactor (LBFR) bring the reactor significant advantages in physical characteristics and safe operation. Firstly, the LBFR has high utilization rate of resources. Lead-based materials have lower neutron slowing capacity and smaller capture cross-sections. The reactor core is designed with a harder neutron energy spectrum, which can take advantages of neutrons for nuclear fuel regeneration and nuclear waste transmutation (Hu and Yuan, 1995). The reactor can achieve long core life and is helpful to prevent nuclear proliferation. Secondly, the LBFR has good thermal safety and security (Xu, 2009). The lead-based materials have high thermal conductivity, low melting point, high boiling point and other characteristics. It makes that the reactor can be operated at atmospheric pressure and can achieve high power density. The higher thermal expansion rate of lead-based materials and lower kinematic viscosity coefficient can ensure that the reactor has sufficient natural cycling capacity. What's more, the chemical safety is good. The lead-based materials are chemically inactive and hardly react with water and air, which make the violent chemical reaction impossible. Thirdly, the LBFR has good economy. Lead-bismuth cooled fast reactor eliminates the need for large high-pressure vessels, have simple auxiliary systems, and have low construction and operation and maintenance costs.

The research and development of fast reactors has been pushed globally in recent decade, including in China. The China lead-based reactor (Wu, 2016) and the lead-bismuth eutectic (LBE)–cooled China initiative accelerator driven subcritical system (Liu et al., 2017) have been proposed by two institutes of the Chinese Academy of Sciences.

One of the most important elements of the fast reactor core design is the core neutronics computational analysis. At present, there are two main kinds of calculation methods. First is the one-step calculation method (Rachamin and Kliem, 2017), which is used to simulate the core directly with as few approximations as possible. The other one is the two-step calculation method which is based on the homogenization techniques (Zhang et al., 2016). For the whole core physics simulation, the computational cost of one-step calculation with fully detailed description is too expensive using either stochastic (Wang et al., 2015) or deterministic method (Downar et al., 2016) even with the currently most advanced computing powers. So even though one-step calculation method has a lot of advantages, the dominant method for fast core simulation is the two-step scheme.

In the two-step scheme, the Monte Carlo codes is becoming popular to generate few-group cross-sections for the whole core calculation with the improvement of computer technique and the development of Monte Carlo method in recent decades. The Serpent code has been proven to be feasible (Nikitin et al., 2015), and similar work has also been researched in MCNP (Heo et al., 2013) and TRIPOLI (Cai, 2014). Due to sufficient computational accuracy and high computational efficiency, deterministic procedures are currently the most widely used simulation methods.

In China, the fast reactor code system SARAX (Zheng et al., 2018a; Zheng et al., 2018b) developed by Xian Jiaotong University is well known. The TULIP code is used to generate the 33-group cross-sections, which is based on the 1968-group cross-sections libraries from NJOY (Macfarlane and MUIR, 1994). The narrow resonance approximation (Lee and Yang, 2012) is applied for the resonance calculation. Alternatively, the embedded one-dimensional Monte Carlo calculation is applied as an option to get the ultrafine-group cross-sections. The LEVENDER code is used for the core simulation which is based on the S_N transport equations.

The MC^2/The DIF3D/REBUS system is the best-known fast reactor code system in the United States. MC^2 (Henryson et al., 1973) uses the library generated from ETOE-2 and solves the ultrafine-group (2082 groups) slowing-down equations for different compositions and temperatures to generate the few-group cross-sections. The DIF3D (Derstine, 1984) and code VARIANT (Palmiotti et al., 1995) are used to solve the neutron equations which is applied in REBUS to do the fuel cycle analysis. The ERANOS system is the most widespread in Europe which generates the cross-sections by ECCO (Grimstone, 1990). The subgroup method based on the probability tables is applied for the resonance calculation. The CONSYST-TRIGEX code system is used for fast reactor core simulation in Russia.

In order to improve the accuracy of legacy fast reactor codes, new methods and models have been researched. The two-dimensional capability and calculation of hyper fine group (~400,000 groups) slowing-down equation (Lee and Yang, 2012) were extended in MC^2/DIF3D. A new self-shielding method (Li Z et al., 2017) and new homogenization techniques have been implemented in APOLLO-3 code (Archier et al., 2016). The neutron transport solver is becoming popular in the fast reactor core calculation (Shemon et al., 2017).

In this paper, an overview of the **MO**delling and **S**imul**A**tion code system for neutronic**S** of le**A**d bism**U**th cooled **R**eactor named MOSASAUR is provided which is developed to meet the LBFR engineering design requirements by Nuclear Power Institute of China (NPIC), China National Nuclear Corporation (CNNC). Main functional modules and their models contained in MOSASAUR are introduced in Section 2. Section 3 gives the numerical results of the verification and validation. Section 4 summarizes this paper.

2 Modules of mosasaur

The deterministic two-step calculation strategy based on the homogenization theory is utilized in MOSASAUR to perform the reactor core neutronics analysis. In the first step, the cross-sections generation module named MOCS is used the narrow resonance approximation to solve the resonance problem. For the typical assemblies, ultrafine-group cross-sections and neutron flux will be determined and the few-group homogenized cross-sections will be collapsed based on the flux-volume weight method and the principle of conservation of reaction rate. The calculation process of MOCS is shown in Figure 1.

The homogenized few-group cross-sections are based on the single assembly calculation which is under the reflective boundary

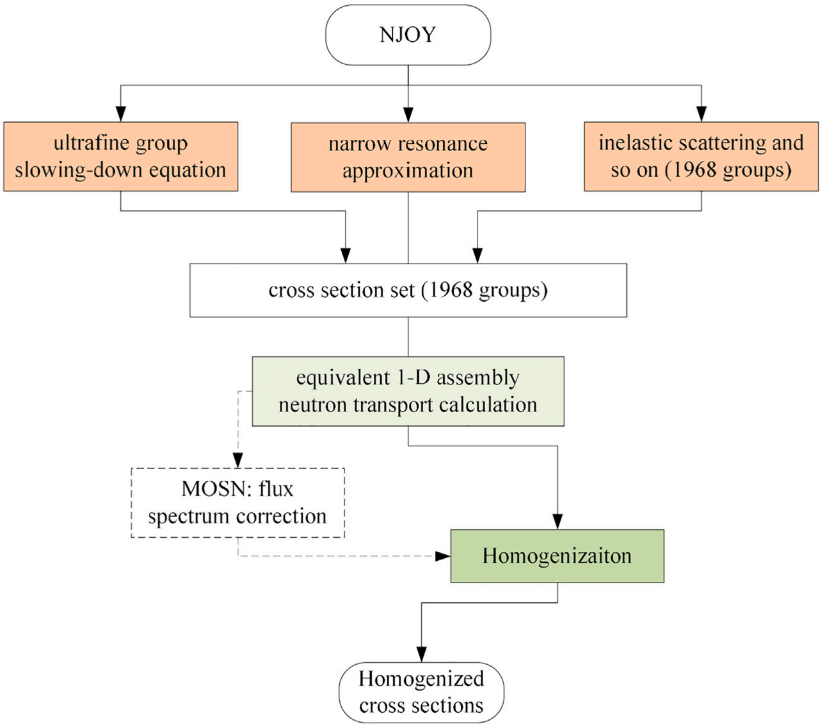

FIGURE 1
The calculation process of MOCS.

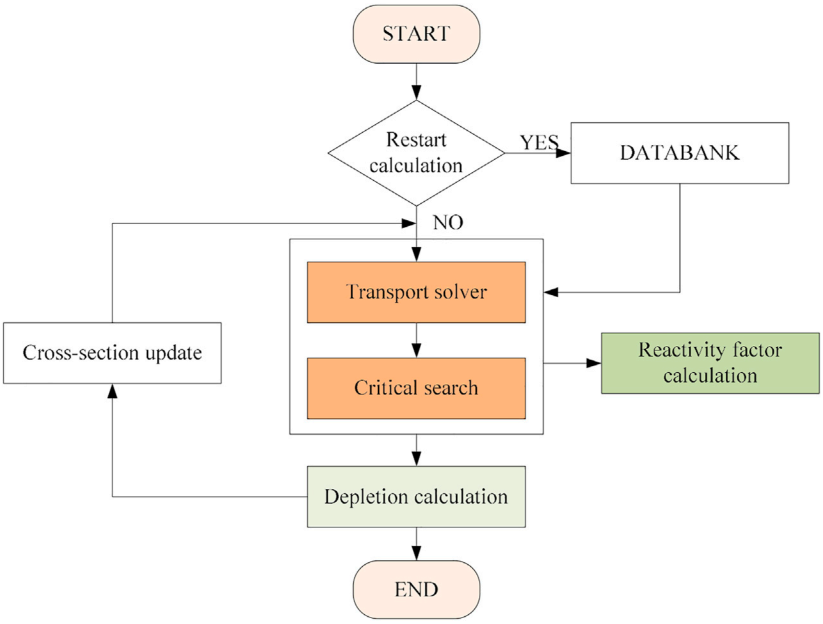

FIGURE 2
The calculation process of MOCO.

condition. It is different from the actual environment of the assembly in the actual core position. Therefore, the second step is optional to perform an equivalent two-dimensional whole core calculation by the flux spectrum correction module named MOSN to modify the single-assembly neutron energy spectrum.

Core simulation module MOCO is used to simulate core neutron behaviors based on the neutron transport solvers and depletion calculation and so on. The calculation process is shown in Figure 2. Besides the neutron flux and burnup calculation, critical research base on the control rod and reactivity coefficients calculation have been developed in MOCO.

For a complete LBFR simulation, both of MOCS and MOCO are indispensable. MOCS is used to generate the homogenized few-group cross sections in advanced for all types of assemblies. Based on the few-group constants, MOCO will be used to simulate the whole reactor core. Due to the whole-core spatial coupling effect, MOSN is applied to modify the flux of MOCS. In the process of the simulation, the data between the three modules is transferred through files.

Finally, the sensitivity and uncertainty analysis module called SUN will be used to evaluate and quantify the confidence of the calculated results. The SUN module will call MOCS as a black box to generate the perturbed multi-group cross-sections, and call MOCO as a black box to get the results of response quantities.

2.1 MOCS: Cross-sections generation module

In order to balance computational accuracy and efficiency, an equivalent one-dimensional assembly is modeled in MOCS. The coupling method based on the narrow resonance approximation and the ultrafine group method is utilized to deal with the complex resonance effect in LBFR. Due to the plausibility in the high energy range, the resonance calculation method based on the narrow resonance approximation is used. As the energy decreases, the error introduced by the narrow resonance approximation gradually increases. So below the energy divider, ultrafine group slowing-down equations are solved to accurately simulate the neutron slowing process directly, which can avoid the error brought by the narrow resonance approximation.

In the high energy range, the effective resonant self-screening cross-sections based on the narrow resonance approximation is calculated as follows:

$$\bar{\sigma}_{x,i,g} = \frac{\int_{\Delta E_g} \sigma_{x,i}(E)\phi(E)dE}{\int_{\Delta E_g} \phi(E)dE} \approx \int_{\Delta E_g} \sigma_{x,i}(E) \frac{\sum_p (E)}{E.\sum_t (E)} dE \Big/ \int_{\Delta E_g} \frac{\sum_p (E)}{E.\sum_t (E)} dE \tag{1}$$

where $\sigma_{x,i}(E)$ is the point-wise cross-section of type x for the resonant isotope i at the energy point E, and ΔE_g is lethargy width in the energy group g.

The potential scattering cross-sections is assumed to be constant in each energy group, so the equation can be further simplified as follows:

$$\bar{\sigma}_{x,i,g} \approx \int_{\Delta E_g} \frac{\sigma_{x,i}(E)}{E \cdot \Sigma_t (E)} dE \Big/ \int_{\Delta E_g} \frac{1}{E \cdot \Sigma_t (E)} dE \tag{2}$$

The elastic scattering matrix is divided into two parts: the total effective elastic scattering cross-sections and the scattering function. Since the information of elastic scattering cross-sections and total cross-sections are given in the form of point cross-sections in the database, the total effective elastic scattering cross-sections can be solved by Eq. 2. The scattering function is calculated as follows:

$$\sigma_s^l (g \to g') = \bar{\sigma}_{s,g}.F(l, \alpha, g \to g') \tag{3}$$

$$F(l, \alpha, g \to g') = \frac{\int_{\Delta E_g} \int_{\Delta E_{g'}} \frac{p_l (\mu_s (E,E'))}{E} \sum_{n=0}^{N} (2n+1) a_n (E) p_n (\mu_c (E, E')) dE dE'}{\Delta E_g (1 - \alpha)} \tag{4}$$

Like the elastic scattering matrix, the scattering matrix of the inelastic scattering reaction and the threshold energy reaction also represents the probability of the corresponding reaction. Compared with the elastic scattering reaction, the cross-sections of the inelastic scattering reaction and the threshold energy reaction is flatter with energy, and its resonance effect is much weaker than that of the elastic scattering reaction. Therefore, the scattering matrix of such reactions is less relevant to the problem and is produced in advance in MOCS.

The collision probability method (CPM) is used to determine the neutron flux based on the cross-sections as follows:

$$\phi_{0,g,r} = \sum_{r'} \left[\sum_{g'} \left(\Sigma_{s,0,g' \to g,r'} + \frac{\chi_g}{k_{eff}} \upsilon \Sigma_{f,j,g'} \right) \phi_{0,g',r'} \right] \frac{P_{r \to r',g} V_{r'}}{\Sigma_{t,g,r} V_r} \tag{5}$$

Below the energy divider, the ultrafine group method solves the neutron slowing process precisely to eliminate the approximate. In the lower energy range, MOCS neglects the inelastic scattering source term as well as the fission source term, and set cross-sections as a constant in each ultrafine group. The slowing down equations are as follows:

$$\sum\nolimits_{r,h}^{t} \phi_{r,h} V_r = \sum_{r'} p_{r' \to r,h} V_{r'} \sum_i s_{i,h} \tag{6}$$

$$s_{i,h} = \sum_{h'=1}^{H} N_{r^i,i} \sigma^e_{r',i,h-h'} \phi_{r',h-h'} p_{i,h'} \tag{7}$$

Without using the flux spectrum correction module MOSN, the neutron flux for the equivalent one-dimensional assembly would be calculated in MOCS to collapse the cross-sections from 1968 groups into 33 groups. In the homogenization process, the super homogenization method (SPH method) (Hebert, 2009) is optional to be used as the homogenization technique. In order to

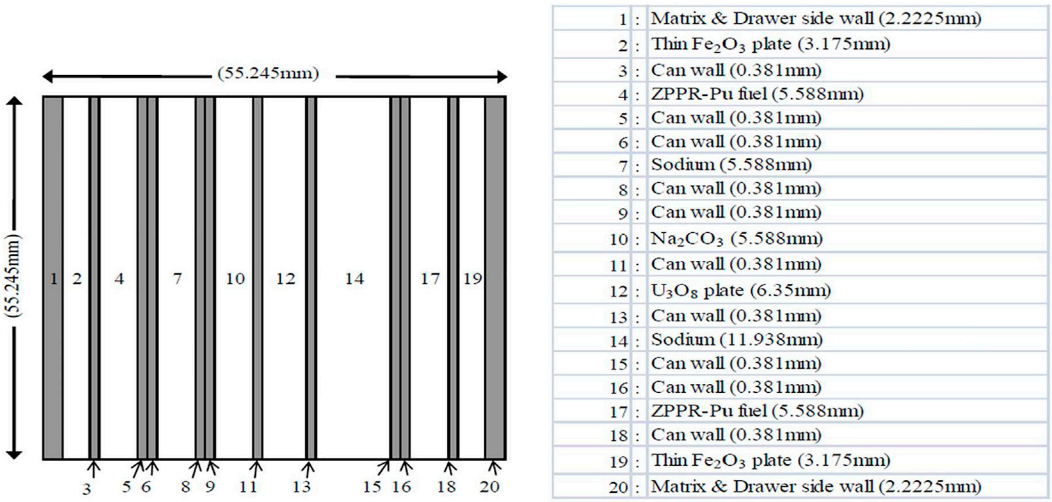

1 :	Matrix & Drawer side wall (2.2225mm)
2 :	Thin Fe_2O_3 plate (3.175mm)
3 :	Can wall (0.381mm)
4 :	ZPPR-Pu fuel (5.588mm)
5 :	Can wall (0.381mm)
6 :	Can wall (0.381mm)
7 :	Sodium (5.588mm)
8 :	Can wall (0.381mm)
9 :	Can wall (0.381mm)
10 :	Na_2CO_3 (5.588mm)
11 :	Can wall (0.381mm)
12 :	U_3O_8 plate (6.35mm)
13 :	Can wall (0.381mm)
14 :	Sodium (11.938mm)
15 :	Can wall (0.381mm)
16 :	Can wall (0.381mm)
17 :	ZPPR-Pu fuel (5.588mm)
18 :	Can wall (0.381mm)
19 :	Thin Fe_2O_3 plate (3.175mm)
20 :	Matrix & Drawer side wall (2.2225mm)

FIGURE 3
Geometry and layout of the ZPPR-10B assembly.

get the cross-sections of the non-fuel assemblies, the multi-zone homogenization calculations would be carried out to determine the SPH factor in MOCS. The cross-sections are modified as follows:

$$\tilde{\Sigma}_{x,i,g}^{hom} = \mu_{i,g}\Sigma_{x,i,g}^{hom} \tag{8}$$

2.2 MOSN: Flux spectrum correction module

Due to the obvious whole-core spatial coupling effect and strong energy spectrum interference effect in the LBFR, A two-dimensional equivalent core is modeled to represent the actual reactor core for the flux spectrum correction in MOSN. The two-dimensional cylindrical core is simplified by using the volume equivalence method.

The two-dimensional core transport calculation is carried out based on the 1968-group cross-sections. The neutron flux of each assembly will be modified to collapses the 33-group cross-sections for use in the MOCO. The S_N method with parallel capability is applied to solve the transport equations in MOSN.

2.3 MOCO: Core simulation module

Based on the 33-group cross-sections generated by MOCS and MOSN, the core simulation is carried out by MOCO. The S_N method with triangular grid is applied as the solver of the transport equations. Functions such as depletion, critical search and reactivity coefficient calculation are included in MOCO.

The three-dimensional multi-group neutron transport equation within the triangular prism grid can be written as follows. MOCO assumes that the fission source is isotropic and scattering sources is anisotropic in the derivation.

$$\mu^m \frac{\partial \Psi_g^m(x,y,z)}{\partial x} + \eta^m \frac{\partial \Psi_g^m(x,y,z)}{\partial y} + \frac{\xi^m}{h_z}\frac{\partial \Psi_g^m(x,y,z)}{\partial z} + \Sigma_t^g \Psi_g^m(x,y,z) = \hat{Q}_g(x,y,z) \tag{9}$$

where m represents a certain angular direction, μ^m, η^m, ξ^m is the component of the angular direction m on the coordinate axis (x, y, z), $\Psi_g^m(x,y,z)$ is the angular flux of the g-th group.

In LBFR, besides of the heat generated by the fission reaction, the energy produced by the capture reaction of neutrons and by the reaction of photons is an important part of the whole power. In order to estimate the energy accurately without much cost, it was assumed that the energy of neutrons produces only from fission reaction and capture reaction, and the energy of photons is deposited at the place where the corresponding reaction occurs. The core power is calculated as the following equation:

$$P = \sum_g \sum_i N_i \left\{ k_i \sigma_{f,i,g} + q_{c,i}\sigma_{c,i,g} - q_{loss} \right\} \phi_g \tag{10}$$

where k_i and $q_{c,i}$ represent the energy produced by each fission reaction and by each radiation capture reaction of nuclide i. $\sigma_{f,i,g}$ and $\sigma_{c,i,g}$ is the fission cross-section and capture cross-section of g-th group, and q_{loss} is the energy lost:

$$q_{loss} = \left[(\nu - 1)\sigma_{f,i,g} - \sigma_{c,i,g} \right] \bar{E} \tag{11}$$

TABLE 1 The k_{inf} results of different assemblies.

Assemblies	k_{inf} of OpenMC	k_{inf} of MOCS	Raltive error/pcm
ZPPR-10B	1.13258	1.13383	125
MET-1000	1.30775	1.30944	169
JOYO	0.18316	0.18142	−174

TABLE 2 Geometric and material parameters of the critical experiments.

Parameters	HMF27	PMF35	HMF57-1	HMF57-2
Fuel	^{235}U	^{239}Pu	^{235}U	^{235}U
Enrichment (%)	90	98	93.17	93.17
Reflector	lead	lead	lead	lead
Radius of center cavity (cm)	1.019	1.2	0.555	0.555
Thickness of fuel (cm)	7.331	4.8	6.555	6.9235
Thickness of reflector (cm)	3.25	3.15	17.22	8.99
Temperature (K)	293	293	293	293

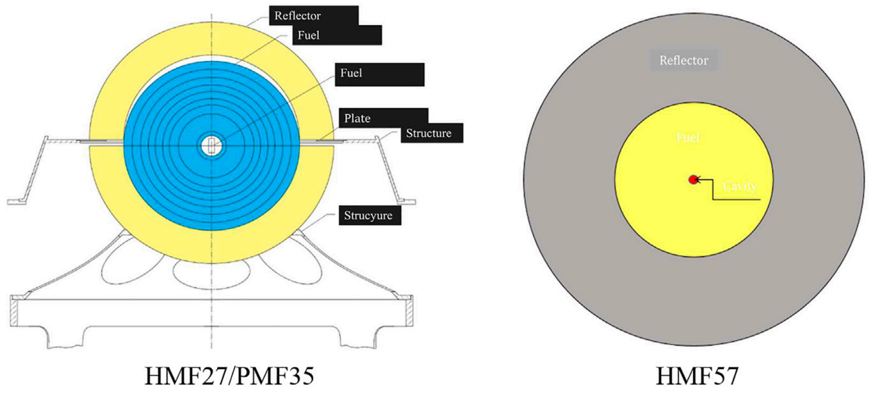

FIGURE 4
Diagrams of lead-based critical experiments.

$$\bar{E} = \frac{\sum \bar{E}_g \phi_g}{\sum \phi_g}, \quad \bar{E}_g = \frac{E_{g=1} - E_g}{\log\left(E_{g+1}/E_g\right)} \tag{12}$$

The micro-depletion scheme is applied to simulate the core burn up and the Chebyshev Rational Approximation Method (CRAM) is used to solve the depletion equation. In MOCO, three different depletion chains, 11 heavy isotopes, 21 heavy isotopes and 118 heavy isotopes, are provided as different options for different core system. For the LBFR, the chain which contains 21 heavy isotopes and 49 fission products is usually used for core simulation.

Considering the weak feedback effect of LBFR, the combination of the direct method and the perturbation theory is used to determine the reactivity coefficients. Based on the neutron transport equation, the form of the perturbation equation can be written as follow:

$$\langle \phi^* \,|\, \delta(L - \lambda F)\phi \rangle = 0 \tag{13}$$

where ϕ^* is the adjoint flux.

TABLE 3 The k_{inf} results of lead-based critical experiments.

Code	Nuclear data file	HMF27 k_{inf}	PMF35 k_{inf}	HMF57-1 k_{inf}	HMF57-2 k_{inf}
		±variance	±variance	±variance	±variance
Measured value	-	1.00000	1.00000	1.00000	1.00000
		±0.00250	±0.00160	±0.00200	±0.00230
MOCS	ENDF/B-VII.0	0.99993	0.99674	0.98870	0.99727
MCNP	ENDF/B-VII β3	1.00070	0.99790	0.98970	0.99850
		±0.00010	±0.00010	±0.00010	±0.00010
MCNP	ENDF/B-VI.8	1.00590	1.00800	1.00230	1.0087
		±0.00010	±0.00010	±0.00010	0 ± 0.00010
KENO	299group ABBN-93	0.99910	0.99830	0.98990	0.99820
		±0.00030	±0.00090	±0.00010	±0.00010

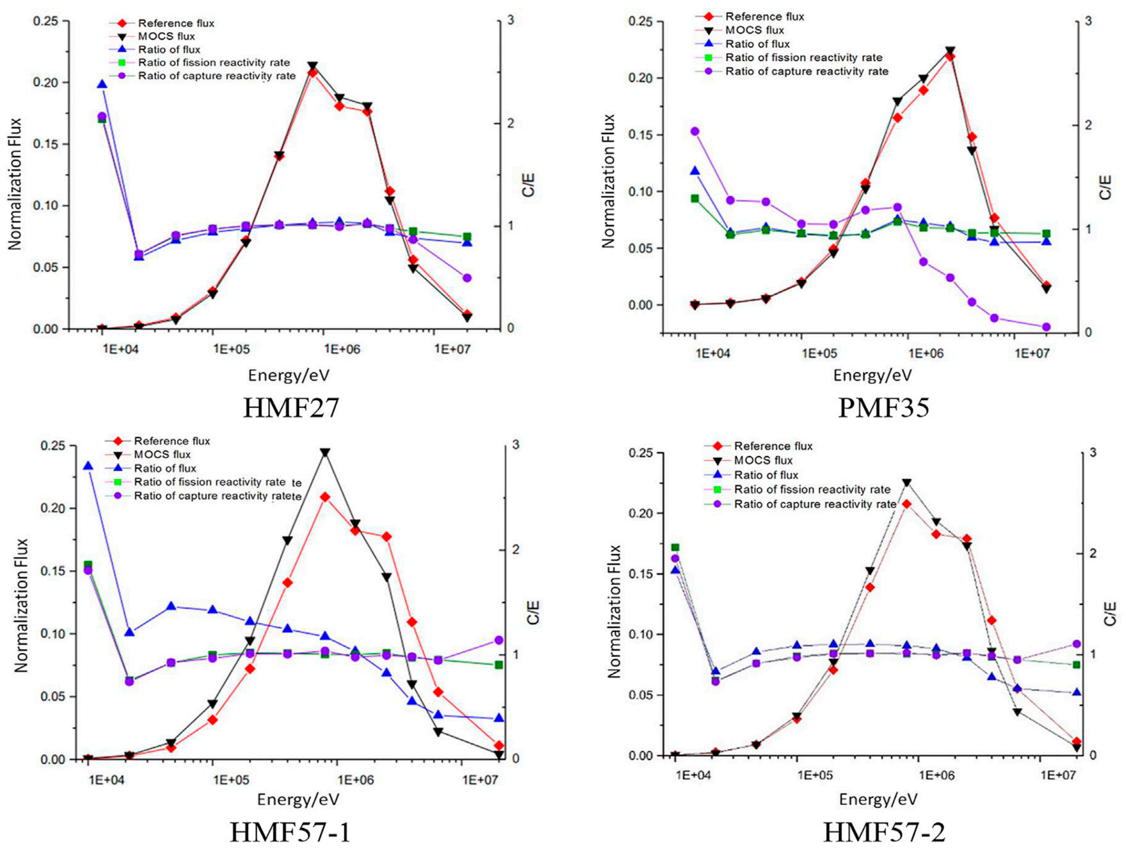

FIGURE 5
Flux and reactivity rate Results of HMF27 and PMF35.

TABLE 4 Results of fission reactivity rate and capture reactivity rate.

Reaction	Nuclide	HMF27		Nuclide	PMF35	
		reference	MOCS		reference	MOCS
Ratio of fission reactivity rate (%)	^{234}U	0.8	0.8	^{239}Pu	94.5	95.4
	^{235}U	86.7	86.8	^{240}Pu	1.1	1.2
	^{238}U	1.4	1.4	^{239}Pu	4	3.3
Ratio of capture reactivity rate (%)	^{234}U	0.2	0.1	^{240}Pu	0.1	0.1
	^{235}U	10.2	10.2	Ga	0.1	0.1
	^{238}U	0.7	0.7	Ni	0.2	0.0

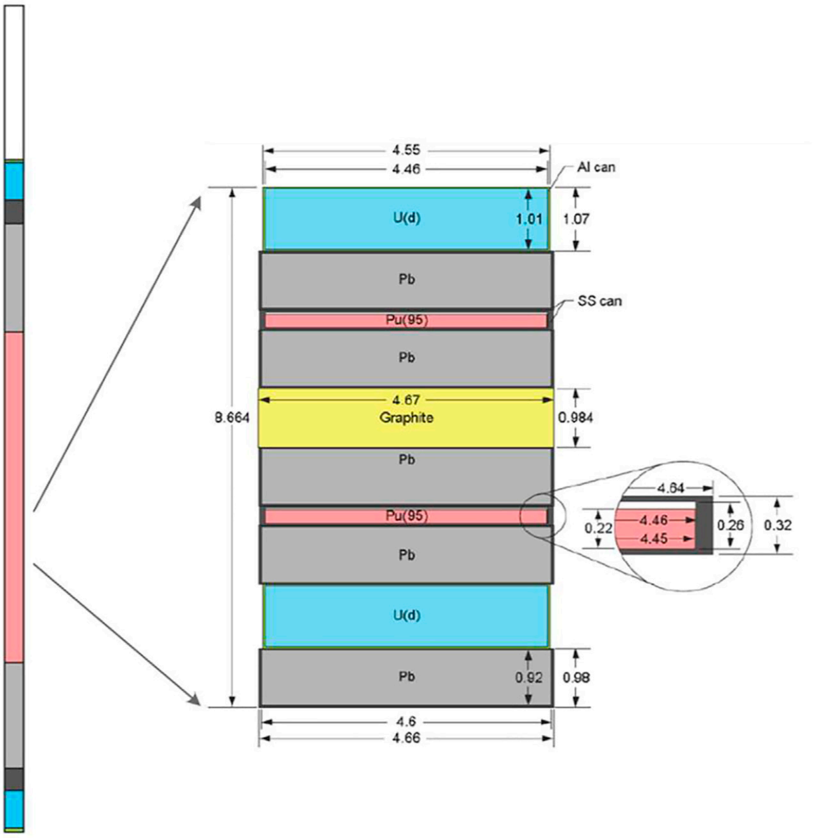

FIGURE 6
Layout of the fuel unit.

2.4 SUN: Sensitivity and uncertainty analysis module

The SUN module is mainly used to perform a sensitivity analysis and quantify uncertainty for the core simulation.

The Latin hypercube sampling method is used to generate the library of the perturbed multi-group cross-sections. The consistency of the perturbed cross-sections is maintained in the process of the cross-section perturbation and MOCO is used to perform the core simulation based on all samples of

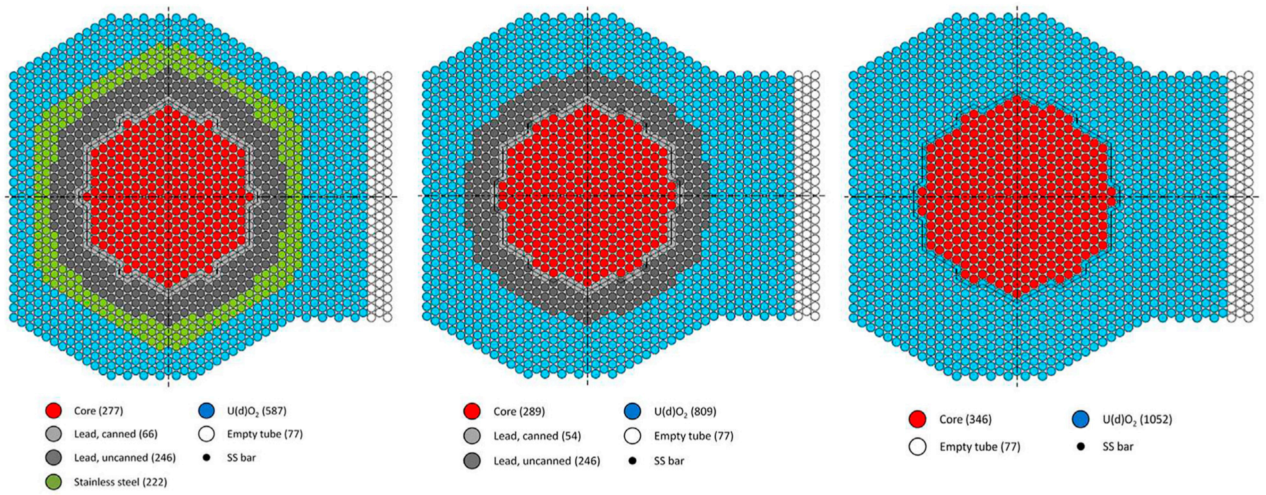

(1) BFS-61-1 (2) BFS-61-2 (3) BFS-61-3

FIGURE 7
Core layout of BFS-61.

TABLE 5 Summary of the eigenvalue results of BFS-61.

CORE	Measured value	MCNP k_{inf}	MOOC k_{inf}	Difference with measured value/pcm	Difference with MCNP/pcm
	±variance	±variance			
BFS-61-1	1.00030	1.0006	0.99487	−545.6	−305.2
	±0.0029	±0.0002			
BFS-61-2	1.00040	0.9978	0.99349	−694.8	−132.1
	±0.0029	±0.0002			
BFS-61-3	1.00040	0.9966	0.99302	−743.3	−170.4
	±0.0027	±0.0002			

the perturbed cross-sections library. Based on the core results, the data statistics as well as uncertainty calculation of the response quantities would be carried out.

The sensitivity analysis calculation is performed by either the direct perturbation method or the reverse sampling method. In the direct perturbation method, a two-way perturbation approach is applied and its sensitivity coefficient is calculated by the following formula:

$$S_j = \frac{\sigma_j \partial R}{\bar{R} \partial \sigma_j} \approx \frac{\sigma_j \mathrm{V} R}{\bar{R} \mathrm{V} \sigma_j} = \frac{\sigma_j (R_+ - R_-)}{\bar{R} \cdot 2\mathrm{V} \sigma_j} \tag{14}$$

where R_+ is the response value under positive perturbation conditions, R_- is the response value under negative perturbation conditions, and $\bar{R}$ is the response value under without perturbation.

The formula for calculating the sensitivity coefficient based on the reverse sampling method is:

$$S_\sigma^k = (A_{\sigma,\sigma})^{-1} A_{k,\sigma} \tag{15}$$

where S_σ^k denotes the sensitivity coefficient of the response k to the cross-sections σ; $A_{\sigma,\sigma}$ is the relative covariance matrix of the cross-sections; $A_{k,\sigma}$ denotes the relative covariance matrix of the response k to the cross-sections.

3 Numerical results

To verify the cross-sections generation module, three kinds of fuel assemblies, including one-dimensional (1-D) flat fuel

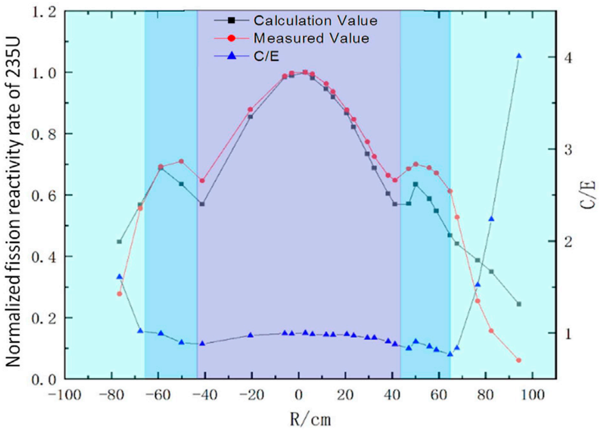

FIGURE 8
Results of normalized ^{235}U fission reactivity rate.

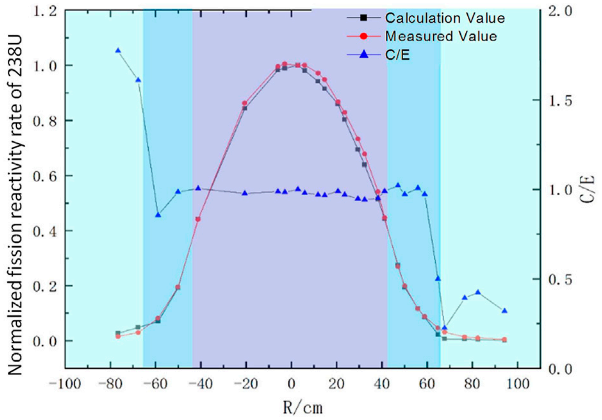

FIGURE 9
Results of normalized ^{238}U fission reactivity rate.

assembly of the critical experiment ZPPR-10B (Sanda et al., 2006a) as shown in Figure 3, 1-D cylindrical fuel assembly of MET-1000 benchmark (OECD/NEA, 2016), and 1-D cylindrical breeding assembly of the JOYO reactor (Yokoyama et al., 2006) are calculated. The accuracy and the ability to handle the heterogeneous effect can be verified. The reference solutions were obtained using the continuous energy Monte-Carlo code OpenMC. The results of eigenvalues are shown in Table 1, and the relative errors are within 200 pcm compared with the reference solutions.

Three lead-based critical experiments, including HEU-MET-FAST-027 (HMF27), PU-MET-FAST-035 (PMF35) and HEU-MET-FAST-057 (HMF57), are modeled for the further validation of MOCS. All three critical experiments consist of high enrichment fuel and lead reflector, the geometric and material parameters are shown in Table 2. The diagrams are shown in Figure 4.

The reference solutions were supported by the benchmark report which are measured values and results determined by the continuous energy Monte-Carlo code MCNP and KENO with different evaluation nuclear data files. The results of eigenvalues are shown in Table 3. Except for HMF57-1, the results of MOCS are in good agreement with the measured values. Compared with the Monte-Carlo code, the relative errors of eigenvalues are very small when the calculations were carried out with the same nuclear data file, and the maximum error is 100pcm.

The results of flux and reactivity rate are shown in Figure 5. Compared with the reference results, the flux at high energy has good calculation accuracy. The errors of flux below 0.01 MeV are much large. Due to the small proportion of the flux below 0.01MeV, they do not increase the error of the whole core calculation. The ratios between the results of MOCO and Monte-Carlo code show the same pattern. The results of fission reactivity rate and capture reactivity rate of different nuclides in the corresponding total reactivity rate agree well with the reference solution as shown in Table 4.

The Russian lead-cooled fast reactor BFS-61 (Manturov et al., 2006) has been modeled to validate MOSASAUR. The BFS-61 is a hexagonal core made of a stainless-steel tube with an outer diameter of 5.0 cm and a height of 216 cm arranged in accordance with a scheme of 5.1 cm rod spacing. Pie-shaped pellets are arranged in the stainless-steel tube in an axially laminated manner, and the pellet material includes fuel, coolant, and reflector and so on. The fuel rod is 86.64 cm high and made of 10 identical units. Each unit is shown in Figure 6. BFS-61 has three different core layouts as shown in Figure 7, and different types and numbers of rods are used.

The reference solution is provided by the benchmark report which contains the measured value and the calculation results of MCNP code. The results of MOSASAUR and MCNP are base on the same evaluation nuclear data files ENDF/B-VII.0. The summary of the eigenvalue results is shown in Table 5 and it is indicated that MOSASAUR has more than 500pcm difference compared with the measured value. While MOSASAUR agrees well with MCNP code based on the same nuclear data file.

The fission reactivity rates of different nuclides at several positions in the central plane were measured in the core BFS-61-1. The measured values are normalized based on that of the central plane of the core which is taken as the origin of R coordinate in Figure 8 and Figure 9. The degree of agreement between the calculation value and the measured value is expressed as the ratio C/E. The three different colored areas in the figures represent the active, reflective, and breeding zones. It can be found that the results of MOSASAUR have high accurate in active and reflective zones. The relative errors increase in the outer breeding zones. The flux value in this area is very small and the uncertainty is larger. In the modeling of the cross-section generation and core simulation, several details of the core structural components have been simplified.

4 Conclusion

The LBFR calculation code system named MOSASAUR developed by NPIC, CNNC is introduced in this paper. The deterministic two-step calculation strategy based on the homogenization theory is utilized in MOSASAUR. Four main functional modules and their models make up the whole code system. MOCS is used to generate the 33-group homogenized cross sections based on the ultrafine-group information (1968 groups). MOSN is used to correct the infinite flux spectrum of the single assembly with the reflective condition. MOCO is the simulation code for the whole life of LBFR. The sensitivity and uncertainty analysis module called SUN is used to evaluate and quantify the confidence of the calculated results. The preliminary verification and validation have been carried out, numerical results demonstrate that compared with the Monte-Carlo code, the relative errors of eigenvalues are smaller than 350pcm when the calculations were carried out with the same nuclear data file. Compared with the measured values, the errors will increase due to the simulation details and the measurement accuracy. The results indicated that MOSASAUR has good performances in dealing with lead-based cooled fast reactor. Modules of coupled neutron and gamma heating calculation, thermal-hydraulic feedback and core transient simulation are being developed and further verification and validation will be carried out later.

Data availability statement

The original contributions presented in the study are included in the article/supplementary material, further inquiries can be directed to the corresponding author.

Author contributions

BZ: Methodology, Software, Investigation, Numerical Analysis, Writing—Original Draft; LW: Methodology, Numerical Analysis; LL: Software, Investigation; CHZ: Numerical Analysis; XP: Methodology, Validation; MY: Methodology; BX: Methodology; CEZ: Numerical Analysis; LQ: Numerical Analysis; QW: Writing—Original Draft.

Funding

This research is supported by the National Natural Science Foundation of China (Approved number Nos. 12075228 and Nos. 12205283).

Acknowledgments

All the authors would like to thank NECP laboratory of Xi'an Jiaotong University for the architecture of the whole system and thank to North China Electric Power University for the help with the sensitivity and uncertainty analysis method.

Conflict of interest

The authors declare that the research was conducted in the absence of any commercial or financial relationships that could be construed as a potential conflict of interest.

Publisher's note

References

Archier, P., Palau, J. M., Vidal, J. F., Pascal, V., and Santandrea, S. (2016). New reference APOLLO3 calculation scheme for sodium cooled fast reactors: From sub-assembly to full-core calculations, Proceeding of the PHYSOR, May 1–5 2016, Sun Valley, USA.

Bouchard, J., and Bennett, R. (2008). Generation IV advanced nuclear energy systems. *Nucl. Plant J.* 26 (5), 42–45.

Cai, L. (2014). *Condensation et homogénéisation des sections efficaces pour les codes de transport déterministes par la méthode de Monte Carlo: Application aux réacteurs à neutrons rapides de GEN IV*. France: Doctoral Dissertation. Université Paris-Sud.

Derstine, K. L. (1984). *DIF3D: A code to solve one-, two-, and three-dimensional finite difference diffusion theory problems, ANL-82-64*. Lemont, Illinois: Argonne National Laboratory.

Downar, T., Kochunas, B., and Collins, B. (2016). *Validation and verification of the MPACT code*[C]. Sun valley ID United States: American Nuclear Society, 2961–2978.

Grimstone, N. M. Marseille, France. April 23–27, 1990. Accurate treatment of fast reactor fuel assembly heterogeneity with the ECCO cell code, Proceeding of PHYSOR90.

Hebert, A. *Applied reactor physics*[M]. Montreal, Canada: Presses Internationales Polytechnique, 2009.

Henryson, H., Toppel, B. J., and Sternberg, C. G. (1973). Paper Presented in Seminar on Nuclear Data Processing Codes. Ispra. Italy: ETOE-2/MC2-2/SDX, multigroup neutron cross section processing system

Heo, W., Kim, W., and Kim, Y., 2013. Feasibility of A Monte Carlo-deterministic hybrid method for fast reactor analysis. In: Proceeding of M&C 2013, May 5–9 2013, Sun Valley, Idaho.

Hu, D. P., and Yuan, H. Q. (1995). Reactor physics characteristics of lead cooled fast reactor-A new type fast nuetron reactor. *Nucl. Power Eng.* 16 (3), 195–198.

Lee, C. H., and Yang, W. S. (2012). *MC2-3: Multigroup cross section generation code for fast reactor analysis, ANL/NE-11-41*. Lemont, Illinois: Argonne National Laboratory.

Li Z, M., Igor Li, M., and Igor, Z. Jeju Korea. April 16–20, 2017. A new tone's method in APOLLO3 and its application to ZPPR benchmarks, Proceeding of the M&C2017.

Liu, S. H., Wang, Z. J., Jia, H., He, Y., Dou, W. P., Qin, Y. S., et al. (2017). Physics design of the CIADS 25MeV DEMO facility. *Nucl. Instrum. Methods Phys. Res. Sect. A Accel. Spectrom. Detect. Assoc. Equip.* 843, 11–17. doi:10.1016/j.nima.2016.10.055

Macfarlane, R. E., and Muir, D. W. (1994). *The NJOY nuclear data processing system*. Los: Alamos National Laboratory.

Manturov, G., Kochetkov, A., Sememnov, M., et al. (2006). *BFS-62-3Aexperiment: Fast reactor core with U and U-Pu fuel of 17% enrichment and partial stainless steel reflector*. Paris, France: NEA/NSC.DOE, 1. IRPHE Handbook.

Nikitin, E., Fridman, E., Mikityuk, K., et al. (2015). Solution of the OECD/NEAneutronic SFR benchmark with serpent-dyn3d and serpent-PARCS code systems. *Ann. Nucl. Energy* 75, 492497. doi:10.1016/j.anucene.2014.08.054

OECD/NEA (2016). *Benchmark for neutronic analysis of sodium-cooled fast reactor cores with various fuel types and core sizes NEA/NSC/R*. Paris, France: OECD/NEA 9.

Palmiotti, G., Lewis, E. E., and Carrico, C. B. (1995). *Variant: VARIational anisotropic nodal transport for multidimensional cartesian and hexagonal Geometry calculation, ANL-95/40*. Lemont, Illinois, Argonne National Laboratory.

Rachamin, R., and Kliem, S. (2017). Validation of the dyn3d-serpent code system for SFR cores using selected BFS experiments. Part I: Serpent calculations. *Ann. Nucl. Energy* 102, 158–167. doi:10.1016/j.anucene.2016.12.023

Sanda, T., Ishikawa, M., Lell, R. M., et al. (2006a). *ZPPR-10Bexperiment: A 650 MWe-class sodium-cooled MOX-fueled fbr homogeneous core mock-up critical experiment with two enrichment zones, seven control rods and twelve control rod positions ZPPR-LMFR-EXP-005*. Paris, France: NEA/NSC/Doc. OECD/NEA 1.

Shemon, E. R., Smith, M. A., and Lee, C. H. (2017). Jeju, Korea. April 16–20, 2017.Direct neutronics modeling approach for deformed core analysis using PROTEUS, Proceeding of M&C 2017.

Wang, K., Li, Z. G., She, D., Liang, J., Xu, Q., Qiu, Y., et al. (2015). Rmc – a Monte Carlo code for reactor core analysis. *Ann. Nucl. Energy* 82, 121–129. doi:10.1016/j.anucene.2014.08.048

Wu, Y. C. (2016). Design and R&D progress of China lead-based reactor for ads research facility. *Engineering* 2 (1), 124–131. doi:10.1016/j.eng.2016.01.023

Xu, M. (2009). Fast reactor and sustainable nuclear energy development in China. *China Nucl. Power* 2 (2), 106–120.

Yokoyama, K., Shono, A., Sanda, T., et al. (2006). *Japans experimental fast reactor JOYOMKI core: Sodium-cooled uranium-plutonium mixed oxide fueled fast core surrounded by UO2 blanket JOYO-LMFR-RSR-001*. Paris, France: NEA/NSC/Doc.OECD/NEA 1.

Zhang, B., Li, Y. Z., Wu, H. C., Cao, L., and Shen, W. (2016). Evaluation of pin-cell homogenization techniques for PWR pin-by-pin calculation. *Nucl. Sci. Eng.* 186 (2), 134–146. doi:10.1080/00295639.2016.1273018

Zheng, Y. Q., Du, X. N., Xu, Z. T., Zhou, S., Liu, Y., Wan, C., et al. (2018). Sarax: A new code for fast reactor analysis part I: Methods. *Nucl. Eng. Des.* 340, 421–430. doi:10.1016/j.nucengdes.2018.10.008

Zheng, Y. Q., Qiao, L., Zhai, Z. A., Du, X., and Xu, Z. (2018). Sarax: A new code for fast reactor analysis part II: Verification, validation and uncertainty quantification. *Nucl. Eng. Des.* 331, 41–53. doi:10.1016/j.nucengdes.2018.02.033

Frontiers in
Energy Research

Advances and innovation in sustainable, reliable and affordable energy

Explores sustainable and environmental developments in energy. It focuses on technological advances supporting Sustainable Development Goal 7: access to affordable, reliable, sustainable and modern energy for all.

Discover the latest Research Topics

See more →

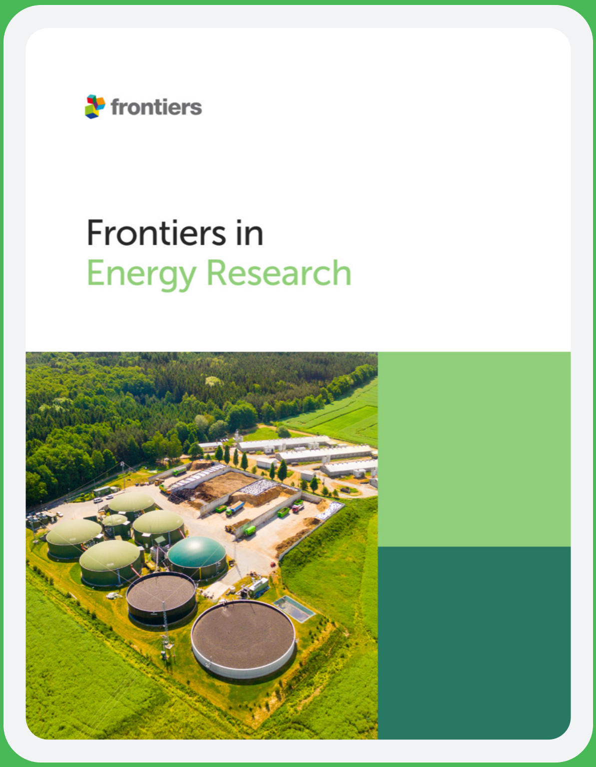
frontiers

Frontiers in
Energy Research

Frontiers

Avenue du Tribunal-Fédéral 34
1005 Lausanne, Switzerland
frontiersin.org

Contact us

+41 (0)21 510 17 00
frontiersin.org/about/contact